

Carbon and Energy Flow Dynamics in a Coastal Salt Marsh

James Chacko Kathilankal
Thiruvananthapuram, Kerala, India

Master of Science (Agricultural Meteorology), CCS Haryana Agricultural University, 2003
Bachelor of Science (Agriculture), Kerala Agricultural University, 2001

A Dissertation presented to the Graduate Faculty
of the University of Virginia in Candidacy for the Degree of
Doctor of Philosophy

Department of Environmental Sciences

University of Virginia
August, 2008



Jose D Fuentes

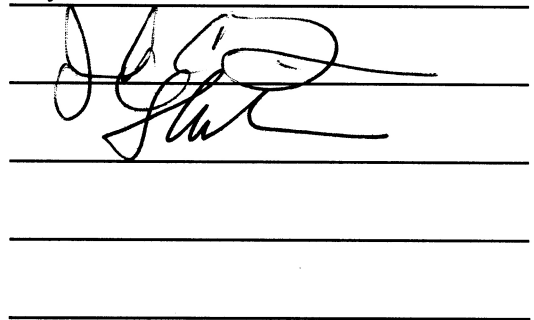


Table of contents.

| | |
|---|----|
| Abstract | iv |
| Acknowledgments | v |
| List of Figures..... | vi |
| List of Tables..... | ix |
| Background and Introduction | 1 |
| References | 5 |
| Chapter 1. Flux tower design and set up | 6 |
| 1.1. Introduction..... | 6 |
| 1.2. Research site characteristics | 7 |
| 1.3. Flux tower construction | 9 |
| 1.4. Power supply system | 10 |
| 1.5. Flux tower instrumentation | 13 |
| 1.6 Data acquisition system | 15 |
| 1.7. Flux calculations | 17 |
| 1.8. Data analysis..... | 19 |
| 1.9. Flux footprint estimates | 20 |
| 1.10. Spectral characteristics of turbulence | 22 |
| 1.11. Summary | 25 |
| References | 25 |
| Chapter 2. Physiological attributes of <i>Spartina alterniflora</i> | 28 |
| 2.1. Introduction..... | 28 |
| 2.2 Site Characteristics | 30 |
| 2.3. Materials and Methods..... | 30 |
| 2.3.1 Plant physiology measurements..... | 30 |
| 2.3.2 Empirical analysis of A-PAR and A-Ci curves | 31 |
| 2.3.3 Determination of plant physiological variables | 32 |
| A) Determination of V_{cmax} and V_{pmax} | 34 |
| B. Determination of J_{max} | 36 |
| C. Temperature relationships for plant physiological constants | 37 |
| 2.3.4. Modeling stomatal conductance | 38 |
| 2.3.5 Rapid light curve measurements | 38 |
| 2.4. Results and Discussion | 40 |
| 2.4.1. Diurnal trends in leaf level assimilation-Mechanistic response curve analysis | 40 |
| 2.4.2 Temperature dependence of V_{cmax} , V_{pmax} , and J_{max} | 43 |
| 2.4.3. Relationship between stomatal conductance and photosynthetic rate..... | 48 |
| 2.4.4. Physiological response to submergence | 50 |
| 2.5. Summary and conclusions | 52 |
| References | 54 |
| Chapter 3. Carbon flow dynamics in an intertidal salt marsh..... | 60 |
| 3.1. Introduction..... | 60 |
| 3.2. Material and Methods..... | 62 |
| 3.2.1. Study site | 62 |
| 3.2.2. Instrumentation | 63 |
| 3.3. Results..... | 64 |
| 3.3.1. Diurnal/Seasonal trends in carbon assimilation and micrometeorological variables.... | 64 |
| 3.3.2. Key environmental forcings on carbon assimilation | 68 |
| A) Photosynthetic active radiation (PAR) | 68 |
| B) Effect of irradiance and cloudiness on NEE..... | 70 |
| C) Temperature and vapor pressure deficit (VPD)..... | 75 |
| D) Ecosystem respiration..... | 77 |
| E) Tidal influences | 78 |
| F) Quantification of loss in CO_2 flux due to tidal inundation | 80 |

| | |
|---|-----|
| G) Quantification of seasonal carbon assimilation | 81 |
| 3.4. Conclusions | 84 |
| References | 85 |
| Chapter 4: Partitioning of available energy in an intertidal salt marsh..... | 93 |
| 4.1. Introduction..... | 93 |
| 4.2. Methodology | 95 |
| 4.2.1. Study site | 95 |
| 4.2.2. Instrumentation | 95 |
| 4.2.3. Bulk canopy parameters estimations | 96 |
| 4.3. Results..... | 98 |
| 4.3.1. Surface energy budget | 98 |
| 4.3.2. Examining energy balance closure and tidal influences..... | 103 |
| 4.3.3. Canopy controls on flux partitioning-influence of bulk canopy parameters | 107 |
| 4.3.4. PAR reflectivity..... | 113 |
| 4.4. Conclusions | 113 |
| References | 114 |
| Chapter 5. Modeling carbon and energy flows in an intertidal coastal marsh | 119 |
| 5.1. Introduction..... | 119 |
| 5.2. Model description | 121 |
| 5.2.1. C ₄ photosynthesis model: Source/Sink strength of CO ₂ | 123 |
| 5.2.2. Temperature and photosynthetic active radiation (PAR) controls on photosynthesis | 126 |
| 5.2.3. Shortwave radiative transfer: Multiple-layer canopy scattering model | 127 |
| 5.2.4. Long wave radiative transfer model: LRTM..... | 131 |
| 5.2.5. Scalar dispersion in plant canopies- Localized Near Field theory..... | 133 |
| 5.2.6. Wind and turbulent statistics within and above plant canopies | 135 |
| 5.2.7. Model Implementation | 136 |
| 5.3. Results and Discussion | 137 |
| 5.3.1. Model representation of canopy processes | 137 |
| 5.3.2. Model outputs –clear and cloudy sky comparisons | 144 |
| 5.3.3. Model performance: tidal influences | 147 |
| 5.3.4. Factors affecting model performance | 150 |
| 5.4. Summary | 151 |
| References | 152 |
| Synthesis..... | 157 |
| Appendix A..... | 159 |
| Appendix-B..... | 162 |
| Appendix C..... | 165 |

Abstract

This dissertation is based on measurements from a flux tower system utilizing eddy covariance methodology and other micrometeorological sensors during the period from May 2007 to December 2007 at the eastern shore of Virginia, USA over an intertidal salt marsh. Leaf level physiology measurements were undertaken to relate leaf-level exchange processes to ecosystem level. The particular physiology of *Spartina alterniflora* with a decreased phospho-enol pyruvate (PEP) carboxylase activity and low light saturation capacity and its implications on ecosystem level exchange processes are identified. *Spartina alterniflora* dominated intertidal salt marshes are moderate sinks for carbon fixing about $8-10 \mu\text{mol m}^{-2} \text{s}^{-2}$ of carbon dioxide during the active growth stage, but become source of carbon dioxide during the inactive or winter months. Tidal activity has a major role in modulating the partitioning of available energy and net ecosystem exchange. The decreased assimilation rates observed under submerged conditions can be interpreted as a possible response of inter-tidal salt marshes to sea level rise as the hydro-period over a marsh increases. Land-sea breeze systems operating in intertidal coastal zones can advect moisture from the ocean surface and ecosystem level flux measurements should be interpreted by considering the advective processes in the interpretation of available energy partitioning. A biophysical model incorporating the C_4 photosynthetic pathway and incorporating the theories of turbulent transport relating source strength to concentration profile have been developed as a tool for accessing ecosystem response to climate forcings.

Acknowledgments

This dissertation could be completed only with the help of many people with whom I interacted during my stay at Charlottesville. First and foremost I acknowledge the tutelage provided by my major advisor, Professor Jose D Fuentes, who has helped me during various phases of this research project and my academic life at the University of Virginia. I express my sincere gratitude to the members of my dissertation committee, Paolo D'Odorico, Karen McGlathery, Joseph Zieman and Irina Mitrea for the continuous support and encouragement they provided for the completion of my research work. Thanks are due to my lab mates and colleagues Stephen, Matt, Marcia, Kendra, Tom and Deanne who provided a motivating environment to work and helped with various aspects of my field work. The support and amity provided by my friends Sujith, Sahoo, Teferi, and Dane require special mention. I take this opportunity to thank the staff of the Anheuser-Busch Coastal Research Center (ABCRC), especially Art, Chris, David and Donna without whom the construction and maintenance of the flux tower would have been impossible. I greatly cherish the opportunity and infrastructure provided by the Department of Environmental Sciences and the University of Virginia would to undertake the Ph.D. program in environmental sciences. The financial support I received from the department and the National Science Foundation (grants BSR-8702333-06, DEB-9211772, DEB-9411974, DEB-0080381 and DEB-0621014) is appreciated at the highest degree. The support and encouragement provided by my family back from India needs special mentioning.

List of Figures

| | |
|--|----|
| Figure 1.0. Conceptual diagram illustrating the environmental forcings on ecosystem-atmospheric exchange of energy and carbon from inter-tidal salt marshes. | 2 |
| Figure 1.1. Location map of the flux tower at the VCR-LTER site. | 7 |
| Figure 1.2. Average monthly temperature and rainfall values (1961-1990) for the VCR-LTER site. | 8 |
| Figure 1.3. Tower base top view (A) and side view (B) showing the structural members. The instruments are oriented in the east-west direction | 11 |
| Figure 1.4. A) Flux tower set up with instrumentation along with the battery bank platform during high tide conditions B) Solar panel setup showing the nine panels framed and mounted. | 12 |
| Figure 1.5. Schematic of the power supply set up showing the wiring diagram for the solar panels, charge controller and battery bank. | 12 |
| Figure 1.6. Schematic representation of all micrometeorological instrumentation on the flux tower. | 15 |
| Figure 1.7. Data acquisitions system set up showing the various components and flow of data from sensors to the system. | 16 |
| Figure 1.8. Screen shot of the LABVIEW based data acquisition program showing the program controls and displays | 17 |
| Figure 1.9. The frequency of occurrence for recorded wind directions, and the average wind speed for each corresponding direction (with standard deviations) at the site. | 20 |
| Figure 1.10. Flux footprint probability density function (x,y,w,u) m ⁻¹ , for a sensor deployed at the height of 3.7 m, estimated for neutral atmospheric conditions. | 23 |
| Figure 1.11. Average half-hourly friction velocity and wind direction values for day of year 204 used in the footprint estimation. | 23 |
| Figure 1.12. Average ensemble power spectral densities of the three velocity components (A) (u,v and w) and ensemble power cospectral density for FCO ₂ , H ₂ O and θ (virtual temperature) with vertical velocity (w) | 24 |
| Figure 2.1. Schematic representation of C4 photosynthesis adapted from von Caemmerer (1999). | 35 |
| Figure 2.2. Light (A-PAR) curves obtained for the three different periods of the day. The best fit line was obtained by fitting the data to equation (2.1) is also provided. The measurements were obtained during the peak growing season from June to August 2007. | 42 |
| Figure 2.3. Comparison of A-Ci response curves obtained during different periods of the day. | 44 |
| Figure 2.4. Relationship between Leaf temperature and V _c max obtained from analysis of A-Ci curves. | 45 |
| Figure 2.5. Relationship between Leaf temperature and V _p max obtained from analysis of A-Ci curves. | 46 |
| Figure 2.6. The comparison of A-Ci response curves from this study with typical C ₃ , C ₃ -C ₄ and C ₄ plant types. | 49 |
| Figure 2.7. The relationship between maximum electron transport rate (J _{max}) and leaf temperature. | 49 |
| Figure 2.8. The relationship between stomatal conductance and assimilation. | 50 |
| Figure 2.9. Rapid light curved obtained between 11:00 and 14:00 hours on submerged and exposed <i>Spartina alterniflora</i> plant canopies. | 52 |
| Figure 3.1. Typical diurnal pattern of NEE observed on day of year 182, 2007. | 65 |
| Figure 3.2 Diurnal trends in photosynthetic active radiation (PAR) and air temperature measured above the canopy for day of year 182. | 65 |
| Figure 3.3. Seasonal patterns in NEE for the period from May to December 2007. | 66 |
| Figure 3.4. Diurnal variation in half hourly monthly ensample averages of a) Specific humidity b) PAR C) Soil temperature and D) air temperature during the growing season. | 67 |

| | |
|---|-----|
| Figure 3.5. The relationship between PAR and NEE approximated using a rectangular hyperbolic relationship for three different periods; A) May B) June-July and C) August-September. | 69 |
| Figure 3.6. Relationship between NEE and different PAR components (Direct and Diffuse). | 71 |
| Figure 3.7. Seasonal changes in average monthly values of α and β during the growing season. | 72 |
| Figure 3.8. Relationships between sky conditions and NEE based on clearness index. | 74 |
| Figure 3.9. The relationship between air temperature and day time CO ₂ flux during low tide events of the growing season (May to September) | 75 |
| Figure 3.10. Relationship between VPD and residual NEE (from the estimation of PAR-NEE) relationship | 76 |
| Figure 3.11. Estimated and modeled night time ecosystem respiration as a function of soil temperature. | 78 |
| Figure 3.12. Comparison between CO ₂ assimilation diurnal trends between a day having a high tide-midday event (DOY 244) B) and a low tide mid-day event (DOY 249). | 79 |
| Figure 3.13. The estimation of loss in CO ₂ assimilation capacity due to tidal influence. | 80 |
| Figure 3.14. Comparison between measured and modeled NEE for the month of July. | 82 |
| Figure 3.15. Seasonal patterns in carbon assimilation with positive values indicating a gain and negative indicate a loss in carbon. | 83 |
| Figure 4.1. Energy balance components for three distinct growing periods: A) early and peak growing season (May-July), B) late and end of the growing season (August-October), and C) dormant or inactive period (November to December). | 100 |
| Figure 4.2. Average wind speed and direction for the period from May to July 2007. | 101 |
| Figure 4.3. Computed diurnal Rad values, which represents the percentage of advected latent heat over the marsh surface for the period from May to July, 2007 (low tide). | 103 |
| Figure 4.4. Energy balance closure estimates for three distinct growth periods: A) May-July, B) August-October, C) November-December. | 105 |
| Figure 4.5. Energy balance partitioning for DOY 244 (A) with high tide occurring at the middle of the day and DOY 247 (B) with high tide events occurring during the early morning and evening hours. | 106 |
| Figure 4.6. Relationship between bulk surface conductance (Gs) and atmospheric vapor pressure deficit (D) for the growing season (May-October, 2007). | 108 |
| Figure 4.7. The relationship between bulk canopy conductance and the Priestly-Taylor coefficient (α). | 108 |
| Figure 4.8. Average diurnal decoupling coefficients estimated during the growing season. | 110 |
| Figure 4.9. Trends in monthly ensemble average daytime (10:00 to 14:00 hours) Ω values during the growing season. | 110 |
| Figure 4.10. Relationship between stomatal conductance and Ω for the growing season. | 111 |
| Figure 4.11. Changes in Bowen ratio with the progress of the growing season for the period from 10:00 to 14:00 hours. | 112 |
| Figure 4.12. Monthly average PAR reflectivity estimated during the growing season (May-October, 2007). | 112 |
| Figure 5.1 Schematic representation of the canopy biophysical model. | 137 |
| Figure 5.2. PAR and NIR absorption within the different layers of the canopy simulated by the multiple scattering model for clear sky conditions. The disposition of PAR within the canopy is also provided along with the observed diurnal PAR values measured above the canopy. | 139 |
| Figure 5.3. PAR and NIR absorption within the different layers of the canopy simulated by the multiple scattering model for cloudy sky conditions. | 140 |
| Figure 5.4. Modeled air temperature profiles between clear and cloudy days. | 141 |
| Figure 5.5. Normalized profiles of the Lagrangian time scale (TLu*/h) as a function of normalized height, the standard deviation of vertical velocity (σ_w/u^*) and wind velocity profiles | 142 |
| Figure 5.6. Profiles of CO ₂ mixing ratios modeled above and below the plant canopy as generated from the output obtained from the LNF module of the biophysical model for DOY 187. | 143 |

| | |
|---|-----|
| Figure 5.7. Comparison between estimated and modeled sensible, latent heat and CO ₂ fluxes for clear sky conditions. | 145 |
| Figure 5.8. Comparison between measured and modeled sensible, latent heat and CO ₂ fluxes for cloudy sky conditions. | 146 |
| Figure 5.9. Comparison between estimated and modeled fluxes of sensible heat, latent heat and CO ₂ , for high tide conditions during midday. | 148 |
| Figure 5.10. Comparison between estimated and modeled fluxes of sensible heat, latent heat and CO ₂ fluxes, for low tide conditions during midday. | 149 |

List of Tables

| | |
|--|-----|
| Table 1.1. Micrometeorological instrumentation installed on the flux tower along with the sensor height and numbers of sensors at different levels. | 14 |
| Table 2.1. Summary of all the photosynthetic model parameters used in the determination of plant physiological parameters | 39 |
| Table 2.2. Light curve physiological parameters estimated from non-linear regression analysis. | 41 |
| Table 2.3. A-C _i curve physiological parameters estimated from non-linear regression. | 43 |
| Table 2.4. Non-linear regression coefficients derived for temperature relationships for V_{cmax} , V_{pmax} and J_{max} | 48 |
| Table 2.5. Summary of physiological parameters obtained through non-linear regression analysis from rapid light curve data obtained through pulse amplitude modulated fluometry. | 51 |
| Table 3.1. The coefficients of the rectangular curve fit for the relationship between NEE and PAR. | 70 |
| Table 4.1. Energy balance closure estimate parameters from the RMA analysis | 104 |

Background and Introduction

Recent trends in increasing global temperatures have prompted us to take a closer look at the global carbon cycle. The increased emission of greenhouse gases, a consequence of industrialization, has played a major role in global climate change. Global temperatures have increased by 0.13°C per decade over the last fifty years, whereas the relative sea level rise is of the order of 1.8 mm per year (IPCC report, 2007). The carbon cycle is mainly controlled by the process of photosynthesis and respiration occurring over terrestrial and oceanic ecosystems (Schimel, 1995). Several studies have been initiated to understand ecosystem level carbon cycling in the various biomes of the world. Although different methodologies have been adapted to understand carbon cycling, the eddy covariance method has been accepted as a robust method for ecosystem level flux estimates (Goulden *et al.*, 1996). This dissertation work is based on a long-term eddy covariance data set acquired from a flux tower setup installed at the eastern shore of Virginia, USA. The flux tower is part of the Virginia Coastal Reserve-Long Term Ecological Research (VCR-LTER).

The environmental controls on net ecosystem exchange (NEE) from intertidal salt marshes can be influenced by several factors. The changes in surface energy balance which can occur due to tidal activity (horizontal advection of energy with tidal flows) can affect the distribution of available energy for carbon assimilation in such an environment with short vegetation. The tidal activity can bring in floating algae and other phyto-planktons, which can also increase the carbon dynamics in such a system. The coastal marshes are also exposed to directional winds like sea breezes and land breezes which exhibit a diurnal pattern. The occurrence of such wind patterns can have changes in the footprint of a flux tower system which would be deployed in such an environment. Perturbations such as storms (i.e., tropical and northeastern) have a major role in the redistribution and transport of sediments in a near coastal salt marsh (Wang, 1997). This redistribution can also lead to changes in respiratory and photosynthetic activity in the water column of a salt marsh. The implication of a study on the carbon flow dynamics of any ecosystem is huge. The data on inter annual variability of CO₂ flux, seasonal and diurnal patterns, can lead us to the understanding of whether an ecosystem is

acting as a sink or source of CO_2 (Figure 1). A basic understanding of all these processes can help us a long way in improving the understanding of the role of coastal saline marshes in the global carbon cycle. Human activity can have a huge impact on the carbon sequestration ability of coastal ecosystems and the basic understanding of all processes controlling carbon fluxes can help us in the risk assessment of such systems. Despite the fact that a higher level of understanding of the carbon cycling in terrestrial and oceanic ecosystems has been achieved by programs such as FLUXNET (Baldocchi *et al.*, 2001) and JGOFS (Joint Global Ocean Flux Study) (Doney and Ducklow, 2006), considerable gap still exists in the understanding of carbon cycling in coastal or wetland ecosystems. Field studies have been made on net CO_2 flux in coastal wetlands (Drake *et al.*, 1996), but most of these measurements were undertaken using open-top chambers which tend to modify the microclimate of the system. Such chamber studies were conducted during low tide periods.

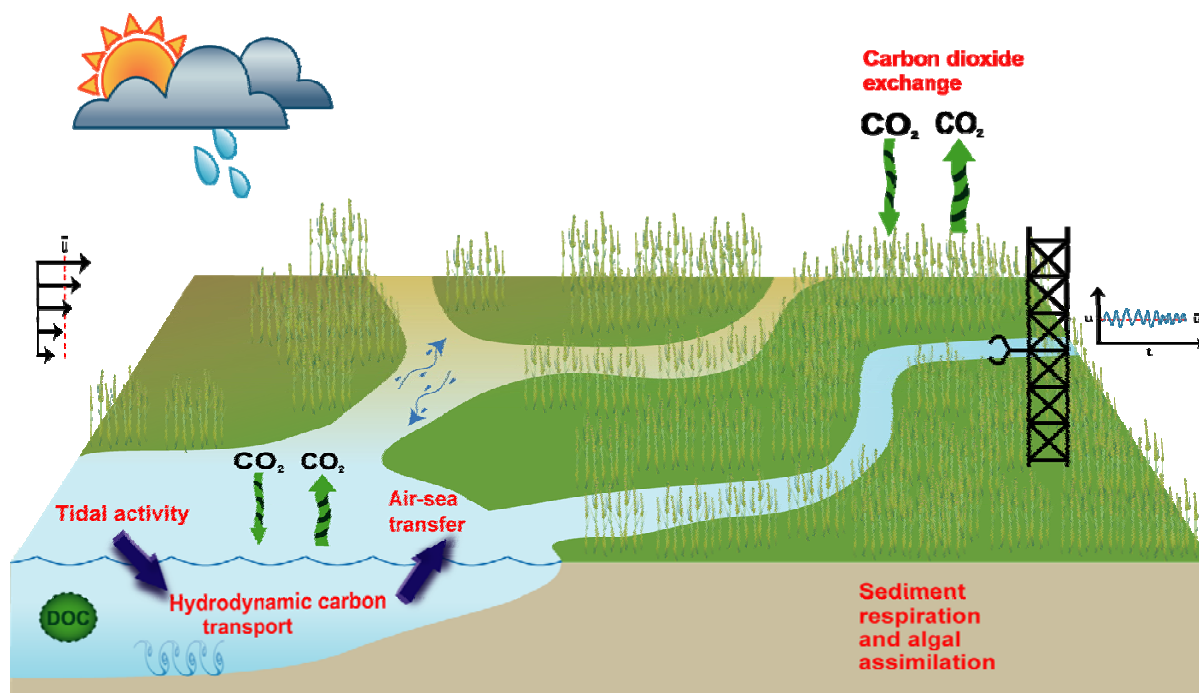


Figure 1.0. Conceptual diagram illustrating the environmental forcings on ecosystem-atmospheric exchange of energy and carbon from inter-tidal salt marshes.

In this dissertation an attempt has been made to address some of the above mentioned issues related to carbon cycling in intertidal systems using tower based eddy covariance measurements.

The principle hypothesis of this study can be stated as

Intertidal salt marshes are major sinks of atmospheric carbon and are the most susceptible ecosystems to regional and global climate changes. The magnitude of the CO₂ assimilation rates by the salt marsh is strongly modulated by tidal activity.

To test this hypothesis the following objectives were achieved:

1. To understand the leaf-level assimilatory response of *Spartina alterniflora* to changes in the physical environment
2. To quantify the atmospheric forcings on the seasonal rates and amounts of carbon assimilation by a *Spartina alterniflora* dominated inter-tidal salt marsh using the tower-based eddy covariance method on a continuous and long term basis.
3. To study the response of salt marsh ecosystem to tidal activity in terms of carbon assimilation and available energy partitioning.
4. To develop numerical models (biophysical) which can predict the carbon dynamics of a salt marsh in response to prevailing environmental conditions and perturbations such as tropical storms and sea level rise.

The dissertation is organized into five different chapters, each chapter addressing separate aspects of the study in the following order:

- 1) Chapter 1: Flux tower design and construction.

This chapter provides a detailed description of the engineering aspects involved in the construction of the flux tower. The construction details are provided with suitable illustrations and schematics. A detailed description of the data acquisition system and the methodologies adopted in data processing are also described as well. The eddy covariance theory and initial data quality control and verification such as footprint estimates and characteristics of turbulent spectra are also discussed in this chapter.

- 2) Chapter 2: Physiological attributes of *Spartina alterniflora*

Leaf-level gas exchange measurements obtained on *Spartina alterniflora* leaves are reported in terms of quantify environmental controls on carbon assimilation and stomatal conductance to

water diffusion. The leaf-level assimilation is directly related to net ecosystem exchange and a comprehensive description of environmental controls on carboxylation rates is essential to quantify canopy-atmosphere carbon exchanges. A detailed description of the estimation of plant physiological variables and their temperature relationships which are essential inputs for canopy biophysical models are also presented in this chapter.

3) Chapter 3: Carbon flow dynamics in an inter-tidal salt marsh

This chapter reports on the season and diurnal patterns in NEE observed over the salt marsh ecosystem based on eddy covariance methodology. The key environmental forcings on seasonal and diurnal NEE patterns are identified and estimates of total seasonal carbon assimilation are presented and discussed.

4) Chapter 4: Partitioning of available energy in an intertidal salt marsh

The partitioning of available energy over the salt marsh surface along with canopy controls on latent and sensible heat transfer are described and discussed. The energy balance closure is examined in terms of tidal activity and influence of energy advection brought about by the presence of land-sea breeze systems on eddy covariance flux estimates is also discussed.

5) Chapter 5: Salt marsh biophysical model

A multilayer canopy biophysical model is developed in this chapter by incorporating the plant physiological constants developed from leaf-level chamber measurements and solving the surface energy balance equation within different layers of the plant canopy. The recent theories of turbulent transport which relate source/sink strength to within canopy scalar profiles is utilized to develop profiles of air temperature, humidity, and carbon dioxide which drive the exchanges of carbon and energy in the model.

References

- Doney, S.C. and Ducklow, H.W. 2006. A decade of synthesis and modeling in the US joint global ocean flux study. *Deep-Sea Research II*, 53: 451–458.
- Drake, B.G., Muehe, M.S., Peresta, G., GonzalezMeler, M.A. and Matamala, R. 1996. Acclimation of photosynthesis, respiration and ecosystem carbon flux of a wetland on Chesapeake Bay, Maryland to elevated atmospheric CO₂ concentration. *Plant and Soil*, 187: 111-118.
- Baldocchi, D., Falge, E., Gu, L. H., Olson, R., Hollinger, D., Running, S., Antoni, P., Bernhofer, C., Davis, K., Evans, R., Fuentes, J., Goldstein, A., Katul, g., Law, B., Lee, X. H., Malhi, Y., Meyers, T., Munger, W., Oechel, W., Paw, K. T., Pilegaard, K., Schmid, H. P., valentine, R., Verma, S., Vesala, T., Wilson, K and Wofsy, S. 2001. Fluxnet: a new tool to study the temporal and spatial variability of eco-system scale carbon dioxide, water vapor and energy densities. *Bulletin of the American Meteorological society*, 82: 2415.
- Goulden, M.L., Munger, J.W., Fan, S.M., Daube, B.C. and Wofsy, S.C. 1996. Measurements of carbon sequestration by long-term eddy covariance: methods and a critical evaluation of accuracy. *Global Change Biology*, 2: 169-182.
- Schimel, D.S. 1995. Terrestrial ecosystems and the carbon-cycle. *Global Change Biology*, 1: 77-91.
- Wang, F.C. 1997. Dynamics of intertidal marshes near shallow estuaries in Louisiana. *Wetlands Ecology and Management*. 5:131-143.

Chapter 1. Flux tower design and set up

1.1. Introduction

Approximately 58 percent of the observed global atmospheric warming is attributed to an increase in carbon dioxide (CO₂) concentrations (Lashof and Ahuja, 1990; IPCC report 2007). Global initiatives such as the FLUXNET (Baldocchi *et al.*, 2001), a network of long-term CO₂ flux monitoring sites, have been established to understand the surface-to-atmosphere exchange of carbon at the ecosystem level. The FLUXNET sites feature micrometeorological instrumentation mounted on towers to estimate scalar concentrations and turbulence characteristics over plant canopies. About 400 FLUXNET sites are currently operational, although most of these sites are situated in terrestrial landscapes with an extremely limited representation of wetland ecosystems. This knowledge deficit for coastal ecosystem must be filled because wetlands are among the most productive ecosystems in the world (Mitsch and Gooselink, 2000). Additionally, they play an important role in the global carbon cycle because they represent the largest component of the terrestrial biological carbon pool. Coastal saline salt marshes have an unusually large capacity to sequester carbon due to high sediment accretion rates and their ability to bury sediments rich in organic matter (Duarte *et al.*, 2005). Despite recent information of CO₂ cycling in terrestrial and oceanic ecosystems gleaned from programs such as FLUXNET and the Joint Global Ocean Flux Study (JGOFS) (Doney and Ducklow, 2006), considerable gaps still exist in our fundamental understanding of carbon cycling in coastal or wetland ecosystems. Comprehensive studies have been carried on net CO₂ flux in coastal wetlands (Drake *et al.*, 1996), but most of these studies were an undertaken using open-top chambers which tend to modify the microclimate of the system. Also, chamber studies have been carried out during periods of low tide periods limiting our understanding of ecosystem exchange processes under tidal submergence. Hence new insights are needed for coastal ecosystems to quantify the seasonal controls on net carbon ecosystem exchange processes.

The main objectives of this chapter are to: 1) describe the construction and set up of an eddy covariance flux tower in a lagoonal salt marsh at the eastern shore of Virginia, USA and

2) review the theory used to determine carbon and energy fluxes for the salt marsh. A brief description of 'flux footprint' or the source area of fluxes detected by tower sensors and spectral characteristics of the quantities measured is also provided.

1.2. Research site characteristics

The research was conducted at the Virginia Coastal Reserve Long Term Ecological Research (VCR LTER) site at the eastern shore of Virginia, USA. The flux tower site ($37^{\circ}24'39.85''\text{N}$, $75^{\circ}50'0.53''\text{W}$) a lagoonal salt marsh which is located near the area of Fowling point (Figure 1.1). The site is located at about 2.2 kilometers away from the mainland and 10.7 kilometers away from Hog Island, the nearest barrier island. The flux tower is situated at about 80 meters away from the creek edge, on the lagoonal salt marsh.

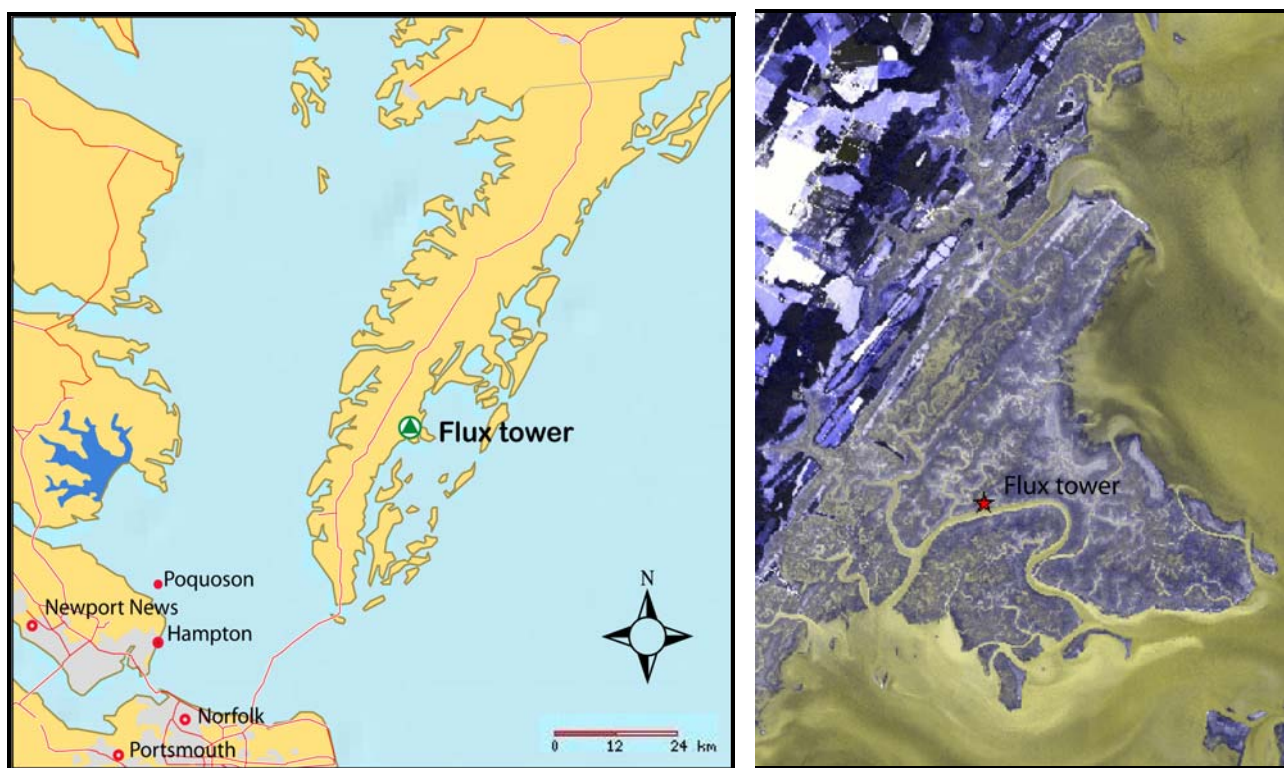


Figure 1.1. Location map of the flux tower at the VCR LTER site along with a magnified satellite image (IKONOS imagery ©2000 Space Imaging) of Fowling point marsh, where the flux tower is located.

The mean annual temperature of the area is 14.2°C and the mean daily maximum and minimum temperatures are 19.5°C and 8.9°C, respectively (Figure 1.2). The mean annual precipitation recorded at this site is about 1065 mm VCR LTER data base.

(<http://intranet.lter.net.edu/archives/documents/Publications/climdes/vcr/vcrclim.htm>)

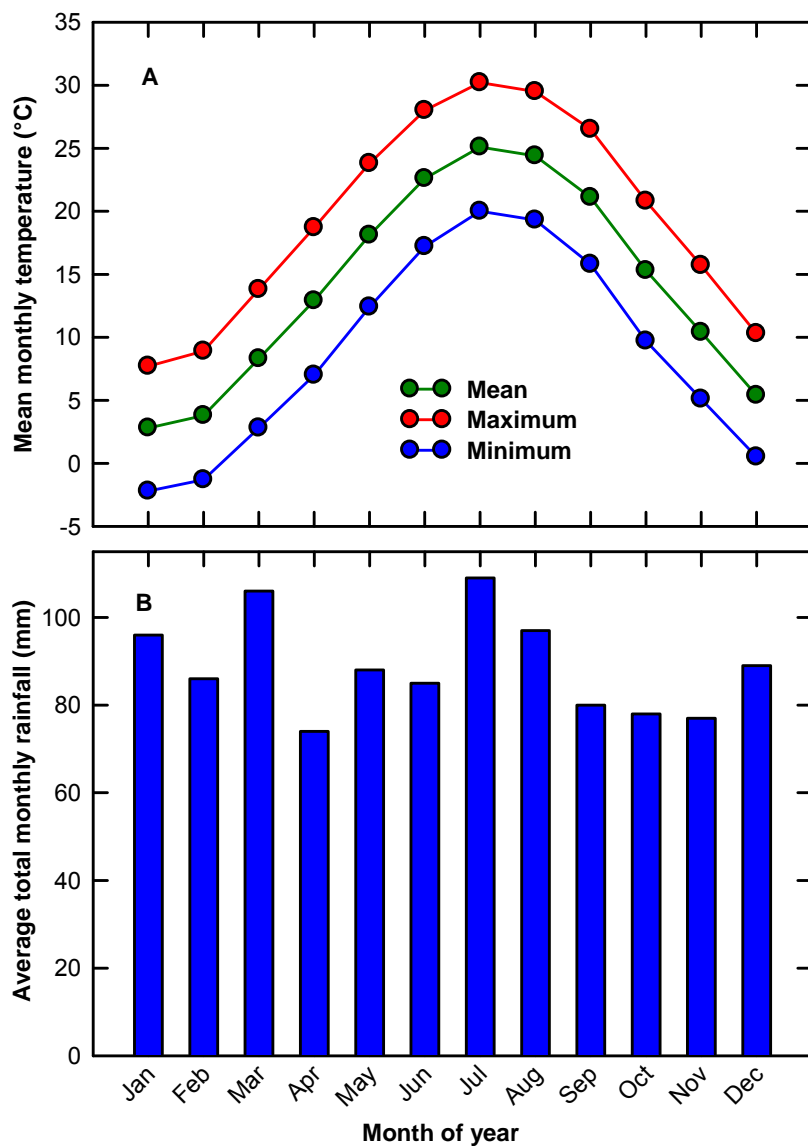


Figure 1.2. Average monthly temperature and total rainfall amounts (1961-1990) for the VCR LTER site (Source: VCR-LTER data base).

The weather patterns at the VCR LTER site are influenced by westerly flows from October to January and southerly flows from April to August (Bryson and Hare, 1974). Extra-tropical storms, tropical storms and hurricanes play an important role in regulating the climatic patterns

at the study site. The majority of the summer rainfall is obtained from the tropical storms whereas the extra-tropical storms or 'northeasters' produce high tides coupled with strong east-northeast winds and heavy rains (Davis and Dolan, 1993). Species composition, biodiversity and community structure at the study site is controlled by several factors including marine water inundation, groundwater salinity variations, and changes in the depth of the fresh water table.

The tower is located in a *Spartina alterniflora* mudflat, typical of eastern coasts. The prominent vegetation in these mud flats is the salt marsh Cod grass (*Spartina alterniflora*), which covers extensive areas of the study region. *Spartina alterniflora* is a C₄ grass and is well adapted to saline marsh conditions. The average height of the canopy at this site is about 60-70 cm, with a leaf area index of 2-2.5. The mudflats are separated by meandering tidal creeks, and morphologically different forms of *Spartina alterniflora* occur in different areas depending upon the degree of tidal flushing from the creeks. With a mean relief of only 2 meters and high erosion and deposition rates of 13 m per year (in the horizontal dimension), the ecosystem is highly dynamic, and is susceptible to physical forcings such as sea level rise (Van Cleve and Martin, 1991).

1.3. Flux tower construction

The flux tower was constructed in accordance with the legal requirements following section 113.1 of the registered design policy 2000 Virginia uniform statewide building code established in 2005. Engineering plans were prepared and were certified by a structural engineering firm (George, Miles & Buhr, LLC, Salisbury, MD USA), and they were submitted to the Northampton County authorities to obtain the required permits. On January 5, 2007 the Northampton County authorized the tower installation.

The construction methodologies were adopted from the previous work of Barr (2005), who described the construction of a flux tower located at a riverine mangrove forest in the western Florida Everglades. The tower base consists of two platforms, one for the aluminum tower base and the other for the battery bank and electronics. The tower base and the battery platform are 0.61 m and 1.4 m high from the sediment surface, respectively. The platforms are constructed on 11 wooden pilings (4"x4") pressure treated lumber that were sunk into the

sediment to a suitable depth for stability (~1.5 m). To ensure equal weight distribution on all 11 tiers and to prevent tiers from settling, pressure treated foundation beams (2"x8") were bolted to the pilings using galvanized 7"x1½" carriage bolts. Scrap boards of 2"x12" treated lumber were installed around the base of vertical tiers; these planks rest flat on the sediment and provide extra surface area to prevent foundation beams from sinking. The floor of the tower base and the ancillary platform were constructed with 2"x8" pressure treated planks (Figure 1.3), which rest on floor beams made up of 2" x 4" pressure treated lumber. Band boards (2" x 6" pressure treated lumber) were also installed around the base to provide extra strength and stability. A shelter structure was made on top of the ancillary platform using pressure treated plywood sheets to house the data acquisition system, battery bank, and electronics.

The flux tower was constructed using pre-fabricated aluminum tower sections (Universal towers, Clinton Township, MI, USA). Each section is 3 m long, and two sections were used in the tower construction giving a total height of 6.7 m from the soil sediment surface. The tower sections were mounted on an aluminum base (3' x 3' x 3/8") that was bolted onto the main platform base. To maintain structural stability, the tower was anchored to the sediment surface using a set of three guy wires attached to the top of the tower. These guy wires were attached to wooden pilings on the ground through galvanized turnbuckles (Model 3000T566, McMaster-Carr, Atlanta, GA, USA). Although two tower sections do not require the use of guy wires, these were added for extra stability as the tower may be exposed to high force winds.

A boardwalk was also constructed from the base of the tower platform to the edge of the creek to provide easy access to the flux tower and thus avoid vegetation disturbance. Each section of the boardwalk consists of two parallel 2"x6"x8" pressure treated planks supported by stakes of 2"x4" treated lumber. The boardwalk extends for about 80 meters from the creek edge and rests just above the sediment surface.

1.4. Power supply system

The flux tower was powered by an array of batteries (model WKG12-100J, Werker batteries, Batteries plus, Hartland, WI, USA) which were recharged by a set of 9 solar panels. The battery

bank included 8 gel cell, 100 amp hours 12-volt batteries capable of storing 800 amp hours of charge. The 9 solar panels (KC module, Kyocera, Scottsdale, Arizona, USA) produced a maximum of 24 amps at 16.9 volts during midday solar irradiance conditions thus giving a maximum of 124 watts of power.

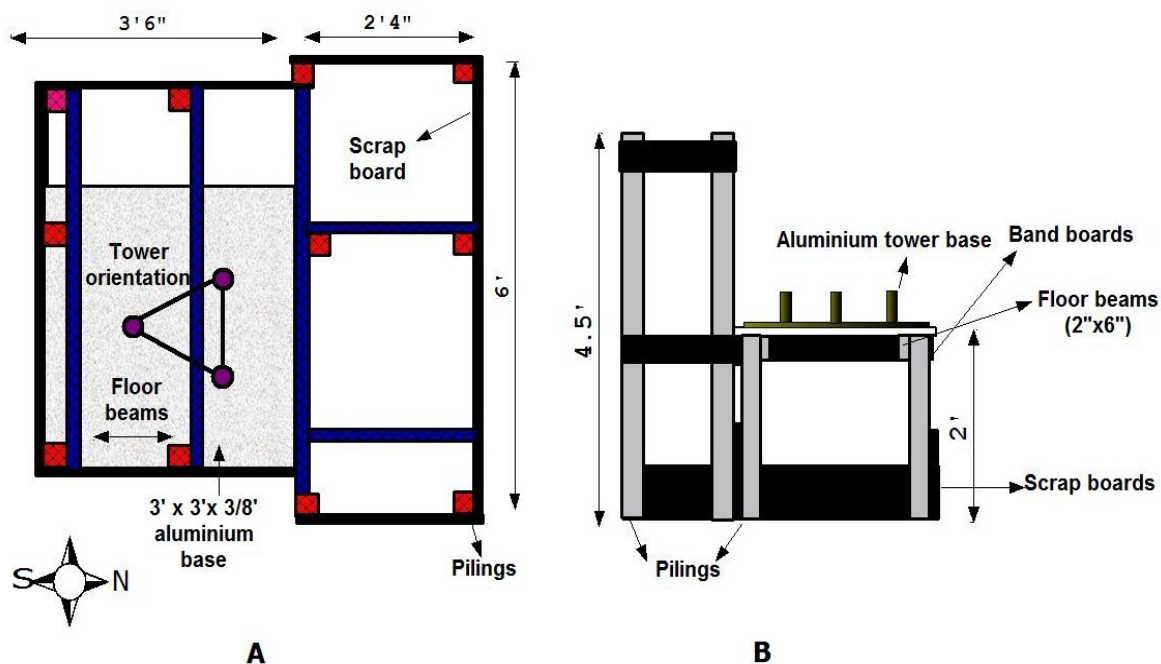


Figure 1.3. Tower base top view (A) and side view (B) showing the structural members. The instruments are oriented in the east-west direction.

The solar panels were framed using pressure treated lumber and were installed at an angle of 52° from the horizon (latitude + 15°) to maximize sunlight interception during winter months.

The panels were elevated about 1.2 m from the sediment surface using four pressure treated 4" x 4" pilings. In order to minimize the impact of solar panels on radiation measurements, they were installed at a distance of 24 m southwest from the tower (Figure 1.4) facing south. A charge controller (Model PS30M, Morningstar Corp, Washington Crossing, PA, USA), rated for 30 amps, controls the charging of the batteries and also provides information on power consumption and solar charging. A DC to AC converter provided AC current to the laptop computer and other electronics. Circuit breakers are provided at various points in the circuit for added safety (Figure 1.5).



Figure 1.4. A) Flux tower set up with instrumentation along with the battery bank platform during high tide conditions, and B) solar panel setup showing the nine panels framed and mounted above the sediment.

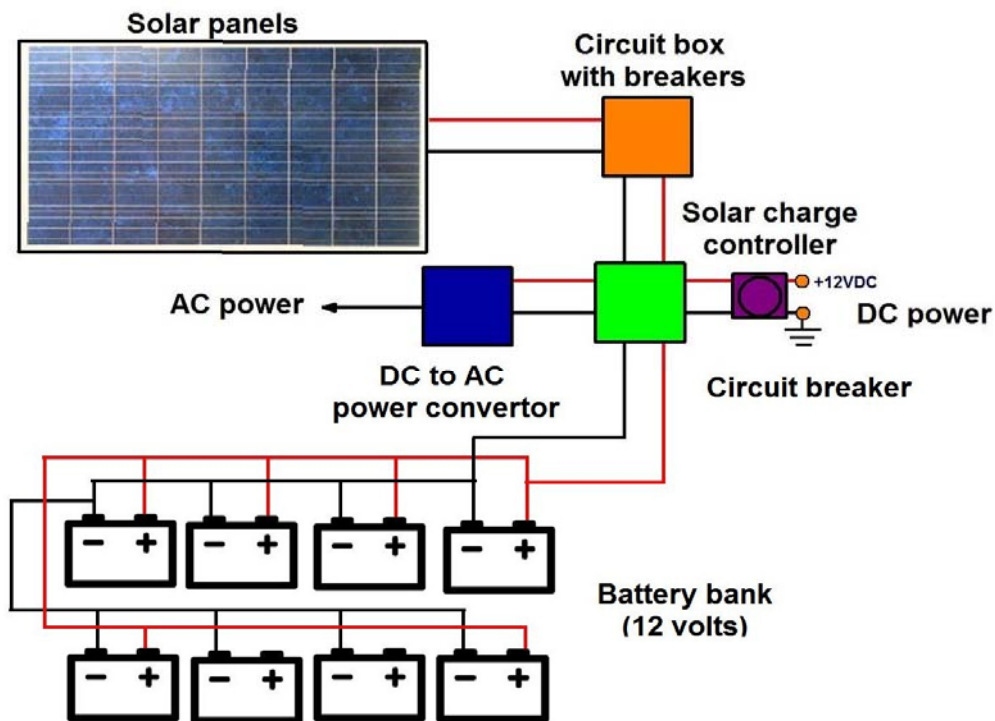


Figure 1.5. Schematic of the power supply setup showing the wiring diagram for the solar panels, charge controller, and battery bank. Eight gauge wire is used to connect the solar panels to the batteries to prevent power transmission losses.

1.5. Flux tower instrumentation

The flux tower instrumentation includes an eddy covariance system and various micrometeorological sensors. The eddy covariance system consists of a three dimensional sonic anemometer (model CSAT3, Campbell Scientific Inc, Logan UT, USA), which measures the components of the wind velocity in the x, y, and z directions along with virtual temperature and an open path gas analyzer (model LI-7500, Licor Inc, Lincoln, NE, USA) which measures the concentration of CO₂ and H₂O in the air. These measurements were used to estimate the fluxes of carbon dioxide, latent heat, and sensible heat.

The microclimate over the canopy was quantified by a variety of sensors mounted on the flux tower. Temperature measurements were made at three different heights above the canopy (2.1, 3.7 and 6.7 m); humidity measurements were made at two different levels (2.1 and 6.7 m). The temperature/humidity sensors (model 41382/42342, RM Young, Traverse City, Michigan, USA) were housed in white PVC fan-ventilated shields and all the connections were made using military style connectors to protect from corrosion resulting from salt spray. The radiation measurements included net radiation (model CNR1, Kipp and Zonen, Bohemia, NY, USA), along with incoming and reflected photosynthetic active radiation (model LI190SB, LICOR Inc, Lincoln, NE USA) at 5.2 m above the surface. Wind direction and speed were measured using a propeller anemometer (model 05103, RM Young, Traverse city, MI, USA) that was installed at 7 m from the surface. The flow of heat into and out of soil was estimated using two soil heat flux plates (model HFT 3.1, Campbell Scientific Inc, Logan, UT, USA) installed at 5 cm below the sediment surface. The temperature profile of the soil was monitored using three soil thermometers (model 105T, Campbell Scientific Inc. Logan, UT, USA), installed at 5, 10, and 25 cm depths. Rainfall estimates were obtained using a tipping bucket rain gauge (model Met One-385, Campbell Scientific Inc, Logan, UT, USA). Additionally, a water level recorder (model WL 400, Global Water Instrumentation Inc., Gold River, CA, USA) was used to measure tidal fluctuations over the marsh surface. A set of 5 thermocouples (model Type E, Omega Engineering Inc. Stamford, CT, USA) were used to estimate temperature changes within the plant canopy (0, 5, 10, 50, and 80 cm). A schematic of the sensor locations on the flux tower is provided in Figure 1.6. Table 1.1 provides a detailed description of the type of

measurements and sensors utilized in this study. Finally, a lightning conductor (McMaster Carr, Aurora, OH, USA) was installed at the top of the flux tower to protect all instrumentation from electrical damage, including lightning strikes.

Table 1.1. Micrometeorological instrumentation installed on the flux tower along with the sensor height and numbers of sensors at different levels.

| Measurement (Units) | Level (meters) | Instrument |
|--|--------------------------|--|
| Air temperature (°C)/ relative humidity (%) | 2.1, 6.7 | Relative humidity/temperature probes (2 Nos) |
| Air temperature (°C) | 3.7 | Thermistors |
| Wind speed (m s^{-1}) and direction(°) | 7 | Propeller Anemometer |
| Incoming shortwave radiation (W m^{-2}) | | Pyranometer |
| Outgoing shortwave radiation (W m^{-2}) | 5.2 | Pyranometer |
| Incoming longwave radiation (W m^{-2}) | | Pyrgeometer |
| Outgoing longwave radiation (W m^{-2}) | | Pyrgeometer |
| Soil heat flux (W m^{-2}) | ground | Soil heat flux plate-(2 Nos) |
| Soil temperature (°C) | -0.05, -0.1, and -0.25 m | Thermocouple sensor (3 Nos) |
| CO ₂ and H ₂ O concentration (mg m^{-3}) | 3.7 | IRGA (LI-7500) |
| Three dimensional wind speed (m s^{-1}) | 3.7 | Sonic anemometer |
| Air temperature (°C) | 0, 0.05, 0.1, 0.5, 0.8 | Type E thermocouples |
| Water level (m) | 0 | Water level sensor |
| Rain (mm) | 1.2 | Rain gauge |
| Photosynthetic active radiation (PAR)- ($\mu \text{mol m}^{-2} \text{s}^{-1}$) | 5.2 | Quantum sensors-(2 Nos) |

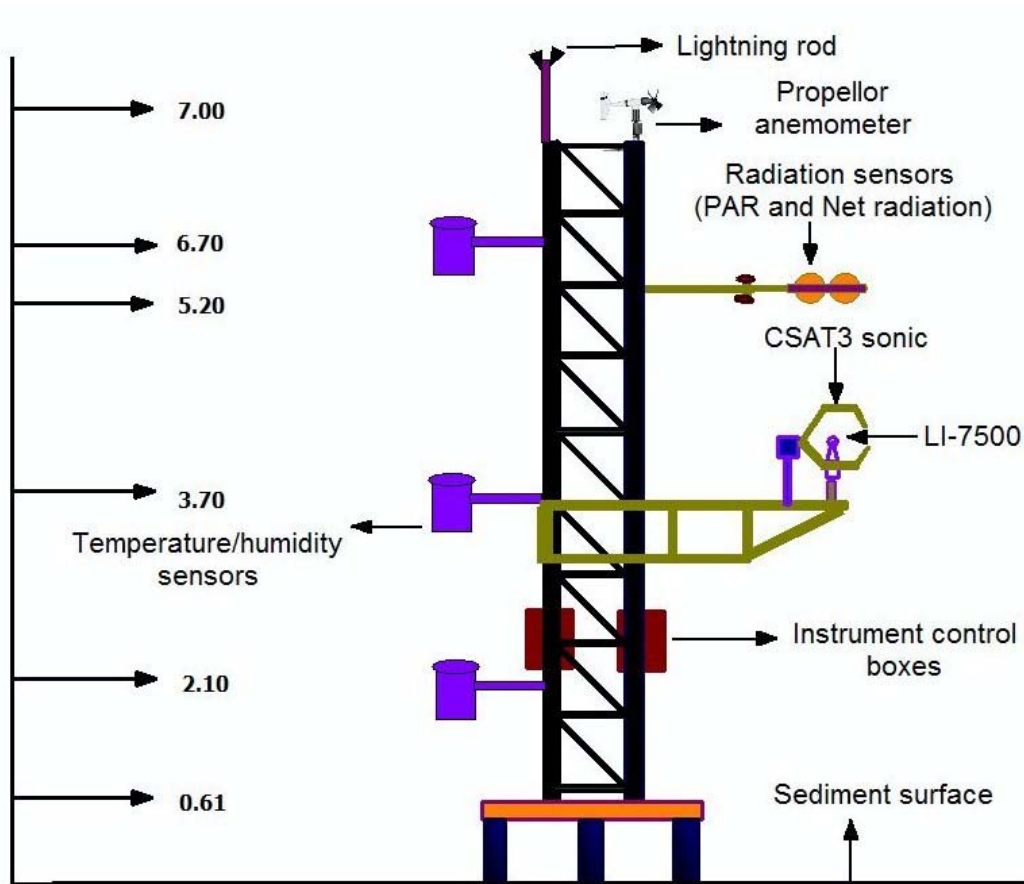


Figure 1.6. Schematic representation of all micrometeorological instrumentation on the flux tower (elevations are provided in meters above the sediment surface).

1.6 Data acquisition system

A laptop computer-based data acquisition system was developed and utilized to acquire and store meteorological data via data loggers and high frequency data directly from the eddy covariance system. The storage capacity of a laptop computer allowed data to be stored over long time periods, which was a necessity because the site was not frequently visited. Moreover, it is advantageous to record and store all high frequency data to ensure that data quality control can be maintained through extensive filtering and or flux corrections (e.g., Burba *et al.*, 2006). In addition to a laptop, the data acquisition system consisted of two data loggers (model CR3000 and CR21X, Campbell Scientific Inc. Logan, UT, USA). This laptop computer-based data system was developed using LABVIEW™ (National Instruments, Austin, TX, USA), a graphical programming language for data acquisition. The data acquisition offers flexibility for

collecting high frequency measurements from the eddy covariance instruments directly through the computer's RS 232 ports, with half-hourly files written in manageable sizes. The data acquisition system also collects data from the two data loggers and writes separate files for each in half-hourly intervals. The files are conveniently named using the time stamp of their creation, and each is formatted in tab delimited ASCII. The eddy covariance system outputs data at 10 Hz frequency, whereas the data loggers scan all other instruments at 1 second intervals and outputs one minute averages. The data acquisition system schematic is detailed in Figure 1.7.

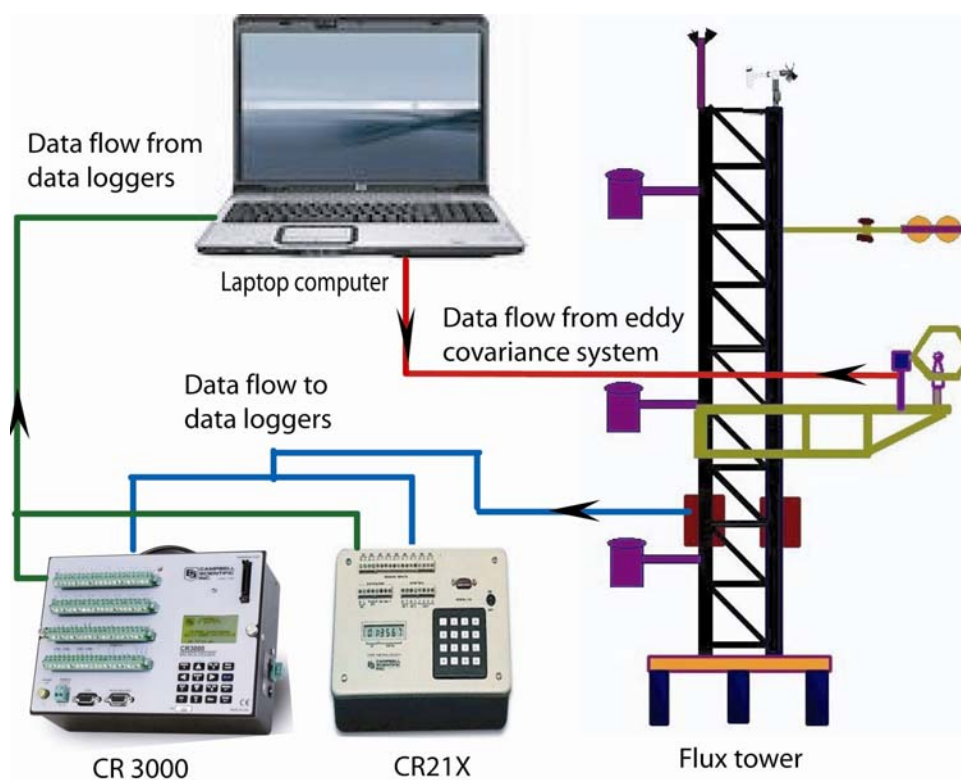


Figure 1.7. Data acquisitions system set up showing the various components and flow of data from sensors to the system. The system consists of two data loggers (CR 3000 and CR 21X) and a laptop computer for high frequency data acquisition and storage.

All the electronic components, including the laptop and data loggers, were stored in waterproof fiber glass boxes (model AM series, Allied Moulded Products, Inc, Bryan, OH, USA), which were kept on the battery platform. A screenshot of the data acquisition program is provided in Figure 1.8. The data acquisition system triggered both the eddy covariance sensors

(software trigger) enabling proper alignment of data transmission and acquisition and avoiding lags. The flux tower also features a client radio (wireless 802.11 b/g, Model Wireless-B&G MIMO performance, Buffalo technology Inc, Austin, TX, USA) with an amplified omni-directional antenna, for connecting to an established wireless network at the VCR-LTER. This wireless network connection enables remote access to the data acquisition system for monitoring and maintenance purposes.

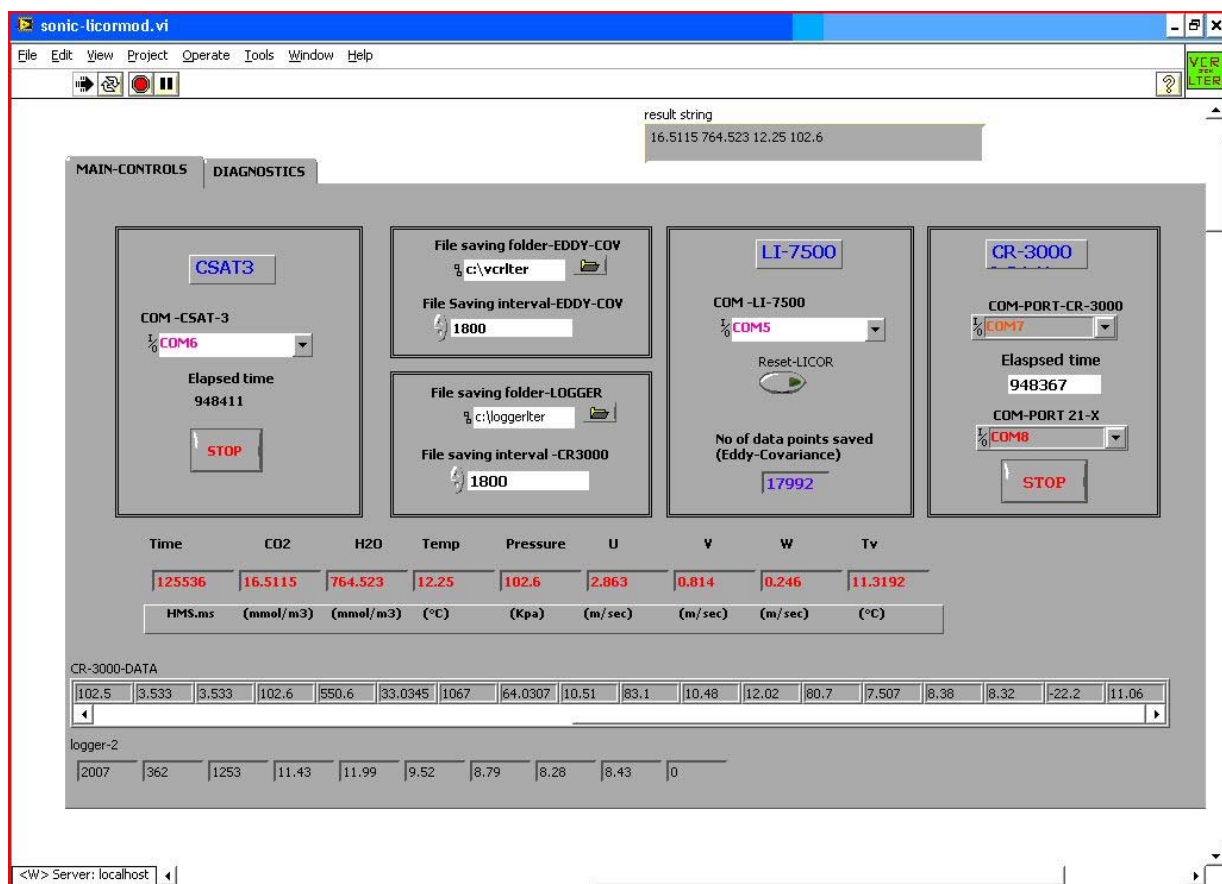


Figure 1.8. Screen shot of the LABVIEW based data acquisition program showing the program controls and displays.

1.7. Flux calculations

The flux of a scalar is calculated as the covariance between vertical velocity and the concentration of the scalar, taking into account the equations of mass flow and Reynolds decomposition (Baldocchi, 2003). This definition of flux is derived from the advection dispersion equation (1.1), which describes the change in concentration of a scalar with time.

$$\frac{dc(t, x, y, z)}{dt} = \frac{\partial c}{\partial t} + u \frac{\partial c}{\partial x} + v \frac{\partial c}{\partial y} + w \frac{\partial c}{\partial z} = D_c \left(\frac{\partial^2 c}{\partial x^2} + \frac{\partial^2 c}{\partial y^2} + \frac{\partial^2 c}{\partial z^2} \right) + S(x, y, z) \quad (1.1)$$

I II III IV V

The total change in concentration of a scalar (term I), which is the sum of local change (II), and advective change (III) is contributed by dispersion (IV), and the presence of source/sink for this scalar (V). The term D_c indicates the molecular diffusivity of the scalar. Applying Reynolds decomposition, which is a mathematical technique to separate the mean and fluctuating parts of a quantity ($c = \bar{c} - c'$) (In Reynolds decomposition the time average of perturbations is considered to be zero ($\overline{c'} = 0$)) and assuming steady state ($\frac{\partial c}{\partial t} = 0$) and non-advective conditions, equation 1.1 reduces to

$$0 = -\frac{\partial \overline{w'c'}}{\partial z} + S(z) \quad (1.2)$$

The dispersive terms are much smaller in magnitude than the covariance terms and are therefore ignored. This equation is integrated over the control volume with a lower boundary at the interface between air, soil, and vegetation and with an upper boundary taken as the measurement height (h) in above the surface.

$$\overline{w'c'(h)} = \overline{w'c'(0)} + \int_0^h S(z) \quad (1.3)$$

The term $\overline{w'c'(h)}$ represents the flux determined at a specific height using the eddy covariance. It is equal to the net flux of material leaving or entering the soil-plant-atmosphere interface ($\overline{w'c'(0)}$). Further if we assume that the scalar mixing ratios do not change between 0 and h due to changes in source/sink strength the source/strength term can be ignored. Since the canopy is short, the storage term can be assumed to be small, or negligible, and is hence set to be zero. Following this framework, the eddy fluxes for sensible heat (H), latent heat (LE), and carbon dioxide (F_{CO_2}) can be determined as

$$H = \rho_a C_p \overline{w'T'_v} \quad (1.4)$$

$$LE = \lambda \overline{w' \rho'_v} \quad (1.5)$$

$$F_{CO_2} = \overline{w' \rho'_c} \quad (1.6)$$

ρ_a , C_P , and λ are the density of air (g m^{-3}), specific heat capacity of air at constant pressure ($\text{J g}^{-1} \text{K}^{-1}$), and latent heat of vaporization (J mmol water^{-1}), respectively. T_v , w , ρ_v , and ρ_c indicate virtual temperature ($^{\circ}\text{C}$), vertical velocity (m s^{-1}), water vapor density (mmol m^{-3}), and CO_2 density (mmol m^{-3}), respectively. The over bars indicate an average and the prime indicates the fluctuation from the means.

The LE and F_{CO_2} equations are modified to account for the variation of mixture density caused by temperature variations and the changes in vertical velocity induced by evaporative flux of water from the surface (Webb *et al.*, 1980). The Webb *et al.* corrections are observed to reduce daytime CO_2 and latent heat fluxes by 25-30% and 2-3%, respectively (Liebethal and Foken, 2003).

$$LE = \lambda \times (1 + \mu \times \sigma) \times \overline{w' \rho'_v} + \frac{\overline{\rho_v}}{T_v} \times \overline{w' T'_v} \quad (1.7)$$

$$F_{CO_2} = \overline{w' \rho'_c} + \mu \times \frac{\overline{\rho_c}}{\rho_a} \times \overline{w' \rho'_v} + (1 + \mu \times \sigma) \times \frac{\overline{\rho_c}}{T_v} \times \overline{w' T'_v} \quad (1.8)$$

Where $\mu = M_a / M_v$, M_a is the molecular weight of air and M_v is the molecular weight of water vapor and $\sigma = \rho_v / \rho_a$. Scalar fluxes estimated with the eddy covariance technique assume that the concentration of the scalars and wind velocities do not change (i.e., stationarity assumption) over the averaging period (30 minutes) and the concentration of the scalar is uniform over the surface of measurement (isotropy). The relationships described by Webb *et al.*, (1980) were shown to be correct for both steady and non-steady horizontally homogeneous flows (Leuning, 2007).

1.8. Data analysis

The half-hourly high frequency data files are analyzed using a MATLAB program (The Math works Inc, Natick, MA, USA). The program (see appendix) reads data files for individual days or

months, and then analyzes them to produce summarized output files. The raw measurements are then filtered to remove outliers considered in this research as four times the standard deviation of the data series. Lag correlation analysis indicate no lags between the CSAT3 and LI-7500 measurements. Co-ordinate rotation was done on the turbulence data to align the measurements to a regular Cartesian co-ordinate system (Kaimal and Finnigan, 1994; Lee, 2004). The fluxes are calculated to incorporate the density corrections and outputs are written as individual files for each day analyzed. The data logger files are also processed in a similar manner. The matlab code utilized for processing eddy co-variance files is given in the appendix-A

1.9. Flux footprint estimates

Flux footprint estimates are necessary to understand the source area or 'footprint' over which the flux tower can measure. Based on wind speed data obtained on the flux tower, the site is influenced by southerly winds, with the highest wind speeds observed from the northeast direction (Figure 9).

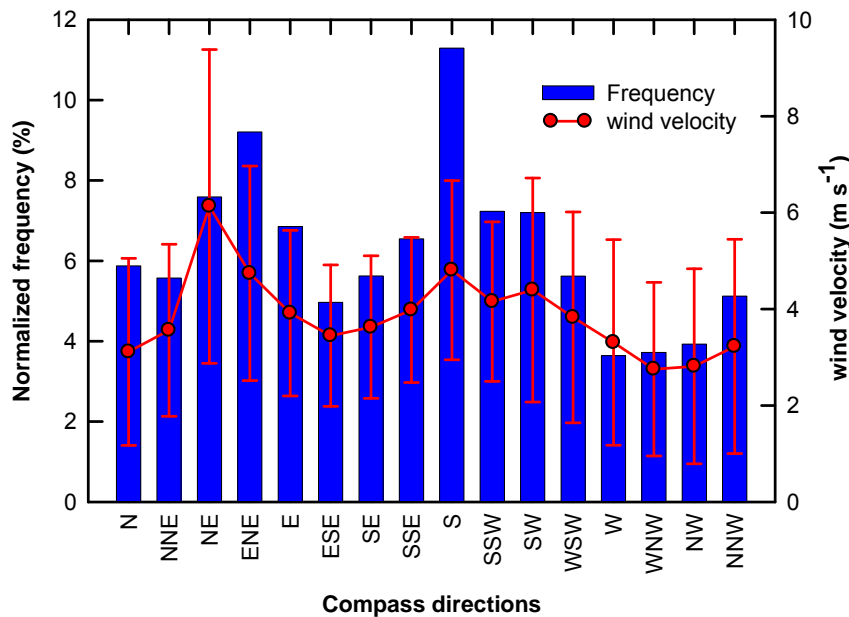


Figure 1.9. The frequency of occurrence for recorded wind directions, and the average wind speed for each corresponding direction (with standard deviations) at the site. The data presented are obtained by analyzing one minute interval values collected during the growing season.

It is essential to know what the extent of the flux footprint is in order to determine if the fluxes come from the marsh canopy or the water surface. A two dimensional Lagrangian random walk (LRW) model (Baldocchi, 1997) was used to estimate the flux footprint.

In the LRW model a large number of particles (5000) were released from the top of the canopy (60 cm) and the probability that the particles cross the sensor height (3.7 m) at a particular distance is determined to obtain the flux footprint probability density function (Baldocchi, 1997). The source/sink of carbon in this case was considered as a single vegetation layer at the top of the canopy as the amount of vegetation available for the exchange of energy and carbon may change with the tidal cycle. The particle motion was determined in terms of its horizontal (dx) and vertical displacement (dz) as estimated by changes in the horizontal and vertical velocity, following the Langevin relationship (Baldocchi, 1997).

$$dx = (\bar{u} + u') dt \quad (1.9)$$

$$du = a_u(z, t, u') dt + b_u(z, t, u') d\xi \quad (1.10)$$

$$dz = (\bar{w} + w') dt \quad (1.11)$$

$$dw = a_w(z, t, w) dt + b_w(z, t, w) d\xi \quad (1.12)$$

The coefficients a_u , b_u , a_w , and b_w represent non-linear functions of the air parcel's momentum and atmospheric turbulence statistics. u and w indicate the horizontal and vertical velocity. To determinate the change of horizontal and vertical velocity, a random forcing term ($d\xi$) is included to account for the random nature of air parcel movement. A detailed description of the determination of the non-linear coefficients can be found in Baldocchi (1997) and Strong *et al* (2004). The time step for particle movement is considered as 10% of the Lagrangian time scale at the top of the canopy. The Lagrangian time scale is represented in equation 1.13.

$$T_L = 2 \overline{(w')^2} / \varepsilon \quad (1.13)$$

The term ε denotes the average rate of turbulent kinetic energy dissipation and is determined as $u^{*3}/0.4z$, where z is the altitude above ground and u^* is the friction velocity (Kaimal and

Finnigan 1994). Particles returning to the release point (in this case the top of the canopy) were perfectly reflected, thus requiring only turbulent statistics above the canopy to be modeled for flux footprint determination. The Monin-Obukhov similarity relationships (Monin and Obukhov, 1954) are used to describe the behavior of the normalized standard deviation of vertical velocity in the inertial sub-layer above the canopy.

To illustrate the extent of source area sensed by the flux tower (flux footprint), the flux footprint was estimated for a day of year 204 (23 July 2007) and is represented in Figure 1.10. The flux footprint was estimated based on the average wind direction and friction velocity values observed during the entire course of the day (48 half hourly data points). The flux footprint probability density functions estimated are subjected to a kriging procedure to obtain the contour plot. The flux footprint estimates (Figure 1.10) indicate that the peak of the flux footprint lies within 20 to 30 m with little contribution to fluxes arising from distances greater than a 100 m from the flux tower.

The prominent source areas for this particular day were from 50° and 300° from the north as these two directions were associated with the highest friction velocity values (Figure 1.11). The prominent wind direction during the growing season (south) has a fetch of about 80 m before it encounter a tidal creek, which indicate an adequate source area for flux estimates. All the other directions have sufficient fetch (>200 m) with uniform vegetation, before any prominent channel or creek is encountered.

1.10. Spectral characteristics of turbulence

The spectral characteristic of signals helps us to determine the frequency requirements for sensors operating at different heights above the surface. Ideally eddy covariance measurements should be undertaken in the inertial sub layer (where similarity theory applies) above plant canopies, which extend from two to three times the height of the canopy to the top of the surface layer (Kaimal and Finnigan, 1994).

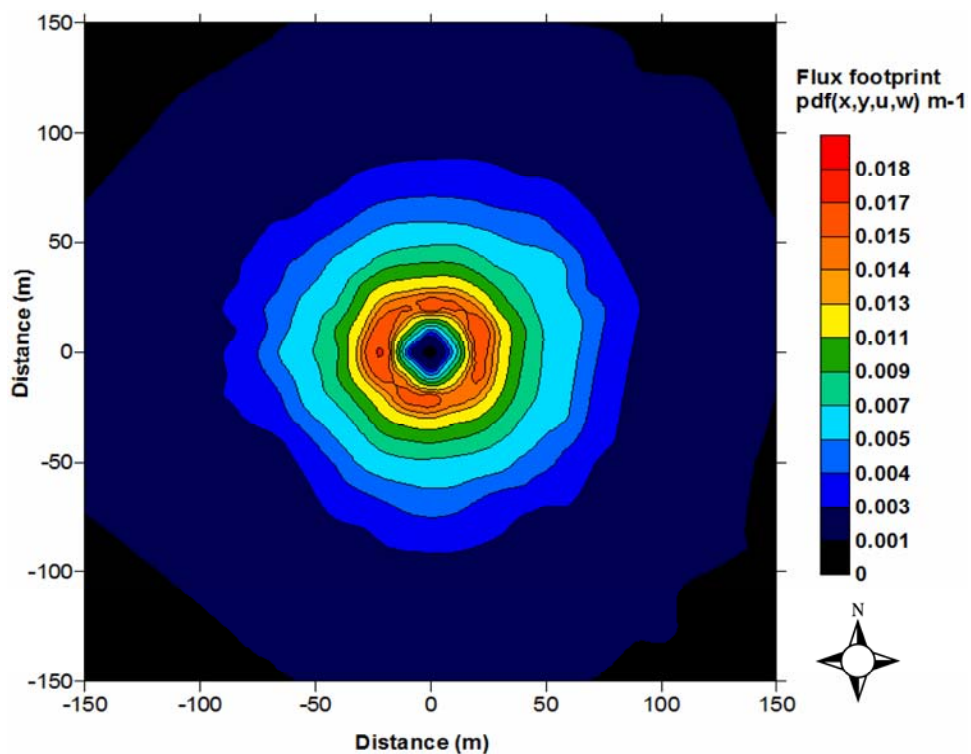


Figure 1.10. Flux footprint probability density function pdf $(x,y,w,u) \text{ m}^{-1}$, for a sensor deployed at the height of 3.7 m, estimated for neutral atmospheric conditions. The friction velocity and wind direction data for day of year 204 was used to estimate the flux footprint.

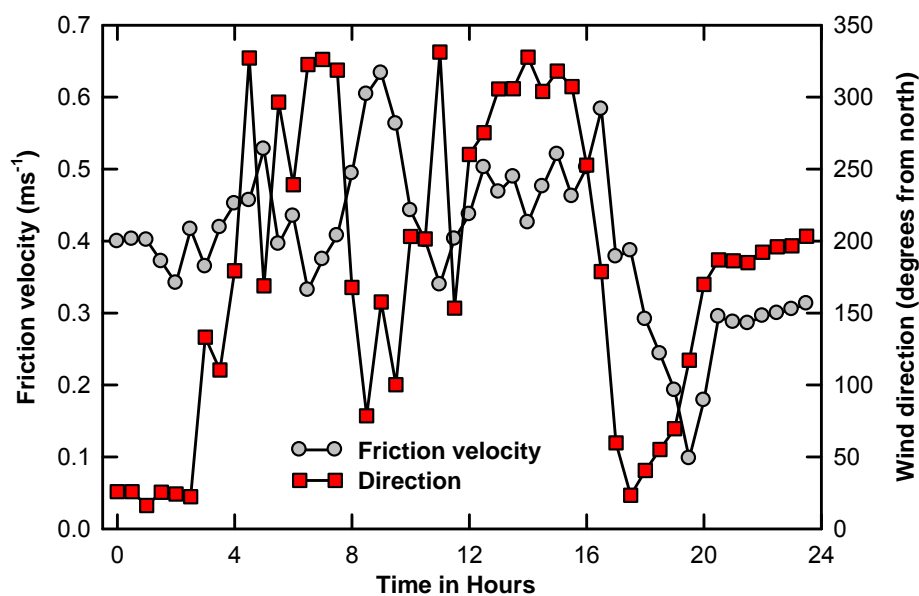


Figure 1.11. Average half-hourly friction velocity and wind direction values for day of year 204 used in the footprint estimation. The highest friction velocity values are observed for the directions 50° and 300° from the north.

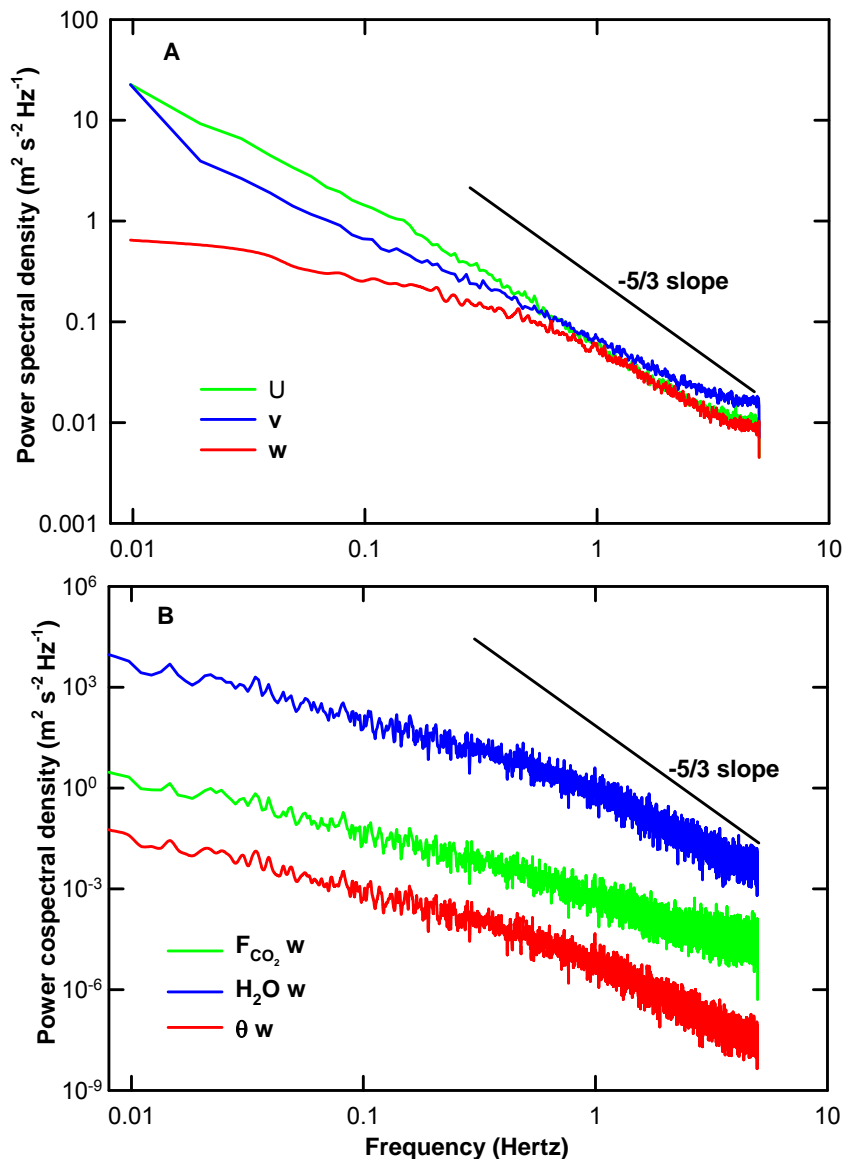


Figure 1.12. Average ensemble power spectral densities of the three velocity components (A) (u,v and w) and ensemble power cospectral density for F_{CO_2} , H_2O and θ (virtual temperature) with vertical velocity (w) depicting the inertial sub-range with a slope closer to -5/3. The frequency given in the x-axis is the cyclic frequency.

The spectrum of turbulence in the inertial sub range tends to have a -5/3 slope in the inertial sub layer (Kolmogorov, 1941, Wilson *et al.*, 1982; Amiro, 1990). The day time ensemble (10:00 to 14:00 hours) power spectral density (PSD) ($\text{m}^2 \text{s}^{-2} \text{Hz}^{-1}$) for the three velocity components (u, v and w) and power cospectral density between F_{CO_2} , H_2O and θ with vertical velocity (w) estimated for day of year 199 are represented in Figure 1.12. The spectral calculations were done using hourly overlapping windows of data using the *pwelch* algorithm for power spectral

density and cpsd algorithm for cospectral power density in Matlab, a scientific programming language (Mathworks Inc, Natick, MA, USA) by implementing a linear detrend and a hamming windowing of 10^{12} data points. The PSDs of the three components have a slope close to $-5/3$, with a slight increase towards the end of the inertial sub range, which may be attributed to spectral short circuiting (which refers to the direct transfer of energy from the energy production range to the dissipation range without cascading through the inertial sub range) where the energy may be transferred from larger eddies and converted into smaller waving scales (a special case observed in cereal crops where the plant waving frequency can coincide with the energy containing frequency) (Inoue, 1963, Kaimal and Finnigan, 1994). The cospectral power densities also exhibited slopes close to $-5/3$ in the sub inertial range.

1.11. Summary

The construction of a flux tower in a lagoonal salt marsh is described in detail in this chapter. The construction methodologies are adopted from the previous work of Barr, (2005). The remote location of the tower required the development of a self-contained power supply and data acquisition system where little maintenance is mandatory. The LABVIEW-based system provides easy access to diagnose and monitor the system from a remote location and it can be used as a model data acquisition system for future studies. Flux footprint estimates indicate that the site has sufficient fetch for micrometeorological flux investigations. Finally, this flux tower design and construction has produced a unique and reliable data set pertaining to fluxes of carbon and energy from lagoonal salt marshes. Scientific analysis of this data set can provide information to understand environmental forcings and controls on fluxes of carbon and energy from intertidal salt marshes.

References

- Amiro, B. D. 1990. Drag coefficients and turbulent spectra within three boreal forest canopies. *Boundary-Layer Meteorology*, 52: 227-246.
- Baldocchi, D., Falge, E., Gu, L. H., Olson, R., Hollinger, D., Running, S., Antoni, P., Bernhofer, C., Davis, K., Evans, R., Fuentes, J., Goldstein, A., Katul, g., Law, B., Lee, X. H., Malhi, Y., Meyers, T., Munger, W., Oechel, W., Paw, K. T., Pilegaard, K., Schmid, H. P.,

- valentine, R., Verma, S., Vesala, T., Wilson, K and Wofsy, S. 2001. FLUXNET: A new tool to study the temporal and spatial variability of ecosystem-scale carbon dioxide, water vapor, and energy flux densities. *Bulletin of the American Meteorological Society*, 82: 2415-2434.
- Baldocchi, D. 1997. Flux footprints within and over forest canopies. *Boundary-Layer Meteorology*, 85: 273-292.
- Barr, J, G. 2005. Carbon assimilation by riverine mangroves in the Florida Everglades. Ph. D Thesis, Department of Environmental Sciences, University of Virginia. 155 pp.
- Bryson, R. A. and Hare, F. K. 1974. The Climates of North America. pp. 1-47. In *Climates of North America*. Bryson, R. A. and F. K. Hare. eds. *World Survey of Climatology*, Vol. 11. Elsevier. Amsterdam. 420 pp.
- Burba, G.G., Anderson, D.J., Xu, L and McDermitt, D.K. 2006. Additional term in the Webb-Pearman-Leuning correction due to surface heating from an open-path gas analyzer. *Eos Trans. AGU* 87 (52), Fall Meeting. Supplement C12A-03.
- Davis, R.E. and Dolan, R. 1993. Noreasters. *American scientist* 81: 428-439.
- Doney, S.C. and Ducklow, H.W. 2006. A decade of synthesis and modeling in the US Joint global ocean flux study. *Deep-Sea Research II*, 53: 451-458.
- Duarte, C. M., Middelburg, J. J and Caraco, N. 2005. Major role of marine vegetation in ocean carbon cycle. *Biogeosciences*, 2:1-8.
- Hayden, B.P., Santos, M.C.F.V., Shao, G. and Kochel, R.C. 1995. Geomorphological controls on coastal vegetation at the Virginia Coast Reserve. *Geomorphology*, 13(1-4): 283.
- Inoue, E., 1963. On the turbulent structure of air flow within crop canopy. *Journal of Meteorological Society of Japan*, 1: 317-346.
- Kaimal, J. C and Finnigan, J. J. 1994. *Atmospheric boundary layer flows*. Oxford university press, New York. pp 90.
- Kolmogorov, A. N. 1941. The local structure of turbulence in incompressible viscous fluid for very large Reynolds number. *Doklady, ANSSSR*, 30: 301-304.
- Lashof, D. A. and Ahuja, D. R. 1990 Relative contributions of green house gas emissions to global warming. *Nature*, 344: 529-531

- Lee, X., Finnigan, J. and Paw, U. K. T. 2004. Coordinate system and flux bias error. In: X. Lee, B. Law and W. Massman (Editors), Handbook of micrometeorology: a guide for surface flux measurements. Kluwer academic publications, Dordrecht, The Netherlands, pp. 116.
- Leuning, R. 2007. The correct form of the Webb, Pearman and Leuning equation for eddy fluxes of trace gases in steady and non-steady state, horizontally homogeneous flows. *Boundary-Layer Meteorology*, 123: 263-267.
- Liebenthal, C. and Foken, T. 2003. On the significance of Webb correction to fluxes. *Boundary-Layer Meteorology*, 109: 99-106.
- Mitsch, W. J and Gosselink, J. G. 2000. In *Wetlands*. John Wiley and sons Inc. New York. pp: 3.
- Strong, C. Fuentes, J. D and Baldocchi, D. 2004. Reactive hydrocarbon flux footprints during canopy senescence. *Agricultural and Forest Meteorology*, 127: 159-173.
- The fourth assessment report: Climate change 2007. The fourth IPCC assessment report. Intergovernmental Panel on Climate Change.
- van Cleve, K., and Martin, S. 1991. Long-Term Ecological Research in the United States: A Network of research sites 1991. Long Term Ecological Research Network Office. University of Washington. College of Forest Resources. AR-10. Seattle. Washington 98195. pp 158-165.
- Webb, E.K., Pearman, G. I. and Leuning, R. 1980. Correction of flux measurements for density effects due to heat and water vapor transfer. *Quarterly Journal of Royal Meteorological Society*, 106: 85-100.
- Wilson, J. D., Ward, D. P., Thurtell, G. W. and Kidd, G. E. 1982. Statistics of atmospheric turbulence within and above a corn canopy. *Boundary-Layer Meteorology*, 24: 495-519.

Chapter 2. Physiological attributes of *Spartina alterniflora*

2.1. Introduction

It is critical to understand plant physiology to explain ecosystem-level responses to environmental forcings such as the changes in temperature, precipitation, storminess and sea-level rise associated with global climate change. Physiological measurements can help us to understand the efficiency of chemical pathways involved in carbon dioxide (CO₂) fixation (carboxylation) and to estimate plant physiological variables, which can be used as input for biophysical models predicting ecosystem-level fluxes of carbon and energy (e.g., Baldocchi and Meyers, 1998; Gu *et al.*, 1999). A detailed description of plant physiology at the leaf level is critical to improve the understanding of source/sink distribution of carbon and energy in an ecosystem. Leaf-based measurements provide information on the temperature and light response of plant metabolism, which can help us link environmental factors to canopy-level exchanges of energy and carbon.

Spartina alterniflora Loiseleur dominated salt marshes are a common feature along the east coast of the continental United States (Thomson, 1991). This species is native to the east coast, but is categorized as an invasive species on the Pacific coast (Callaway and Josselyn, 1994). *Spartina alterniflora* is a halophytic C₄ grass with a maximum canopy height of about 1.2-1.5 meters (Dai and Wiegert, 1996). The productivity of *Spartina alterniflora* is highest along creek banks and lower in the high marsh where soil characteristics such as lower soil water exchange and redox potential and higher sulfide content and high salinity inhibit its growth (Howes *et al.*, 1985; Pezeshki *et al.*, 1989). It can occur in different morphological forms of the same genotype: a tall form (1-2 m) that occurs near the edge of tidal creeks and the short form (< 1 m) that is found growing a few meters away from the creek banks through the high marsh (Anderson and Reshow, 1980; Dai and Wiegert, 1997). The carbon assimilation rates of the taller ecotypes range from 8 to 25 $\mu\text{mol m}^{-2}$ (leaf area) s^{-1} whereas the shorter ecotypes exhibit rates varying between 4 to 19 $\mu\text{mol m}^{-2}$ (leaf area) s^{-1} (Pezeshki and Delaune, 1988). It is estimated that 95% of the carbon fixed by a *Spartina alterniflora* dominated ecosystem is lost either to respiration or burial and only 5% is exported from the sediment surface to the coastal waters (Howes *et al.*, 1985).

They also estimated that *Spartina alterniflora* grass canopy can fix about 58-75 mol C m⁻² yr⁻¹ as below ground biomass. Although classified as halophytes, *Spartina alterniflora* have been found to have decreased quantum use efficiency under conditions of high salinity and conditions of low irradiance (Maricle *et al.*, 2007). *Spartina alterniflora* can tolerate high salinity levels (up to 0.6 M NaCl) and uses metabolic energy to take up fresh water for physiological processes, and as a result has a higher water use efficiency than C₃ marsh grass species (Vasquez *et al.*, 2006). The *Spartina alterniflora* plants also possess a well developed aerenchymatous system to transport oxygen from the shoots to the root to tolerate anaerobic conditions (Maricle and Lee, 2002).

Spartina alterniflora belongs to the phosphoenolpyruvate carboxykinase (PEP-CK) subtype, and has the most complex biochemistry among the three C₄ subtypes (Voznesenskaya *et al.*, 2006). The three C₄ subtypes differ in the type of enzyme involved in the decarboxylation of the C₄ acids in the bundle sheath cells namely NAD-ME (NAD-malic enzyme) NADP-ME (NADP-malic enzyme) and PCK (phosphoenolpyruvate carboxykinase) (Hatch, 1987). The three biochemical subtypes are characterized by distinct anatomical features such as suberized lamella in the cell wall between bundle sheath and mesophyll cells, which can be responsible for lower bundle sheath conductance values (Hatch and Osmond, 1976) and centripetal or centrifugal location of chloroplasts.

Although leaf-level photosynthesis models of C₄ plants have been developed, they are rarely used in modeling studies as the various physiological variables needed for these models are difficult to obtain experimentally. The graphical techniques used to determine physiological constants from response curves used for C₃ plants cannot be used for C₄ plants as the biochemical mechanisms involved are much complex. Therefore, the objectives of this chapter are two fold. First, the diurnal variations in plant physiological characteristics of *Spartina alterniflora* are investigated to establish how the leaf-level assimilation rates depend on prevailing environmental conditions. Second, plant physiological quantities are determined so that they can be utilized as inputs to canopy biophysical models.

2.2 Site Characteristics

The plant physiological attributes were made at two field sites: (1) the Fowling Point marsh (flux tower site) (37°24' N, 75°50' W), which is a typical lagoonal salt marsh, and (2) Oyster (37° 17' N 75° 55' W) which is an intertidal salt marsh. Both sites are exposed to diurnal tidal fluctuations (≤ 1 m), which can either completely or partially cover the vegetation during different periods of the day. These two sites are dominated by the intermediate forms of *Spartina alterniflora*, with a height of 62.63 ± 1.87 cm in the low marsh; the short form occupies the elevated terrain marsh areas. The mean annual temperature of the area is 14.2°C and the mean maximum and minimum daily temperatures are 19.5°C and 8.9°C, respectively. The mean annual precipitation recorded in this region is about 1065 mm with the largest rainfall received during the months of July and March (<http://intranet.lternet.edu/archives/documents/Publications/climdes/vcr/vcrclim.htm>) (VCR LTER data base). The 2007 growing season (May–October) was characterized by extremely dry conditions with a rainfall of 295 mm.

2.3. Materials and Methods

2.3.1 Plant physiology measurements

Plant physiology measurements were made using a photosynthesis system—an infrared gas analyzer (Model LI 6400, LICOR Biosciences, Lincoln, NB, USA). The instrument has a closed-system chamber design with a light emitting diode (LED) light source for controlling light levels and a CO₂ injector for controlling ambient carbon dioxide concentrations inside the leaf cuvette. Photosynthesis measurements were carried out to investigate the dependence of assimilation (A) on photosynthetically active radiation (light curves), and the dependence of A on intercellular CO₂ concentrations (C_i) (A-C_i curves). Light curves were obtained by subjecting a leaf to different light levels (2000, 1500, 1000, 750, 300, 150, 50, and 0 $\mu\text{mol m}^{-2} \text{s}^{-1}$) and the assimilation rates were measured under constant temperature and humidity conditions (similar to the external environment) with a constant CO₂ mixing ratio of 400 ppm maintained in the leaf chamber. The higher than ambient CO₂ conditions were maintained inside the chamber so as to avoid CO₂ limitations under different irradiance levels. The A-C_i curves were obtained by subjecting the leaf to different external mixing ratios of CO₂ (0, 150 300, 400, 600 and 800 ppm of CO₂) under

constant temperature and humidity conditions with the leaf irradiated with $1800 \mu\text{mol m}^{-2} \text{s}^{-1}$ of PAR. The high irradiance level was maintained inside the leaf chamber to avoid light limitation of photosynthesis under different external concentrations of CO_2 . The plant physiology measurements were made during three different times of the day corresponding to A) Morning (8 to 11:00 hours), B) Noon (12:00 to 14:00 hours), and C) Evening (16:00 to 18:00 hours). These measurements were made during June to August 2007, which corresponded with the peak of the growing season. The measurements were made by selecting the third leaf from the top on healthy intermediate forms of the plant (>0.40 m tall and reaching up to 1m in height (Shea *et al.*, 1975)) and attaching the chamber to the mid part of the leaf.

2.3.2 Empirical analysis of A-PAR and A-Ci curves

The light (A-PAR) and A-Ci curves for the different periods of the day were analyzed using rectangular hyperbolic relationships to quantify the efficiency of the photosynthetic system. The data for the A-PAR curves were fitted to a non-linear Mitscherlich model (Potvin *et al.*, 1990)

$$A = A_{\max} \left[1 - e^{-A_{qe}(PAR-LCF)} \right] \quad (2.1)$$

where A is the net assimilation rate, A_{\max} is the maximum net assimilation, A_{qe} is the initial slope of the light curve at low light levels (apparent quantum yield) and LCF is the light compensation point, which is the PAR level where net assimilation is zero. The A-C_i curves were fitted to a non-linear rectangular hyperbolic equation, which models the response of assimilation (A) as a function of the internal concentration of CO_2 (C_i) (Olsson and Leverenz, 1994).

$$A = \left[C_E \times C_i \times A_{\max} \right] / \left[C_E + C_i + A_{\max} \right] - R_e \quad (2.2)$$

C_E represents the carboxylation efficiency and R_e is the respiration rate expressed in $\mu\text{mol m}^{-2} \text{s}^{-1}$. These models were fit to response curve values obtained during different periods of the day using the dynamic curve fit tool in the scientific graphing software Sigmaplot, (Systat Inc, San Jose, CA, USA). This empirical curve analysis provides us with estimates of physiological parameters that can quantify the efficiency of photosynthetic metabolism. Physiological parameters such as maximum assimilation rate (A_{\max}), quantum efficiency (A_{qe}), and light compensation point (LCF) are directly related to light use efficiency of the plant, whereas carboxylation efficiency (CE) characterizes the efficiency of the biochemical system.

2.3.3 Determination of plant physiological variables

A mathematical description of the C₄ photosynthetic pathway is provided as a background for explaining the methodology in determining the plant physiological variables relevant for canopy biophysical models. The equations described here are based on C₄ biochemical models described by Berry and Farquhar (1978) and Peisker (1979) which are very similar in their representation of the C₄ biochemical pathway. Several modifications have been suggested to these original models (eg Peisker (1986), Collatz *et al.* (1992), and Peisker and Henderson, 1992) which are incorporated in the work of von Caemmerer and Furbank (1999).

The net rate of CO₂ assimilation by C₄ photosynthesis can be described in terms of rubisco carboxylation in bundle sheath cells (equation 2.3)

$$A = V_c - 0.5V_o - R_d \quad (2.3)$$

or mesophyll cells (equation 2.4)

$$A = V_p - L - R_m \quad (2.4)$$

where V_c and V_o represent the rates of rubisco carboxylation and oxygenation, and R_d is the mitochondrial respiration which is the sum of mitochondrial respiration occurring in the mesophyll (R_m) and bundle sheath (R_s) cells. V_p is the rate of PEP carboxylation and L represents the rate of CO₂ leakage from bundle sheath to mesophyll cells and is given as

$$L = g_{bs} (C_s - C_m) \quad (2.5)$$

where g_{bs} is the conductance of bundle sheath cells to CO₂ and C_s and C_m are the concentration of CO₂ in the bundle sheath and mesophyll cells, respectively. The carboxylation (V_c) at high irradiance can be described in terms of the maximum rubisco carboxylation rate (V_{cmax}) or in terms of the maximum PEP carboxylation rate (V_{pmax}) expressed in units of μmol m⁻² s⁻¹.

$$V_c = \frac{C_s V_{c \max}}{C_s + K_c (1 + O_s / K_o)} \quad (2.6)$$

$$V_p = \frac{C_m V_{p \max}}{C_m + K_p} \quad (2.7)$$

where K_c, K_o and K_p are the Michaelis–Menten constants for Rubisco carboxylation, oxygenation and PEP carboxylation, respectively, and O_s and O_b is the oxygen concentration in the mesophyll

and bundle sheath cells, respectively. The rate of rubisco oxygenation (V_o) can be expressed as a function of CO_2 compensation point (Γ^*) (CO_2 concentration at which net assimilation is zero) and C_s .

$$V_o = V_c \times \frac{2\Gamma^*}{C_s} \quad (2.8)$$

The Γ^* can be expressed as a function of rubisco specificity (γ^*) and oxygen concentration in the bundle sheath cells (O_s) as

$$\Gamma^* = \gamma^* O_s \quad (2.9)$$

The net rate of CO_2 assimilation can also be expressed in terms of the CO_2 concentration in the intercellular spaces (C_i) and the mesophyll CO_2 concentration (C_m) as

$$A = g_i(C_i - C_m) \quad (2.10)$$

where g_i is the mesophyll conductance to CO_2 whose value needs to be assumed as there exists no reliable technique to estimate this conductance value because CO_2 diffuses directly from the intercellular spaces to the cytoplasm. Therefore, g_i is likely to be proportional to the surface area of mesophyll surface area exposed to the intercellular air space (Evans and vonCaemmerer, 1996).

The energy requirement for regeneration of RuBP is obtained through the electron transport processes (J_t), which can occur in mesophyll (J_m) and bundle sheath (J_s) chloroplasts ($J_t = J_m + J_s$). The electron transport rate depends upon the availability of incident light and is represented as following (Farquhar and Wong, 1984)

$$J_t = \frac{I_2 + J_{\max} - \sqrt{(I_2 + J_{\max})^2 - 4\theta I_2 J_{\max}}}{2\theta} \quad (2.11)$$

where I_2 is the total light absorbed, J_{\max} is the maximum electron transport rate ($\mu\text{mol electrons m}^{-2} \text{ s}^{-1}$), and θ is an empirical curvature factor. The total absorbed radiation is related to the incident radiation (I) as

$$I_2 = I \times abs(1 - f) / 2 \quad (2.12)$$

where abs is the leaf absorbance and f is a correction factor for spectral quality of light.

The electron transport limited expressions for V_c and V_p can be represented as

$$V_c = \frac{(1-x)J_t}{3 \left(1 + \frac{7}{3} \frac{\gamma^* O_s}{C_s} \right)} \quad (2.13)$$

$$V_p = \frac{xJ_t}{2} \quad (2.14)$$

where x is a partitioning factor of electron transport. The relationships described above form the basic equations which can simulate the biochemical pathways involved in photosynthesis. These relationships are used in combination with response curve measurements to derive the plant physiological variables of maximum carboxylation and electron transport rates.

A) Determination of V_{cmax} and V_{pmax}

The values of V_{cmax} and V_{pmax} were determined following the methodology of Massad *et al.*, 2007. This methodology involves solving a system of 6 non-linear equations derived from three basic relationships obtained by combining the various C_4 photosynthetic pathway relationships and using the A-Ci curve measurements. The first equation represents the net CO_2 assimilation in terms of CO_2 concentration in the intercellular spaces and the mesophyll cells as given in equation 2.10. The second and third equations were developed by replacing the expressions of V_c (equation 2.6) and V_p (equation 2.7) in equations (2.3) and (2.4) to obtain

$$A = \frac{C_s V_{cmax}}{C_s + K_c (1 + O/K_o)} \left(1 - \frac{\gamma^* O_s}{C_s} \right) \quad (2.15)$$

$$A = \frac{C_m V_{pmax}}{C_m + K_p} - g_{bs} (C_s - C_m) - R_m \quad (2.16)$$

The values of K_o , K_c , K_p , γ^* , O_s , g_i , and g_{bs} are constants at a given temperature and the values of A and C_i can be obtained from an A-Ci curve. Thus, this system has three equations and four unknowns, with the unknowns being C_s , C_m , V_{cmax} , and V_{pmax} . The values of R_d and R_m are assumed to be functions of V_{cmax} with $R_d=0.01V_{cmax}$ and $R_m=0.5R_d$.

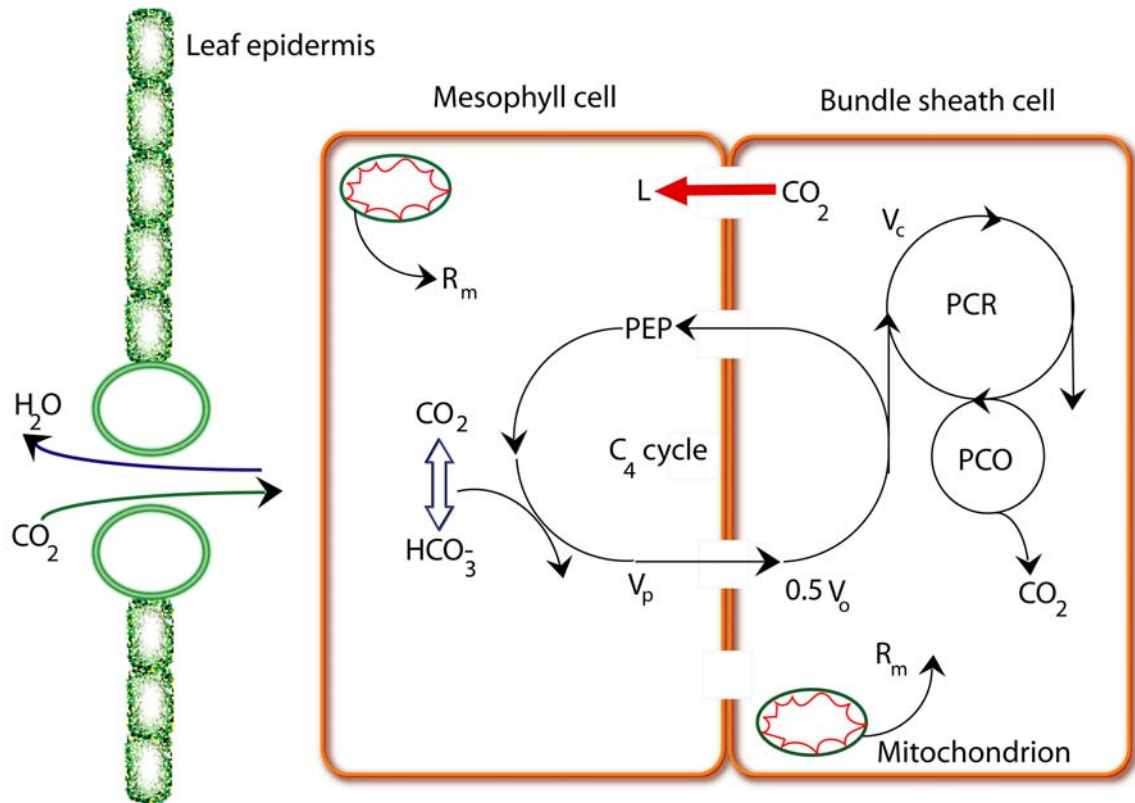


Figure 2.1. Schematic representation of C_4 photosynthesis (adapted from von Caemmerer 1999). The CO_2 diffusing from the outside into the mesophyll cells is converted to HCO_3^- which is fixed by PEP carboxylase and transported into the bundle sheath where it can be either fixed by rubisco in the photosynthetic carbon reduction cycle (PCR) or can leak (L) back into the mesophyll cells. The photosynthetic carbon oxidation (PCO) cycle which is involved in oxygenation of rubisco is also represented along with mitochondrial respiration occurring in mesophyll (R_m) and bundle sheath cells (R_s).

To solve this system, two set of experimental points were selected on an A-Ci curve (A_1, C_{i1}) and (A_2, C_{i2}). The three equations were rewritten for these two set of points to obtain a system of six non-linear equations with six unknowns.

$$A_1 = g_i (C_{i2} - C_{m1}) \quad (2.17)$$

$$A_2 = g_i (C_{i2} - C_{m2}) \quad (2.18)$$

$$A_1 = \frac{C_{s1} V_{c \max}}{C_{s1} + K_c (1 + O_{s1} / K_o)} \left(1 - \frac{\gamma^* O_{s1}}{C_{s1}} \right) \quad (2.19)$$

$$A_2 = \frac{C_{s2} V_{c \max}}{C_{s2} + K_c (1 + O_{s2} / K_o)} \left(1 - \frac{\gamma^* O_{s2}}{C_{s2}} \right) \quad (2.20)$$

$$A_1 = \frac{C_{m1}V_{p\max}}{C_{m1} + K_p} - g_{bs}(C_{s1} - C_{m1}) - R_m \quad (2.21)$$

$$A_2 = \frac{C_{m2}V_{p\max}}{C_m + K_p} - g_{bs}(C_{s2} - C_{m2}) - R_m \quad (2.22)$$

The six unknowns in this system of equations include, C_{m1} , C_{m2} , C_{s1} , C_{s2} , $V_{p\max}$, and $V_{c\max}$ with the oxygen concentration in the bundle sheath cells (O_{s1} and O_{s2}) derived from the oxygen concentration in the mesophyll cells as shown in the relationship 2.2.3

$$O_{s(1,2)} = \frac{\alpha_o A_{(1,2)}}{0.047 g_{bs}} + O_{m(1,2)} \quad (2.23)$$

where α_o ($0 < \alpha_o < 1$) denotes the fraction of the O_2 evolution occurring in the bundle sheath cells (Farquhar, 1983). The oxygen concentration in the mesophyll is derived from the oxygen concentration in the atmosphere and the leaf temperature (Long, 1991)

$$O_{m(1,2)} = O_a [(4.7 \times 10^{-2} - 1.3087 \times 10^{-3} T_{\text{leaf}} + 2.5603 \times 10^{-5} T_{\text{leaf}}^2) - 2.1441 \times 10^{-7} T_{\text{leaf}}^3 / 2.6934 \times 10^2] \quad (2.24)$$

where T_{leaf} is the leaf temperature and O_a is the oxygen concentration in air. The A_1 and A_2 values and corresponding quantities for C_{i1} and C_{i2} were obtained from A- C_i curves taken during different times of the day. The C_{i1} and C_{i2} values were selected with CO_2 mixing ratio values between 30 and 90 ppm as stable results are obtained at lower CO_2 mixing ratios corresponding with the linear part of the A- C_i curve (Massad *et al.*, 2007). This analysis was done on A- C_i curves obtained during different parts of the day so that temperature relationships could be developed for $V_{p\max}$ and $V_{c\max}$.

B. Determination of J_{\max}

The value of J_{\max} can be solved as a system of three non-linear equations using the measurements obtained from A-PAR curves. The relationships between assimilation (A) and electron transport rate can be rewritten by substituting the electron transport limited expressions of V_c (equation 2.13) and V_p (equation 2.14) in equation (2.3) and equation (2.4) to obtain

$$A = \frac{\left(1 - \gamma^* \frac{O_s}{C_s}\right) (1-x) J_t}{3 \left(1 + \frac{7}{3} \frac{\gamma^* O_s}{C_s}\right)} - R_d \quad (2.25)$$

$$A = \frac{x J_t}{2} - g_{bs} (C_s - C_m) - R_m \quad (2.26)$$

These two equations along with equation (2.10) form a system of three non-linear equations with three unknowns C_s , C_m and J_t . Once the value of J_t is obtained by solving this system of equation then the value of J_{\max} can be estimated by substituting the value of J_t for a specific light intensity in equation (2.11). The bundle sheath respiration (R_d) was assumed to be $2.5 \mu\text{mol CO}_2 \text{ m}^{-2} \text{ s}^{-1}$ which was an average value observed from all the different light curves. The mesophyll respiration was assumed to be half of the R_d following the results obtained by Massad *et al.* (2007).

C. Temperature relationships for plant physiological constants

The temperature dependencies of $V_{c\max}$, $V_{p\max}$ and J_{\max} are reflected in the temperature dependency of the CO_2 assimilation rates for leaves (Bjorkman *et al.*, 1980). The temperature dependencies adopted here are described by an Arrhenius function with a 25°C reference temperature (Farquhar *et al.*, 1980).

$$P(J_{\max}, V_{c\max}, V_{p\max}) = P_{25} \left[\exp\left(-\frac{E}{R} \left(\frac{1}{T} - \frac{1}{T_{25}}\right)\right) \right] \times \left[1 + \exp\frac{ST_{25} - H}{RT_{25}} \right] / \left[1 + \exp\frac{ST - H}{RT} \right] \quad (2.27)$$

where P represents the plant physiological variable, P_{25} the value of the variable at 25°C , T represents the absolute temperature in Kelvin, E (J mol^{-1}) is the activation energy, H (J mol^{-1}) represents the deactivation factor (*i.e.* the rate of decrease of the function above an optimum temperature), S is the entropy factor ($\text{J K}^{-1} \text{ mol}^{-1}$), and R represents the universal gas constant ($\text{J K}^{-1} \text{ mol}^{-1}$). The values of E , H and S must be determined using non-linear regression analyses. The temperature dependency of enzyme kinetic parameters K_c , K_p and K_o is described using a Q_{10} relationship following Collatz *et al.*, 1991.

$$Parameter(T) = Parameter(25^{\circ} C) Q_{10}^{[(T-25)/10]} \quad (2.28)$$

The temperature T is expressed in degree Celsius and the Q_{10} is the relative increase in reaction rate over a 10C temperature range for the parameters K_c , K_p , and K_0 . The Q_{10} values are adapted from Chen *et al.*, (1994). A detailed description of all the constants in the C_4 photosynthesis model for determining the plant physiological variables as adapted from (von Caemmerer and Furbank, 1999), along with other physiological constants, is provided in Table 2.1

2.3.4. Modeling stomatal conductance

The Ball and Berry (Ball *et al.*, 1987) stomatal conductance model, which expresses stomatal conductance as a function of assimilation, relative humidity over the leaf surface and leaf surface CO_2 concentration, has been used in this study to develop an empirical model for stomatal conductance to water vapor diffusion out of stomatal pores. Modifications in the Ball and Berry model to include the CO_2 compensation point term is presented in equation (2.29) following Leuning (1990)

$$g_{sv} = g_0 + a \frac{A_n RH}{(C_s - \Gamma)} \quad (2.29)$$

where g_{sv} is the stomatal conductance to water vapor expressed in units of ($mol\ m^{-2}\ s^{-1}$), g_0 is a intercept parameter and a is a constant (slope of the line). RH is the relative humidity expressed in percentage and C_s and Γ are the leaf surface CO_2 concentration and the CO_2 compensation point respectively. The $A-C_i$ response curve measurements were used to develop the relationship between stomatal conductance and assimilation.

2.3.5 Rapid light curve measurements

Leaf fluorescence measurements, which are directly related with electron transport rates in photosystem II were taken using a pulse amplitude modulated (PAM) fluorometer (Diving PAM, Walz, Hamburg, Germany) to determine the physiological response of *Spartina alterniflora* to

submergence. (The results presented in this section are from a collaborative work with Thomas J. Mozdzer, Department of Environmental Sciences, University of Virginia).

Table 2.1. Summary of all the photosynthetic model constants used in the determination of plant physiological variables

| Constants | Value |
|---|---|
| K_c at 25° C (Michaelis-Menten constant for rubisco for CO ₂) | 650 μbar |
| K_o at 25° C (Michaelis-Menten constant for rubisco for O ₂) | 450 mbar |
| K_p at 25° C (Michaelis-Menten constant for PEP carboxylase for CO ₂) | 80 μbar |
| g_{bs} (Bundle sheath conductance to CO ₂) | 3 mmol m ⁻² s ⁻¹ |
| g_i (Mesophyll conductance to CO ₂) | 2 mol m ⁻² s ⁻¹ |
| Θ (Empirical curvature factor) | 0.7 |
| γ^* (Half the reciprocal of rubisco specificity) | 0.000193 |
| α_o (Fraction of O ₂ evolved in mesophyll cell) | 0.5 |
| abs (Leaf absorbance) | 0.85 |
| f (Correction for spectral quality of light) | 0.15 |
| O_a (Oxygen mixing ratio in the atmosphere) | 210000 ppm |
| $Q_{10} K_c$ | 2.1 |
| $Q_{10} K_o$ | 1.2 |
| $Q_{10} K_p$ | 2.1 |
| R (Universal gas constant) | 8.314 J K ⁻¹ mol ⁻¹ |

Rapid light curves (RLC) were collected by subjecting the leaf to eight increasing levels of light for 10 seconds. The RLCs were fitted to a double exponential decay function following Platt *et al.*, (1980).

$$P = P_s \left(1 - e^{-\alpha \frac{PAR}{P_s}} \right) \times e^{-\beta \frac{PAR}{P_s}} \quad (2.30)$$

P represents the modeled relative electron transport rate, P_s represents a scaling factor which is the maximum potential rETR, α is the initial slope of the RLC before the onset of saturation, PAR

is the downwelling irradiance and β represents the slope of the RLC where photosystem II activity declines. The maximum relative electron transport rate ($rETR_{\max}$) (a proxy for maximum assimilation rate) can be expressed following Ralph and Gademann, (2005).

$$rETR_{\max} = P_s \left(\frac{\alpha}{(\alpha + \beta)} \right) \left(\frac{\beta}{(\alpha + \beta)} \right)^{\frac{\beta}{\alpha}} \quad (2.31)$$

The minimum saturating irradiance (E_k) which is the minimum amount of PAR required for attaining photo-saturation can be expressed as a function of $rETR_{\max}$ and α as

$$E_k = rETR_{\max} / \alpha \quad (2.32)$$

The RLCs were obtained between 11:00 and 13:00 hours (local time) on day of year 191 and 198 of 2007, representing both exposed and submerged canopy conditions, respectively.

2.4. Results and Discussion

2.4.1. Diurnal trends in leaf level assimilation-Mechanistic response curve analysis

The diurnal patterns in leaf level assimilation were examined through a mechanistic analysis of $A-C_i$ and A -PAR relationships. The light curves indicate that the maximum rate of assimilation (A_{\max}) was observed during the morning period, with light saturation observed in all periods at PAR values above $1000 \mu\text{mol photons m}^{-2} \text{s}^{-1}$. These results (Figure 2.2) are similar to those obtained by Dai and Wiegert (1997) also for *Spartina alterniflora*. The lower light compensation point and increased apparent quantum yield observed during noon time could be attributed to the increased carboxylation enzyme activity observed at higher leaf temperatures. The decreased A_{\max} values observed during noon hours could be attributed to low CO_2 partial pressures as assimilation may be limited by PEP carboxylase activity or by the regeneration of PEP (von Caemmerer, 1999) (Table 2.2). The highest assimilation rate ($30 \mu\text{mol CO}_2 \text{ m}^{-2} \text{s}^{-1}$) was observed during the morning hours. Photo-inhibition was observed during all periods under high light intensities as indicated by the gradual decrease in assimilation rates above PAR levels of $1000 \mu\text{mol photons m}^{-2} \text{s}^{-1}$. The lower light saturation values observed for *Spartina alterniflora* suggests that maximum CO_2 assimilation likely under PAR levels associated with cloudy skies or during morning or late afternoon hours, however temperature does impose stress on the photosynthetic

mechanism thus decreasing the efficiency of light interception under high temperatures observed during the late after noon hours. The inter-cellular CO₂ concentration also decreases with increasing light intensities and reaches a constant value which lies between 125 and 175 $\mu\text{mol mol}^{-1}$ at PAR values $>350 \mu\text{mol photons m}^{-2} \text{s}^{-1}$ (results not presented here), which was similar to results observed by Dai and Wiegert (1997). The lower internal CO₂ concentration observed here is comparatively lower than other C₄ agricultural crops and C₃ plants (Bunce, 2005), indicating a lower efficiency in utilization of CO₂ under ambient concentrations and higher light levels (PAR $>1000 \mu\text{mol photons m}^{-2} \text{s}^{-1}$).

Table 2.2. Light curve physiological variables estimated from non-linear regression analysis. The standard errors for the estimates are provided in the parenthesis.

| Physiological Variables | Morning | Noon | Evening |
|---|-----------------------|-----------------------|-----------------------|
| A_{max} ($\mu\text{mol m}^{-2} \text{s}^{-1}$) | 16.12 \pm 1.48 | 12.49 \pm 0.79 | 13.34 \pm 1.10 |
| α (Apparent quantum yield) | 0.00417 \pm 0.00125 | 0.00529 \pm 0.00108 | 0.00331 \pm 0.00104 |
| Light compensation point | 85.70 \pm 21.53 | 76.36 \pm 13.12 | 46.66 \pm 23.12 |

The A-C_i curve analysis indicates that the maximum CO₂ assimilation rate was observed during the noon hours, compared to morning and evening periods (Table 2.3). The high assimilation rates could be attributed to the higher temperatures observed during the noon hours (Figure 2.3). The increased carboxylation efficiency (which is the initial slope of the A-C_i curve) and respiration rates observed during the noon period also indicated the effect of increased temperatures. The A-C_i curves leveled off at an intercellular CO₂ molar mixing ratio between 100 and 130 $\mu\text{mol mol}^{-1}$. The A-C_i curve analysis results indicate that *Spartina alterniflora* has a higher degree of temperature tolerance compared to other C₄ plants, and in the presence of increased concentration of CO₂ the plants will have an increased net assimilation rate. It could be further inferred that the low light saturation point observed in *Spartina alterniflora* could be attributed to CO₂ limitation rather than light inhibiting the photosynthetic mechanism. The average CO₂ compensation point (8.73 ppm) was lower during the morning hours compared to the noon (13.91 ppm) and evening hours (15.57 ppm). The CO₂ compensation point values are similar to reported in previous studies (Dai and Wiegert, 1997; Giurgevich and Dunn, 1979) and are in the range of typical C₃ or C₃-C₄ intermediate plant types.

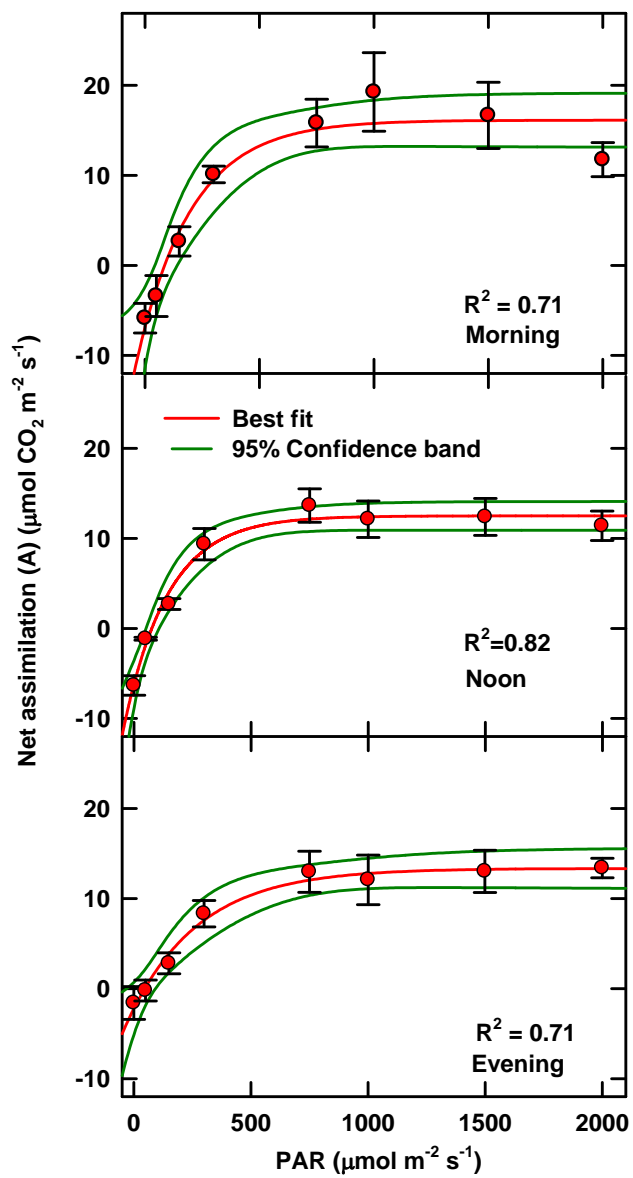


Figure 2.2. Light (A-PAR) curves obtained for the three different periods of the day. The best fit line was obtained by fitting the data to equation (2.1). The measurements were obtained during the peak growing season from June to August 2007.

Table 2.3. A-C_i curve physiological variables estimated from non-linear regression. The standard error for the estimates is given in the parenthesis.

| Physiological Variables | Morning | Noon | Evening |
|--|------------------|------------------|------------------|
| Amax ($\mu \text{ mol m}^{-2} \text{ s}^{-1}$) | 28.62 \pm 2.90 | 36.30 \pm 2.78 | 22.55 \pm 2.36 |
| Respiration ($\mu \text{ mol m}^{-2} \text{ s}^{-1}$) | 3.59 \pm 0.74 | 7.31 \pm 3.13 | 4.63 \pm 2.79 |
| Carboxylation Efficiency | 0.49 \pm 0.20 | 0.74 \pm 0.28 | 0.39 \pm 0.20 |
| Average CO ₂ compensation point (ppm) | 8.73 | 13.91 | 15.57 |

It is expected that in a scenario of global warming with increased concentration of CO₂ in the atmosphere, *Spartina alterniflora* will carry out photosynthesis in a more efficient manner owing to its higher temperature optima for carboxylation reactions and increased assimilation rates observed under higher CO₂ mixing ratios.

2.4.2 Temperature dependence of V_{cmax}, V_{pmax}, and J_{max}.

Determination of plant physiological parameters such as maximum rate of carboxylation (V_{cmax}/V_{pmax}) and maximum electron transport rate (J_{max}) is critical in modeling leaf-level CO₂ exchange using canopy biophysical models (e.g., Baldocchi and Wilson, 2001). The V_{cmax} and V_{pmax} values determined from the A-C_i curve analysis are shown in Figures 2.4 and 2.5 as a function of leaf temperature. The best fit line was obtained by fitting the non-linear function (2.27) to the measured values of leaf temperature and estimated values of V_{cmax}/V_{pmax}. The value of V_{cmax25}, which represents the rubisco carboxylation rate at 298 K (base temperature) as estimated from this analysis, is about 44.25 $\mu\text{mol m}^{-2} \text{ s}^{-1}$. The peak value of V_{cmax} (105 $\mu\text{mol m}^{-2} \text{ s}^{-1}$) observed around 311 K was similar to values reported by Harley *et al.*, (1992) for cotton and Chen *et al.*, (1994) for *Andropogon gerardii*. A gradual drop in V_{cmax} values is expected at temperatures above 311 K.

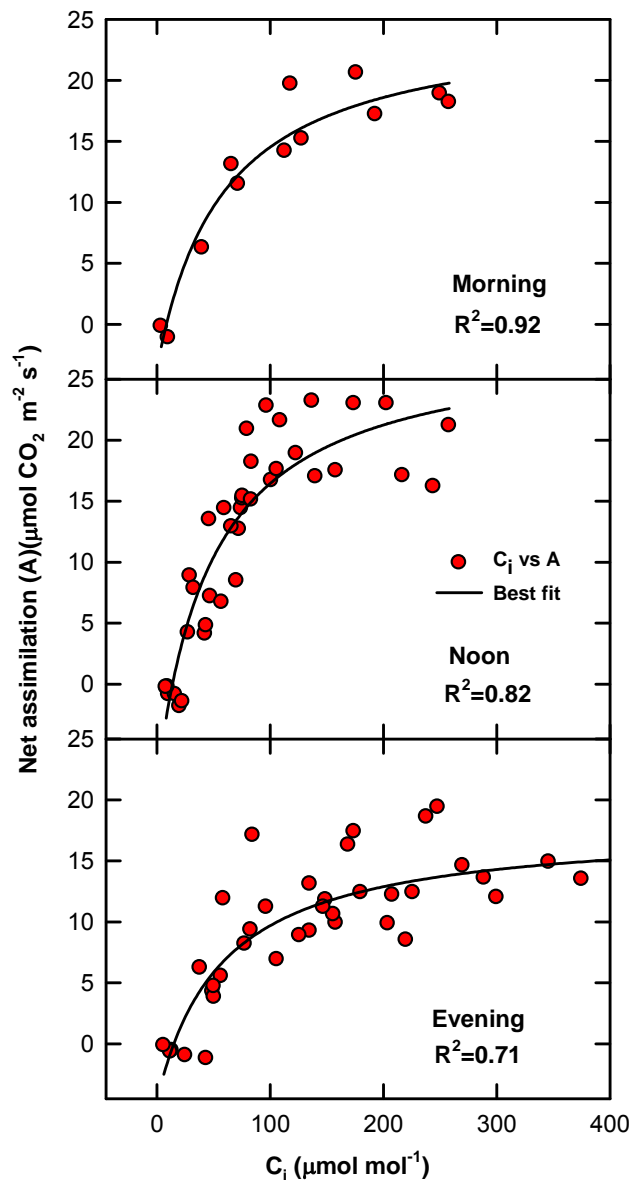


Figure 2.3. Comparison of A-C_i response curves obtained during different periods of the day. The best fit line is obtained by fitting the measured values to equation (2.2) using a non-linear regression procedure. The measurements were obtained during the peak growing season from June to August 2007. The high variability associated in the CO₂ response curves could be attributed to the usage of the LI-6400 automated program for CO₂ response curves.

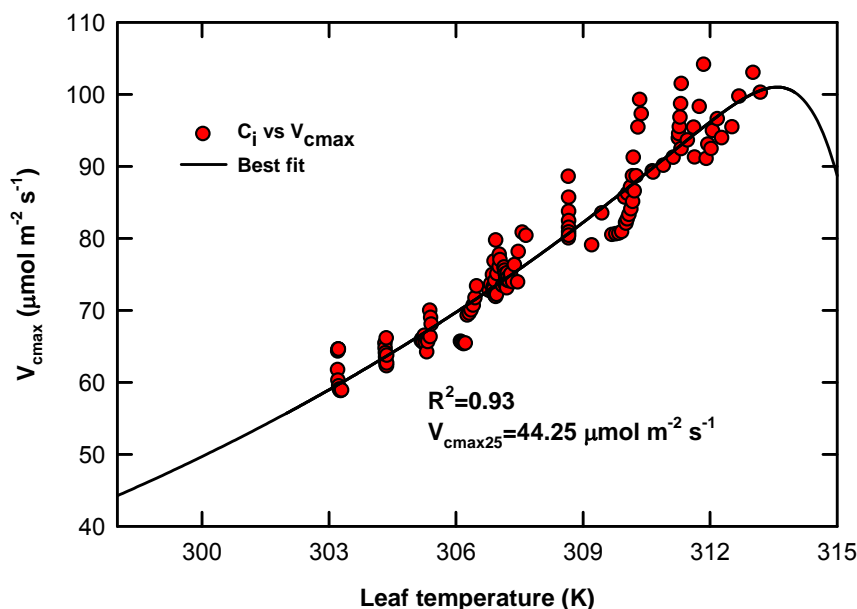


Figure 2.4. Relationship between leaf temperature and V_{cmax} obtained from analysis of A-C_i curves. A total of 14 A-C_i curves containing 93 observations was used to develop this relationship. The solid black line is the best fit line obtained by nonlinear least square regression procedures on the measurements

The V_{pmax} values increased with increasing leaf temperatures to a peak value of $80.6 \mu\text{mol m}^{-2} \text{s}^{-1}$ at a leaf temperature of about 35°C . The value of V_{pmax25} , which represents the PEP carboxylation rate at 25°C (base temperature) as estimated from this analysis, was $13.03 \mu\text{mol m}^{-2} \text{s}^{-1}$. The magnitude of the V_{pmax} values estimated were comparatively smaller than observed in maize—a C₄ plant species (Massad *et al.*, 2007) and in the C₄ grass species *Andropogon gerardii* (Chen *et al.*, 1994). The typical V_{pmax} to V_{cmax} ratios of terrestrial plants range from 2 to 8, and in some cases even 14 to 20 have been observed (Hunt *et al.*, 1985; Sage and Sharkey, 1987; Wong *et al.*, 1985). In contrast the observed ratios in this study fell between 0.27 and 0.92 for different leaf temperatures. The high ratios reported in literature are measured by *in vitro* techniques which may not capture the effect of other metabolites acting on PEP carboxylase and regulating its activity in the *in vivo* state (Doncaster and Leegood, 1987). The initial slope of the A-C_i curve is proportional to the PEP carboxylase activity and typical C₄ plants have been shown to have large initial slopes in their CO₂ response curve, thus accounting for larger V_{pmax} values.

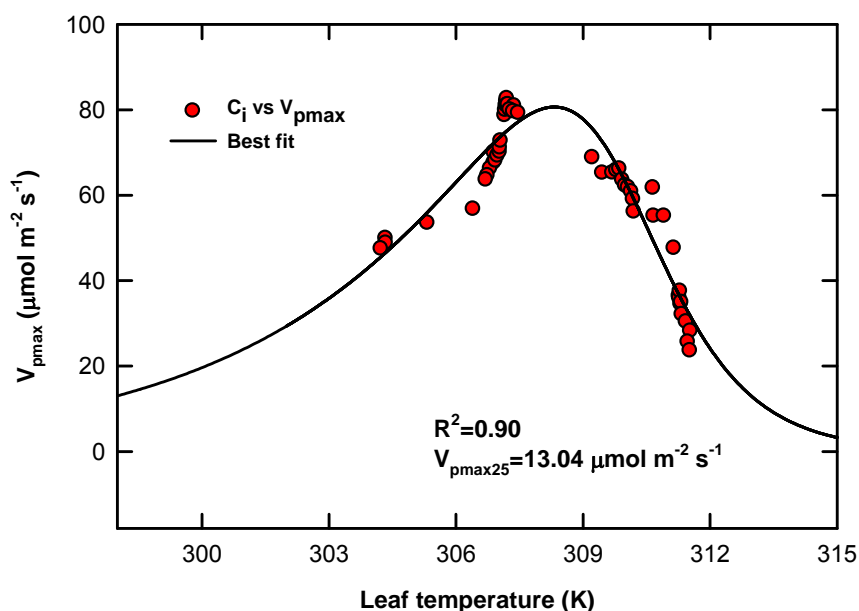


Figure 2.5. Relationship between leaf temperature and V_{pmax} obtained from analysis of A- C_i curves. A total of 14 A- C_i curves containing 93 observations was used to develop this relationship.

The A- C_i curves obtained for *Spartina alterniflora* did not have large initial slopes as compared to most C_4 species, but the ranges of CO_2 assimilation values observed for various C_i values fall in the C_3 - C_4 intermediate or even closer to the C_3 range. A comparison of CO_2 response curves obtained in this study to typical C_4 , C_3 and C_3 - C_4 intermediate plant types is presented in Figure 2.6. The A- C_i response curve obtained by Dai and Wiegert (1997) in *Spartina alterniflora* is also included as a comparison. The reduced PEP-carboxylase activity could be associated with the limitations on diffusion of CO_2 from the intercellular spaces into the mesophyll cells (von Caemmerer, 1999). Mutants of *Amaranthus edulis* have been developed showing similar reduced PEP carboxylase activity with no changes in rubisco activity (Dever *et al.*, 1995). Although the reduction in PEP carboxylase activity can be associated with other factors such as changes in leaf age or nitrogen nutrition, a corresponding reduction in rubisco activity is observed in most cases (Hunt *et al.*, 1985). *Spartina alterniflora* has a peculiar anatomy with the chloroplast in mesophyll and bundle sheath cells having similar granal index (granal index is the percentage of appressed thylakoids, which are membrane-bound compartments inside the chloroplasts where light reactions of photosynthesis take place) (Voznesenskaya *et al.*, 2006).

This means that the mesophyll and bundle sheath cells should provide an identical reductive power in the process of carbon assimilation, reducing the ratio of V_{pmax} to V_{cmax} . The decrease in PEP carboxylase activity could be also due to limitations on its regeneration as controlled by the various enzymes involved in the C_4 cycle (von Caemmerer, 1999). The low CO_2 saturated rates of carbon assimilation (low C_i values for peak assimilation rates) observed in the A- C_i curve analysis also indicate enzyme limitations on PEP carboxylase regeneration. The low light saturation capacity observed in *Spartina alterniflora* which was attributed to CO_2 limitations (in the previous section) can be further supported by the low regeneration of PEP carboxylase, which may occur at high light intensities as found in Maize (Sugiyama and Hirayama 1983). All these results indicate the presence of a peculiar biochemical pathway in *Spartina alterniflora* compared to other terrestrial C_4 plants. Similar biochemical modifications were reported in transgenic *Flaveria bidentis*, a C_4 plant and certain group of *Flaveria* species earlier identified as C_4 species and now been classified as C_4 -like species as they possess small amounts of rubisco in the mesophyll cells. The possibility of existence of similar C_3 - C_4 intermediate biochemical mechanism in *Spartina alterniflora* cannot be ruled out, but further biochemical studies and accurate gas exchange measurements are required to verify this result.

The increased assimilation rates observed under noon conditions with high CO_2 mixing ratios could be attributed to the high temperature optimum observed for V_{cmax} and V_{pmax} . The maximum electron transport rate (J_{max}) increased with increasing leaf temperatures and reached an optimum value around $138 \mu\text{mol of electrons m}^{-2} \text{s}^{-1}$ at a leaf temperature of $31.6 \text{ }^\circ\text{C}$ and thereafter decreased with increasing leaf temperatures. The value of J_{max25} , which is the maximum electron transport at a base temperature of $25 \text{ }^\circ\text{C}$, is around $108.08 \mu\text{mol of electrons m}^{-2} \text{s}^{-1}$. The J_{max} values at $40 \text{ }^\circ\text{C}$ ($73.5 \mu\text{mol m}^{-2} \text{s}^{-1}$) reported here are lower compared to values obtained in maize ($225 \mu\text{mol m}^{-2} \text{s}^{-1}$) (Massad *et al.*, 2007) and tobacco ($300 \mu\text{mol m}^{-2} \text{s}^{-1}$) (Bernacchi *et al.*, 2003). Although there are no previous studies determining maximum electron transport rate in *Spartina alterniflora*, the decreased J_{max} values can be associated with the low maximum assimilation rates (A_{max}). Most C_4 plants have light response curves which saturate only at very high irradiance levels, but *Spartina alterniflora* exhibits light saturation at PAR values $>1000 \text{ photons } \mu\text{mol m}^{-2} \text{s}^{-1}$, which could also account for the decreased J_{max} values. The

comparatively lower quantum yield observed in *Spartina alterniflora* can also account for the lower maximum electron transport rates. The weak relationship between J_{\max} and leaf temperature observed in this study was also reported in other plant physiology studies (Midgley *et al.*, 2004). A summary of nonlinear regression coefficients obtained from the temperature relationships of carboxylation and electron transport rates are provided in Table 2.4.

Table 2.4. Non-linear regression coefficients derived for temperature relationships for V_{cmax} , V_{pmax} , and J_{max} from equation 2.27.

| Regression coefficients | V_{cmax} | V_{pmax} | J_{max} |
|---|-------------------|-------------------|------------------|
| E (J mol ⁻¹) | 43113.99 | 152271.66 | 70000.00 |
| H (J mol ⁻¹) | 1116346.17 | 727809.94 | 174243.92 |
| S (J K ⁻¹ mol ⁻¹) | 3533.23 | 2349.49 | 571.15 |
| Value @25°C (μmol m ⁻² s ⁻¹) | 44.25 | 13.03 | 109.03 |

2.4.3. Relationship between stomatal conductance and photosynthetic rate

The relationship between stomatal conductance and assimilation incorporating the effects of relative humidity and CO₂ concentration on the leaf surface is presented in Figure 2.8. Even though several improvements have been suggested for the Ball and Berry relationships to include effects of vapor pressure deficit (Leuning, 1995), soil moisture status (Yu *et al.*, 2004) and intercellular CO₂ concentration (C_i) (Barr, 2005), the Ball and Berry model in its original form captured the variations ($R^2=0.99$) in stomatal conductance as a function of CO₂ assimilation rates. Moreover, the saturated soil conditions existing in salt marshes mean that the modifications to account for soil moisture deficit cannot be implemented in this case. Further *Spartina alterniflora* being a C₄ plant has the ability to concentrate CO₂ in the bundle sheath cells and thus could continue assimilation even if complete stomatal closure occurs.

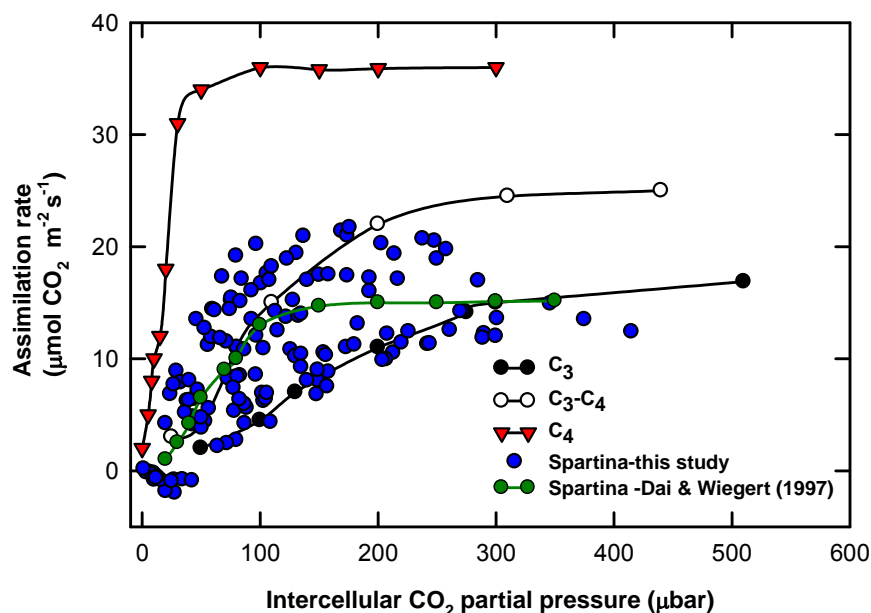


Figure 2.6. The comparison of A-C_i response curves from this study with typical C₃, C₃-C₄ and C₄ plant types. The A-C_i response curve obtained by Dai and Wiegert (1997) in *Spartina alterniflora* is also included. Figure adapted from von Caemmerer (1999).

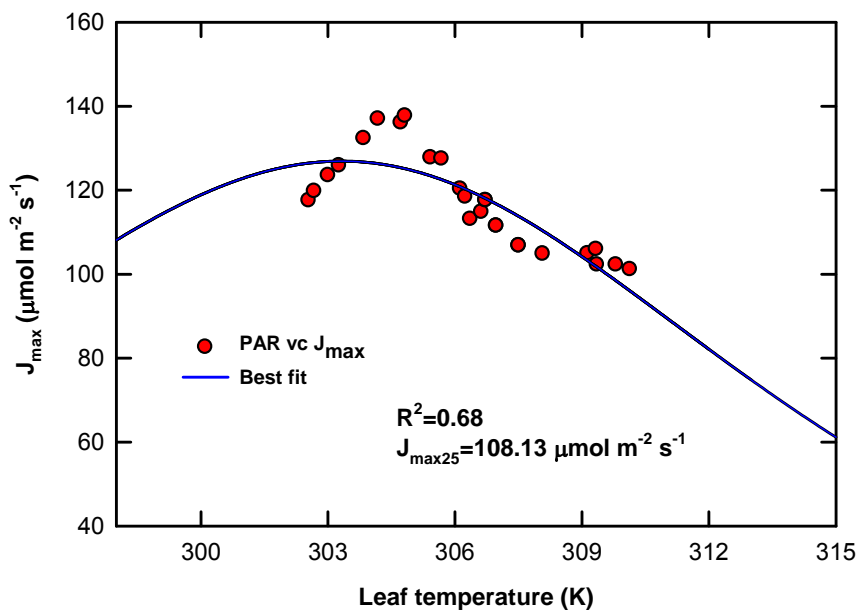


Figure 2.7. The relationship between maximum electron transport rate (J_{\max}) and leaf temperature. The relationship was derived from a total of 11 light response curves having 90 set of values. The data collected were fitted to equation (2.27) using a non-linear regression procedure to obtain the best fit line.

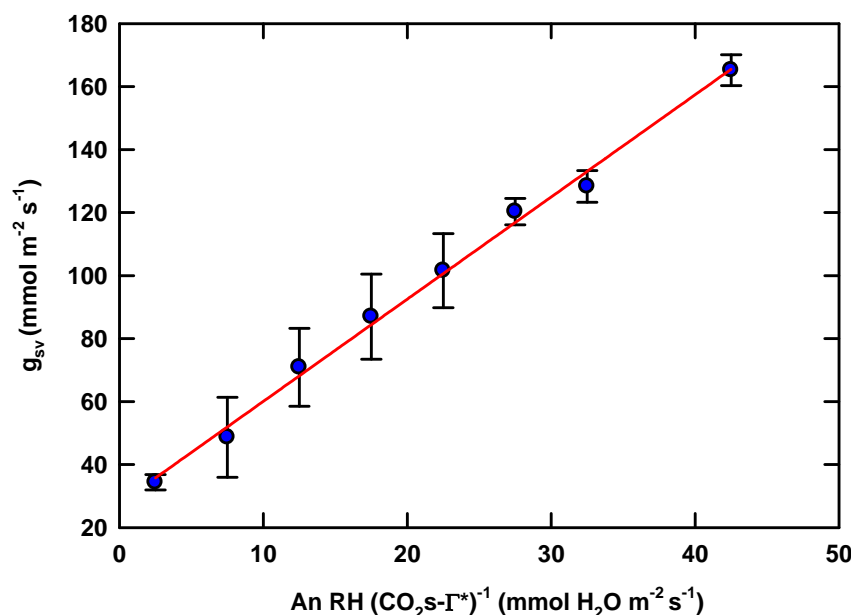


Figure 2.8. The relationship between stomatal conductance and assimilation following Ball *et al.* (1987). The relationship is applied to binned data obtained from A-C_i response curves (14 response curves) collected throughout the growing season.

The Ball and Berry intercept (g_0) obtained from the analysis is about $0.028 \text{ mol m}^{-2} \text{ s}^{-1}$ (± 0.002) and the slope obtained is 3.24 (± 0.09) (dimensionless). The relationship exhibits some degree of curvilinearity at low assimilation rates indicating the presence of water stress similar to observations made in oak savanna trees (Xu and Baldocchi, 2003). The maximum g_{sv} values were about $0.20 \text{ mol H}_2\text{O m}^{-2} \text{ s}^{-1}$, which is comparable to values obtained by Dai and Wiegert (1997) for *Spartina alterniflora*.

2.4.4. Physiological response to submergence

Spartina alterniflora being an intertidal species is subjected to tidal activity twice a day, where the plants can be partially or completely submerged. Since gas exchange measurements are not possible under submerged leaf conditions, the physiological response to flooding is examined in terms of rapid light curves obtained through PAM measurements, which provide estimates of relative electron transport rates- a proxy for photosynthesis. Further, it is critical to understand the physiological response to submergence as in a scenario of increased global temperatures and

associated sea level rise the intertidal salt marshes may be subjected to increased hydro-periods, subjecting the plants to increased periods of submergence.

Table 2.5. Summary of physiological parameters obtained through non-linear regression analysis from rapid light curve data obtained through pulse amplitude modulated fluometry. A total of 293 submerged and 243 exposed light curve points were utilized in this analysis. The values given in the parenthesis represent the standard error of the estimates.

| Physiological variables | Submerged | Exposed |
|---|---------------------|--------------------|
| Ps | | |
| ($\mu\text{mol photons m}^{-2} \text{ s}^{-1}$) | 30.70 \pm 1.79 | 109.40 \pm 16.71 |
| α | 0.208 \pm 0.010 | 0.319 \pm 0.012 |
| β | 0.0008 \pm 0.0022 | 0.0711 \pm 0.024 |
| rETR _{max} | 29.94 | 61.21 |
| E _k | | |
| ($\mu\text{mol photons m}^{-2} \text{ s}^{-1}$) | 143.92 | 191.89 |

The results indicate that there is a clear reduction in photosynthetic rates under submerged conditions with the submerged conditions having a lower rETR_{max} and E_k values compared to the exposed plants (Figure 2.9). The quantum efficiency also showed a similar trend with submerged plants having lower values than exposed ones. Although submergence acts as a physical barrier for gas exchange, (since CO₂ diffuses 10, 000 times slower in water than in air), the plants still continue to photosynthesize as evidenced by the E_k and rETR_{max} values (Table 2.5). One plausible explanation for this response would be the internal recycling of CO₂ through the extensive gas-filled aerenchymatous tissues present in *Spartina alterniflora*.

The photo-inhibition observed under exposed conditions (at PAR values > 600 $\mu\text{mol m}^{-2} \text{ s}^{-1}$) was not observed for submerged conditions as the submerged plants are not light saturated under and more reaction centers are available for electron transport in photosystem II, with CO₂ being the only limiting substrate.

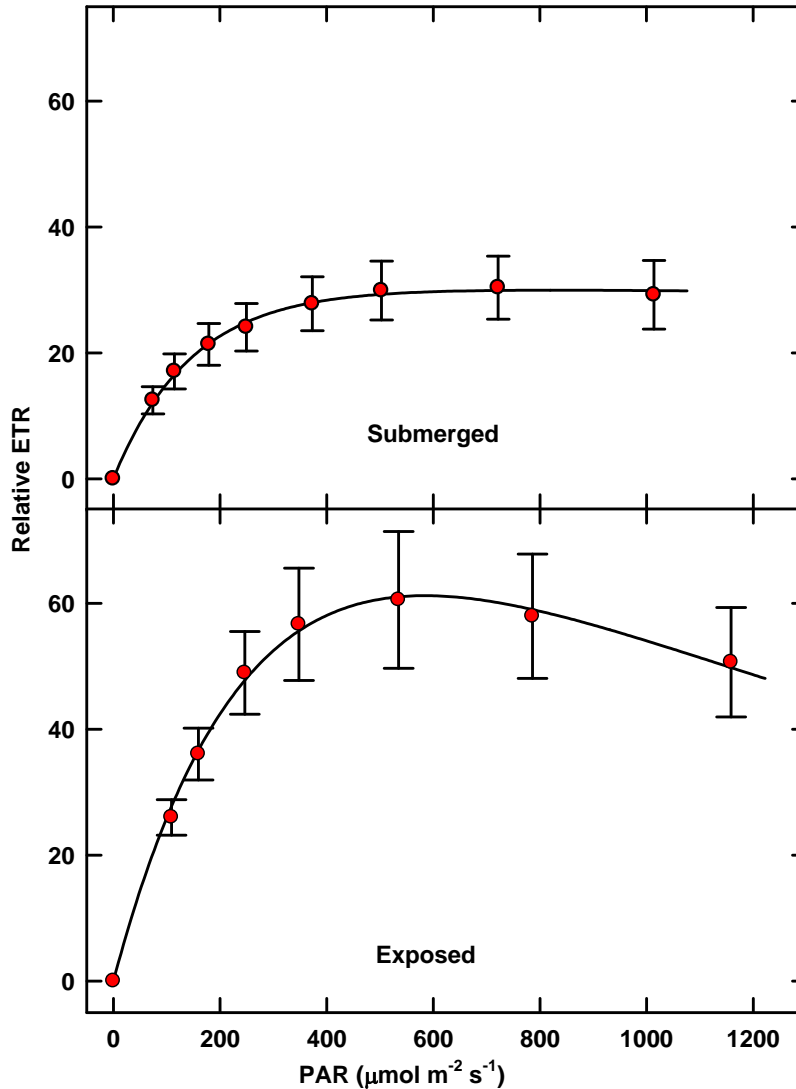


Figure 2.9. Rapid light curved obtained between 11:00 and 14:00 hours on submerged and exposed *Spartina alterniflora* plants. The solid line indicates the best fit of the observed values to the equation (2.30) and the error bars represents the standard deviation of ETR values observed for a specific PAR bin.

2.5. Summary and conclusions

A detailed description of photosynthetic response as governed by physiological variables in *Spartina alterniflora* is reported in this chapter. The low light saturation point and the decreased PEP carboxylase activity exert limitations on assimilation by *Spartina alterniflora* compared to other C_4 plants. *Spartina alterniflora* has a higher rubisco activity compared to other C_4 plants, which may be supported by the peculiar anatomy with larger mitochondria in the bundle sheath cells (Voznesenskaya *et al.*, 2006). The high temperature optima observed for V_{cmax} and V_{pmax}

along with a light saturation point indicate that the productivity of *Spartina alterniflora* will be higher under high temperature environments and low light levels as observed under cloudy sky conditions. The low light saturation observed can be attributed to CO₂ limitations and in a scenario of rising CO₂ concentrations it is expected that *Spartina alterniflora* will have increased light use efficiency. The physiological constants determined in this study are based on several assumptions related to the photosynthesis process; hence caution must be exercised in interpreting these values. Since there exists no reliable method for estimating mesophyll and bundle sheath conductance, these values are assumed to be constants in this study. The mesophyll conductance determine the availability of CO₂ as a substrate for PEP carboxylase and the bundle sheath conductance determine the rubisco activity and the leakage of CO₂ back into the mesophyll cells. The PEP-CK subtype to which *Spartina alterniflora* belongs has a complex biochemistry and distinct anatomical features among C₄ plants. The A-C_i curves obtained in this study demonstrate the peculiar assimilatory response of *Spartina alterniflora* which is different from other C₄ plants. Thus, there exists the need for developing more species-specific photosynthetic models, rather than adapting already existing C₄ models with a better representation of plant biochemistry. Further being an inter-tidal species, *Spartina alterniflora* may be exposed to different levels of submergence as a result of tidal activity. PAM measurements in *Spartina alterniflora* indicated a reduction in maximum electron transport rates and apparent quantum efficiencies in submerged plants compared to exposed ones. The changes in plant physiology when submerged needs further investigation.

The following key conclusions are derived from the results presented in this chapter

- 1) *Spartina alterniflora* has a low light saturation capacity as it exhibits photo-saturation at light levels above 1000 $\mu\text{mol m}^{-2} \text{s}^{-1}$ and lower electron transport rates. The lower light saturation values can be attributed to CO₂ limitation rather than light stress as higher light saturation points are observed under higher CO₂ mixing ratios.
- 2) The carboxylation reaction rates (V_{cmax} and V_{pmax}) in *Spartina alterniflora* have a higher temperature (>35°C) optimum, which indicate that the plant will become more efficient in a scenario of increased temperatures and CO₂ concentrations.

- 3) Submergence can significantly reduce the assimilation capacity of *Spartina alterniflora* and in a scenario of rapid sea level rise, which can increase the hydro-period over a marsh surface, the carbon fixing capability of *Spartina alterniflora* dominated inter-tidal salt marshes may be affected.

References

- Anderson, C.M. and Treshow, M. 1980. A review of environmental and genetic factors that affect height in *Spartina alterniflora* Loisel (salt-marsh cord grass). *Estuaries*, 3: 168-176.
- Baldocchi, D., Falge, E., Gu, L. H., Olson, R., Hollinger, D., Running, S., Antoni, P., Bernhofer, C., Davis, K., Evans, R., Fuentes, J., Goldstein, A., Katul, g., Law, B., Lee, X. H., Malhi, Y., Meyers, T., Munger, W., Oechel, W., Paw, K. T., Pilegaard, K., Schmid, H. P., valentine, R., Verma, S., Vesala, T., Wilson, K and Wofsy, S. 2001. FLUXNET: A new tool to study the temporal and spatial variability of ecosystem-scale carbon dioxide, water vapor, and energy flux densities. *Bulletin of the American Meteorological Society*, 82: 2415-2434.
- Baldocchi, D. and Meyers, T. 1998. On using eco-physiological, micrometeorological and biogeochemical theory to evaluate carbon dioxide, water vapor and trace gas fluxes over vegetation: a perspective. *Agricultural and Forest Meteorology*, 90: 1-25.
- Baldocchi, D.D. and Wilson, K.B. 2001. Modeling CO₂ and water vapor exchange of a temperate broadleaved forest across hourly to decadal time scales. *Ecological Modeling*, 142: 155-184.
- Ball, J.T., Woodrow, I.E. and Berry, J.A. 1987. A model predicting stomatal conductance and its contribution to the control of photosynthesis under different environmental conditions. *Progress in Photosynthesis Research*, IV. Martinus-Nijhoff Publishers, Dordrecht, The Netherlands., 221–224 pp.
- Barr, A.G. 2005. Carbon assimilation by riverine mangroves in the Florida Everglades. PhD Thesis, University of Virginia, Charlottesville., 155 pp

- Bernacchi, C.J., Pimentel, C. and Long, S.P. 2003. In vivo temperature response functions of parameters required to model RuBP-limited photosynthesis. *Plant Cell and Environment*, 26: 1419-1430.
- Berry, J. A and Farquhar, G. D. 1978. The CO₂ concentration function of C₄ photosynthesis: a biochemical model. In: Hall, D., Coombs, J and Goodwin, T. (ed). *Proceeding of the 4th international congress on photosynthesis*. Biochemical Society, London, 954-967 pp.
- Bunce, J.A. 2005. What is the usual internal carbon dioxide concentration in C₄ species under midday field conditions? *Photosynthetica*. 43:603-608.
- Bjorkman, O., Badger, M.R. and Armond, P.A. 1980. Response and adaptation of photosynthesis at high temperature. In: N.C. Turner and P.J. Kramer (Editors), *Adaptation of plants to water and high temperature stress*. John Wiley and Sons Inc, New York.
- Callaway, J.C., and Josselyn, M. N. 1992. The introduction and spread of smooth cord grass (*Spartina alterniflora*) in South San Francisco Bay. *Estuaries* 15: 218-226.
- Chen, D.X., Coughenour, M.B., Knapp, A.K. and Owensby, C.E. 1994. Mathematical simulation of C₄ grass photosynthesis ambient and elevated CO₂. *Ecological Modeling*, 73: 63-80.
- Collatz, G.J., Ball, J.T., Grivet, C. and Berry, J.A. 1991. Physiological and environmental-regulation of stomatal conductance, photosynthesis and transpiration - a model that includes a laminar boundary-layer. *Agricultural and Forest Meteorology*, 54: 107-136.
- Collatz, G. J., Ribas-Carbo M and Berry, J. A. 1992. Coupled photosynthesis-stomatal conductance model for leaves of C₄ plants. *Australian Journal of Plant Physiology*, 19: 519-538.
- Dai, T. and Wiegert, R.G. 1997. A field study of photosynthetic capacity and its response to nitrogen fertilization in *Spartina alterniflora*. *Estuarine Coastal and Shelf Science*, 45: 273-283.
- Dai, T and Wiegert, R. G. 1996. Estimation of productivity of *Spartina alterniflora* using a canopy model. *Ecography*, 19: 410-423

- Dever, L.V., Blackwell, R.D., Fullwood, N.J., Lacuesta, M., Leegood, R.C., Onek, L.A., Pearson, M. and Lea, P.J. 1995. The isolation and characterization of mutants of the C₄ photosynthetic pathway. *Journal of Experimental Botany*, 46: 1363-1376.
- Doncaster, H.D. and Leegood, R.C. 1987. Regulation of phosphoenolpyruvate carboxylase activity in maize leaves. *Plant Physiology*, 84: 82-87.
- Evans, J.R. and vonCaemmerer, S. 1996. Carbon dioxide diffusion inside leaves. *Plant Physiology*, 110: 339-346.
- Farquhar, G.D. 1983. On the nature of carbon isotope discrimination in C₄ species. *Australian Journal of Plant Physiology*, 10: 205-226.
- Farquhar, G.D., Caemmerer, S.V. and Berry, J.A. 1980. A biochemical model of photosynthetic CO₂ assimilation in leaves of C₃ species. *Planta*, 149: 78-90.
- Farquhar, G.D. and Wong, S.C. 1984. An Empirical-Model of Stomatal Conductance. *Australian Journal of Plant Physiology*, 11: 191-209.
- Giurgevich, J.R. and Dunn, E.L. 1979. Seasonal patterns of CO₂ and water-vapor exchange of the tall and short height forms of *Spartina alterniflora* Loisel in a Georgia salt-marsh. *Oecologia*, 43: 139-156.
- Gu, L.H., Shugart, H.H., Fuentes, J.D., Black, T.A. and Shewchuk, S.R. 1999. Micrometeorology, biophysical exchanges and NEE decomposition in a two-story boreal forest - development and test of an integrated model. *Agricultural and Forest Meteorology*, 94: 123-148.
- Harley, P.C., Thomas, R.B., Reynolds, J.F. and Strain, B.R. 1992. Modeling photosynthesis of cotton grown in elevated CO₂. *Plant Cell and Environment*, 15: 271-282.
- Hatch, M. D. and Osmond, C. B. 1976. Compartmentation and transport in C₄ photosynthesis. In: Stocking, C. R., and Heber U. (eds). *Transport in plants III. Intercellular interactions and transport processes Encyclopedia of plant physiology, new series, Vol. 3.* Springer-Verlag, Berlin, pp. 144-184.
- Hatch, M. D. 1987. C₄ photosynthesis: a unique blend of modified biochemistry, anatomy and ultrastructure. *Biochemica et Biophysica Acta*, 895: 81-106.

- Howes, B.L., Dacey, J.W.H. and Teal, J.M. 1985. Annual carbon mineralization and belowground production of *Spartina alterniflora* in a New-England salt-marsh. *Ecology*, 66: 595-605.
- Hunt, E.R., Weber, J.A. and Gates, D.M. 1985. Effects of nitrate application on *Amaranthus powellii* Wats.3 optimal allocation of leaf nitrogen for photosynthesis and stomatal conductance. *Plant Physiology*, 79: 619-624.
- Jenkins, C.L.D., Furbank, R.T. and Hatch, M.D. 1989. Mechanism of C₄ photosynthesis - a model describing the inorganic carbon pool in bundle sheath-cells. *Plant Physiology*, 91: 1372-1381.
- Leuning, R. 1990. Modeling stomatal behavior and photosynthesis in *Eucalyptus grandis*. *Australian Journal of Plant Physiology*, 17: 159-175.
- Leuning, R. 1995. A critical-appraisal of a combined stomatal-photosynthesis model for C₃ plants. *Plant Cell and Environment*, 18: 339-355.
- Long, S.P. 1991. Modification of the response of photosynthetic productivity to rising temperature by atmospheric CO₂ concentrations - has its importance been underestimated. *Plant Cell and Environment*, 14: 729-739.
- Maricle, B.R. and Lee, R.W. 2002. Aerenchyma development and oxygen transport in the estuarine cord grasses *Spartina alterniflora* and *S. anglica*. *Aquatic Botany*, 74: 109-120.
- Maricle, B.R., Lee, R.W., Hellquist, C.E., Kiirats, O. and Edwards, G.E. 2007. Effects of salinity on chlorophyll fluorescence and CO₂ fixation in C₄ estuarine grasses. *Photosynthetica*, 45: 433-440.
- Massad, R.S., Tuzet, A. and Bethenod, O. 2007. The effect of temperature on C₄-type leaf photosynthesis parameters. *Plant Cell and Environment*, 30: 1191-1204.
- Midgley, G.F., Aranibar, J.N., Mantlana, K.B. and Macko, S. 2004. Photosynthetic and gas exchange characteristics of dominant woody plants on a moisture gradient in an African savanna. *Global Change Biology*, 10: 309-317.
- Olsson, T. and Leverenz, J.W. 1994. Non-uniform stomatal closure and the apparent convexity of the photosynthetic photon flux-density response curve. *Plant Cell and Environment*, 17: 701-710.

- Peisker, M. 1979. Conditions for low and oxygen-independent CO₂ compensation concentration in C₄ plants as derived from a simple model. *Photosynthetica*, 13: 198-207.
- Peisker, M. 1986. Models of carbon metabolism in C₃-C₄ intermediate plants as applied to the evolution of C₄ photosynthesis. *Plant Cell and Environment*, 9: 627-635.
- Peisker, M. and Henderson, S. A. 1992. Carbon: terrestrial C₄ plants (commissioned review). *Plant Cell and Environment*, 15: 987-1004.
- Pezeshki, S.R. and Delaune, R.D. 1988. Carbon assimilation in contrasting streamside and inland *Spartina alterniflora* salt-marsh. *Vegetatio*, 76: 55-61.
- Pezeshki, S.R., Delaune, R.D. and Patrick, W.H. 1989. Effect of fluctuating rhizosphere redox potential on carbon assimilation of *Spartina alterniflora*. *Oecologia*, 80: 132-135.
- Platt, T., Gallegos, C.L. and Harrison, W.G. 1980. Photoinhibition of photosynthesis in natural assemblages of marine phytoplankton. *Journal of marine research*, 38: 687-701.
- Potvin, C., Lechowicz, M.J. and Tardif, S. 1990. The statistical-analysis of ecophysiological response curves obtained from experiments involving repeated measures. *Ecology*, 71: 1389-1400.
- Ralph, P. J. and Gademann, R. 2005. Rapid light curves: A powerful tool to assess photosynthetic activity. *Aquatic Botany* 82: 222-237.
- Sage, R.F. and Sharkey, T.D. 1987. The effect of temperature on the occurrence of O₂ and CO₂ insensitive photosynthesis in field-grown plants. *Plant Physiology*, 84: 658-664.
- Shea, M. L., Warren, R.S. and Niering, W. A. 1975. Biochemical and transplantation studies of the growth form of *Spartina alterniflora* on Connecticut salt marshes. *Ecology* 56: 461-466.
- Sugiyama, T. and Hirayama, Y. 1983. Correlation of the activities of of phosphoenolpyruvate carboxylase and pyruvate, orthophosphate dikinase with biomass in maize seedlings. *Plant Cell Physiology* 24: 783-787
- Thompson, J. D. 1991. The biology of an invasive plant. *Bioscience*.41: 393-401.
- Vasquez, E.A., Glenn, E.P., Guntenspergen, G.R., Brown, J.J. and Nelson, S.G. 2006. Salt tolerance and osmotic adjustment of *Spartina alterniflora* (Poaceae) and the invasive M

- haplotype of *Phragmites australis* (Poaceae) along a salinity gradient. *American Journal of Botany*, 93: 1784-1790.
- von Caemmerer, S. 1999. *Biochemical models of leaf photosynthesis*. CSIRO Publishing, Victoria.
- von Caemmerer, S. and Furbank, R.T. 1999. The modeling of C₄ photosynthesis. *The biology of C₄ photosynthesis*. Academic Press, New York, 169:207 pp.
- Voznesenskaya, E.V., Franceschi, V.R., Chuong, S.D.X. and Edwards, G.E. 2006. Functional characterization of phosphoenolpyruvate carboxykinase-type C₄ leaf anatomy: Immuno-, cytochemical and ultrastructural analyses. *Annals of Botany*, 98: 77-91.
- Wong, S.C., Cowan, I.R. and Farquhar, G.D., 1985. Leaf conductance in relation to rate of CO₂ assimilation. 1. influence of nitrogen nutrition, phosphorus-nutrition, photon flux-density, and ambient partial-pressure of CO₂ during ontogeny. *Plant Physiology*, 78: 821-825.
- Xu, L.K. and Baldocchi, D.D. 2003. Seasonal trends in photosynthetic parameters and stomatal conductance of blue oak (*Quercus douglasii*) under prolonged summer drought and high temperature. *Tree Physiology*, 23: 865-877.
- Yoshimura, Y., Kubota, F. and Ueno, O. 2004. Structural and biochemical bases of photorespiration in C-4 plants: quantification of organelles and glycine decarboxylase. *Planta*, 220: 307-317.
- Yu, Q., Zhang, Y.G., Liu, Y.F. and Shi, P.L. 2004. Simulation of the stomatal conductance of winter wheat in response to light, temperature and CO₂ changes. *Annals of Botany*, 93: 435-441.

Chapter 3. Carbon flow dynamics in an intertidal salt marsh

3.1. Introduction

The carbon cycle has received particular attention because of the fact that 58 percent of the observed global warming is attributed to the increase in atmospheric carbon dioxide (CO₂) concentrations (Lashof and Ahuja, 1990; IPCC 2007 report). Much importance has been given to the understanding of the carbon cycle on the ecosystem scale with the recent international initiatives such as the FLUXNET (Baldocchi *et al.*, 2001) which is a network of long-term CO₂ flux measuring sites situated in different ecosystems of the world. Long term studies (e.g., Black *et al.*, 1996; Law *et al.*, 2002; Lee *et al.*, 1999; Wofsy *et al.*, 1993) have helped us to understand the key environmental forcings on ecosystem-level fluxes of CO₂ and energy from diverse biomes on a range of spatial and temporal scales. Environmental variations have significant effects on short term or seasonal vegetation-atmosphere carbon exchange, whereas inter annual or long term exchange processes are governed by biotic responses to environmental forcings (Richardson *et al.*, 2007). The key forcings on seasonal carbon assimilation patterns include the quality and quantity of received photosynthetic active radiation (PAR) (Gu *et al.*, 2002a; Gu *et al.*, 2003), soil moisture (Krishnan *et al.*, 2006), changes in leaf area index (LAI) (Flanagan *et al.*, 2002) and changes in vegetation physiological attributes (Wilson *et al.*, 2001). Ecosystem respiration depends to a large extent on changes in soil temperature (Lloyd and Taylor, 1994) and soil moisture (Kurc and Small, 2007). Pulse events like rainfall and changes in canopy photosynthesis and stomatal conductance modulated by passage of dry and humid air masses also impact ecosystem level respiration (Baldocchi *et al.*, 2006; Xu *et al.*, 2004).

The global importance of wetlands as carbon sinks is widely recognized (Durate *et al.*, 2005; Adams *et al.*, 1990). Wisniewski and Lugo (1992) stated that it is critical to include “the coastal system along with the terrestrial, oceanic, and atmospheric systems in models of the carbon cycle because this sector of the biosphere (particularly in the tropics) has a high rate of carbon sequestration that has not been accounted for in terrestrial and oceanic carbon models”. Wetlands are important sinks and sources of atmospheric trace gases (e.g., carbon dioxide, nitrous oxide, methane) involved in climate change (Whiting and Chanton, 2001). Wetlands

contain 15-20% of the global terrestrial carbon and can exert a large influence on global climate change (Zhang *et al.*, 2002).

Even though several studies exist regarding ecosystem-level exchanges of CO₂ from freshwater wetland systems (Aurela *et al.*, 2007; Hirano *et al.*, 2007; Lund *et al.*, 2007), considerable gaps still exist in the understanding of carbon cycling in coastal or salt marsh ecosystems. *Spartina alterniflora* dominated inter-tidal salt marshes are a common feature along the east coast of the continental United States. These systems represent the interface between the terrestrial and oceanic environments and are most susceptible to global climate change and associated changes in sea level (Simas *et al.*, 2001). Relative sea-level rise associated with global warming can impact physical and biogeochemical processes in coastal ecosystems. The response of coastal salt marshes to relative sea level rise depends upon various processes including, impact of increased hydro-periodicity on sediment accretion and changes in marsh biogeochemistry which can lead to changes in species composition (Reed, 1995). The absolute increase in marsh elevation in response to sea level rise can cause a landward migration of the marsh ecosystem, which can bring about changes in percentage area of wetlands thus increasing productivity. However, this migration is controlled by factors such as local geomorphology and presence or absence of man made physical barriers (Gardner and Porter, 2001) such as roadways, building and parking lots. Therefore primary production in intertidal salt marshes is primarily governed by the relative sea level and the vegetation in turn constantly adjusts the elevation through sediment accretion (Morris, *et al.*, 2002).

Woodwell *et al.* (1977) estimated that in a tidally influenced salt marsh, the net flux of carbon as dissolved and inorganic carbon was about 51 g C cm⁻² year⁻¹, indicating that salt marshes are sinks of carbon. Wang and Cai (2004) indicated that export of carbon as respiratory product from a salt marsh is the primary process of carbon export from such systems. The high concentration of dissolved carbon in these ecosystems can lead to elevated CO₂ partial pressures in the water column. Newell *et al.*, (1985) estimated that the standing dead mass of plant matter over a salt marsh release steady rates of CO₂ into the air and increased CO₂ emissions are observed for input of freshwater or salt water into the system. Recent estimates indicate that the emissions of CO₂ from estuaries almost fully balance the sink of atmospheric CO₂ computed for continental shelves (Borges *et al.*, 2006). Very few studies exist over salt

marsh ecosystems utilizing micrometeorological methodologies to estimate ecosystem level fluxes of CO₂. In the Flax pond ecosystem study, CO₂ flux estimates were obtained using the aerodynamic methodology indicated that *Spartina alterniflora* dominated salt marshes are net sinks for atmospheric CO₂ fixing 300 g of carbon per year. Heilman *et al.*, (1999) conducted tower-based conditional sampling of CO₂ flux over a coastal wetland dominated by *Borhchia frutescens* a perennial halophyte and estimated that the flux varied between -0.16 mol CO₂ m⁻² day⁻¹ (gain) during flooding to about 0.14 mol CO₂ m⁻² day⁻¹ (loss), while the marsh dried up. Eddy covariance based estimates of carbon assimilation from a *Spartina alterniflora* dominated salt marsh in the east coast of China were in the range of 202.07 μmol m⁻² day⁻¹ of carbon (Yan *et al.*, 2008). Most studies on carbon balance of coastal wetlands consider sediment transport processes or air sea exchange processes and coastal wetlands are found to be huge sinks of carbon transported from offshore and also onshore, but still they are losing more carbon in the gaseous form because of the high partial pressure of CO₂ in coastal wetland waters (Howes *et al.*, 1985). An improved understanding of patterns and processes involved in ecosystem level exchanges of energy and carbon in inter-tidal ecosystems is possible only through continuous and long terms flux estimates.

The main objectives of this chapter are

1. To quantify the atmospheric forcings on the seasonal rates and amounts of carbon assimilation by a *Spartina alterniflora* dominated inter-tidal salt marsh using tower-based eddy covariance studies on a continuous and long term basis.
2. To study the response of salt marsh ecosystem to tidal activity in terms of carbon assimilation.

3.2. Material and Methods

3.2.1. Study site

The flux tower site is a lagoonal salt marsh (37°24' N, 75°50' W) dominated by the salt marsh Cod grass (*Spartina alterniflora*). The site is tidally influenced and composed of accumulated fine sediments, which are rich in organic matter. The site is about 2 kilometers from the mainland and is about 80 meters away from a major creek edge. The average height of the vegetation and leaf area index measured at the site during the 2007 growing season is about 60 cm, and 2 to 2.5 m²

m⁻², respectively. The mudflats are separated by meandering tidal creeks, and morphologically different forms of *Spartina* occur in different areas depending upon the degree of tidal flushing from the creeks. With a mean relief of only 2 meters and an extremely high erosion and deposition rates (13 m per year in the horizontal dimension), the system is highly dynamic, and is susceptible to physical forcings such as sea level rise (Van Cleve and Martin, 1991). The period of study (May-December, 2007) was characterized by extremely dry conditions with a rainfall of only 295 mm received during the growing season (May-September).

3.2.2. Instrumentation

The data presented here was obtained from a 6.7m tall flux tower established at the site. The flux tower features an eddy covariance system consisting of a sonic anemometer (model CSAT3, Campbell Scientific, Inc, Logan, Utah, USA) and a infra red gas analyzer (model LI-7500, Licor, Biosciences, Lincoln, NE USA) mounted at 3.7 m from the sediment surface. Several other micrometeorological variables, such as net radiation, photosynthetic active radiation, air temperature and humidity, sediment temperature, and water level on the marsh surface were also recorded. The raw turbulence and scalar concentration data were collected at the 10 Hz frequency and were filtered to remove spikes, density corrections were applied to the raw eddy fluxes (Webb *et al.*, 1980). Flux footprint estimates at the site, using a two dimensional Lagrangian random walk model (Baldocchi, 1997a) indicated that the peak contribution to the estimated fluxes comes within a radius of 20 to 30 meters away from the base of the tower.

A detailed description of the flux tower set up and data acquisition is provided in chapter 2. The environmental data collected during the active growing season (May to September, 2007) are used to develop the relationship between environmental variables and carbon assimilation rates. Missing data can occur in the data due to instrument failure and breakdown of the solar power supply system. Loss in data can also occur due to the presence of spikes (caused by rain on sonic anemometer) and conditions of low and weak atmospheric turbulence. In addition when eddy covariance assumptions are not valid, then data have to be removed. The data set presented here has about 30% of the data missing, the majority of which can be associated with the failure of the power supply system. Further, the remote location of the tower site makes it difficult for frequent visits for maintenance and periodic repairs. A detailed description of the gap

filling strategy using artificial neural networks (ANN) is presented in the results section of this chapter. The availability of water level data on the marsh surface facilitate the segregation of data into high and low tide events, thereby enabling quantification of tidal effects on net carbon ecosystem exchange.

3.3. Results

3.3.1. Diurnal/Seasonal trends in carbon assimilation and micrometeorological variables

The diurnal patterns in net ecosystem exchange (NEE) were closely associated with changes in availability of photosynthetic active radiation (PAR) and changes in soil and air temperature. The positive value of NEE indicates respiration (a gain for the atmosphere), where as negative values indicate assimilation of CO₂ (a loss from atmosphere). A typical carbon assimilation pattern observed over diurnal cycle is represented in figure 3.1, the data presented is for day of year 182 (July 1st 2008). Rapid increase in NEE rates was observed within few hours of sunrise during the growing season (May-September). The peak NEE rates were observed between the period from 9 am to 12 pm corresponding with optimum conditions of temperatures and PAR. The rapid decline in NEE during the afternoon periods can be attributed to increased temperature stress (which increases the ecosystem respiration) and increased radiation loading on the plant canopy. The diurnal trends in air temperature and PAR recorded above the canopy for day of year 182 is provided in Figure 3.2.

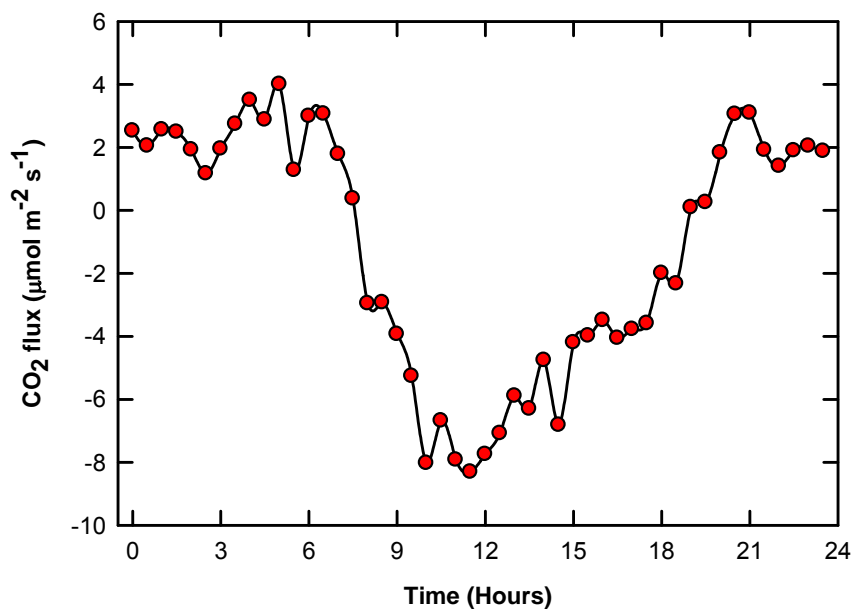


Figure 3.1. Diurnal pattern of NEE as observed for day of year 182, 2007. The peak NEE values are observed between 9:00 and 12:00 hours. Extreme high tides were not observed during this day.

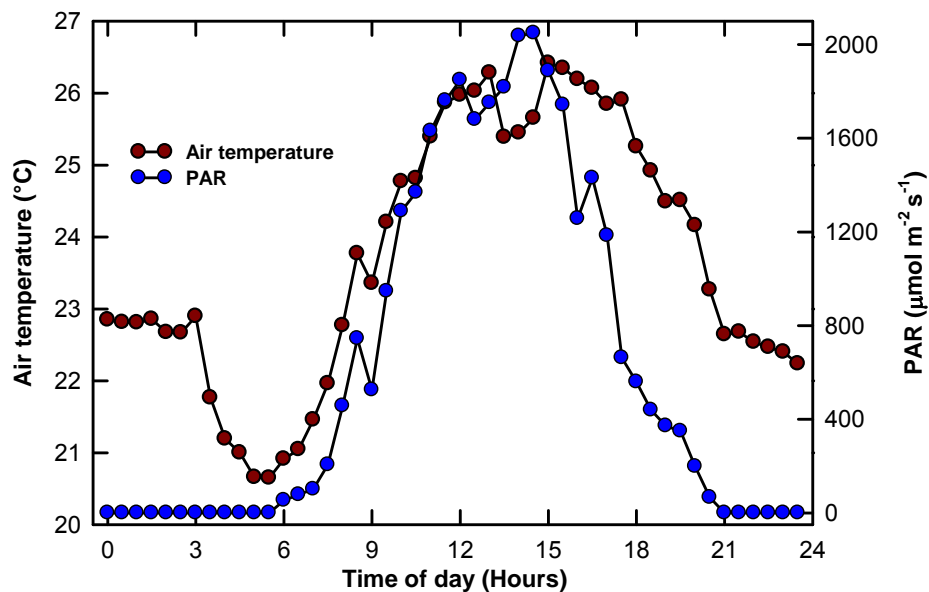


Figure 3.2 Diurnal trends in photosynthetic active radiation (PAR) and air temperature measured above the canopy for day of year 182.

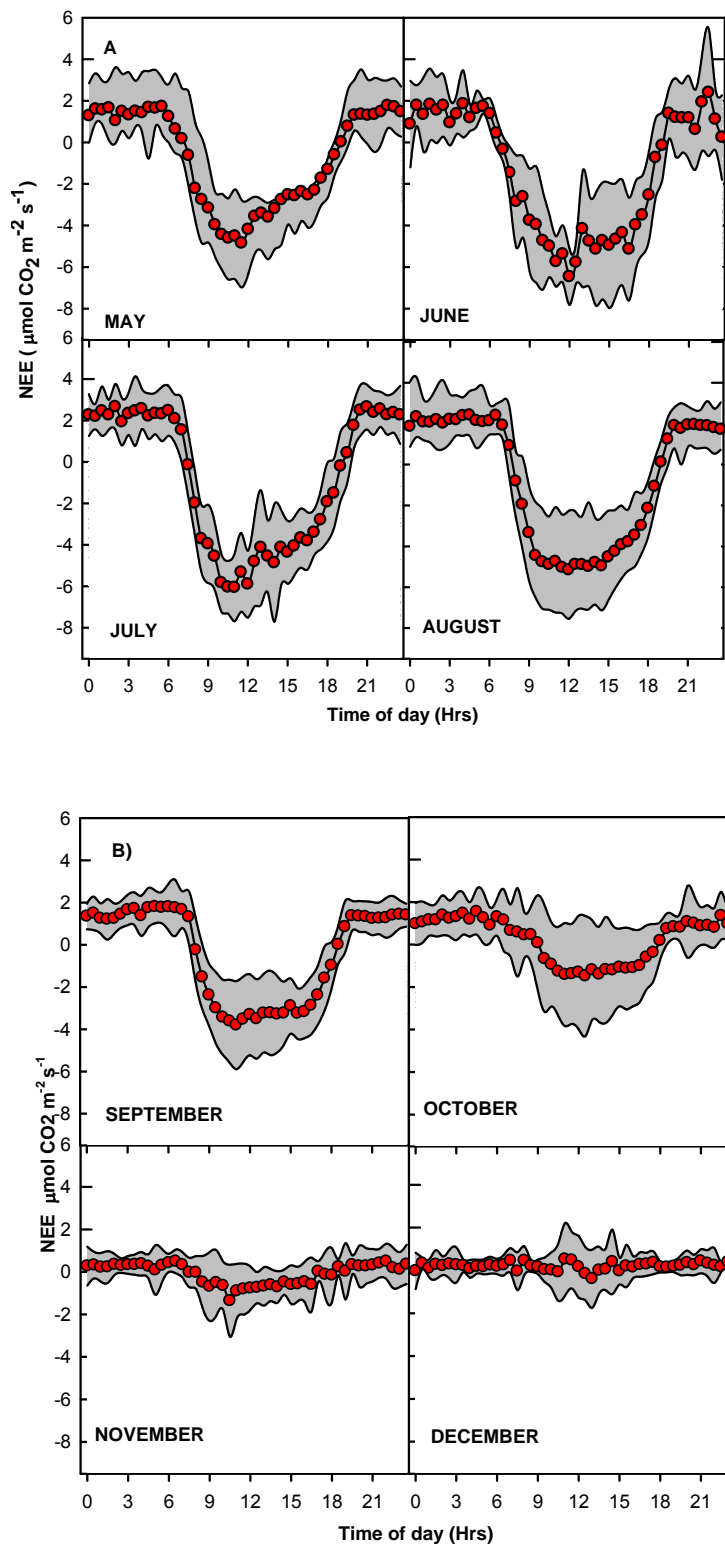


Figure 3.3. A and B. Seasonal patterns in net ecosystem exchange for the period from May to December 2007. The average daily pattern in NEE for each month is plotted with the standard deviation represented as the shaded region.

The average diurnal trends in NEE indicate strong seasonal trends with peak assimilation rates observed during the month of June and July ($6-8 \mu\text{mol m}^{-2} \text{s}^{-1}$) corresponding with the periods of maximum leaf area index and thereafter decrease in assimilation rates was observed towards the end of the growing season (Figure 3.3 A and B). The night time respiration rates rapidly increased with the progress of the growing season with maximum respiration rates observed in the month of July ($>5 \mu\text{mol m}^{-2} \text{s}^{-1}$). The respiration rates started to decrease rapidly during the month of September which could be attributed to the rapid decline in soil/air temperatures (Figure 3.4) and the onset of senescence.

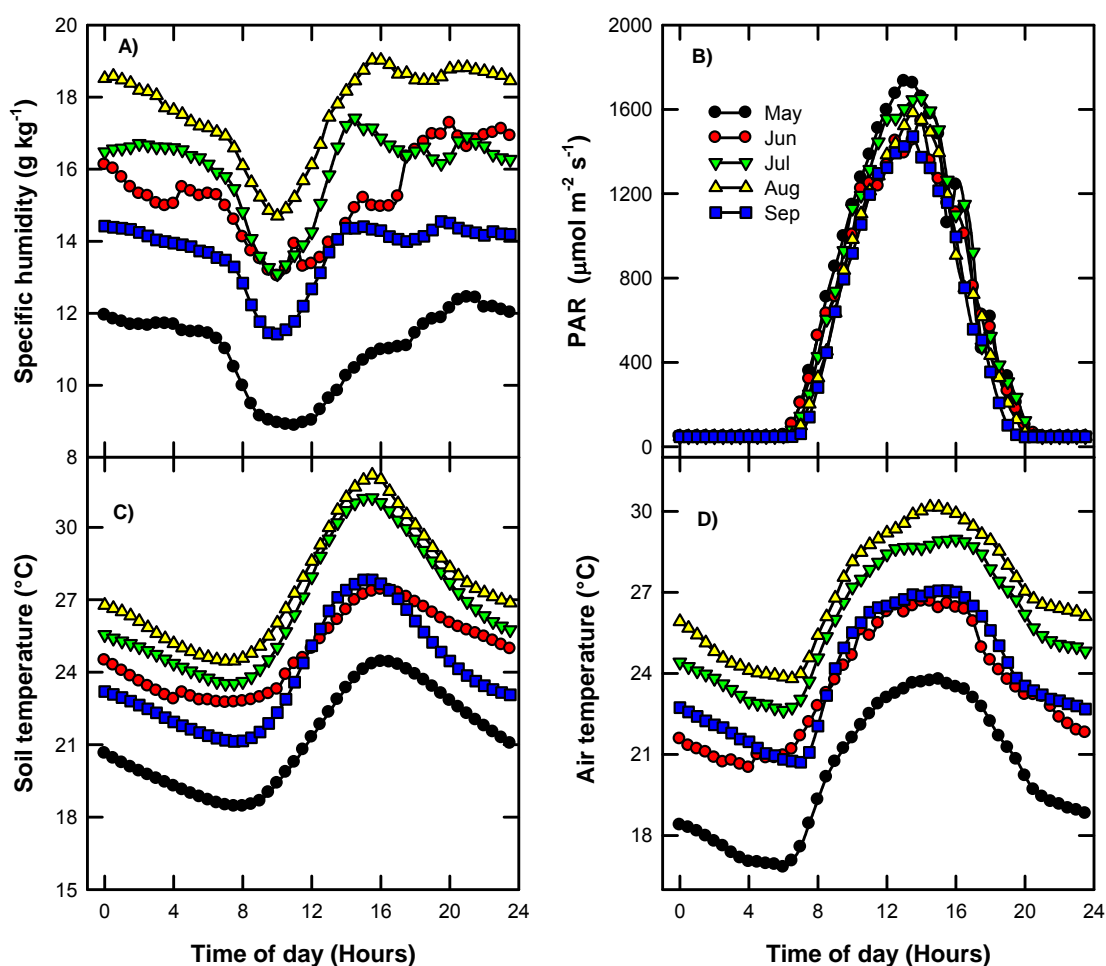


Figure 3.4. Diurnal variation in half hourly monthly ensemble averages of A) Specific humidity B) PAR levels C) Soil temperature and D) air temperature during the growing season.

Rapid decline in NEE is observed after 12:00 hours during the months of May, June and July, whereas in other months a smooth transition was observed in NEE diurnal trends. This can be attributed to photo-inhibition occurring under high light intensities and temperatures occurring

during these months. The specific humidity values exhibited large variability ranging from 9-19 g kg⁻¹, with the maximum values observed during the month of August which corresponded with higher air temperatures. Peak diurnal specific humidity values were observed late in the afternoon (around 16:00 hours), which could be attributed to moisture advection associated with the land-sea breeze system which becomes strongest at this period. Air temperatures and soil temperature values exhibited strong diurnal patterns with the maximum values observed around 16:00 hours, which corresponded well with the period of rapid decline in NEE. Maximum PAR values were observed during the month of May whereas the minimum PAR values were observed during the month of September.

3.3.2. Key environmental forcings on carbon assimilation

The research site is influenced twice a day with a tidal amplitude that can submerge the plant canopy either partially or completely, thus affecting the gas exchange and aerodynamic surface characteristics. Hence to develop the relationship between state variables and NEE, only low tide or exposed canopy periods are considered in the following data analysis. A detailed description of the impact of tides is presented in the following section.

A) Photosynthetic active radiation (PAR)

The influence of PAR on NEE was examined in terms of rectangular hyperbolic relationships (Moncrieff *et al.*, 1997).

$$NEE = \left[\frac{a \times PAR}{a/b + PAR} \right] + c \quad (3.1)$$

Where b is the initial slope of the curve and the reciprocal of this value is the apparent quantum requirement (AQR) (the number of moles of photons required to fix one mole of CO₂) and $a+c$ represents the point at which light saturation for photosynthesis occurs and c represents the mean night time respiration. The relationship was developed by classifying the growing season into three separate periods: A) initial growth period (May), B) active growth period (June-July), and C) end of growing season (August-September). The coefficients determined for the rectangular hyperbolic relationship for the different seasons are provided in Table 3.1

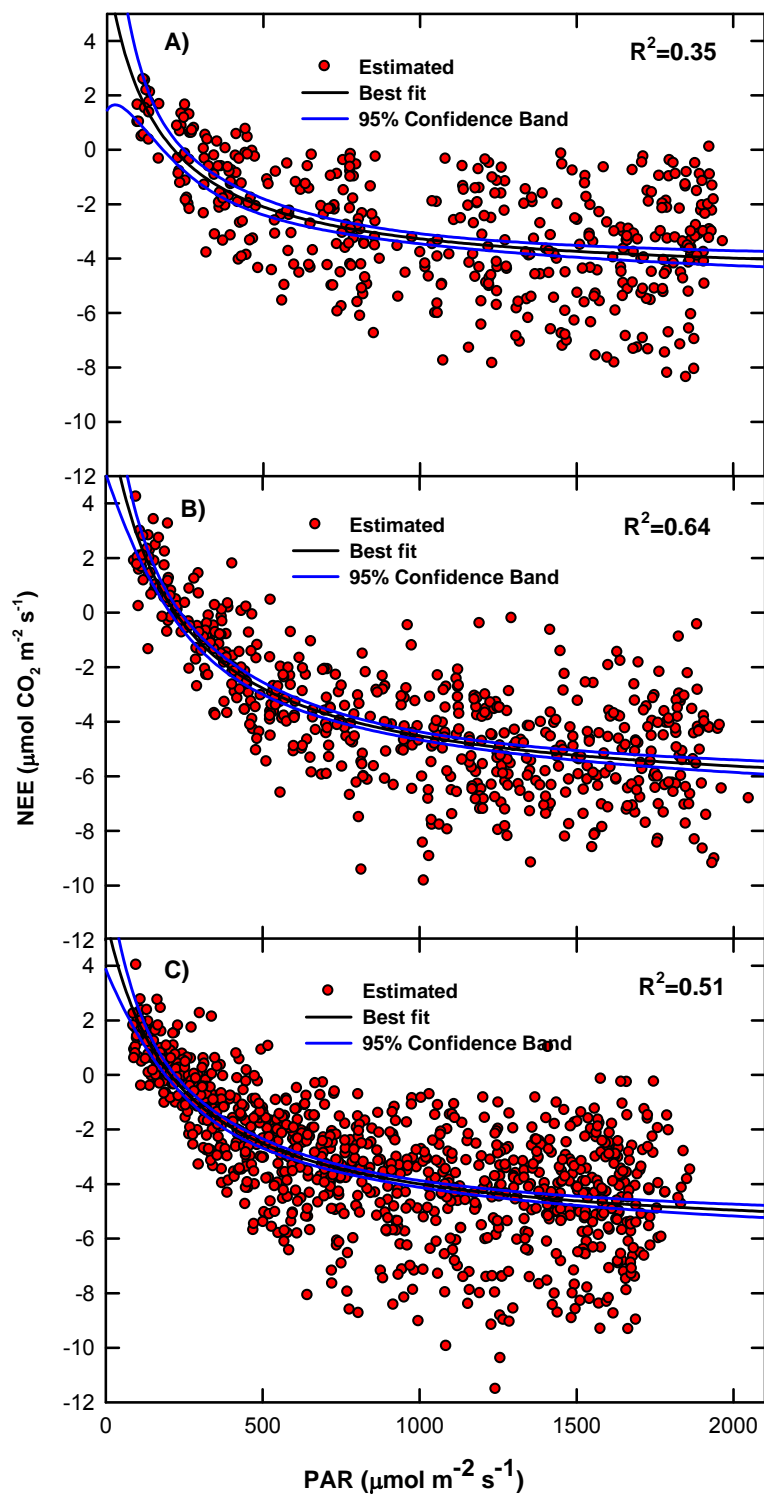


Figure 3.5. The relationship between photosynthetic active radiation and net ecosystem exchange approximated using a rectangular hyperbolic relationship for three different periods: A) May, B) June-July, and C) August-September.

Table 3.1. The coefficients of the rectangular curve fit for the relationship between NEE and PAR

| Coefficient | May | June-July | August-September |
|--|--------------------|--------------------|--------------------|
| a ($\mu\text{mol m}^{-2} \text{s}^{-1} \text{CO}_2$) | -11.43 ± 2.43 | -14.74 ± 1.18 | -11.94 ± 0.83 |
| b ($\mu\text{mol m}^{-2} \text{s}^{-1} \text{CO}_2$) | -0.074 ± 0.047 | -0.075 ± 0.021 | -0.055 ± 0.015 |
| c ($\mu\text{mol m}^{-2} \text{s}^{-1} \text{CO}_2$) | 6.63 ± 2.63 | 7.79 ± 1.36 | 5.82 ± 0.991 |
| AQR (mol photon per mol CO_2) | 13.51 | 13.33 | 18.18 |
| a+c ($\mu\text{mol m}^{-2} \text{s}^{-1} \text{CO}_2$) | -4.8 | -6.95 | -6.12 |

The highest potential rate of NEE (a+c) was observed for the period between June to July ($-6.95 \mu\text{mol m}^{-2} \text{s}^{-1}$). This period was also characterized by high respiration rates ($7.79 \mu\text{mol m}^{-2} \text{s}^{-1}$), which could be attributed to the higher air/soil temperatures that promoted rapid metabolic activity. The maximum apparent quantum requirement was observed during the period from August to September (18.18 mol photons per mol of CO_2), which indicates that the efficiency of the photosynthetic mechanism decreases towards the end of the growing season. Throughout the growing season, photo-saturation was observed when the PAR values were greater than $1000 \text{ m}^{-2} \text{ s}^{-1}$. The low photo-saturation observed in *Spartina alterniflora* was similar to that observed in leaf-level physiology measurements (chapter 2). The weak relationship ($R^2 < 0.65$) between PAR and NEE observed in the three different periods indicate that other environmental factors such as temperature and specific humidity do play an important role in modulating NEE.

B) Effect of irradiance and cloudiness on NEE

Several studies have indicated the increased carbon assimilation rates observed under conditions of more diffuse radiation which can be attributed to the higher radiation use efficiency of diffused radiation compared to direct radiation (Healey *et al.*, 1998; Rochette *et al.*, 1996). In this study the relationship between diffuse radiation fraction and NEE was examined by following the methodology proposed by (Gu *et al.*, 2002) using a rectangular hyperbolic relationship.

$$P = \frac{\alpha PAR \beta}{\beta + \alpha PAR} \quad (3.2)$$

P is the canopy photosynthetic flux density which is described as $P=R_e-NEE$, where R_e is the ecosystem respiration and was estimated following the methodology described in section D. α is the canopy quantum yield and β represents the closeness to linear response (CLR) index of the canopy photosynthetic response curve. This relationship was used to fit P as a function of direct (r) and diffuse (f) PAR under low tide conditions. The separation of total PAR into diffuse and direct components was done following methodology prescribed by Hollinger *et al.*, (1998); and Spitters *et al.*, 1986). P values showed a steep increase with increase in direct PAR and leveled off at values $>600 \mu\text{mol m}^{-2} \text{s}^{-1}$. In the case of diffuse PAR, the P value increased gradually with increase in PAR and were lower than corresponding values observed for direct PAR at values lesser than $600 \mu\text{mol m}^{-2} \text{s}^{-1}$, thereafter increase in diffuse PAR produced greater increase in P, than direct PAR. However, the photo-saturation observed in the case of direct PAR was not observed in the diffuse PAR relationship. The strong linear relationship between diffuse irradiance and NEE observed in forest ecosystems (Law *et al.*, 2000) was not observed in this system, indicating lower light use efficiency.

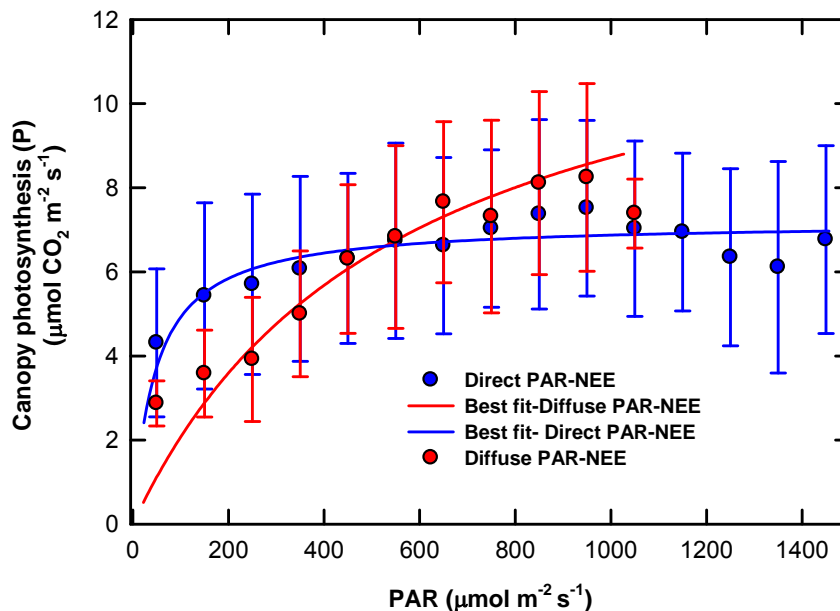


Figure 3.6. Relationship between canopy photosynthetic flux density (P) and different photosynthetic active components (direct and diffuse). The best fit lines are obtained by fitting the data points to equation 3.2. The P values are binned for each PAR class of $50 \mu\text{mol m}^{-2} \text{s}^{-1}$.

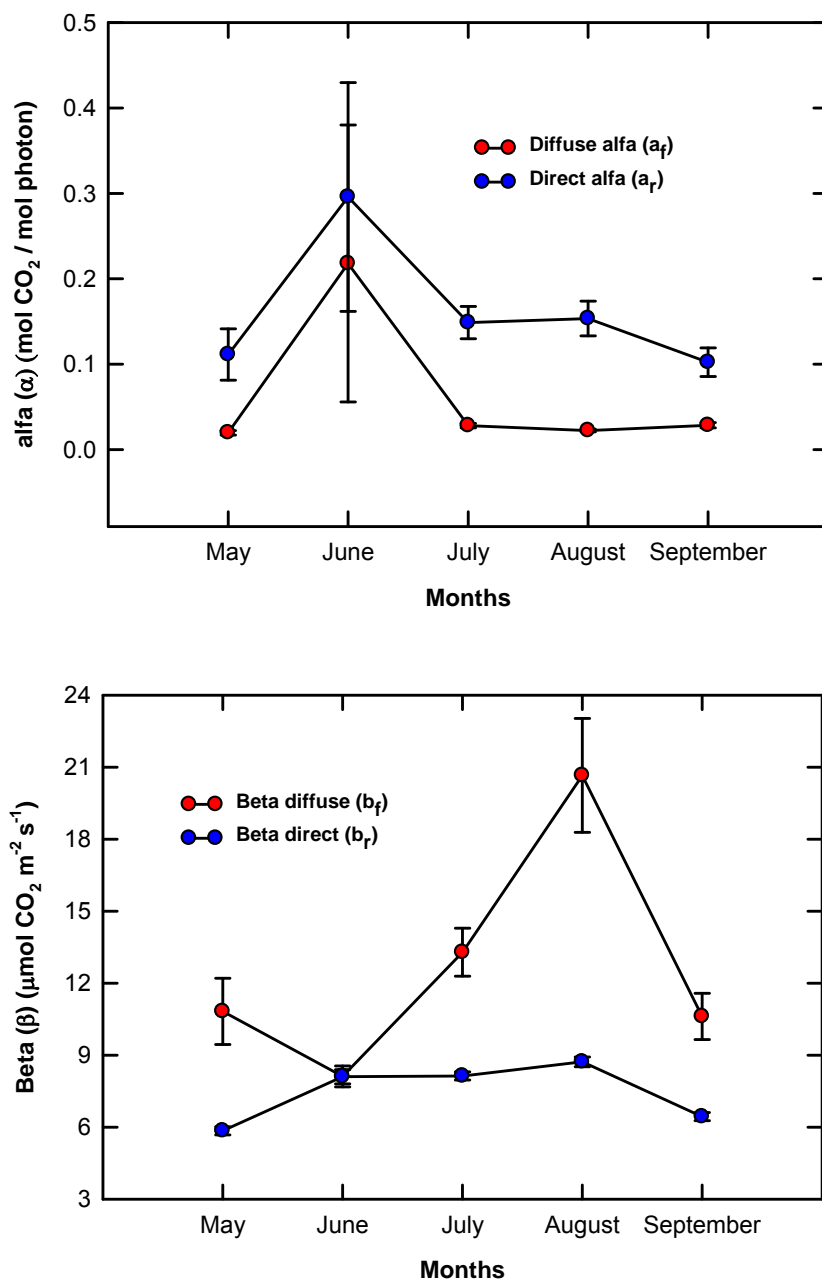


Figure 3.7. Seasonal changes in average monthly values of α and β during the growing season. The error bars represents the standard error in the estimation of the coefficients.

Although initial quantum efficiency for diffuse PAR (α_f) was observed to be lower ($0.025 \pm 0.001 \text{ mol CO}_2/\text{mol photon}$) than for direct PAR (α_r) ($0.156 \pm 0.01 \text{ mol CO}_2/\text{mol photon}$), the β values for diffuse PAR (β_f) were greater ($13.55 \pm 0.67 \mu\text{mol m}^{-2} \text{ s}^{-1}$), than for direct PAR ($7.19 \pm 0.09 \mu\text{mol m}^{-2} \text{ s}^{-1}$). Since greater values of β indicate a lower tendency for photo-saturation (Gu *et al.*, 2002), diffuse PAR can be inferred to have a greater effectiveness in canopy photosynthesis

in this ecosystem. To further investigate seasonal changes in the utilization of diffuse and direct fractions of PAR, the seasonal changes in α and β for direct and diffuse radiation was estimated for the growing season (May-September) during low tide events (Figure 3.7).

The α values were observed to be higher for direct PAR compared to diffuse PAR throughout the growing season, whereas the β values were always higher for diffuse PAR. The α values increased with the progress of the growing season, attaining the maximum in June and thereafter decreased with the progress of the growing season, whereas the β values increased throughout the growing season attaining peak values during the month of August. The larger initial quantum yield observed during the month of June for both diffuse and direct PAR, could be attributed to the occurrence of peak vegetative growth during this period. Further the α values were much higher for direct radiation compared to forest ecosystem (Gu et al., 2002) as *Spartina alterniflora* is a C₄ plant. The diffuse radiation provided maximum enhancement in NEE during the month of August (highest β_f values ($20.65 \pm 3.75 \mu\text{mol m}^{-2} \text{s}^{-1}$)), which can be inferred as the having the optimum conditions of radiation with lower tendency for photo-saturation.

Although conditions of increased diffuse radiation are associated with cloudy skies, presence of increased amounts of atmospheric aerosols can also increase the amount of diffuse radiation in the sky (Roderick et al., 2001), especially in a coastal environment where marine aerosols dominate. Cloudiness can indirectly affect the NEE by reducing the vapor pressure deficit and decreasing air temperature, thus lowering temperature and moisture stress on plants (Wang et al., 2005). To understand the effect of cloudiness on NEE, a comparison was made between NEE under clear and cloudy sky conditions. The days were classified into sunny and cloudy days based on the clearness index (K_t) (Liu and Jordan, 1960), which is the ratio of global solar irradiance received at Earth's surface (S) to the extra-terrestrial irradiance received at the top of the atmosphere on a plane parallel to the Earth's surface (S_e).

$$K_t = \frac{S}{S_e} \quad (3.3)$$

$$S_e = S_{sc} [1 + 0.033 \cos(360t_d / 365)] \sin \beta \quad (3.4)$$

S_{sc} is the solar constant (1370 W m^{-2}), β is the solar elevation angle, and t_d is the day of year. The clearness index was calculated for only those periods of a day for which the loss in CO₂ flux

was estimated to classify a day as clear or cloudy. An average clearness index value greater than 0.65 indicates a clear day, whereas values lower than 0.65 were classified as a cloudy day. This classification is based solely on the clearness index and does not depend on the amount of direct or diffuse radiation in the sky. The results (Figure 3.8) indicate that there is an increased NEE under cloudy skies compared to clear sky conditions.

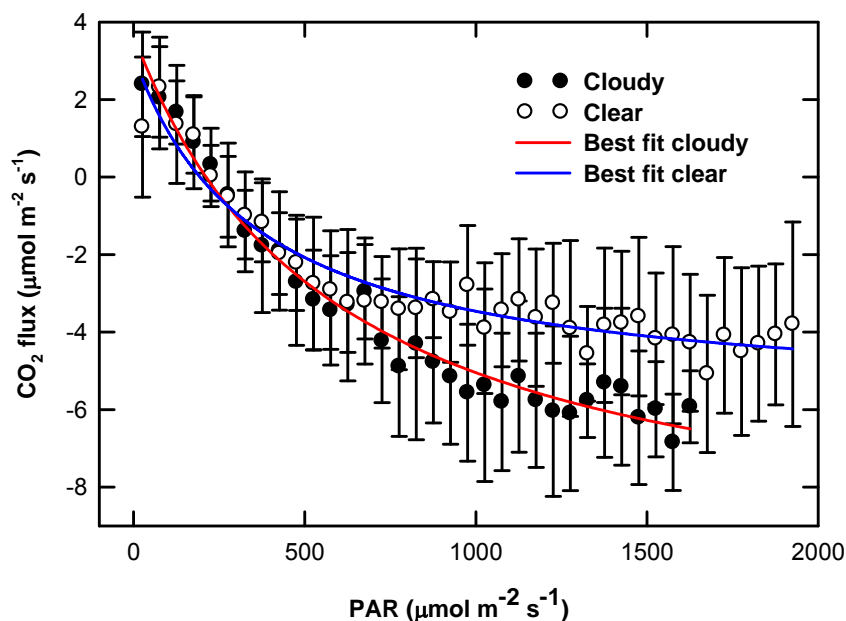


Figure 3.8. Relationships between sky conditions and net ecosystem exchange based on clearness index. The error bars indicate one standard deviation for each PAR class. The best fit lines were obtained by fitting equation to the data.

A greater light use efficiency is observed under cloudy sky conditions as evidenced by the steeper slope of the PAR-CO₂ relationship, compared to clear sky conditions. Photosaturation is observed under lower light levels under clear sky conditions whereas, the canopy is not light saturated under cloudy conditions. The increased assimilation observed under cloudy conditions can also be attributed to the cloud gap effect (Gu *et al.*, 2001), which causes sunlit ground surfaces to receive more diffuse radiation in addition to the same amount of radiation received under clear sky conditions due to the increased reflection and scattering of radiation by clouds. Although 30 to 60 percent enhancement has been observed in NEE from deciduous forest of North America under cloudy sky conditions (Gu *et al.*, 1999), the salt marsh ecosystem showed enhancement in NEE in the range of 25 to 50 percent. The decreased enhancement in salt marsh system could be attributed to the short canopy stature and low leaf area index of

Spartina alterniflora, which provided identical radiation penetration and light use efficiency under cloudy and clear sky conditions. The increased NEE in salt marsh ecosystem could be related more with indirect effects of cloudy skies such as decreased thermal and radiation stress.

C) Temperature and vapor pressure deficit (VPD)

Temperature is an important environmental variable affecting NEE on a seasonal and annual scale (Baldocchi, 2008; Falge *et al.*, 2002). The increasing temperatures can promote increases in respiration rates, thus leading to decreased NEE. The increasing temperatures have been associated with the losses in carbon as CO₂ dioxide from northern ecosystems during the growing season (Piao *et al.*, 2008). The daytime NEE values have been found to be positively correlated with air temperature in tropical ecosystems (Powell *et al.*, 2006). The relationship between air temperature and daytime NEE values is represented in Figure 3.9.

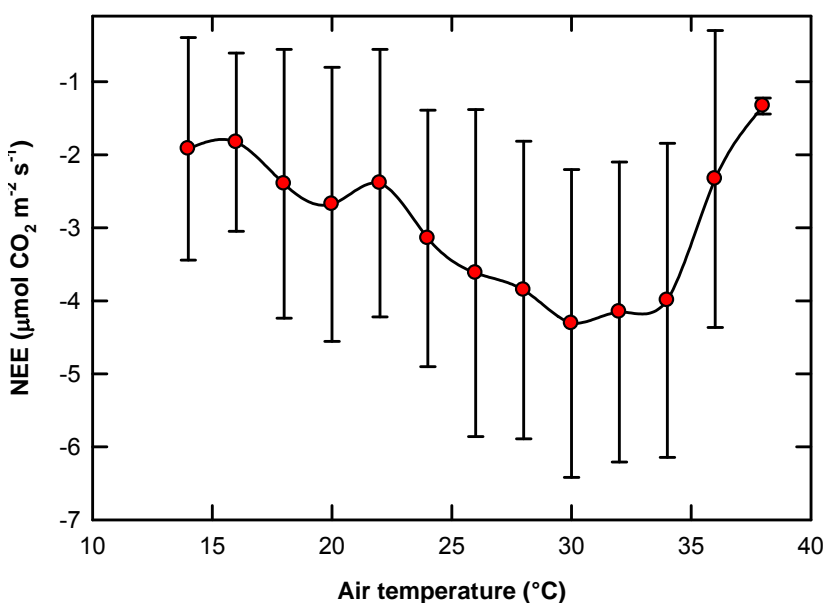


Figure 3.9. The relationship between air temperature and day time CO₂ flux during low tide events throughout the growing season (May to September). The error bars indicate the standard deviations for each temperature class. The NEE values are binned based on air temperature classes of 2° C starting from 14° C.

The relationship was developed using day time NEE values observed during low tide events when there was no water level on the marsh surface. It is observed that the NEE rates increased with increasing temperature until an optimum temperature was reached (in this case around 30°C) and thereafter a decreasing trend was observed, similar to conclusions presented by Saxe

et al. (2001) in a review article on this subject matter. The decreased NEE observed under higher air temperatures could be attributed to increased respiration rates and inhibition of plant physiological processes such as electron transport (Farquhar *et al.*, 1980), carboxylation rates and photo-inhibition (Massad *et al.*, 2007). Indirect effects of high temperatures on NEE can be related to changes in plant pigment concentration, apparent quantum yields and changes in soil biogeochemical interactions (Bassow and Bazzaz, 1998).

The vapor pressure deficit (VPD) is closely related to the water stress which is directly related to the plant growth and thus affecting NEE (Chen *et al.*, 1999; Monson *et al.*, 2002). The VPD is more closely related to the residual in the estimation of day time NEE (difference between estimated and modeled NEE from equation 3.1) as the lack of fit between NEE and PAR can be accounted by changes in VPD (Wang *et al.*, 2004).

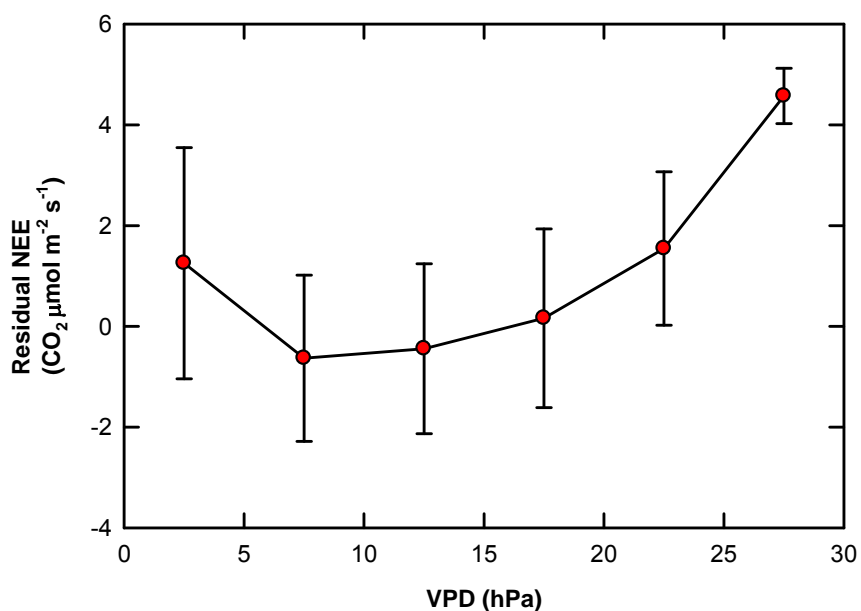


Figure 3.10. Relationship between vapor pressure deficit (VPD) and residual et ecosystem exchange (NEE) (from the estimation of PAR-NEE) relationship. The residual values are selected for PAR above $700 \mu\text{mol m}^{-2} \text{s}^{-1}$ during low tide events following the methodology of Wang *et al.*, (2004). The Residuals are binned for VPD classes of 5 hPa.

The NEE was affected when the VPD was greater 20 hPa (Figure 3.10), which is slightly lower than observed in other ecosystems such as forests (Hollinger *et al.*, 1998; Wang *et al.*, 2004). The lower threshold of VPD (20 hPa) for optimum NEE observed in the salt marsh ecosystem

could be attributed to the fact that the plant has to utilize more metabolic energy to extract moisture under conditions of large VPD from the salty soil.

D) Ecosystem respiration

The conventional method of determining ecosystem level respiration involve developing relationships between soil or air temperature, and night-time filtered CO₂ flux estimates (filtered to avoid conditions of low turbulence) and applying this relationship on a diurnal scale or to use light response curves (Falge *et al.*, 2002). The inherent limitations of this method include the lack of applicability in ecosystems with large carbon pools as in a salt marsh and that the temperature relationships observed may not be valid with changes in VPD (Reichstein *et al.*, 2005). Further, the CO₂ flux observed during sunrise and sunset periods can be highly transient and may involve conditions of non-stationarity, which can affect the temperature relationships. Recent advances in measurement techniques have helped in more accurate estimation of ecosystem level respiration using stable carbon isotopes (Bowling *et al.*, 2001; Knohl and Buchmann, 2005), but still large uncertainties exists in the determination of soil respiration. In this study soil temperature and night time CO₂ flux estimates obtained during the growing season were used to develop Arrhenius-type relationships (Lloyd and Taylor, 1994) to estimate ecosystem level respiration (R_e).

$$R_e = R_{T_{ref}} \exp \left[\left(\frac{E_a}{T_{ref} \times R} \right) \times \left(1 - \frac{T_{ref}}{T_{soil}} \right) \right] \quad (3.3)$$

R is the universal gas constant ($R=8.314 \text{ JK}^{-1} \text{ mol}^{-1}$) and T_{soil} is absolute soil temperature (K) at 5 cm soil depth. The non-linear regression coefficients which include the activation energy E_a (Jmol^{-1}) and the respiration ($R_{T_{ref}}$) at a reference temperature, T_{ref} (in this case 283.16 K) were determined using dynamic curve fit routine in the scientific graphing software SigmaPlot (Systat Software Inc, San Jose, CA, USA). Since tidal activity can modify the surface-atmosphere CO₂ exchange, CO₂ flux estimates during periods when there was no water on the marsh surface (low tide) was used to develop relationship 3.5. A minimum friction velocity threshold value of 0.10 ms^{-1} and a global radiation threshold value of 10 Wm^{-2} were used to select the nighttime CO₂ fluxes.

The regression coefficients $R_{T_{ref}}$ and E_a were estimated to have values of $0.82 \text{ } \mu\text{mol m}^{-2} \text{ s}^{-1}$ and $45212.85 \text{ Jmol}^{-1}$ respectively. The poor coefficient of determination ($R^2=0.22$) between the estimated and modeled respiration rates indicates that respiration rates may also be controlled by

other factors such as the size of the available carbon pool, VPD or even the activity of organisms such as fiddler crabs on the marsh surface (Nielsen *et al.*, 2003). *Spartina alterniflora* salt marshes are found to have substantial carbon pools compared to mud flats (Liu *et al.*, 2007), which can affect the temperature-respiration relationship.

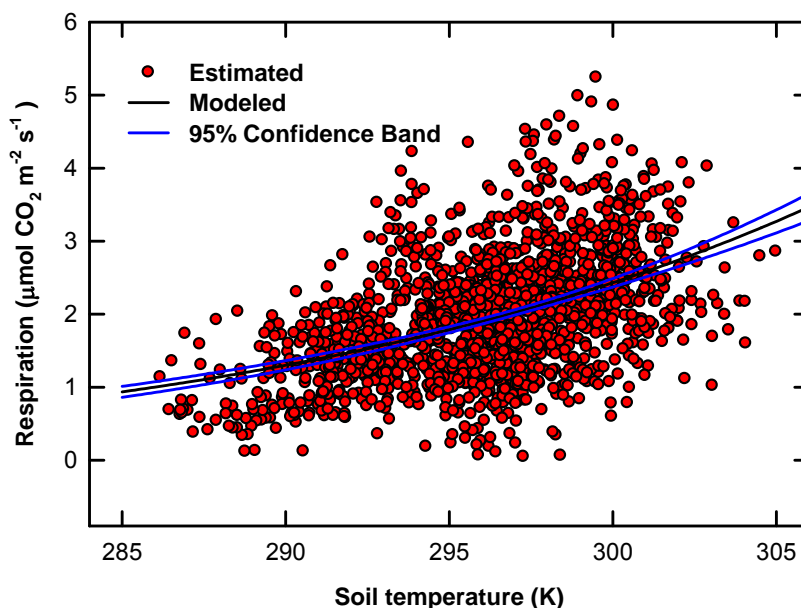


Figure 3.11. Estimated and modeled night time ecosystem respiration as a function of soil temperature at 5 cm. The 95 percent confidence and prediction bands are also provided in the figure.

E) Tidal influences

Tidal activity had an impact on diurnal carbon assimilation patterns. The short stature of the canopy (50-60 cm) coupled with a large tidal amplitude (1 m and higher) provided an interesting scenario where the plant canopy can be completely or partially submerged during various times of the day, thus providing an ideal setting for understanding the ecosystem-level response and function due to submergence. For example, in the case of day of year 244, when there was a high tide occurring at a period corresponding to peak NEE values, then the NEE correspondingly declined with the rising tide (Figure 3.12). In comparison for a typical day (DOY 249), when the high tide occurred at a period which doesn't correspond to midday peak irradiance levels, the changes in distribution of CO_2 fluxes were not observed (Figure 3.11). This decrease in CO_2 flux was observed mostly during a spring tide event, when very high tidal levels (>0.25 cm) were

experienced. The respiration rates also showed a decline with increasing water levels under a significant high tide event.

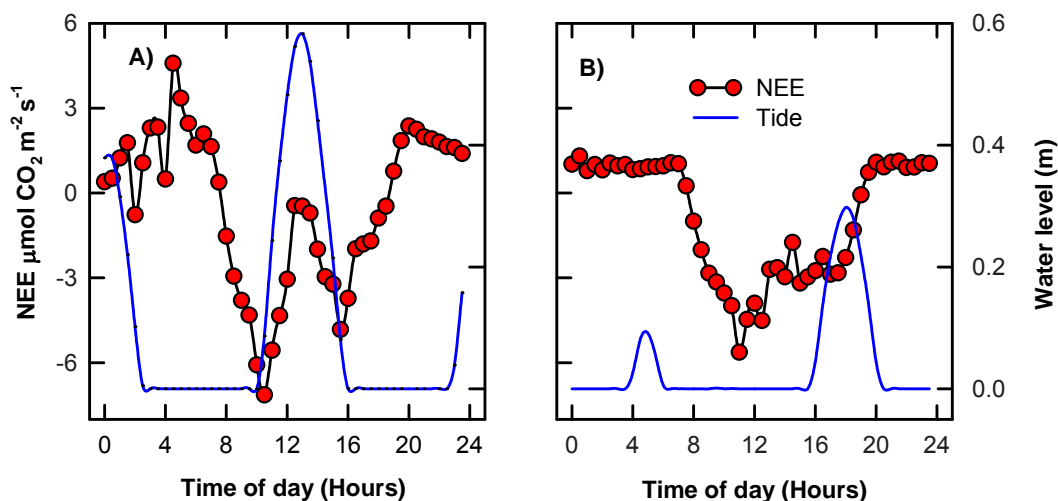


Figure 3.12. Comparison between net CO_2 ecosystem exchange diurnal trends during (A) a day with high tide-midday event (DOY 244) and (B) a day with low tide mid-day event (DOY 249).

The rapid decrease in CO_2 assimilation/respiration rates under flooded conditions can be mostly attributed to water acting as a physical barrier for gas exchange. Although *Spartina alterniflora* have been found to fluoresce underwater which indicates its capability to photosynthesize, the efficiency of the photosynthetic system is greatly reduced (see Chapter 2). Even partial canopy submergence showed decreased NEE, which could be attributed to the low aerenchymatous gas transport observed in *Spartina alterniflora* (Maricle and Lee, 2002). Additionally submergence of the marsh surface can change the aerodynamic characteristics of the surface as the gas exchange occurs from a smoother surface. Under these conditions, air-water gas exchange may be the dominant mechanism responsible of scalar fluxes. The air water CO_2 exchange depends upon the concentration of dissolved CO_2 ($p\text{CO}_2$) in the water and also on other environmental variables such as temperature and pressure (Holmen and Liss, 1984). Further, the amount of active leaf area available for photosynthesis changes with the water level thus changing the source/sink distribution for CO_2 in the ecosystem.

F) Quantification of loss in CO₂ flux due to tidal inundation

In order to quantify the loss in CO₂ flux due to tidal activity, only those days were selected when there was a mid-day high tide event which has high enough to cover the vegetation. A total of 24 days was identified for the 2007 growing season. The midday high tide events were characterized by rapid drop in NEE, corresponding with the increasing water level. A fourth order Fourier curve was fitted to the diurnal CO₂ flux data, by excluding those CO₂ flux data points which were estimated during the midday high tide event from the eddy covariance system. The points to be excluded were determined based on the water level over the marsh surface, which had to be above 0.25 meters. This level was chosen as substantial decrease in CO₂ flux was observed when the water level on the marsh surface was greater than this value. The fourth order Fourier curve fit (non-linear least square) was estimated using the curve fitting toolbox of Matlab (The Mathworks Inc, Natick, MA, USA) using the trusted region algorithm. The fourth order Fourier curve used for fitting is represented in equation (3.6).

$$y = a_0 + a_1 \cos(tw) + b_1 \sin(tw) + a_2 \cos(2tw) + b_2 \sin(2tw) + a_3 \cos(3tw) + b_3 \sin(3tw) + a_4 \cos(4tw) + b_4 \sin(4tw) \quad (3.6)$$

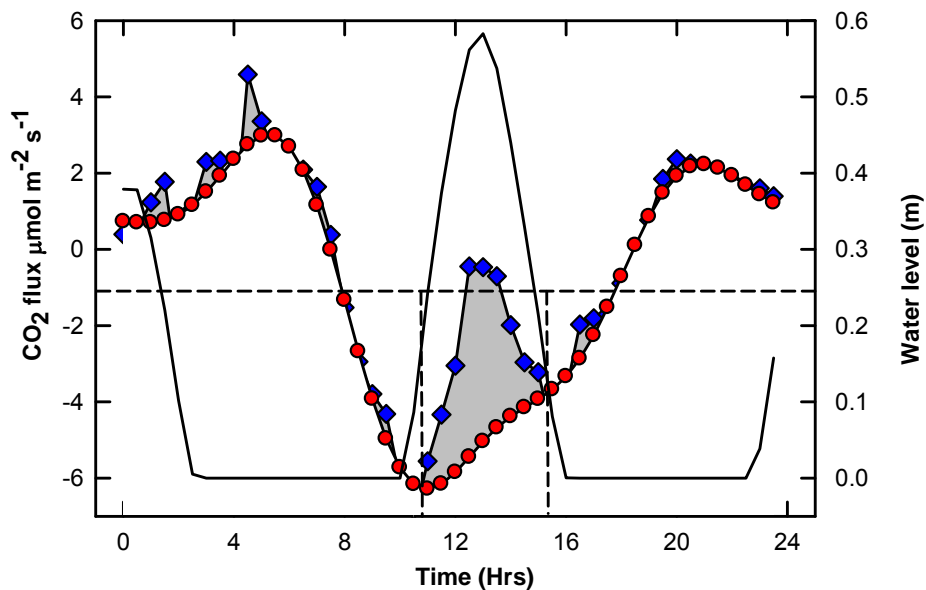


Figure 3.13. The estimation of loss in CO₂ assimilation capacity due to tidal influence is represented here. The red circles indicate the Fourier fit; the blue squares indicate the estimated NEE values and the back like denote the water level. The shaded region between the two dashed vertical lines indicates the loss in CO₂ assimilation occurred, due to the high tide event. The dashed vertical line indicates the midday period during which the water level was above 0.25m.

The coefficients $a_0, a_1 \dots a_4, b_0, b_1 \dots b_4$ and w were determined by the non-linear estimation procedure, t is the time in hours and y is the fit obtained. The choice of curve fit was determined by the fact that a fourth order Fourier curve was able to capture the sinusoidal trends in daily NEE under all environmental conditions ($R^2 > 0.85$).

An example of such a fit for DOY 244 is represented in Figure 3.13. The data was further classified into cloudy and clear sky conditions following the methodology described in subsection B. The average loss in CO_2 flux due to tidal activity as inferred from the analysis was about $0.83 (\pm 0.75) \text{ g CO}_2 \text{ m}^{-2} \text{ d}^{-1}$. The maximum loss in CO_2 assimilation capacity was observed DOY 243 ($2.44 \text{ g m}^{-2} \text{ d}^{-1}$) and the minimum loss was estimated on DOY 259 ($0.009 \text{ g CO}_2 \text{ m}^{-2} \text{ d}^{-1}$). The results indicates that the clear sky conditions produced slightly larger losses in NEE ($1.00 \text{ g CO}_2 \text{ m}^{-2} \text{ d}^{-1}$), compared to cloudy days ($0.41 \text{ g CO}_2 \text{ m}^{-2} \text{ d}^{-1}$), even though there was no significant difference ($p < 0.05$) between the means (two sample independent t-test). This could be due to the smaller sample size or unequal distribution of samples between cloudy and clear sky conditions. The decreased loss in CO_2 flux during cloudy conditions could be attributed to the increased NEE often observed under cloudy conditions (Baldocchi, 1997b).

G) Quantification of seasonal carbon assimilation

Eddy covariance data can help us to understand the controls on the seasonal NEE and to construct the carbon budget of an ecosystem, which can help us to identify whether an ecosystem acts as a sink or source for carbon. Considerable gaps can occur in eddy covariance data (20-60%) sets due to low turbulence conditions (when the assumptions in eddy covariance are not valid) or due to sensor failure or error (Moffat *et al.*, 2007). These gaps can either be short term (which occurs for few hours or few half hours during a day) or can be long term (for several days). The short-term gaps are usually associated with conditions of low turbulence or due to rain events which can affect the sensor readings (Moffat *et al.*, 2007). It is possible to fill these gaps with data recreated from meteorological variables. Many of these methodologies are based on nonlinear regression between meteorological variables such as PAR or air/soil temperature and NEE (Barr *et al.*, 2004; Falge *et al.*, 2002; Hollinger *et al.*, 2004). The NEE from the inter-tidal salt marshes depends on a variety of factor such as tides and VPD which can alter the relationships between state variable like PAR and air/soil temperature and NEE. Artificial neural networks

(ANN) have been used with reasonable accuracy in predicting NEE from various micrometeorological variables (Leuning *et al.*, 2005; van Wijk and Bouten, 1999). Artificial neural networks can provide a mathematically flexible structure to identify the complex non-linear relationships between micrometeorological variables and NEE (Melesse and Hanley, 2005). A standard two-layer feed forward neural network having 40 hidden layers trained with the Levenberg-Marquardt algorithm (Levenberg, 1944) was used to fill the gaps existing in the data. The ANN was implemented for each individual month using the Neural Network tool box of Matlab, a scientific programming language (The Mathworks Inc, MA, USA).

The large gaps existing in this data set are associated with the failure of the solar power supply system, which meant that no data acquisition was possible. Therefore, it was necessary to use micrometeorological data from a nearby site, Hog Island (Lat 37.42°, Lon -75.76°) (VCR LTER database) to gap fill the flux data. The input data which included incoming solar irradiance (Wm^{-2}), wind speed (m s^{-1}) air temperature ($^{\circ}\text{C}$) and relative humidity (%) were selected solely based on the availability of micrometeorological variables at the Hog Island site. The ANN was trained using the data collected at the flux tower site by utilizing data filtered for conditions of low turbulence (friction velocity $< 0.1 \text{ ms}^{-1}$) and spikes.

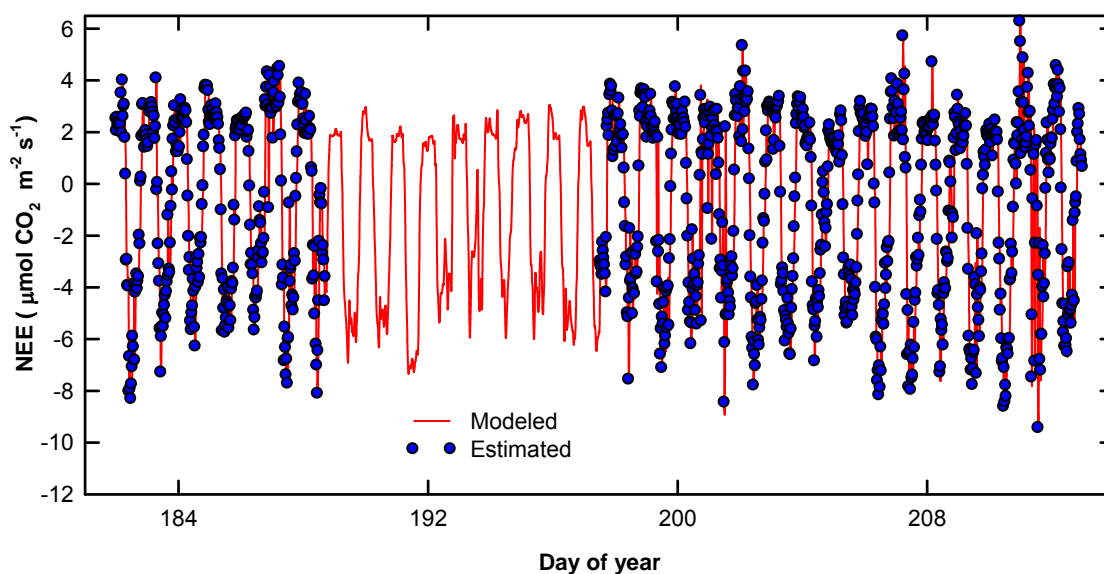


Figure 3.14. Comparison between measured and modeled net ecosystem exchange for July 2007. The NEE was modeled using a two-layer feed forward artificial neural network was able to capture the trends that were determined with eddy covariance in the estimate NEE ($R^2 = 0.94$)

The ANN was able to recreate the trends in NEE with reasonable accuracy ($R^2 > 0.80$) for all months. An example of such a fit for the month of July is provided in Figure 3.14.

The gap filled NEE time series was integrated over each month to obtain an estimate of total monthly carbon fixed by the ecosystem. The maximum amount of carbon fixed through atmospheric exchange was in the month of June (55.2 g C m^{-2}) and thereafter a decrease in assimilation was observed (Figure 3.15). The seasonality in carbon fixed depends considerably on the trends in PAR and soil/air temperature. A considerable loss in carbon fixed was observed in the month of October (-9.8 gm^{-2}), which can be attributed to the decrease in assimilatory response of the canopy with the progress of the growing season and the increased respiratory rates. The ecosystem was carbon neutral or a source ($+2.63 \text{ gm}^{-2}$) during the month of November, which could be attributed to the decreased respiratory rates (corresponding with decreased temperatures) and residual assimilation exhibited by the late season growth or algal mats on the marsh surface. The system then reverts into a respiratory state in December, with the decreasing temperatures observed during that period. The total amount of carbon fixed during the period from May to December was about 133.66 gm^{-2} . This value compared well with annual estimates ($77\text{-}169 \text{ gm}^{-2}$) for a salt marsh estimated using chamber studies (Miller *et al.*, 2001).

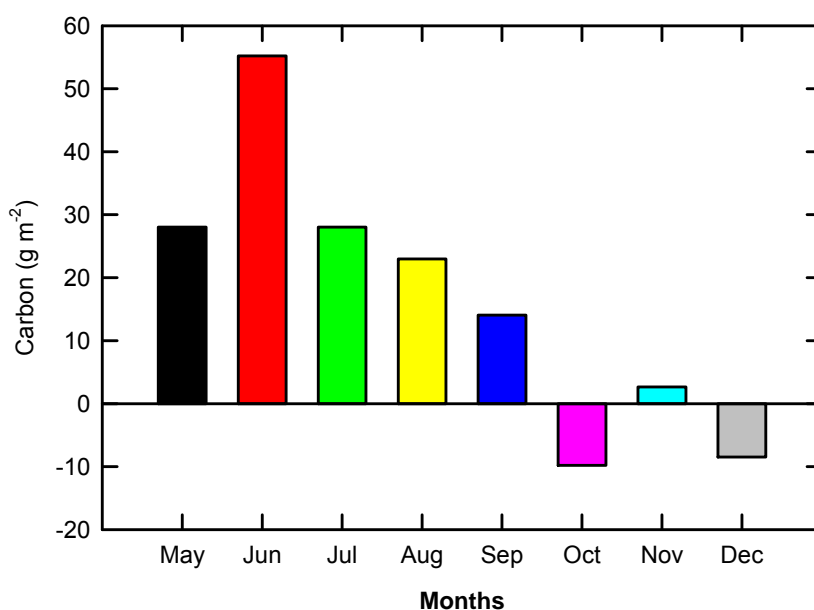


Figure 3.15. Seasonal patterns in carbon assimilation with positive values indicating a gain and negative indicate a loss in carbon. The total carbon fixed during this period was about 133 gm^{-2} .

3.4. Conclusions

The NEE on a diurnal scale was controlled mainly by the quantity and quality of solar irradiance, as less seasonal variations occurred in the radiation regime during the short growing season of *Spartina alterniflora*. The comparatively inefficient light interception apparatus in *Spartina alterniflora* allows light saturation under low light levels, hence light never becomes a limiting factor with the progress of the season. On a seasonal basis, changes in air temperature and specific humidity exerted strong control on NEE patterns by modulating ecosystem respiration and stomatal conductance. Tidal activity exerted control on both diurnal and seasonal NEE as tidal activity depended on the lunar cycle and local wind patterns. Tides had an important role in regulating the assimilatory and respiratory response of the system, by acting as a physical barrier for surface-air CO₂ exchange and also by affecting the plant physiological processes such as stomatal conductance. High tides contributed to 3-91% reductions in midday NEE, with an average loss of about 46 (±26) percent. The projected sea level rise by the end of 21st century, according to the reports of the intergovernmental panel on climate change (Solomon, 2007), is about 18-59 cm. The rapid sea level rise experienced as a consequence of global climate change may increase the frequency and duration of inundation (Baldwin and Mendelssohn, 1998) thereby leading to decreased CO₂ assimilation rates from inter tidal salt marshes. Cloudy sky conditions or conditions of increased diffuse radiation can substantially increase the NEE for a salt marsh ecosystem. Intertidal salt marshes can fix substantial amounts of carbon via atmosphere-ecosystem exchange during the growing season (133 gm⁻²), but thereafter the system reverts back to a respiratory state. Even though this amount is considerably lower compared to forests (600-800 gm⁻²), (Baldocchi *et al.*, 2001), the leaf area of this ecosystem is nearly half that observed for different forest ecosystems. Although the salt marsh ecosystem is stressed by increased temperatures and VPD values, the system can assimilate about 8-10 μmol m⁻² s⁻¹, during the peak growing season. Although the key process by which intertidal salt marshes fix carbon has been identified as the accretion and burial of sediments (Duarte *et al.*, 2005), the present study indicates that these ecosystems do fix a considerable amount of carbon through canopy-atmosphere exchange processes.

References

- Adams, J.M., Faure, H., Fauredenard, L., Mcglade, J.M. and Woodward, F.I. 1990. Increases in terrestrial carbon storage from the last glacial maximum to the present. *Nature*, 348: 711-714.
- Aurela, M., Ruita, T., Laurila, T., Tuovinen, J., Vesala, T., Tuittila, E., Rinne, J., Happpanala, S. and Laine, J. 2007. CO₂ exchange of a sedge fen in southern Finland - The impact of a drought period. *Tellus series B-Chemical and Physical Meteorology*, 59: 826-837.
- Baldocchi, D. 1997a. Flux footprints within and over forest canopies. *Boundary-Layer Meteorology*, 85: 273-292.
- Baldocchi, D. 1997b. Measuring and modeling carbon dioxide and water vapor exchange over a temperate broad-leaved forest during the 1995 summer drought. *Plant Cell and Environment*, 20: 1108-1122.
- Baldocchi, D. 2008. Breathing of the terrestrial biosphere: lessons learned from a global network of carbon dioxide flux measurement systems. *Australian Journal of Botany*, 56: 1-26.
- Baldocchi, D., Falge, E., Gu, L. H., Olson, R., Hollinger, D., Running, S., Antoni, P., Bernhofer, C., Davis, K., Evans, R., Fuentes, J., Goldstein, A., Katul, G., Law, B., Lee, X. H., Malhi, Y., Meyers, T., Munger, W., Oechel, W., Paw, K. T., Pilegaard, K., Schmid, H. P., valentine, R., Verma, S., Vesala, T., Wilson, K and Wofsy, S. 2001. FLUXNET: A new tool to study the temporal and spatial variability of ecosystem-scale carbon dioxide, water vapor, and energy flux densities. *Bulletin of the American Meteorological Society*, 82: 2415-2434.
- Baldocchi, D., Tang, J.W. and Xu, L.K. 2006. How switches and lags in biophysical regulators affect spatial-temporal variation of soil respiration in an oak-grass savanna. *Journal of Geophysical Research-Biogeosciences*, 111: G02008.
- Baldocchi, D. and Wilson, K.B. 2001. Modeling CO₂ and water vapor exchange of a temperate broadleaved forest across hourly to decadal time scales. *Ecological Modeling*, 142: 155-184.
- Baldwin, A.H. and Mendelssohn, I.A. 1998. Effects of salinity and water level on coastal marshes: an experimental test of disturbance as a catalyst for vegetation change. *Aquatic Botany*, 61: 255-268.

- Barr, A.G., Black, T. A., Hogg, E. H., Kljun, N., Morgenstern, K. and Nesic, Z. 2004. Inter-annual variability in the leaf area index of a boreal aspen-hazelnut forest in relation to net ecosystem production. *Agricultural and Forest Meteorology*, 126: 237-255.
- Bassow, S. L. and Bazzaz, F. A. 1998. How environmental conditions affect canopy leaf-level photosynthesis in four deciduous tree species. *Ecology*, 79 2660–2675.
- Black, T.A., Hartog, G. D., Neumann, H. H., Blanken, P. D., Yang, P. C., Russel, C., Nesic, Z, Chen, S. G., Staebler, R. and Novak, M. D. 1996. Annual cycles of water vapor and carbon dioxide fluxes in and above a boreal aspen forest. *Global Change Biology*, 2: 219-229.
- Borges, A.V., Schiettecatte, L.S., Abril, G., Delille, B. and Gazeau, E. 2006. Carbon dioxide in European coastal waters. *Estuarine Coastal and Shelf Science*, 70: 375-387.
- Bowling, D. R., Tans, P. P. and Monson, R. K. 2001. Partitioning net ecosystem carbon exchange with isotopic fluxes of CO₂. *Global Change Biology*, 7:127-145
- Chen, W.J., Black, T. A., Yang, P. C., Barr, A. G., Neumann, H. H., Nesic, Z., Blanken, P. D., Novak, M. D., Eley, J., Ketler, R. J. and Cuenca, R. 1999. Effects of climatic variability on the annual carbon sequestration by a boreal aspen forest. *Global Change Biology*, 5: 41-53.
- Duarte, C.M., Middelburg, J.J. and Caraco, N. 2005. Major role of marine vegetation on the oceanic carbon cycle. *Biogeosciences*, 2: 1-8.
- Falge, E., Baldocchi, D., Tenhunen, J., Aubinet, M., Bakwin, P., Berbigier, P., Bernhofer, C., Burba, G., Clement, R., Davis, K. J., Elbers, J. A., Goldstein, A. H., Grelle, A., Granier, A., Granier, A., Guomundsson, J., Hollinger, D., Kowalski, A. S., Katul, G., Law, B. E., Malhi, Y., Meyers, T., Monson, R. K., Munger, J. W., Oechel, W., Paw, K. U. T., Pilegaard, K., Rannik, U., Rebmann, C., Suyker, A., Valentine, R., Wilson, K. and Wofsy, S. 2002. Seasonality of ecosystem respiration and gross primary production as derived from FLUXNET measurements. *Agricultural and Forest Meteorology*, 113: 53-74.
- Farquhar, G.D., Caemmerer, S.V. and Berry, J.A. 1980. A biochemical-model of photosynthetic CO₂ assimilation in leaves of C₃ Species. *Planta*, 149: 78-90.

- Flanagan, L.B., Wever, L.A. and Carlson, P.J. 2002. Seasonal and inter-annual variation in carbon dioxide exchange and carbon balance in northern temperate grassland. *Global Change Biology*, 8: 599-615.
- Gardner, L. R., and Porter, D. E. 2001. Stratigraphy and geologic history of a southeastern salt marsh basin, North Inlet, South Carolina, USA. *Wetlands Ecology and Management* 9:371-382.
- Gu, L. H., Fuentes, J. D., Shugart, H., Staebler, R. M. and Black, T. A. 1999. Response of net ecosystem exchanges of carbon dioxide to changes in cloudiness: results from two North American deciduous forests. *Journal of Geophysical Research*, 104: 31421-31434
- Gu, L.H., Baldocchi, D., Verma, S.B., Black, T.A., Vesala, T., Falge, E.M. and Dowty, P.R. 2002. Advantages of diffuse radiation for terrestrial ecosystem productivity. *Journal of Geophysical Research-Atmospheres*, 107: D5-6.
- Gu, L.H., Baldocchi, D.D., Wofsy, S.C., Munger, J.W., Michalsky, J.J., Urbanski, S.P. and Boden, T.A. 2003. Response of a deciduous forest to the Mount Pinatubo eruption: Enhanced photosynthesis. *Science*, 299: 2035-2038.
- Healey, K.D., Rickert, K.G., Hammer, G.L. and Bange, M.P. 1998. Radiation use efficiency increases when the diffuse component of incident radiation is enhanced under shade. *Australian Journal of Agricultural Research*, 49: 665-672.
- Heilman, J.L., Cobos, D.R., Heinsch, F.A., Campbell, C.S. and McInnes, K.J. 1999. Tower-based conditional sampling for measuring ecosystem-scale carbon dioxide exchange in coastal wetlands. *Estuaries*, 22: 584-591.
- Hirano, T., Segah, H., Harada, T., Limin, S., June, T., Hirata, R. and Osaki, M. 2007. Carbon dioxide balance of a tropical peat swamp forest in Kalimantan, Indonesia. *Global Change Biology*, 13: 412-425.
- Hollinger, D.Y., Aber, J., Dail, B., Davidson, E.A., Goltz, S.M., Hughes, H., Leclerc, M.Y., Lee, J.T., Richardson, A.D., Rodrigues, C., Scott, N.A., Achuatavarier, D. and Walsh, J. 2004. Spatial and temporal variability in forest-atmosphere CO₂ exchange. *Global Change Biology*, 10: 1689-1706.
- Hollinger, D.Y., Kelliher, F.M., Schulze, E.D., Bauer, G., Arneeth, A., Byers, J.N., Hunt, J.E., McSeveny, T.M., Kobak, K.I., Milukova, I., Sogatchev, A., Tatarinov, F., Varlargin, A.,

- Ziegler, W. and Vygodskaya, N.N. 1998. Forest-atmosphere carbon dioxide exchange in eastern Siberia. *Agricultural and Forest Meteorology*, 90: 291-306.
- Holmen, K. and Liss, P. 1984. Models for air water gas transfer - an experimental investigation. *Tellus series B-Chemical and Physical Meteorology*, 36: 92-100.
- Howes, B.L., Dacey, J.W.H. and Teal, J.M. 1985. Annual carbon mineralization and belowground production of *Spartina alterniflora* in a New-England salt marsh. *Ecology*, 66: 595-605.
- Knohl, A. and Buchmann, N. 2005. Partitioning the net CO₂ flux of a deciduous forest into respiration and assimilation using stable carbon isotopes. *Global Biogeochemical Cycles*, 19: GB4008
- Krishnan, P., Black, T.A., Grant, N.J., Barr, A.G., Hogg, E.T.H., Jassal, R.S. and Morgenstern, K. 2006. Impact of changing soil moisture distribution on net ecosystem productivity of a boreal aspen forest during and following drought. *Agricultural and Forest Meteorology*, 139: 208-223.
- Kurc, S.A. and Small, E.E. 2007. Soil moisture variations and ecosystem-scale fluxes of water and carbon in semiarid grassland and shrub land. *Water Resources Research*, 43: W06416.
- Lashof, D.A. and Ahuja, D.R. 1990. Relative contributions of greenhouse gas emissions to Global Warming. *Nature*, 344: 529-531.
- Law, B. E., Williams, M., Anthoni, P., Baldocchi, D. D. and Unsworth, M. H. 2000. Measuring and modeling seasonal variation of carbon dioxide and water vapor exchange of a *Pinus ponderosa* forest subject to soil water deficit. *Global Change Biology*, 6: 613–630.
- Law, B.E., Falge, E., Gu, L., Baldocchi, D.D., Bakwin, P., Berbigier, P., Davis, K., Dolman, A.J., Falk, M., Fuentes, J.D., Goldstein, A., Granier, A., Grelle, A., Hollinger, D., Janssens, I.A., Jarvis, P., Jensen, N.O., Katul, G., Mahli, Y., Matteucci, G., Meyers, T., Monson, R., Munger, W., Oechel, W., Olson, R., Pilegaard, K., Paw, K.T., Thorgeirsson, H., Valentini, R., Verma, S., Vesala, T., Wilson, K. and Wofsy, S. 2002. Environmental controls over carbon dioxide and water vapor exchange of terrestrial vegetation. *Agricultural and Forest Meteorology*, 113: 97-120.

- Lee, X.H., Fuentes, J.D., Staebler, R.M. and Neumann, H.H., 1999. Long-term observation of the atmospheric exchange of CO₂ with a temperate deciduous forest in southern Ontario, Canada. *Journal of Geophysical Research-Atmospheres*, 104: 15975-15984.
- Leuning, R., Cleugh, H.A., Zegelin, S.J. and Hughes, D., 2005. Carbon and water fluxes over a temperate Eucalyptus forest and a tropical wet/dry savanna in Australia: measurements and comparison with MODIS remote sensing estimates. *Agricultural and Forest Meteorology*, 129: 151-173.
- Levenberg, K. 1944. A method for the solution of certain non-linear problems in least squares. *Quarterly Journal of Applied Mathematics*, 2:164–168.
- Liu, B.Y.H. and Jordan, R.C., 1960. The interrelationship and characteristic distribution of direct, diffuse and total solar radiation. *Solar Energy*, 7: 53-65.
- Liu, J., Zhou, H.X., Qin, P. and Zhou, J., 2007. Effects of *Spartina alterniflora* salt marshes on organic carbon acquisition in intertidal zones of Jiangsu Province, China. *Ecological Engineering*, 30: 240-249.
- Lloyd, J. and Taylor, J.A., 1994. On the temperature-dependence of soil respiration. *Functional Ecology*, 8: 315-323.
- Lund, M., Lindroth, A., Christensen, T.R. and Strom, L., 2007. Annual CO₂ balance of a temperate bog. *Tellus Series B-Chemical And Physical Meteorology*, 59: 804-811.
- Maricle, B.R. and Lee, R.W., 2002. Aerenchyma development and oxygen transport in the estuarine cordgrasses *Spartina alterniflora* and *S. anglica*. *Aquatic Botany*, 74: 109-120.
- Massad, R.S., Tuzet, A. and Bethenod, O., 2007. The effect of temperature on C-4-type leaf photosynthesis parameters. *Plant Cell and Environment*, 30: 1191-1204.
- Melesse, A.M. and Hanley, R.S., 2005. Artificial neural network application for multi-ecosystem carbon flux simulation. *Ecological Modeling*, 189: 305-314.
- Miller, W.D., Neubauer, S.C. and Anderson, I.C., 2001. Effects of sea level induced disturbances on high salt marsh metabolism. *Estuaries*, 24: 357-367.
- Moffat, A.M., Papale, D., Reichstein, M., Hollinger, D.Y., Richardson, A.D., Barr, A.G., Beckstein, C., Braswell, B.H., Churkina, G., Desai, A.R., Falge, E., Gove, J.H., Heimann, M., Hui, D.F., Jarvis, A.J., Kattge, J., Noormets, A. and Stauch, V.J. 2007. Comprehensive

- comparison of gap-filling techniques for eddy covariance net carbon fluxes. *Agricultural and Forest Meteorology*, 147: 209-232.
- Moncrieff, J.B., Monteny, B., Verhoef, A., Friborg, T., Elbers, J., Kabat, P., deBruin, H., Soegaard, H., Jarvis, P.G. and Taupin, J.D. 1997. Spatial and temporal variations in net carbon flux during HAPEX-Sahel. *Journal of Hydrology*, 189: 563-588.
- Monson, R.K., Turnipseed, A.A., Sparks, J.P., Harley, P.C., Scott-Denton, L.E., Sparks, K. and Huxman, T.E., 2002. Carbon sequestration in a high-elevation, subalpine forest. *Global Change Biology*, 8: 459-478.
- Morris, J. T., Sundareshwar, P. V., Nietch, C. T., Kjerfve, B. D. and Cahoon, R. 2002. Response of coastal wetlands to rising sea-level. *Ecology*, 83: 2869-2877.
- Newell, S.Y., Fallon, R.D., Rodriguez, R.M.C. and Groene, L.C. 1985. Influence of rain, tidal wetting and relative-humidity on release of carbon-dioxide by standing-dead salt-marsh plants. *Oecologia*, 68: 73-79.
- Nielsen, O.I., Kristensen, E. and Macintosh, D.J. 2003. Impact of fiddler crabs (*Uca spp.*) on rates and pathways of benthic mineralization in deposited mangrove shrimp pond waste. *Journal of Experimental Marine Biology and Ecology*, 289: 59-81.
- Piao, S.L., Ciais, P., Friedlingstein, P., Peylin, P., Reichstein, M., Luysaert, S., Margolis, H., Fang, J.Y., Barr, A., Chen, A.P., Grelle, A., Hollinger, D.Y., Laurila, T., Lindroth, A., Richardson, A.D. and Vesala, T., 2008. Net carbon dioxide losses of northern ecosystems in response to autumn warming. *Nature*, 451: 49-52.
- Powell, T.L., Bracho, R., Jiahong, L., Dore, S., Ross, H. C. and Drake, B. G. 2006. Environmental controls over net ecosystem carbon exchange of scrub oak in central Florida. *Agricultural and Forest Meteorology*, 141: 19-34.
- Reed, D. J. 1995. The response of coastal marshes to sea-level rise: Survival or submergence. *Earth Surface Processes and Landforms*. 20: 39-48.
- Reichstein, M., Falge, E., Baldocchi, D., Papale, D., Aubinet, M., Berbigier, P., Bernhofer, C., Buchmann, N., Gilmanov, T., Granier, A., Grunwald, T., Havrankova, K., Ilvesniemi, H., Janous, D., Knohl, A., Laurila, T., Lohila, A., Loustau, D., Matteucci, G., Meyers, T., Miglietta, F., Ourcival, J. M., Pumpanen, J., Rambal, S., Rotenberg, E., Sanz, M., Tenhunen, J., Seutert, G., Vaccari, F., Vesala, T., Yakir, D. and Valentine, R. 2005. On

- the separation of net ecosystem exchange into assimilation and ecosystem respiration: review and improved algorithm. *Global Change Biology*, 11: 1424-1439.
- Richardson, A.D., Hollinger, D.Y., Aber, J.D., Ollinger, S.V. and Braswell, B.H. 2007. Environmental variation is directly responsible for short- but not long-term variation in forest-atmosphere carbon exchange. *Global Change Biology*, 13: 788-803.
- Rochette, P., Desjardins, R.L., Pattey, E. and Lessard, R. 1996. Instantaneous measurement of radiation and water use efficiencies of a maize crop. *Agronomy Journal*, 88: 627-635.
- Roderick, M.L., Farquhar, G.D., Berry, S.L. and Noble, I.R. 2001. On the direct effect of clouds and atmospheric particles on the productivity and structure of vegetation. *Oecologia*, 129: 21-30.
- Saxe, H., Cannel, M.G.R., Johnsen, Q., Ryan, M.G. and Vourlitis, G. 2001. Tree and forest function in response to global warming. *New Phytologist* 149: 369–399
- Simas, T., Nunes, J.P. and Ferreira, J.G. 2001. Effects of global climate change on coastal salt marshes. *Ecological Modeling*, 139: 1-15.
- Solomon, S., D. Qin, M. Manning, Z. Chen, M. Marquis, K.B. Averyt, M.Tignor and Miller, H. L. (eds), 2007. IPCC, 2007: Climate Change 2007: the physical science basis. Contribution of working group to the fourth assessment report of the intergovernmental panel on climate change, Cambridge University Press, Cambridge, United Kingdom and New York, NY, USA.
- Spitters, C.J.T., Toussaint, H. and Goudriaan, J. 1986. Separating the diffuse and direct component of global radiation and its implications for modeling canopy photosynthesis.1. Components of incoming radiation. *Agricultural and Forest Meteorology*, 38: 217-229.
- Titus, J. G., Park, R. A., Leatherman, S. P., Weggel, J. R., Greene, M. S., Maisel, P. W., Gaunt, G., Trehan, M. and Yohe, G. 1991. Greenhouse effect and sea level rise: The cost of holding back the sea. *Coastal Management*, 19: 171-204.
- van Wijk, M.T. and Bouten, W. 1999. Water and carbon fluxes above European coniferous forests modeled with artificial neural networks. *Ecological Modeling*, 120: 181-197.
- Wang, H., Saigusa, N., Zu, Y., Yamamoto, S., Kondo, H., Yang, F., Wang, W., Hirano, T. and Funjinuma, Y. 2005. Response of CO₂ flux to environmental variables in two larch forest ecosystems in East Asia. *Phyton-Annales Rei Botanicae*, 45: 339-346.

- Wang, H., Saigusa, N., Yamamoto, S., Konda, H., Hirano, T., Toriyama, A. and Fujinuma, Y. 2004. Net ecosystem CO₂ exchange over a larch forest in Hokkaido, Japan. *Atmospheric Environment*, 38: 7021-7032.
- Wang, Z.H.A. and Cai, W.J. 2004. Carbon dioxide degassing and inorganic carbon export from a marsh-dominated estuary (the Duplin River): A marsh CO₂ pump. *Limnology and Oceanography*, 49: 341-354.
- Webb, E.K., Pearman, G.I. and Leuning, R. 1980. Correction of flux measurements for density effects due to heat and water-vapor transfer. *Quarterly Journal of the Royal Meteorological Society*, 106: 85-100.
- Whiting, G.J. and Chanton, J.P. 2001. Greenhouse carbon balance of wetlands: methane emission versus carbon sequestration. *Tellus series B-Chemical and Physical Meteorology*, 53: 521-528.
- Wilson, K. B., Baldocchi, D. D and Hanson, P. J. 2001. Leaf age affects the seasonal pattern of photosynthetic capacity and net ecosystem exchange of carbon in a deciduous forest. *Plant Cell and Environment*, 24: 57-583
- Wisniewski, J. and Lugo, A.E. 1992. Natural sinks of CO₂ - preface. *Water air and Soil Pollution*, 64: R9-R10.
- Wofsy, S.C., Goulden, M. L., Munger, J. W., Fan, S. M., Bakwin, P. S., Daube, B. C., Bassow, S. L. and Bazzaz, F. A. 1993. Net exchange of CO₂ in a mid-latitude forest. *Science*, 260: 1314-1317.
- Woodwell, G.M., Whitney, D.E., Hall, C.A.S. and Houghton, R.A. 1977. Fax pond ecosystem study - exchanges of carbon in water between a salt-marsh and Long Island Sound. *Limnology and Oceanography*, 22: 833-838.
- Xu, L.K., Baldocchi, D.D. and Tang, J.W. 2004. How soil moisture, rain pulses, and growth alter the response of ecosystem respiration to temperature. *Global Biogeochemical Cycles*, 18: GB4002
- Zhang, Y., Li, C.S., Trettin, C.C., Li, H. and Sun, G. 2002. An integrated model of soil, hydrology, and vegetation for carbon dynamics in wetland ecosystems. *Global Biogeochemical Cycles*, 16: 1:17.

Chapter 4: Partitioning of available energy in an intertidal salt marsh

4.1. Introduction

Coastal wetlands are unique ecosystems in terms of available energy partitioning as they are located at the interface between terrestrial and aquatic surfaces and thus are subjected to land and oceanic environmental forcings. Tidal activity can transform the marsh surface from being a wet soil surface to an open water surface within short time scales, thereby leading to drastic changes in available energy partitioning. Although several studies exist regarding energy fluxes from coastal wetlands (Burba *et al.*, 1999a; Burba *et al.*, 1999b; Koch and Rawlik, 1993; Silis *et al.*, 1989), no long-term eddy covariance based studies are available over intertidal wetlands. Coastal salt marshes are the most susceptible ecosystems to sea level rise associated with global climate change and long-term tower-based studies are critical to understand the ecosystem response in terms of available energy partitioning and trace gas exchanges between these systems and overlying atmosphere. It is critical to understand the partitioning of available energy into sensible and latent heat fluxes over an ecosystem as this process dictates the weather and climate of the system (Wilson *et al.*, 2002). In addition, the partitioning of available energy controls the radiative and temperature regimes transport of water in the ecosystem, biogeochemical cycling, and ecosystem productivity (Burba *et al.*, 1999b).

The incoming solar energy remaining after undergoing reflection, absorption and scattering is the available energy utilized in various physical processes such as sensible heating (heating of air), latent heating (conversion of water to vapor) and heating of the soil. The surface energy balance in a wetland or tidally influenced ecosystem can be expressed in the form of the following relationship as adapted from Tsai *et al.*, 2007.

$$R_n - G - S - W - F = LE_c + H_c + C + A \quad (4.1)$$

R_n is the net radiation, G is the soil heat flux, S is the storage of heat between the soil surface and the location of the soil heat flux plates, W is the storage of heat in the water column when tide is present, and F is the photosynthetic energy flux (the energy utilized in photosynthesis), C is the canopy heat storage (heat stored between the land surface and the eddy covariance measurement point, LE_c and H_c represent the latent heat and sensible exchanges between the plant canopy at the measurement point and atmosphere, and A represents the advection of

energy. A detailed description of the terms involved in the energy balance equation is provided below.

$$R_n = (K \downarrow - K \uparrow) + (L \downarrow - L \uparrow) \quad (4.2)$$

$$S = \rho_g c_g z_g \frac{\partial T_g}{\partial t} \quad (4.3)$$

$$W = \rho_w c_w z_w \frac{\partial T_w}{\partial t} \quad (4.4)$$

$$C = \rho_a c_p h_c \frac{\partial \theta}{\partial t} + \rho_a L_v h_c \frac{\partial q}{\partial t} \quad (4.5)$$

$$A = \rho_a c_p h_c \left(u \frac{\partial \theta}{\partial t} + v \frac{\partial \theta}{\partial t} \right) + \rho_a L_v h_c \left(u \frac{\partial q}{\partial t} + v \frac{\partial q}{\partial t} \right) \quad (4.6)$$

$$F = -\frac{C_{CO_2}}{M_{CO_2}} F_{CO_2} \quad (4.7)$$

$K \downarrow$ is the downwelling short wave radiation, $K \uparrow$ is the outgoing short wave radiation, $L \downarrow$ is the incoming long wave radiation and $L \uparrow$ is the total outgoing long wave radiation (surface emission and surface reflected incoming). The subscripts g , a , and w indicate soil, air and water with ρ denoting density, T the temperature, and t the time. M_{CO_2} is the molecular weight of carbon dioxide (CO_2), F_{CO_2} is the flux of CO_2 determined from the eddy covariance system, C_{CO_2} is the energy required to fix CO_2 via photosynthesis ($422 \text{ kJ g mol}^{-1}$) (Nobel, 1999). Based on the available information, the partitioning of R_n is studied in terms of the ecosystem-level sensible heating (H), latent heating (LE), and soil heating/cooling (G). Considering the short stature of the canopy and the flat topography of the study site, the canopy storage and the advective terms can be considered negligible. In this study, eddy covariance-based estimates of energy fluxes are utilized to understand the patterns and processes involved in energy partitioning and to quantify canopy controls on energy partitioning.

The objectives of this chapter are 1) to understand the patterns in energy partitioning in an intertidal salt marsh and to provide estimates of energy balance closure as influenced by factors such as tidal activity, 2) to investigate canopy controls on ecosystem available energy partitioning through the estimation of bulk canopy variables such as canopy conductance to water vapor, surface-atmosphere coupling (Ω) Priestly-Taylor coefficient and Bowen ratio.

4.2. Methodology

4.2.1. Study site

The flux tower site is a lagoonal salt marsh (37°24' N, 75°50' W) which is dominated by the smooth cord grass (*Spartina alterniflora*). The site is tidally influenced and composed of accumulated fine sediments, which are rich in organic matter. The site is about 2 kilometers from the mainland and is about 80 meters away from a major creek edge. The average height of the vegetation and leaf area index measured at the site during the growing season were 60 ± 1.87 cm and $2.4 \text{ m}^2 \text{ m}^{-2}$, respectively. The mudflats are separated by meandering tidal creeks, and morphologically different forms of *Spartina alterniflora* occur in different areas depending upon the degree of tidal flushing from the creeks. With a mean relief of only 2 meters from the mean sea level and an extremely high erosion and deposition rates (13 m per year in the horizontal dimension), the system is highly dynamic and is susceptible to physical forcings such as sea level rise (Van Cleve and Martin, 1991). The period of study (May-December, 2007) was characterized by extremely dry conditions with a rainfall of only 295 mm received during May to September.

4.2.2. Instrumentation

The data presented here were obtained from a 6.7m tall flux tower which was established at the site during February 2007. The flux tower features an eddy covariance system consisting of a sonic anemometer (model CSAT3, Campbell Scientific, Inc., Logan, Utah, USA) and an infrared gas analyzer (model LI-7500, Licor, Biosciences, Lincoln, NE USA) mounted at 3.7 m from the sediment surface. Several other micrometeorological variables, such as net radiation, photosynthetic active radiation, air temperature and humidity, sediment temperature and water level on the marsh surface were also recorded. The raw turbulence and scalar concentration data were collected at the frequency of 10 Hz and were filtered to remove spikes. Since the gas analyzer recorded gas concentrations, density corrections were applied on the raw eddy covariance fluxes (Webb *et al.*, 1980). Flux footprint estimates at the site were performed using a two dimensional Lagrangian random walk model (Baldocchi, 1997). Results indicated that the peak contribution to the estimated fluxes resulted from about 20 to 30 m from the base of the tower.

4.2.3 Bulk canopy parameters estimations

Bulk canopy parameters such as canopy conductance, Priestly-Taylor coefficient, Bowen ratio and decoupling coefficient have been used to characterize canopy exchange processes and environmental control on it (Wilson and Baldocchi, 2000). Further these parameters are important inputs for defining boundary conditions in land-atmosphere modeling schemes, hydrological and climate models (Baldocchi and Meyers, 1998). The bulk canopy conductance to water vapor was estimated by inverting the Penman-Monteith equation (Monteith, 1965; Shuttleworth *et al.*, 1984)

$$\frac{1}{G_s} = \frac{1}{G_a} \left\{ \frac{\varepsilon(R_n - G) + \rho C_p G_a D / \gamma}{\lambda E} - \varepsilon - 1 \right\} \quad (4.1)$$

where C_p is the specific heat capacity of air at constant pressure ($1006 \text{ J kg}^{-1} \text{ K}^{-1}$), D the atmospheric water vapor pressure deficit (kPa), and ε is S/γ where S is the slope of the vapor pressure-temperature relationship ($\text{kPa } ^\circ\text{C}^{-1}$) (equation 4.2), and γ is the psychrometric “constant” (equation 4.3).

$$S = \frac{4099e_s}{(T_{air} + 237.3)^2} \quad (4.2)$$

$$\gamma = 0.00163 \frac{P}{\lambda} \quad (4.3)$$

e_s is the saturation vapor pressure in kPa, T_{air} is the air temperature in $^\circ\text{C}$, P is the atmospheric pressure in kPa, and λ is the latent heat of vaporization (MJ kg^{-1}). The saturation vapor pressure (in kPa) is expressed as a function of air temperature following Bolton (1980) (equation 4.4)

$$e_s = 0.6112 \times \exp\left(\frac{17.67 \times T_{air}}{T_{air} + 243.5}\right) \quad (4.4)$$

The bulk aerodynamic conductance, G_a required in the estimation of canopy conductance is calculated as the reciprocal of the bulk aerodynamic resistance which is the sum of the aerodynamic resistance for momentum transfer (R_{am}) and the quasi-laminar boundary layer resistance (R_b) (equation 4.5).

$$R_a = R_{am} + R_b \quad (4.5)$$

The R_{am} ($s\ m^{-1}$) is estimated as the ratio of wind velocity (u) to the square of the friction velocity (u^*) measured over the canopy (equation 4.6)

$$R_{am} = \frac{u}{u^{*2}} \quad (4.6)$$

The value of R_b is determined as a function of the von Karmen's constant (k) and the friction velocity (equation 4.7), where B is an empirical constant. The value of kB^{-1} is taken as 2, a value suitable for dense grass canopies (Garratt and Hicks, 1973; Ma *et al.*, 2007)

$$R_b = kB^{-1} / ku^* \quad (4.7)$$

Although canopy conductance estimates includes non-linear effects of soil moisture and canopy turbulence, it can be related to a weighted integration of stomatal conductance from all the leaves (Baldocchi and Meyers, 1998). The decoupling coefficient (Ω) (Jarvis and McNaughton, 1986); which explains the degree of coupling between the environment and the canopy was determined from the estimated values of G_s , G_a and ε . The Ω value can vary between 0 (perfect coupling) and 1 (perfect decoupling) and stomatal control on transpiration weakens as Ω approaches 1 (Jarvis and McNaughton, 1986; Kumagai *et al.*, 2004).

$$\Omega = \frac{\varepsilon + 1}{\varepsilon + 1 + \frac{G_a}{G_s}} \quad (4.8)$$

The Priestly-Taylor coefficient (α) (Priestly and Taylor, 1972), which is the ratio of the estimated evaporation to the equilibrium evaporation (λE), was estimated following equation 4.9 and 4.10.

$$\alpha = \frac{\lambda E}{\lambda E_{eq}} \quad (4.9)$$

$$\lambda E_{eq} = \frac{(R_n - G)}{s + \gamma} \quad (4.10)$$

The values of α close to 1 indicate equilibrium with the climatologically possible evaporation rate from a steady state completely closed system (equilibrium evaporation), whereas lower values indicate drier or conditions of low evapo-transpiration (Wilson *et al.*, 2002).

The various surface bulk parameters as described above were estimated from half hourly estimates of energy fluxes and other micrometeorological variables obtained during 10:00 and 14:00 hours. This time interval was selected to avoid instabilities in calculations associated with low LE values and measurement errors occurring in the early morning and late evening hours and avoid periods of increased advection in the late afternoon. The canopy bulk parameters were analyzed for the period from May to October 2007 as the canopy became dormant during the winter months (November to December). The time periods corresponding with high tide events, which can produce standing water on the marsh surface, was removed from the data sets to isolate canopy influences rather than considering energy exchange from an open water surface. Although complete energy balance closure is a requirement for estimation of bulk canopy parameters from the Penman-Monteith equation, the estimated values of fluxes during low tide conditions was used as a high degree of energy balance closure is obtained for low tide periods.

4.3. Results

4.3.1. Surface energy budget

In order to closely examine surface energy balance partitioning, the study period May to December 2007 is split into three distinct periods: A) early and peak growing season (May-July), B) late and end of growing season (August to October), and C) inactive or dormant period. This classification is based on the growth characteristics of *Spartina alterniflora* and also based on changes in local climate.

The initial peak growth period (May-June) was characterized by increased partitioning of available energy for latent heating. The marsh surface in effect acted as an open water surface as the soil was always saturated. The average daytime (10:00 to 14:00 hours) latent heating accounted for 45.7% of the available energy whereas the sensible and ground heat flux accounted for 27.1 and 9.2 %, respectively. The energy partitioning observed in this study is similar to other wetland ecosystems such as bogs (Admiral *et al.*, 2006) where higher latent heat was observed during snow free periods. The late and end of year growing season also showed similar partitioning of available energy with sensible heating accounting for 25.6 %, latent heating 43.8%, and ground heat flux 7.28 % of the available energy. The inactive or dormant period was marked by a decreased available energy and an almost equal distribution among sensible

(35.02%) and latent heat (42.4%) fluxes (Figure 4.1). The sensible heat partitioning of available energy observed in this intertidal salt marsh was higher compared to other studies over similar marshes with C_3 grasses (5-10% of R_n) though out the growing season (Burba *et al.*, 1999c). The highest value of R_{net} , H and LE was observed for the initial growth period (May to July) and thereafter with the progress of the season the R_{net} values decreased and the partitioning of available energy between sensible and latent heat fluxes became identical.

It was further observed that during in the early and late growing seasons, the latent heat fluxes exceed the amount of available energy, after 16:00 hours local time. This could be attributed to advection of energy brought about by a sea breeze which develops in this coastal region. The average daily wind speed and direction for the period from May to July is presented in Figure 4.2.

It is observed that there was a rapid change in wind direction from a south westerly to a south easterly flow during the early morning hours. The wind velocity also increased with the progress of the day and reached a peak value around 16:00 hours coinciding with the period of increased advection of moisture and thereafter a reduction in wind velocity was noticed. The sea breeze was initiated by the differential heating of the land and ocean advected moisture from the ocean surface towards the land, increasing the partitioning of energy for latent heating (McKendry and Roulet, 1994). The wind direction shifted back to a westerly flow during the evening hours as the sea breeze change to a land breeze. This phenomenon is not observed during the winter months or inactive period (November to December) as the land-estuary temperature differences in the lower atmosphere did not provide enough energy for the differential heating of the land and sea.

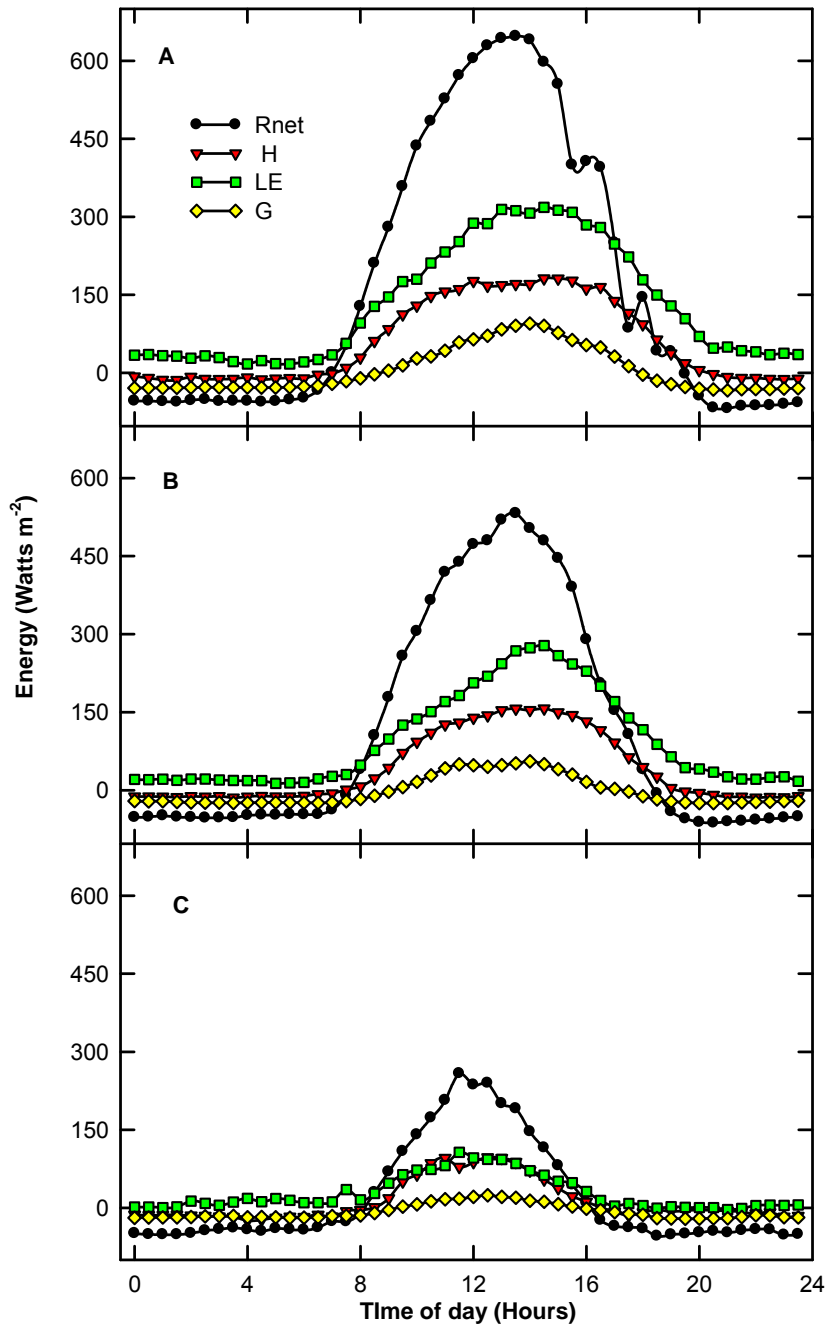


Figure 4.1. Energy balance components for three distinct growing periods: A) early and peak growing season (May-July), B) late and end of the growing season (August-October), and C) dormant or inactive period (November to December).

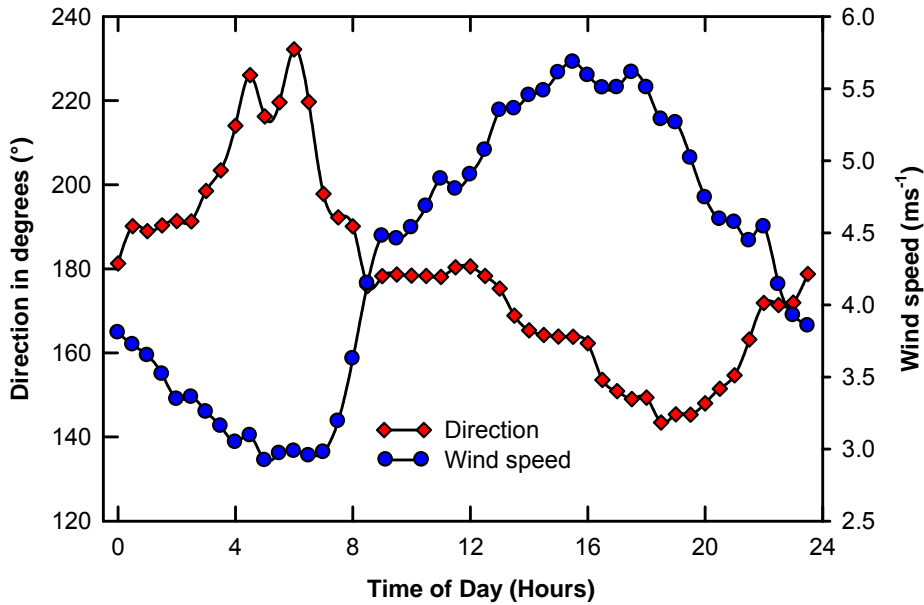


Figure 4.2. Average wind speed and direction for the period from May to July 2007. The occurrence of sea breeze is observed as the rapid change in direction occurring after 06:00 hours local time with a gradual increase in wind velocity

Advective effects are amplified in coastal ecosystems due to the differential surface characteristics and heating between the terrestrial and marine environments (Weick and Rouse, 1991). Advection of energy caused by directional winds such as sea breeze can change boundary layer characteristics such as potential temperature profiles and mixed layer height over inter-tidal coastal regions (Chen and Oke, 1994). Local circulations developing around river or lake systems have been reported to cause energy imbalances (Hiyama, 2007). Advection can be induced in the horizontal and vertical domains by heterogeneity in topography (land and ocean interface), canopy cover and distribution of sources and sinks over an intertidal salt marsh. Although modifications have been proposed to account for the horizontal (Aubinet *et al.*, 2003; Marcolla *et al.*, 2005) and vertical advection in sloped terrain (Lee, 1998) these corrections need scalar and turbulence measurements at multiple heights and locations. The horizontal (H_{adv}) and vertical advective (V_{adv}) terms can be represented as

$$H_{adv} = \int_0^h \overline{u(z)} \frac{\partial \overline{\chi(z)}}{\partial x} dz \quad (4.11)$$

$$V_{adv} = \int_0^h \overline{w(z)} \frac{\partial \overline{\chi(z)}}{\partial z} dz \quad (4.12)$$

where $\overline{u}(z)$ and $\overline{w}(z)$ are the vertically averaged (from the ground surface to the measurement point, h) horizontal and vertical velocity and $\overline{\chi}(z)$ is the vertically averaged scalar concentration. Since no concentration profile measurements or transect measurements along the dominant flow directions existed for water vapor an alternative approach to quantify latent heat advection would be to introduce the concept of advective enhancement or advective depression on evaporation rates (McNaughton, 1976). The evaporative flux (λE) measured at a particular location can be described in terms of the equilibrium evapotranspiration (λE_{eq}) and advective terms which accounts for the extra energy available through advection (λE_{ad}).

$$\lambda E = \lambda E_{eq} + \lambda E_{ad} \quad (4.13)$$

Evapotranspiration is advectively enhanced when E is greater than E_{eq} and conversely if E is less than E_{eq} , advective depression is observed. The advective effects can be quantified in terms of the deviation of λE from λE_{eq} ($\lambda E_{eq} - \lambda E$) and the negative ratio of this deviation to λE represents the percent contribution of advection (R_{ad}) to λE (Smith *et al.*, 1997). Positive values of R_{ad} indicated advective enhancement, where as negative values indicate advective depression.

$$R_{ad} = -\frac{\lambda E_{eq} - \lambda E}{\lambda E} \quad (4.14)$$

The average ensemble percentage of advection calculated for the initial growth period (May to July) for low tide conditions on a diurnal scale is represented in Figure 4.3. Advective enhancement occurred during the late afternoon periods (after 14:00 hours) and reached peak values after 16:00 hours. Although advective depression is observed during early morning hours, its extent is lower than the enhancement observed in late afternoon period. Similar advective patterns were observed for the other growth periods (data not presented here), but the amount of advected energy was comparatively lower for the inactive growth period (November-December) compared to other periods. Maximum average advection can be up to 80% of estimated LE, indicating that advection has a significant effect on latent heat flux estimates, especially in the late afternoon hours. The peak advective depression values are observed in the morning hours (around 10:00 hours), which corresponds to the peak assimilation period and can be attributed to canopy controls on transpiration rather than advection.

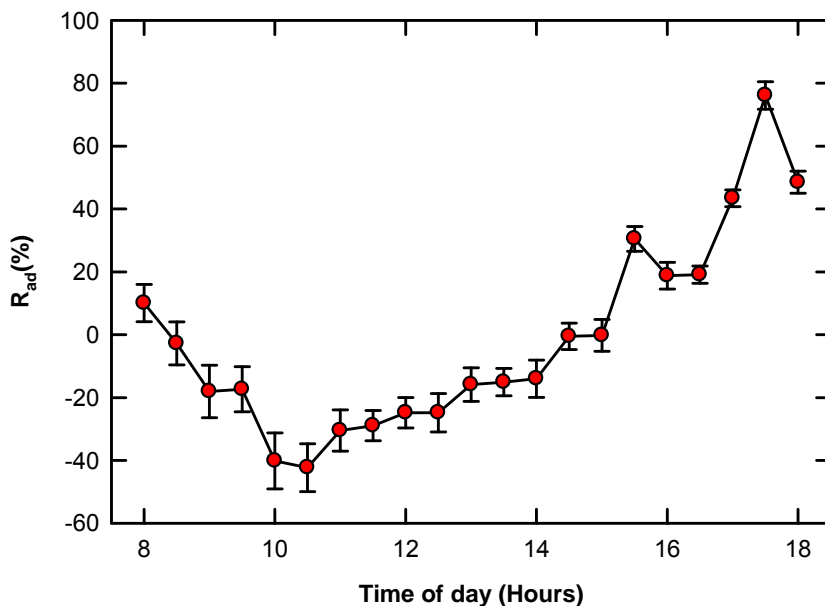


Figure 4.3. Computed diurnal R_{ad} values, which represents the percentage of advected latent heat over the marsh surface for the period from May to July, 2007 (low tide). Positive values indicate advective enhancement whereas negative values indicate advective depression. The error bars represents the standard error of the mean for each time class.

The net radiation measured over the marsh surface during the peak sunshine hours (10:00 to 14:00 hours) was about $77.48\% \pm 0.11\%$ of the downwelling solar irradiance during the growing season (May to October). Such values were similar to results obtained by Crabtree and Kjerfve (1978) over a *Spartina* marsh.

4.3.2. Examining energy balance closure and tidal influences

Estimation of energy balance closure is critical in evaluating the reliability of eddy covariance measurements (Wilson *et al.*, 2002). Although energy balance closure calculations provide reliability estimates for latent heat and sensible heat measurements, the transport mechanisms estimated by eddy covariance methodology and the measurement principle are similar for all scalars (Paw *et al.*, 2000), making it applicable for CO_2 fluxes. The energy balance closure is examined by estimating the slope and intercept of the regressions between half hourly sum of latent and sensible heat fluxes ($H+LE$) and the difference between net radiation and soil heat flux ($R_{net}-G$) (Wilson *et al.*, 2002). The energy closure is characterized by an intercept of 0 and a slope of 1. Since the errors associated with estimation of net radiation and soil heat flux are comparatively less compared to H and LE (Twine *et al.*, 2000), $R_{net}-G$ can be considered as the

independent variable in the regression estimate. The reduced major axis method (RMA) (Sokal and Rohlf, 1981) is implemented here to account for the random errors occurring in the independent variable. The energy balance closure for the three distinct growth periods is provided by including periods with tides over the marsh surface and also without tides (Table 4.1). The data were selected for energy balance closure estimates based on an incoming radiation and friction velocity threshold of 20 Wm^{-2} and 0.1 ms^{-1} , respectively.

Table 4.1. Energy balance closure estimate parameters from the RMA analysis. The non-tidal and tidal classes are based on the absence or presence of water over the marsh surface. The standard errors of the estimates are provided in the parenthesis.

| Growth period | Intercept | | Slope | | R ² | |
|---------------|-----------|----------|-----------|---------|----------------|---------|
| | Non-tidal | Tidal | Non-tidal | Tidal | Non-tidal | Tidal |
| May-Jul | 66.22 | 78.04 | 0.84 | 0.79 | 0.62 | 0.58 |
| | (±6.44) | (±4.46) | (±0.02) | (±0.01) | (±0.02) | (±0.02) |
| Aug-Oct | 24.17 | 31.06 | 0.92 | 0.80 | 0.69 | 0.58 |
| | (± 3.45) | (±3.08) | (±0.01) | (±0.02) | (± 0.02) | (±0.02) |
| Nov-Dec | 11.28 | 11.27 | 0.77 | 0.70 | 0.81 | 0.60 |
| | (±3.25) | (± 3.72) | (±0.02) | (±0.04) | (±0.02) | (±0.04) |

The intercept in all cases was positive, indicating incomplete closure with a slope which was always lesser than 1. The intercept decreased with the progress of the season (78.04 to 11.27 Wm^{-2}) and the slope ranged between 0.92 and 0.70. The larger slopes obtained in this analysis could be attributed to the inclusion of only day-time turbulent fluxes in the analysis as night-time energy balance closure is typically less than day time values (Wilson *et al.*, 2002). The low R² values estimated for the RMA regression could be attributed to the advection of energy occurring in the late afternoon periods as the regressions improved greatly during the winter months when sea breeze activity decrease. The presence of water on the marsh surface due to tidal activity had consequences on energy balance closure. The inclusion of high tide events in the data set increased the intercept and the slopes moved further away from 1 compared to the data set when there was no water on the marsh surface (Figure 4.4).

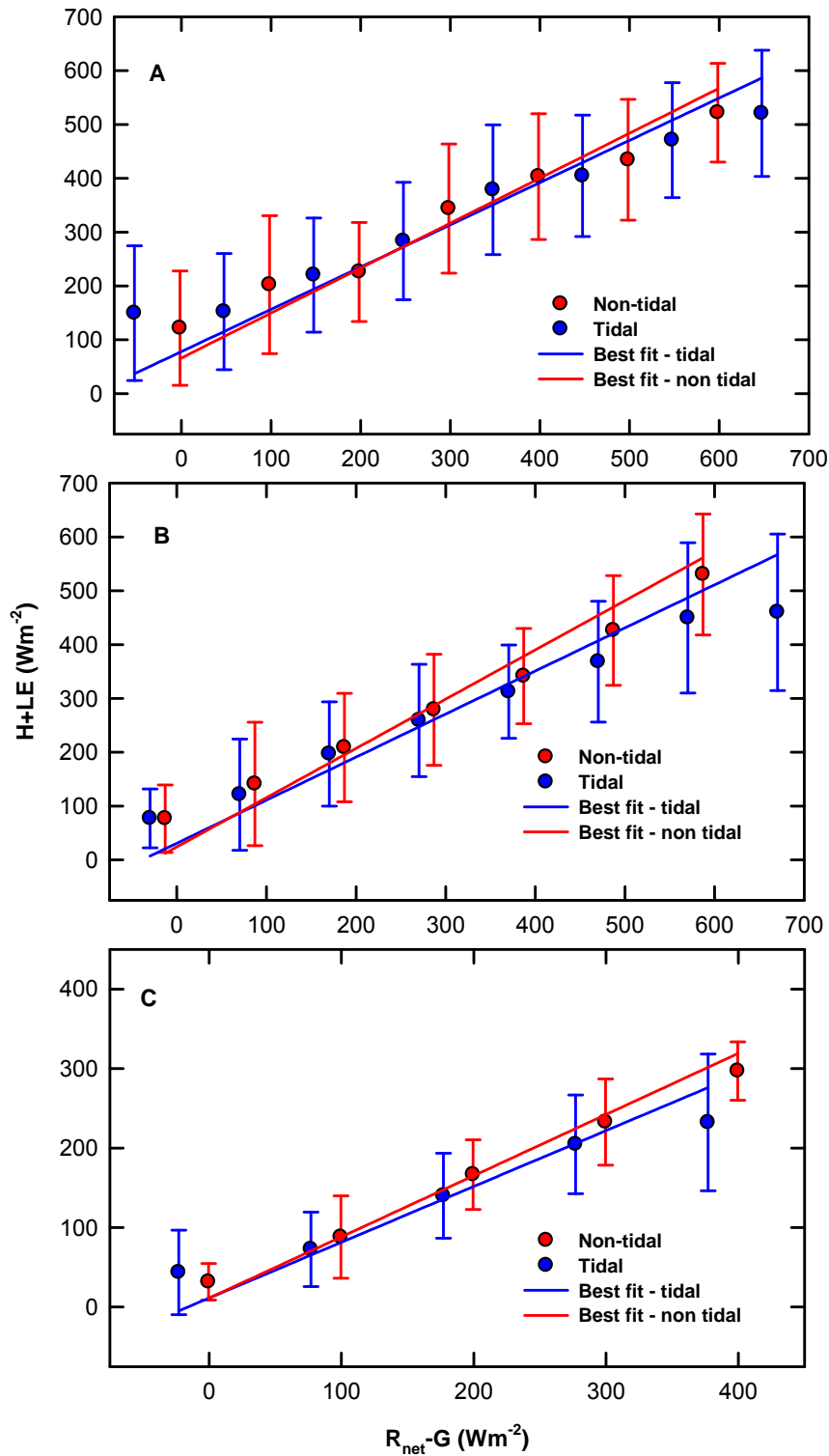


Figure 4.4. Energy balance closure estimates for three distinct growth periods: A) May-July, B) August-October, C) November-December. The mean $H+LE$ values for each $R_{\text{net-G}}$ classes of 100 Wm^{-2} is represented for tidal and non-tidal periods with the error bars representing one standard deviation. The best fit lines obtained from the reduced major analysis are also provided.

In order to examine the impact of tides on the partitioning of available energy, two days are compared where tidal activity occurred at different periods of the day. In the case of a day of year 244 when high tide occurred at a period corresponding with maximum available energy, there was an increased partitioning of energy for latent heating and a corresponding decrease in sensible heating. This can be attributed to the change in surface characteristics from a wet soil surface to a free water surface with the progress of the high tide.

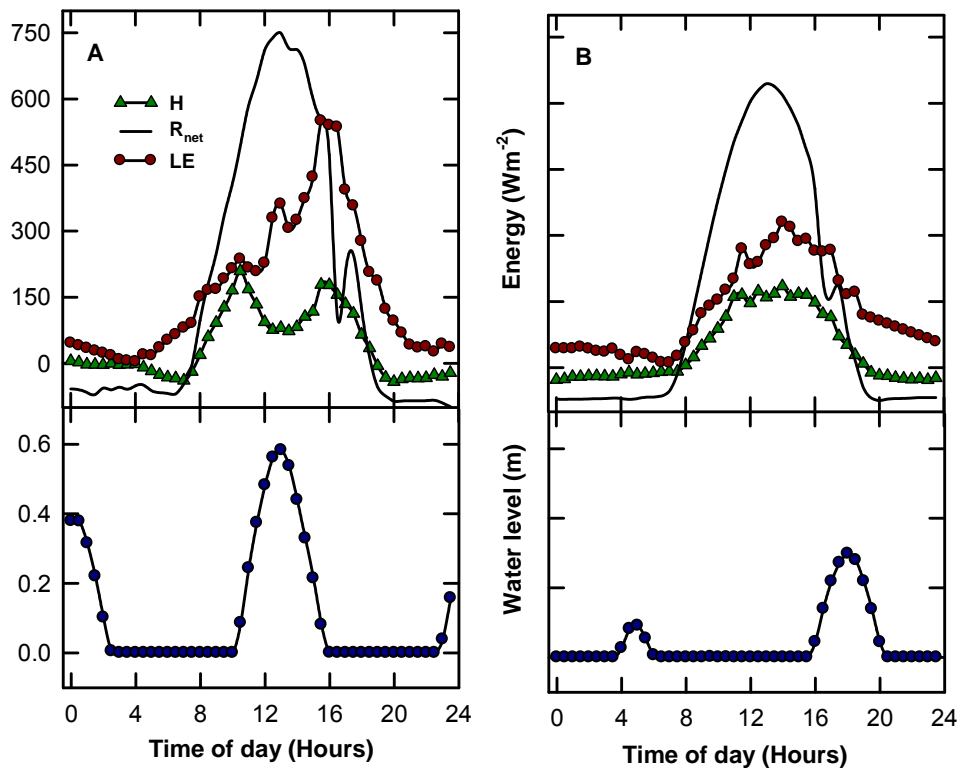


Figure 4.5. Energy balance partitioning for DOY 244 (A) with high tide occurring at the middle of the day and DOY 247 (B) with high tide events occurring during the early morning and evening hours. The water level over the marsh surface is also represented in the corresponding bottom panels. But here we have strong advection for the case in (A). The breeze was stronger than the second day (B).

In comparison, day of year 247 had high tides occurring early in the morning and late in the afternoon corresponding with periods of low available energy. For this day, the increased redistribution of available energy for latent heating was not observed as the amount of available energy observed during the period of high tide was comparatively less (Figure 4.5). The time of occurrence of the high tide is critical in determining the partitioning of available energy in this system.

The increased partitioning of available energy for latent heating can be attributed to the decreased surface resistance when the evaporating surface becomes a free water surface (Hughes, 2001). Similar increased partitioning of available energy for latent heating in response to flooding was observed in other wetland ecosystems (Heilman *et al.*, 2000). In general a high degree of energy balance closure was observed for low tide periods when water was not present on the marsh surface compared to most ecosystems (eg Ameriflux sites, Wilson *et al.*, 2002) and consistent with other short canopies (Heusinkveld *et al.*, 2004; Ma *et al.*, 2007; Meyers and Hollinger, 2004)

4.3.3. Canopy controls on flux partitioning-influence of bulk canopy parameters

In this section the results from the determination and analysis of bulk canopy parameters such as canopy conductance, decoupling coefficient, Priestly-Taylor coefficient and Bowen ratio are presented. The maximum bulk surface conductance values were observed during the month of June corresponding with the peak assimilation period. The daily average bulk surface conductance value ranged between 1.78 to 22 mm s⁻¹ (data not presented here). The maximum daily bulk conductance values observed in this study was comparable to terrestrial grassland ecosystems (Kim and Verma, 1990; Ma *et al.*, 2007; Stewart and Verma, 1992). The highest D values were observed during the month of August and the lowest bulk conductance values were observed during the month of October, corresponding with the senescence of the canopy. An exponential decrease in G_s (Figure 4.6) was observed with increasing D values in this ecosystem similar to other studies in grassland ecosystems (Ma *et al.*, 2007).

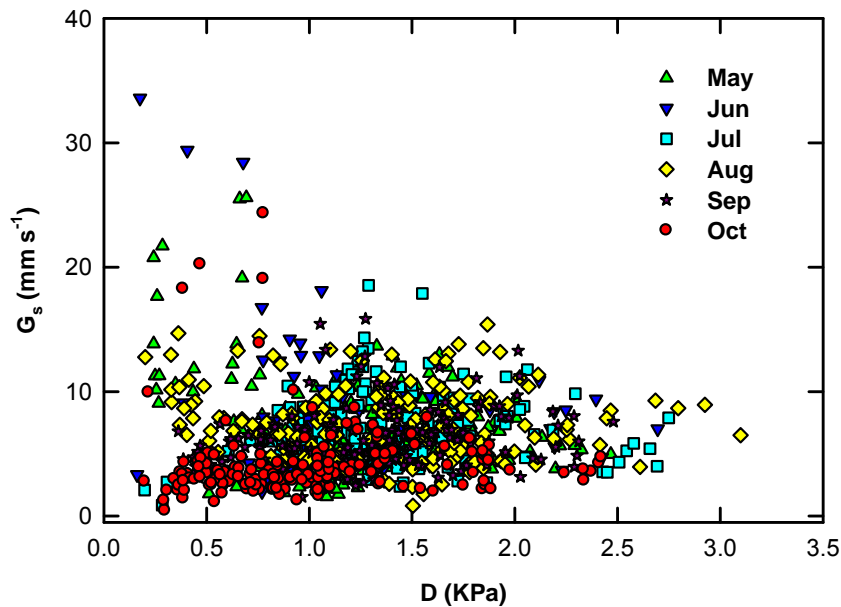


Figure 4.6. Relationship between bulk surface conductance (G_s) and atmospheric vapor pressure deficit (D) for the growing season (May-October, 2007). The data presented here are half hourly estimated values for the time period from 10:00 to 14:00 hours.

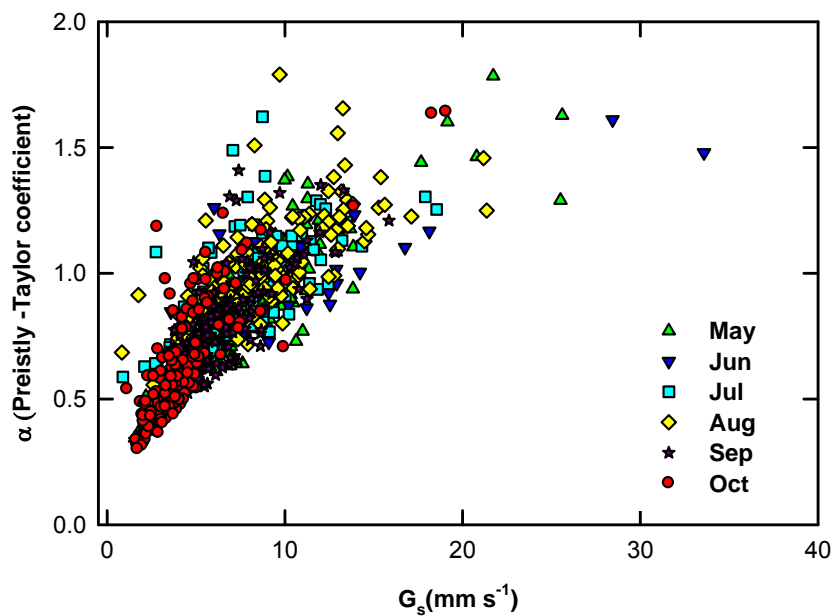


Figure 4.7. The relationship between bulk canopy conductance and the Priestly-Taylor coefficient (α). The data presented here are half hourly estimates excluding high tide periods during 10:00 and 14:00 hours.

The α values ranged from a minimum of 0.32 to 1.79 during the growing season with a mean value for the period of $0.90 (\pm 0.03)$. The α observed over this system is higher than most terrestrial grassland ecosystems (Ma *et al.*, 2007) but lower than well watered cropland systems

(Debruin, 1983), where typical α values reach 1.26. Further, the α values in the range of 1 to 1.26 have been used in many wetland ecosystems for estimation of evapo-transpiration using the Priestly-Taylor equation (Price and Woo, 1988; Souch *et al.*, 1998). The occurrence of large α values (>1.3) can be attributed to the advection of moisture over the marsh surface by the sea breeze activity, and thus leading to overestimation of LE. Although the soil is always saturated, lower α values can be estimated, mostly towards the end of the growing season as the canopy becomes dormant. The lower α values estimated for the peak of the growing season could be attributed to plant physiological limitations as the plant had to utilize metabolic energy to obtain fresh water from a saline environment. The wide range of α value can be attributed to the fact that transpiration may not be the dominant flow path of water and evaporative processes may dominate owing to the increased solute concentration (Hussey and Odum, 1974). A logarithmic relationship was observed between G_s and α , but the strength of the relationship was not stronger compared to other grassland ecosystems (Ma *et al.*, 2007). The α values became insensitive to G_s , when G_s exceeded 15 mm s^{-1} which was similar to theoretical values estimated by (Mcnaughton and Spriggs, 1986)

The average diurnal (08:00 to 18:00 hours) trends in the decoupling coefficient for the growing season indicate that the highest canopy-atmosphere coupling (lower Ω values) was observed around 10:00 hours. This period coincided with the peak assimilation period (refer Chapter-3), and thereafter an increase in decoupling was observed (Figure 4.8). The Ω values depended upon the ratio of boundary layer conductance to canopy conductance, and the lower Ω values indicated that that the leaf surface saturation deficit was similar to that existing in the atmosphere (Jones, 1992). However, on a monthly scale, the average daytime (10:00 to 14:00 hours) decoupling coefficient value increased with the progress of the growing season, achieving the highest values in the month of August and thereafter the Ω values decreased (Figure 4.9). The Ω values were higher (0.48-0.30) through out the growing season compared to other tree species such as red maple (0.12 to 0.37) (Wullschlegel *et al.*, 2000), but was lower than observed for other grass species (0.8 to 0.50) (Goldberg and Bernhofer, 2001).

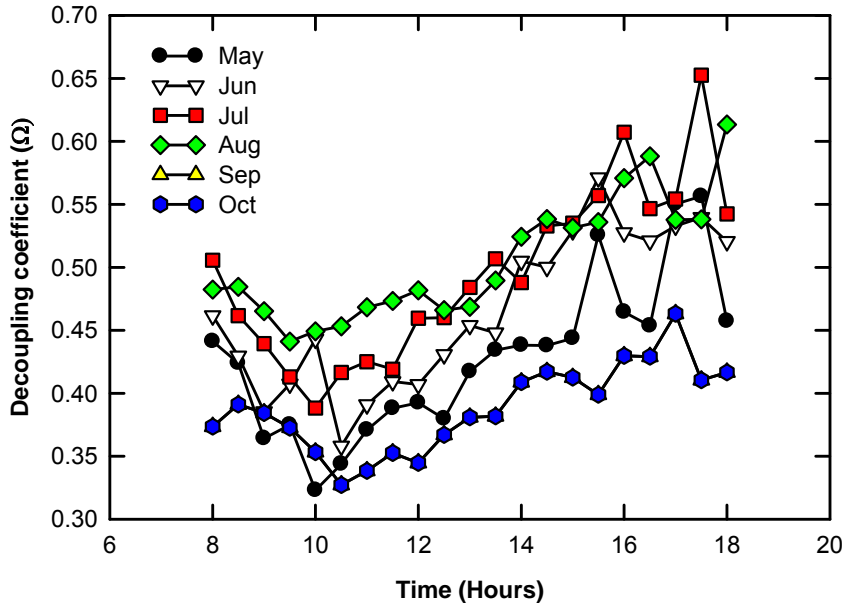


Figure 4.8. Average diurnal decoupling coefficients estimated during the growing season. The peak coupling (lowest decoupling) is observed around 10:00 hours local time.

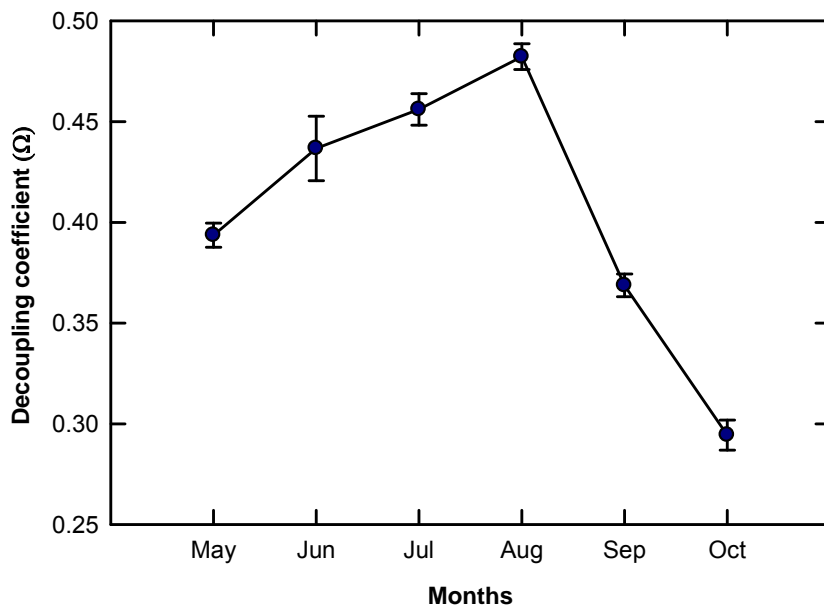


Figure 4.9. Trends in monthly ensemble average daytime (10:00 to 14:00 hours) Ω values during the growing season. The data represented here correspond to periods of low tide when there was no significant water level on the marsh surface.

The positive logarithmic relationship between canopy conductance and Ω is presented in Figure 4.10. Similar to α value, the Ω quantity also exhibited insensitive to G_s value when G_s value exceeds 15 mm s^{-1} . The average monthly Ω values were less than 0.5 for all the different months indicating that the evaporative demand primarily drove LE in this system.

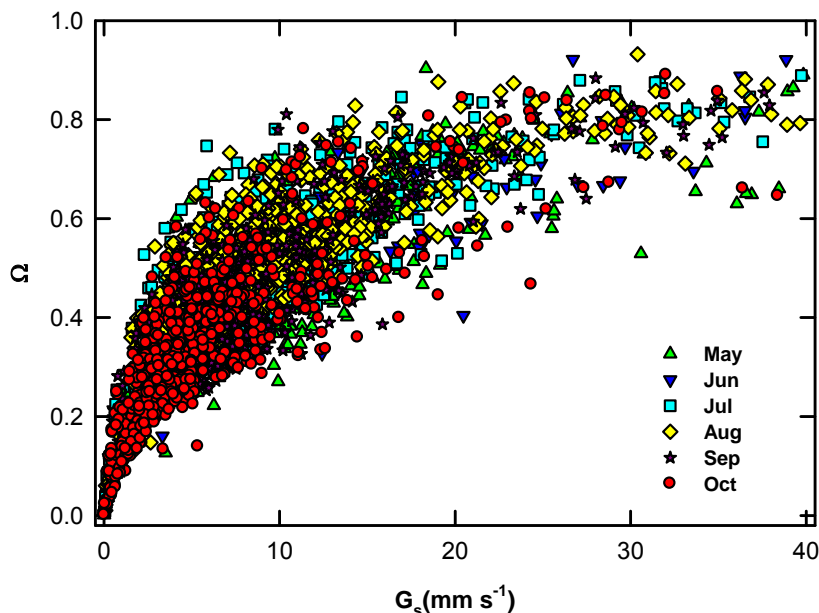


Figure 4.10. Relationship between stomatal conductance and Ω for the growing season. The data presented here are half hourly day time (10:00 to 14:00 hours) estimates for low tide periods.

The Bowen ratio, which is the ratio of sensible to latent heat fluxes, increased with the progress of the growing season, with the lowest bower ratios observed during the initial growth period and thereafter increases as the growth slowed down and average values reached about 0.8 during the November-December inactive or dormant period (Figure 4.11). The low Bowen ratios (>0.4) occurring in all season can be attributed to the advection of moisture from the ocean to the marsh surface by the sea breeze occurring at the site. The Bowen ratios were estimated as an average value for each day of year considering the period from 10:00 to 14:00 hours.

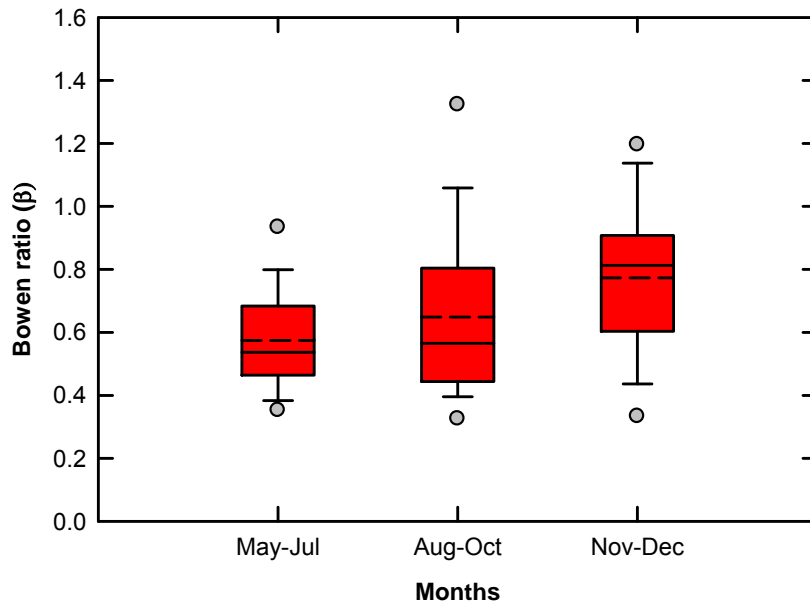


Figure 4.11. Changes in Bowen ratio with the progress of the growing season for the period from 10:00 to 14:00 hours. The mean values are depicted as the dotted lines in the middle of the box plots and the solid line represents the median values. The 5th and 95th percentile values are represented as filled circles for each box. The top edge of the boxes represents the 75th percentile and the bottom edge the 25th percentile.

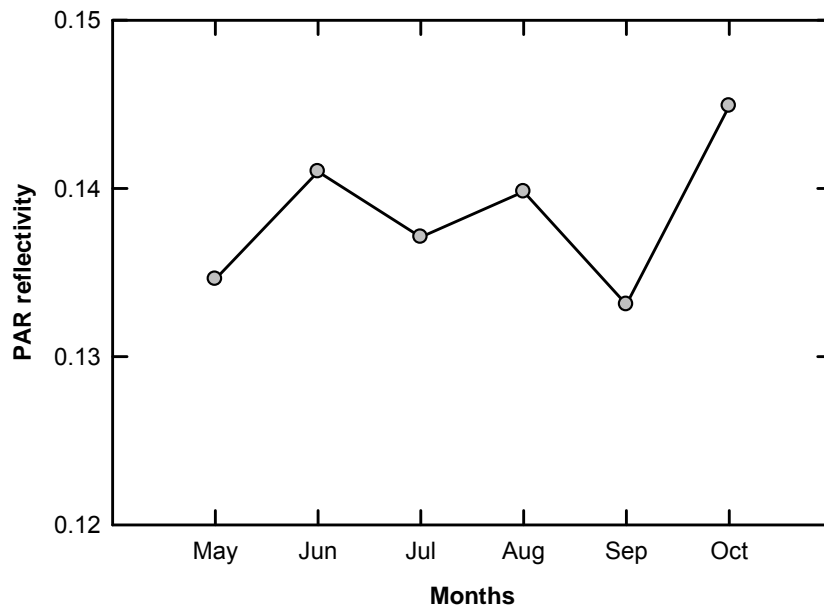


Figure 4.12. Monthly average PAR reflectivity estimated during the growing season (May-October, 2007). The PAR reflectivity values are estimated for day time hours (10:00 to 14:00 hours) and excluding periods of high tide when water is present on the marsh surface.

4.3.4. PAR reflectivity

PAR reflectivity is directly related to the greenness of the canopy and thus it is a good indicator of plant phenology (Ma *et al.*, 2007). The average monthly PAR reflectivity values for the growing season estimated as the ratio of the sum of the reflected PAR to incoming PAR for each month is presented in Figure 4.12. The average growing season PAR reflectivity value is about 0.14 with, the lowest value observed during the month of September. Although no clear trends are observed in the reflectivity values, a large increase in PAR reflectivity was observed during the month of October, corresponding with the onset of senescence.

4.4. Conclusions

Spartina alterniflora dominated intertidal salt marshes partitioned greater amounts of available energy for latent heating during the peak growing season and thereafter a reduction in latent heat partitioning was observed with the progress of the season. Tides influence energy partitioning by decreasing the surface resistance to water vapor transport as energy exchange occurred from the open water surface. The increased latent heat flux during high tides caused a corresponding reduction in sensible heat fluxes. Although Bowen ratio (0.6 -0.8) estimated at this site was higher than most agricultural and grassland ecosystems, the estimated canopy conductance values were comparable to other grassland ecosystems. Tidal activity affected the energy balance closure at the site. In general, the exclusion of high tide events improved the degree of surface energy closure. Tides play an important role in redistribution of available energy with an increased latent heating and decreased sensible heating observed during periods of high tide. The presence of flow regimes such as land-sea breezes in this intertidal zone can lead to advection of moisture from the ocean surface, leading to increased latent heat flux estimates especially in the late afternoon, when high wind velocities were observed. Although the salt marsh soils were saturated, the average α values were less than well watered agricultural crops, indicating water stress resulting from the high solute concentrations. The diurnal trends in decoupling coefficient (Ω) indicate that the canopy was coupled to the environment during the morning hours. The LE was primarily driven by VPD and G_s , but with the progress of the day the canopy became more decoupled and under such conditions the LE was driven more by available

energy. Advection contributed significantly to latent heat fluxes due to the presence of land-sea breezes.

References

- Admiral, S.W., Lafleur, P.M. and Roulet, N.T. 2006. Controls on latent heat flux and energy partitioning at a peat bog in eastern Canada. *Agricultural and Forest Meteorology*, 140: 308.
- Aubinet, M., Heinesch, B. and Yernaux, M. 2003. Horizontal and vertical CO₂ advection in a sloping forest. *Boundary-Layer Meteorology*, 108: 397-417.
- Baldocchi, D.D., and Meyers, T.P. 1998. On using eco-physiological, micrometeorological and biogeochemical theory to evaluate carbon dioxide, water vapor and trace gas fluxes over vegetation: a perspective. *Agricultural and Forest Meteorology*, 90: 1-25
- Baldocchi, D.D. 1997. Flux footprints within and over forest canopies. *Boundary-Layer Meteorology*, 85: 273-292.
- Bolton, D. 1980. The computation of equivalent potential temperature. *Monthly weather Review*, 108: 1046-1053.
- Burba, G.G., Verma, S.B. and Kim, J. 1999a. A comparative study of surface energy fluxes of three communities (*Phragmites australis*, *Scirpus acutus*, and open water) in a prairie wetland ecosystem. *Wetlands*, 19: 451-457.
- Burba, G.G., Verma, S.B. and Kim, J. 1999b. Energy fluxes of an open water area in a mid-latitude prairie wetland. *Boundary-Layer Meteorology*, 91: 495-504.
- Burba, G.G., Verma, S.B. and Kim, J. 1999c. Surface energy fluxes of *Phragmites australis* in a prairie wetland. *Agricultural and Forest Meteorology*, 94: 31-51.
- Hughes C.E., Kalma J.D., Binning P., Willgoose G.R. and Vertzonis M. 2001 Estimating evapotranspiration for a temperate salt marsh, Newcastle, Australia. *Hydrological Processes* 15: 957-975.
- Chen, J.M. and Oke, T.R. 1994. Mixed-layer heat advection and entrainment during the sea breeze. *Boundary-Layer Meteorology*, 68: 139-158
- Crabtree, S.J. and Kjerfve, B. 1978. Radiation balance over a salt marsh. *Boundary-Layer Meteorology*, 14: 59-66

- Debruin, H.A.R. 1983. A model for the Priestley-Taylor parameter-alpha. *Journal of Climate and Applied Meteorology*, 22: 572-578.
- Garratt, J.R. and Hicks, B.B. 1973. Momentum, heat and water-vapor transfer to and from natural and artificial surfaces. *Quarterly Journal of the Royal Meteorological Society*, 99: 680-687.
- Heilman, J.L., Heinsch, F.A., Cobos, D.R. and McInnes, K.J. 2000. Energy balance of a high marsh on the Texas Gulf Coast: Effect of water availability. *Journal of Geophysical Research-Atmospheres*, 105: 22371-22377.
- Heusinkveld, B.G., Jacobs, A.F.G., Holtslag, A.A.M. and Berkowicz, S.M. 2004. Surface energy balance closure in an arid region: role of soil heat flux. *Agricultural and Forest Meteorology*, 122: 21-37.
- Hiyama, T., Strunin, M.A., Tanaka, H. and Ohta, T. 2007. The development of local circulations around the Lena River and their effect on tower-observed energy imbalance. *Hydrological Processes*, 21: 2038-2048.
- Hussey, B. and Odum, W. 1974. Evapotranspiration in tidal marshes. *Estuaries and Coasts*, 15: 59-67
- Jarvis, P.G. and Mcnaughton, K.G. 1986. Stomatal control of transpiration - Scaling up from leaf to region. *Advances in Ecological Research*, 15: 1-49.
- Jones, H.G. 1992. *Plants and microclimate*. Cambridge University press, Cambridge. pp, 452
- Kim, J. and Verma, S.B., 1990. Components of surface-energy balance in a temperate Grassland ecosystem. *Boundary-Layer Meteorology*, 51(4): 401-417.
- Koch, M.S. and Rawlik, P.S. 1993. Transpiration and stomatal conductance of two wetland macrophytes (*Cladium jamaicense* and *Typha domingensis*) in the subtropical everglades. *American Journal of Botany*, 80: 1146-1154.
- Kumagai, T. O., Saitoh, T. M., Sato, Y., Morooka, T., Manjroi, O., Kuraji, K. and Suzuki, M. 2004. Transpiration, canopy conductance and the decoupling coefficient of a lowland mixed dipterocarp forest in Sarawak, Borneo: dry spell effects. *Journal of Hydrology*, 287: 237-251
- Lee, X.H. 1998. On micrometeorological observations of surface-air exchange over tall vegetation. *Agricultural and Forest Meteorology*, 91: 39-49.

- Ma, S.Y., Baldocchi, D.D., Xu, L.K. and Hehn, T. 2007. Inter-annual variability in carbon dioxide exchange of an oak/grass savanna and open grassland in California. *Agricultural and Forest Meteorology*, 147: 157-171.
- Marcolla, B., Cescatti, A., Montagnani, L., Manca, G., Kerschbaumer, G. and Minerbi, S. 2005. Importance of advection in the atmospheric CO₂ exchanges of an alpine forest. *Agricultural and Forest Meteorology*, 130: 193-206.
- McKendry, I. and Roulet, N. 1994. Sea breezes and advective effects in southwest James bay. *Journal of Geophysical Research-Atmospheres*, 99: 1623-1634.
- McNaughton, K.G. 1976. Evaporation and advection II: evaporation downwind of a boundary separating regions having different surface resistances and available energies. *Quarterly Journal of the Royal Meteorological Society*, 102: 193-202.
- Mcnaughton, K.G. and Spriggs, T.W. 1986. A mixed-layer model for regional evaporation. *Boundary-Layer Meteorology*, 34: 243-262.
- Meyers, T.P. and Hollinger, S.E. 2004. An assessment of storage terms in the surface energy balance of maize and soybean. *Agricultural and Forest Meteorology*, 125: 105-115.
- Monteith, J.L., 1965. Evaporation and environment. In: G.E. Fogg (Editor), *The state and movement of water in living organisms*. Symposium of the society of experimental biology. Academic press, Inc, New York, USA, pp. 205-234.
- Nobel, P.S. 1999. *Physiochemical and environmental plant physiology*. Academic press, 435 pp.
- Paw U, K.T., Baldocchi, D.D., Meyers, T.P. and Wilson, K.B. 2000. Correction of eddy-covariance measurements incorporating both advective effects and density fluxes. *Boundary-Layer Meteorology*, 97: 487-511.
- Price, J.S. and Woo, M.K. 1988. Studies of a subarctic coastal marsh.1. hydrology. *Journal of Hydrology*, 103: 275-292.
- Priestly, C.H.B. and Taylor, R.J. 1972. On the assessment of surface heat flux and evaporation using large-scale parameters. *Monthly Weather Review*, 100: 81-92.
- Sokal, R. R. and Rohlf, F.J. 1981. *Biometry*. 2nd edition. Freeman, New York, USA.
- Shuttleworth, W.J., Gash, J.H.C., Lloyd, C.R., Moore, C.J., Roberts, J., Filho, A.D.O.M., Fisch, G., Filho, V.D.P.S., Ribeiro, M.D.N.G., Molion, L.C.B., Sa, L.D.D.A., Nobre, J.C.A.,

- Cabral, O.M.R., Patel, S. and Moraes, J.C.D. 1984. Eddy correlation measurements of energy partition for Amazonian forest. *Quarterly Journal of the Royal Meteorological Society*. 110: 1143–1162.
- Silis, A., Rouse, W.R. and Hardill, S. 1989. Energy-balance of the intertidal zone of western Hudson-bay.1. ice-free period. *Atmosphere-Ocean*, 27: 327-345.
- Smith, D.M., Jarvis, P.G. and Odongo, J.C.W. 1997. Energy budgets of windbreak canopies in the Sahel. *Agricultural and Forest Meteorology*, 86: 33-49.
- Souch, C., Grimmond, C.S.B. and Wolfe, C.P. 1998. Evapotranspiration rates from wetlands with different disturbance histories: Indiana Dunes National Lakeshore. *Wetlands*, 18: 216-229.
- Stewart, J.B. and Verma, S.B. 1992. Comparison of surface fluxes and conductances at two contrasting sites within the FIFE area. *Journal of Geophysical Research-Atmospheres*, 97: 18623-18628.
- Hiyama, T. Strunin, M. A., Tanaka, H. and Ohta, T. 2007. The development of local circulations around the Lena River and their effect on tower-observed energy imbalance. *Hydrological Processes*, 21: 2038-2048.
- Tsai, J.L., Tsuang, B.J., Lu, P.S., Yao, M.H. and Shen, Y. 2007. Surface energy components and land characteristics of a rice paddy. *Journal of Applied Meteorology and Climatology*, 46: 1879-1900.
- Twine, T.E., Kustas, W.P., Norman, J.M., Cook, D.R., Houser, P.R., Meyers, T.P., Prueger, J.H., Starks, P.J. and Wesely, M.L. 2000. Correcting eddy-covariance flux underestimates over a grassland. *Agricultural and Forest Meteorology*, 103: 279-300.
- Van Cleve, K. and Martin, S., 1991. Long-term ecological research in the United States: A network of research sites 1991. AR-10, long-term ecological research network office, University of Washington. College of forest resources, Seattle. Washington 98195.
- Webb, E.K., Pearman, G.I. and Leuning, R. 1980. Correction of flux measurements for density effects due to heat and water-vapor transfer. *Quarterly Journal of the Royal Meteorological Society*, 106: 85-100.
- Weick, E.J. and Rouse, W.R. 1991. Advection in the coastal Hudson-bay lowlands, Canada.1. The terrestrial surface-energy balance. *Arctic and Alpine Research*, 23: 328-337.

- Wilson, K., Goldstein, A., Falge, E., Aubinet, M., Baldocchi, D., Berbigier, P., Bernhofer, C., Ceulemans, R., Dolman, H., Field, C., Grelle, A. Ibrom, A., Law, B.E., Kowalski, A., Meyers, T., Moncrieff, J., Monson R., Oechel, W., Tenhunen, J., Valentini, R. and Verma, S. 2002. Energy balance closure at FLUXNET sites. *Agricultural and Forest Meteorology*, 113: 223-243.
- Wilson, K.B. and Baldocchi, D.D. 2000. Seasonal and interannual variability of energy fluxes over a broadleaved temperate deciduous forest in North America. *Agricultural and Forest Meteorology*, 100: 1-8
- Wullschleger, S.D., Wilson, K.B., and Hanson, P.J. 2000. Environmental control of whole-plant transpiration, canopy conductance and estimates of the decoupling coefficient for large red maple trees. *Agricultural and Forest Meteorology*. 104: 157-168.

Chapter 5. Modeling carbon and energy flows in an intertidal coastal marsh

5.1. Introduction

Canopy biophysical models are essential tools for studying ecosystem-level response to changes in local and global climate. Plant canopies are an integral part of the land surface which plays an important role in modulating regional and local climate. It is essential to accurately represent the transfer of mass and energy in the plant-soil-atmosphere continuum in global and meso-scale biogeochemical models to reduce systematic errors (Xue *et al.*, 1996; Foley *et al.*, 1996). Canopy biophysical models have been developed as tools for integrating field observation and predicting canopy response to changes in local climate. Such models have been employed to quantify land surface response to global climate change in terrestrial ecosystems. Land surface or canopy biophysical models can be used for integrating microclimatic data sets to quantify regional biogeochemical cycles and ecosystem response to disturbances such as sea level rise and increased greenhouse gases.

A vast body of knowledge exists regarding cycling of carbon and energy in various ecosystems of the world as a result of numerous tower-based eddy covariance studies (Baldochi *et al.* 2001). Although these flux tower measurements are time consuming and costly, the understanding of environmental controls on ecosystem level transfer of mass and energy can be used to develop biophysical models, which can predict fluxes of energy and scalars at the individual ecosystem level. Thus, using basic atmospheric measurements, it is possible to predict surface-atmosphere exchanges in similar ecosystems or estimate ecosystem response in a scenario of global climate change. Canopy biophysical models incorporate various processes such as radiative transfer, transpiration, photosynthesis and sensible heat transfer along with turbulent transport of scalars to represent canopy-atmosphere exchange processes (Gu, 1998; Knohl and Baldocchi, 2008).

Canopy biophysical models can be classified broadly as big-leaf and multi-layer models (Dai *et al.*, 2004). The big-leaf models represent the canopy as a single big leaf and exchange process over the whole canopy is scaled to a single leaf to estimate fluxes (e.g., Bonan, 1996; Sellers *et al.*, 1996). The multilayer models integrate fluxes from multiple canopy layers to estimate the total flux at the top of the canopy (e.g., Sellers *et al.*, 1996; Wang and Jarvis, 1990;

Baldocchi 1992; Baldocchi and Meyers, 1998; Gu, et al., 1999; Baldocchi and Wilson, 2001; Barr, 2005). The multilayer canopy models include detailed description of within canopy exchange processes and take into account the vertical variation in LAI, air temperature and trace gas concentration to simulate fluxes of scalars and hence are more physically robust. Although detailed land surface schemes have been developed to represent canopy-atmosphere exchange processes in mesoscale and global climate models, coastal zones are poorly represented in these models. The greatest error in regional climate model predictions are observed over the coastal zones (Leonard, *et al.*, 1997), indicating inadequacies in the representation of the coastal surfaces in climate models.

The main objective of this chapter is to develop a *Spartina alterniflora* canopy biophysical model incorporating the latest theories of turbulent transport and solving the energy balance equation within the different layers of the canopy. Since *Spartina alterniflora* salt marshes are located or found along the east coast of continental United States, the development of this model can aid in understanding the processes involved in the exchange of energy and carbon in this ecosystem and its representation in regional and global climate models. Further the model can be used as a tool for quality control/quality assurance of the eddy covariance data. The biophysical model can be used as a diagnostic tool to understand ecosystem response to local and global climate change scenarios and to disturbances such as storms and Nor'easters (Davis, 1993). Detailed models of horizontal transport of sediment/carbon over salt marshes have been developed for various intertidal ecosystems (Zang *et al.*, 2002). These models rarely consider the vertical transport of mass and energy between the ecosystem and the atmosphere caused by biological activities such as photosynthesis and respiration. Even though a canopy level model has been developed for *Spartina alterniflora* (Dai and Wiegert, 1996), it does not incorporate the detailed models of photosynthesis and the relationship between distributed sources/sink and their influence on the fluxes of scalars. In this chapter the *Spartina alterniflora* canopy biophysical model is developed and a detailed description of the all the modules used to describe various canopy exchange processes are provided. The model performance is evaluated under different weather conditions and its strengths and weaknesses are evaluated in this chapter.

5.2. Model description

The canopy biophysical model estimates the fluxes of energy and carbon from the plant canopy by solving a system of non-linear system of equations which describe the energy balance and stomatal conductance within different layers of the canopy. In the implementation of this model, the canopy is divided into multiple layers of equal thickness (in this case 6 equal layers, each 0.1 m thick) and the coupled energy balance and stomatal conductance equations are solved. The unknown variables in the system of equations are the leaf temperature, stomatal conductance to water vapor, intercellular concentration of carbon dioxide (CO₂) (C_i) and mesophyll concentration of CO₂ (C_m). Thus, for the 6 layers of the canopy there are 24 equations and 24 unknowns, which can be solved through a hybridized form of Newton's method developed by Kelley (1995). The coupled energy balance and stomatal conductance equations for a canopy layer with a unit leaf area index (LAI) as adapted from (Gu *et al.*, 1999) is modified to include mesophyll CO₂ concentration as given below.

$$S_h + \lambda S_w + L_s + M + R_{as} + R_{al} = 0 \quad (5.1)$$

$$g_{s0} + g_{si} \frac{A_n RH}{(C_s - \Gamma^*)} - g_{sv} = 0 \quad (5.2)$$

$$10^{-3} \frac{C_a - C_{ci}}{1/g_{bc} + 1/g_{sc}} - A_n = 0 \quad (5.3)$$

$$10^{-3} g_i (C_i - C_m) - A_n = 0 \quad (5.4)$$

S_h represents the source strength of leaf surface heating in W m⁻², S_w is the source strength for water vapor (g m⁻² s⁻¹), L_s represents the heat storage in the leaf tissue, and M represents the metabolic energy utilized in photosynthesis (W m⁻²). The terms R_{as} and R_{al} represent the net shortwave and long wave radiation absorbed by the canopy layer.

The leaf heat storage is a function of the density of leaf (ρ_l) (g m⁻³), its specific heat capacity (C_l) (J g⁻¹ K⁻¹), η (in m) is the volume to surface area ratio of the leaf (or the thickness of the leaf) and the change in leaf temperature (∂T_l) (in Kelvin) during a specific time (t in seconds).

$$L_s = \rho_l C_l \eta \frac{\partial T_l}{\partial t} \quad (5.5)$$

The leaf heat storage and the metabolic energy utilized in photosynthesis (M in $W\ m^{-2}$) account for only less than 5% of the total absorbed irradiance and can be ignored (Gu *et al.*, 1999). The source strength of heat ($W\ m^{-2}$) (Gu, 1998c) and water vapor ($mmol\ m^{-2}\ s^{-1}$) (Campbell and Norman, 1998) can be represented as

$$S_h = \rho_a C_p (T_l - T_a) g_{bh} \quad (5.6)$$

$$S_w = \frac{e_s(T_l) - e_a(T_a)/P_a}{1/g_{bv} + 1/g_{sv}} \quad (5.7)$$

ρ_a represents the density of air ($g\ m^{-3}$); C_p represents the specific heat capacity of air ($J\ g^{-1}\ K^{-1}$), T_a represents the air temperature in K and g_{bh} represents the leaf boundary layer conductance to heat ($m\ s^{-1}$) (Sellers *et al.*, 1996).

$$g_{bh} = \frac{6.62 \times 10^{-3}}{p_s} \left(\frac{u}{d_l} \right)^{0.5} \quad (5.8)$$

Where u is the local wind speed ($m\ s^{-1}$), d_l represents the characteristic dimension of the leaf (m), and p_s represents the shelter factor which accounts for the mutual sheltering effects of clustering leaves. In the expression for the source strength of moisture (S_w), e_a represents the actual vapor pressure (Pa), e_s represent the saturation vapor pressure (Pa), and P_a represents the atmospheric pressure (Pa). The saturation vapor pressure (Pa) over the leaf surface is expressed as a function of leaf temperature ($^{\circ}C$) following Bolton (1980).

$$e_s(T_l) = 611 \exp\left(\frac{17.502T_l}{T_l + 240.97}\right) \quad (5.9)$$

The boundary layer conductance (g_{bw}) and stomatal conductance to water vapor (g_{sv}) terms are also part of the relationship describing the source strength of water vapor.

$$g_{bv} = 1.082 g_{bh} \times 10^3 \frac{P}{R(T_a + 273)} \quad (5.10)$$

The stomatal conductance equation (equation 5.2) is the analytical model developed by Ball *et al.*, (1987) and relates stomatal conductance to water vapor (g_{sv}), CO_2 assimilation (A_n), relative humidity (RH), and CO_2 mixing ratios (C_s) ($\mu mol\ mol^{-1}$) on the leaf surface. The constants g_{s0} and g_{si} represents the Ball and Berry intercept and slope parameters (See Chapter 2) and Γ^*

represents the CO₂ compensation point (Leuning, 1990). The leaf surface CO₂ mixing ratio can be derived as a function of ambient (C_a) and intercellular (C_i) CO₂ mixing ratios (in ppm) along with stomatal and leaf boundary layer (g_{bc}) (mmol m⁻² s⁻¹) conductance to CO₂.

$$C_s = \frac{C_a g_{bc} + C_i g_{sc}}{g_{bc} + g_{sc}} \quad (5.11)$$

The boundary layer conductance (g_{bc}) and stomatal conductance (g_{sc}) to CO₂ can be expressed as functions of boundary layer and stomatal conductance to water vapor (mmol m⁻² s⁻¹) as shown in equations (5.12) and (5.13).

$$g_{bc} = 0.714 g_{bv} \quad (5.12)$$

$$g_{sc} = g_{sv}/1.6 \quad (5.13)$$

Following von Caemmerer (1999), the equation (5.4) represents the net assimilation or source/sink strength of carbon as a function of mesophyll and intercellular concentrations of CO₂. The mesophyll conductance to CO₂ (g_i) is difficult to estimate but can be expressed empirically as a function of leaf temperature (Bernacchi *et al.*, 2002) as

$$g_i = g_{i25} \times \frac{\exp(c - \Delta H/RT_l)}{1 + \exp((\Delta ST_l - \Delta H_d)/RT_l)} \quad (5.14)$$

where g_{i25} represents the mesophyll conductance (mol m⁻² s⁻¹) at 25°C (298 °K), c is a scaling constant (20.0), ΔH_a (49.6) and ΔH_d (437.4) represents the energy of activation and deactivation in (J mol⁻¹) and ΔS (1.4) represents the entropy factor in (J K⁻¹ mol⁻¹). The unknowns in this system of four equations (equations 5.1 to 5.4) are leaf temperature (T_l), stomatal conductance to water vapor (g_{sv}), mesophyll concentration of CO₂ (C_m), and intercellular concentration of CO₂ (C_i).

5.2.1. C₄ photosynthesis model: Source/Sink strength of CO₂

In the implementation of multilayer canopy biophysical model it is essential to describe the source/sink strength of CO₂ from the different canopy layers and the soil layer. *Spartina alterniflora*, which forms the canopy at this site, is a C₄ plant. C₄ plant types have a peculiar anatomy and they can fix CO₂ in the mesophyll cells as aspartate or malate (C₄ acids) using phospho-enol pyruvate carboxylase (PEP), which can be transported to the bundle sheath cells

and decarboxylated to supply CO₂ to rubiloso-1,5 biphosphate carboxylase oxygenase (rubisco), which is the main enzyme involved in CO₂ fixation (von Caemmerer, 2000). This CO₂ concentrating mechanism enables the rubisco in the bundle sheath cells to operate under high CO₂ partial pressures thus reducing the oxygenation reaction which inhibits photorespiration.

The C₄ photosynthetic pathway can be expressed as the minimum of rubisco-limited (A_c) and light and electron transport limited (A_j) CO₂ assimilation pathways (von Caemmerer and Furbank, 1999).

$$A_n = \min\{A_c, A_j\} \quad (5.15)$$

$$A_c = \frac{(C_s - \gamma^* O_s) V_{c \max}}{C_s + K_c (1 + O_s / K_o)} - R_d \quad (5.16)$$

$$A_j = \frac{(1 - \gamma^* O_s / C_s)(1 - x) J_t}{3(1 + 7\gamma^* O_s / (3C_s))} - R_d \quad (5.17)$$

C_s and O_s are the CO₂ and O₂ partial pressures in the bundle sheath cells (μbar), $V_{c \max}$ is the maximum rate of rubisco activity ($\mu\text{mol m}^{-2} \text{s}^{-1}$), R_d is the dark respiration ($\mu\text{mol m}^{-2} \text{s}^{-1}$), γ^* is half the value of Rubisco specificity (0.000193), J_t is the total electron transport rate ($\mu\text{mol electrons m}^{-2} \text{s}^{-1}$) and x is a partitioning factor for electron transport rate (Peisker, 1987). K_c and K_o represents the Michaelis constant of Rubisco for CO₂ and O₂, respectively. The bundle concentration of CO₂ (C_s) and O₂ (O_s) are difficult to estimate. Hence, an overall quadratic rate equation for CO₂ assimilation as a function of mesophyll CO₂ and O₂ partial pressures is adopted here for both Rubisco and electron transport limited carbon assimilation (Berry and Farquhar, 1978).

The quadratic expression for enzyme (Rubisco) limited CO₂ assimilation rate is given along with the supporting equations as

$$aA_c + bA_c + c = 0 \quad (5.18)$$

$$A_c = \frac{-b - \sqrt{b^2 - 4ac}}{2a} \quad (5.19)$$

$$a = 1 - \frac{\alpha}{0.047} \frac{K_c}{K_o} \quad (5.20)$$

$$b = - \left\{ \begin{aligned} & (V_p - R_m + g_s C_m) + (V_{c \max} - R_d) + g_s (K_c (1 + O_m / K_o)) \\ & + \left(\frac{\alpha}{0.047} (\gamma^* V_{c \max} + R_d K_c / K_o) \right) \end{aligned} \right\} \quad (5.21)$$

$$c = (V_{c \max} - R_d)(V_p - R_m + g_s C_m) - (V_{c \max} g_s \gamma^* O_m + R_d g_s K_c (1 + O_m / K_o)) \quad (5.22)$$

where V_p is the CO_2 limiting PEP carboxylation ($\mu\text{mol m}^{-2} \text{s}^{-1}$), g_s is the bundle sheath conductance to CO_2 , α is the fraction of photosystem II (the protein complex in chlorophyll cells, which capture light to split water into oxygen, protons and electrons) activity in the bundle sheath cells. The bundle sheath conductance is assumed to be a constant ($3 \text{ mmol m}^{-2} \text{s}^{-1}$), following von Caemmerer (2000) as no field measurements exists. The CO_2 limiting PEP carboxylation rate is estimated as (Berry and Farquhar, 1978)

$$V_p = \frac{C_m V_{p \max}}{C_m + K_p} \quad (5.23)$$

where $V_{p \max}$ is the maximum PEP carboxylase activity ($\mu\text{mol m}^{-2} \text{s}^{-1}$) and K_p is the Michaelis constant of PEP carboxylase for CO_2 .

The quadratic expression for light/electron transport limited CO_2 assimilation rate is given along with the supporting equations as (von Caemmerer, 2000)

$$A_j = \frac{-b - \sqrt{b^2 - 4ac}}{2a} \quad (5.24)$$

$$a = 1 - \frac{7\gamma^* \alpha}{3 \times 0.047} \quad (5.25)$$

$$b = - \left\{ \left(\frac{xJ_t}{2} - R_m + g_s C_m \right) + \left(\frac{(1-x)J_t}{3} - R_d \right) + g_s \left(\frac{7\gamma^* O_m}{3} \right) + \frac{\alpha\gamma^*}{0.047} \left(\frac{(1-x)J_t}{3} + \frac{7R_d}{3} \right) \right\} \quad (5.26)$$

$$c = \left(\left(\frac{xJ_t}{2} - R_m + g_s C_m \right) \left(\frac{(1-x)J_t}{3} - R_d \right) \right) - g_s \gamma^* O_m \left(\frac{(1-x)J_t}{3} + \frac{7R_d}{3} \right) \quad (5.27)$$

where R_m is the mesophyll concentration which is usually taken as a fraction of dark respiration (von Caemmerer, 2000) ($= 0.5 R_d$). The total electron transport rate depends upon the absorbed irradiance as follows (Evans, 1987)

$$J_t = \frac{I_2 + J_{\max} - \sqrt{(I_2 + J_{\max})^2 - 4\theta I_2 J_{\max}}}{2\theta} \quad (5.28)$$

where J_{\max} is the maximum electron transport rate ($\mu\text{mol electrons m}^{-2} \text{s}^{-1}$), θ is an empirical curvature factor, and I_2 is the light absorbed by the photosystem II ($\mu\text{mol m}^{-2} \text{s}^{-1}$). The value of θ is set to be 0.7 in the model calculations following Evans (1989).

5.2.2. Temperature and photosynthetic active radiation (PAR) controls on photosynthesis

Several physiological variables such as $V_{c\max}$, $V_{p\max}$ and J_{\max} , and the Michaelis constant for CO_2 and O_2 reactions with PEP carboxylase and rubisco depend on leaf temperature, whereas light directly controls the electron transport rate. The temperature dependence of $V_{c\max}$, $V_{p\max}$ and J_{\max} adopted here are described by an Arrhenius function with a 25 °C reference temperature (Farquhar *et al.*, 1980)

$$P(J_{\max}, V_{c\max}, V_{p\max}) = P_{25} \left[\exp\left(-\frac{E}{R}\left(\frac{1}{T} - \frac{1}{T_{25}}\right)\right) \right] \times \left[1 + \exp\frac{ST_{25} - H}{RT_{25}} \right] / \left[1 + \exp\frac{ST - H}{RT} \right] \quad (5.29)$$

where P represents the plant physiological variable such as $V_{c\max}$, $V_{p\max}$ or J_{\max} , T represents the temperature (Kelvin), E (J mol^{-1}) is the activation energy, H (J mol^{-1}) represents the deactivation energy (describes the rate of decrease of the function above an optimum temperature) and S is the entropy ($\text{J K}^{-1} \text{mol}^{-1}$). R represents the universal gas constant ($\text{J K}^{-1} \text{mol}^{-1}$) and the values of E, H and S are determined using non-linear regression analyses (refer Chapter 2). The value of $V_{c\max}$, $V_{p\max}$ and J_{\max} determined at 25 °C was obtained from the light and CO_2 response curves reported in Chapter 2. The temperature dependency of enzyme kinetic parameters K_c , K_p and K_o is described using a Q_{10} relationship (the relative increase in reaction rate over a 10 °C temperature range) following (Collatz *et al.*, 1991).

$$\text{Parameter}(T) = \text{Parameter}(25^\circ \text{C}) Q_{10}^{[(T-25)/10]} \quad (5.30)$$

The temperature T is expressed in degree Celsius and the Q_{10} parameters for K_c , K_p and K_o are adapted from Chen *et al.* (1994).

5.2.3. Shortwave radiative transfer: Multiple-layer canopy scattering model

The disposition of short wave radiation within a plant canopy determines the rate of carbon assimilation and energy exchange processes in an ecosystem. The multiple-layer canopy scattering model (**MS**) developed by Zhao and Qualls (2005) is utilized to simulate the shortwave radiation disposition within the plant canopy. The model is implemented separately for both photosynthetic active radiation (PAR) and near infra red radiation (NIR) as the leaf optical properties for these two spectral ranges are different. This model treats canopy as multiple layers and takes into account the direct and diffused component of radiation, considering the various processes such as light reflection, transmission, and scattering. The finite series of scattering between canopy elements can cause a higher fraction of incident radiation being absorbed rather than a single interception. The model assumes that after the first interception of radiation by a canopy it ceases to be directional and becomes hemispherical and the total downward hemispherical shortwave radiation flux density from a vegetation layer $i+1$ to layer i can be represented as an infinite series which converges to

$$SWd_{i+1} = \frac{SWd0_{i+1}}{1 - r_i r_{i+1} (1 - \alpha_i)(1 - \tau_i)(1 - \alpha_{i+1})(1 - \tau_{i+1})} + \frac{r_{i+1} (1 - \alpha_{i+1})(1 - \tau_{i+1}) SWu0_i}{1 - r_i r_{i+1} (1 - \alpha_i)(1 - \tau_i)(1 - \alpha_{i+1})(1 - \tau_{i+1})} \quad (5.31)$$

where α_i and τ_i denote the fraction of hemispheric radiation that gets absorbed and transmitted through a layer of canopy to the total amount of hemispheric radiation received at that layer, respectively. r and $(1-r)$ denote the fraction of hemispheric radiation that gets scattered in the opposite and same direction of the propagation of the aggregate beam prior to the scattering processes. $SWd0$ is the original downward hemispherical radiation before undergoing multiple scattering and $SWu0$ is the original upward hemispherical radiation before undergoing multiple scattering. The transmissivity of direct radiation for a canopy layer can be defined following (Campbell and Norman, 1998) as

$$\tau_b(\psi) = \exp\left(-\sqrt{\alpha} K(\psi) dLAI\right) \quad (5.32)$$

where $K(\psi)$ is the extinction coefficient for direct radiation, $dLAI$ is the leaf area index of the canopy layer and α is the leaf absorptivity. The exponential model describing the transmissivity of direct radiation within the canopy utilized here was described by (Goudriaan, 1977). The

absorptivity of the leaf (α) for PAR and NIR was assumed to be 0.80 and 0.20, respectively, following Campbell and Norman (1998). The extinction coefficient for direct radiation can be approximated for a spherical angle leaf distribution (assumed for *Spartina alterniflora*), following Campbell (1986) as

$$K(\psi) = \frac{\sqrt{x^2 + \tan^2 \psi}}{x + 1.774(x + 1.182)^{-0.733}} \quad (5.33)$$

where x is the ratio of the average projected area of canopy elements (assumed to be 0.96, a representative value observed for wheat, which has a similar morphology as *Spartina alterniflora*) (Campbell and van Evert, 1994).

The scattering coefficient for hemispheric and directional shortwave radiation can be represented as (Zhao and Qualls, 2005)

$$r = \frac{2}{3} \left(\frac{\beta_L}{\beta_L + \tau_L} \right) + \frac{1}{3} \left(\frac{\tau_L}{\beta_L + \tau_L} \right) \quad (5.34)$$

$$r(\psi) = 0.5 - 0.3334 \left(\frac{\beta_L - \tau_L}{\beta_L + \tau_L} \right) \cos(\psi) \quad (5.35)$$

where β_L and τ_L represent the reflection and transmission coefficients of leaves which were taken as 0.11 and 0.07 (typical values for grass leaves-from <http://www.cgd.ucar.edu/tss/clm/pfts/pft-physiology.htm>) for PAR and 0.50 and 0.30 for NIR radiation, respectively. The absorption coefficient of hemispheric radiation (α) for a canopy layer can be expressed as

$$\alpha = 1 - (\beta + \tau) \quad (5.36)$$

where β and τ represent the reflection and transmission coefficient for hemispheric radiation whose values are taken as 0.09 and 0.06 for PAR and 0.51 and 0.34 for NIR following (Ross, 1975). The total upward hemispheric shortwave radiation flux density for vegetation layer i to $i+1$ is given as

$$SWu_i = \frac{SWu_0_i}{1 - r_i r_{i+1} (1 - \alpha_i)(1 - \tau_i)(1 - \alpha_{i+1})(1 - \tau_{i+1})} + \frac{r_i (1 - \alpha_i)(1 - \tau_i) SWd_0_{i+1}}{1 - r_i r_{i+1} (1 - \alpha_i)(1 - \tau_i)(1 - \alpha_{i+1})(1 - \tau_{i+1})} \quad (5.37)$$

The original downward hemispherical shortwave radiation flux density from vegetation layer i to layer $i-1$ before taking the multiple scattering is represented as

$$SWd0_i = \tau_i SWd_{i+1} + (1 - \tau_i)(1 - \alpha_i)(1 - r_i)SWd_{i+1} + [1 - \tau(\psi)_i](1 - \alpha_i)[1 - r(\psi)_i]S_i \quad (5.38)$$

The original upward hemispherical shortwave radiation from layer i+1 to layer i+2 before taking multiple scattering is given as

$$SWu0_{i+1} = \tau_{i+1}SWu_{i+1} + (1 - \tau_{i+1})(1 - \alpha_{i+1})(1 - r_{i+1})SWu_i + r(\psi)_{i+1}[1 - \tau(\psi)_{i+1}](1 - \alpha_{i+1})S_{i+1} \quad (5.39)$$

where S_i represents the direct shortwave radiation reaching the i^{th} layer of the canopy, and $r(\Psi)$ and $\tau(\Psi)$ denote the reflectivity and transmissivity coefficients for direct radiation.

The right hand side of equations (5.38) and (5.39) has three terms, the first terms represents the upward and downward hemispherical shortwave radiation passing through layers i and layer i+1 without being intercepted. The second term in both equations (5.38) and (5.39) represents the downward and upward hemispherical shortwave radiation flux passing through the canopy layers i and i+1 by means of leaf scattering. The third term represents the direct shortwave radiation that is intercepted and scattered down by layer i and scattered up by layer i+1. Substituting back the value of $SWd0_i$ and $SWu0_{i+1}$ in equations (5.36) and (5.37), respectively, and rearranging the terms, a set of equations can be obtained for the different layers of the canopy. The plant canopy is divided into m layers with the layer just above the soil surface taken as layer 1 and the topmost layer as layer m. The soil surface is designated as a layer with 0 transmissivity and a reflectivity coefficient of 1. The total upward directional and hemispherical radiation coming from the ground surface depends upon the albedo of the ground surface. The model assumes an imaginary atmospheric layer above the plant canopy, which transmits all the radiation through it and has a reflectivity coefficient of zero. The directional and hemispheric radiation reaching this layer is transmitted upward or downward through it without being absorbed and the radiation coming down from this layer is the diffuse radiation flux density from the sky. Together with these boundary conditions, the total directional and hemispheric radiation before taking the multiple scattering can be solved as a system of equations of the form

$$A \times SW = C \quad (5.40)$$

where A is a $2m+2$ by $2m+2$ tri-diagonal matrix. The non-zero elements of this tri-diagonal matrix can be represented as

$$\begin{aligned}
a_{1,1} &= 1 \\
a_{2i,2i-1} &= -[\tau_i + (1 - \tau_i)(1 - \alpha_i)(1 - r_i)] \quad (i = 1, 2, 3, \dots, m) \\
a_{2i,2} &= -r_{i-1}[\tau_i + (1 - \tau_i)(1 - \alpha_i)(1 - r_i)](1 - \alpha_{i-1})(1 - \tau_{i-1}) \quad (i = 1, 2, 3, \dots, m) \\
a_{2i,2i+1} &= [1 - r_{i-1}r_i(1 - \alpha_{i-1})(1 - \tau_{i-1})(1 - \alpha_i)(1 - \tau_i)] \quad (i = 1, 2, 3, \dots, m) \\
a_{2i+1,2i} &= [1 - r_i r_{i+1}(1 - \alpha_i)(1 - \tau_i)(1 - \alpha_{i+1})(1 - \tau_{i+1})] \quad (i = 1, 2, 3, \dots, m) \\
a_{2i+1,2i+1} &= -r_{i+1}[\tau_i + (1 - \tau_i)(1 - \alpha_i)(1 - r_i)(1 - \alpha_{i+1})(1 - \tau_{i+1})] \quad (i = 1, 2, 3, \dots, m) \\
a_{2i+1,2i+2} &= -[\tau_i + (1 - \tau_i)(1 - \alpha_i)(1 - r_i)] \quad (i = 1, 2, 3, \dots, m) \\
a_{2m+2,2m+2} &= 1
\end{aligned} \tag{5.41}$$

$$SW = \begin{bmatrix} SW_u 0_0 \\ SWd0_1 \\ SWu0_1 \\ \cdot \\ \cdot \\ SWd0_i \\ SWu0_i \\ \cdot \\ \cdot \\ SWd0_m \\ SWu0_m \\ SWd0_{m+1} \end{bmatrix} \tag{5.42}$$

$$C = \begin{bmatrix} alb_0 S_0 \\ [1 - r_0 r_1 (1 - \alpha_0)(1 - \tau_0)(1 - \alpha_1)(1 - \tau_1)] r(\psi)_1 [1 - \tau(\psi)_1] (1 - \alpha_1) S_1 \\ 1 - r_1 r_2 (1 - \alpha_1)(1 - \tau_1)(1 - \alpha_2)(1 - \tau_2) [1 - \tau(\psi)_1] (1 - \alpha_1) [1 - r(\psi)_1] S_1 \\ \cdot \\ \cdot \\ [1 - r_{i-1} r_i (1 - \alpha_{i-1})(1 - \tau_{i-1})(1 - \alpha_i)(1 - \tau_i)] r(\psi)_i [1 - \tau(\psi)_i] (1 - \alpha_i) S_i \\ 1 - r_i r_{i+1} (1 - \alpha_i)(1 - \tau_i)(1 - \alpha_{i+1})(1 - \tau_{i+1}) [1 - \tau(\psi)_i] (1 - \alpha_i) [1 - r(\psi)_i] S_i \\ \cdot \\ \cdot \\ [1 - r_{m-1} r_m (1 - \alpha_{m-1})(1 - \tau_{m-1})(1 - \alpha_m)(1 - \tau_m)] r(\psi)_m [1 - \tau(\psi)_m] (1 - \alpha_m) S_m \\ 1 - r_m r_{m+1} (1 - \alpha_m)(1 - \tau_m)(1 - \alpha_{m+1})(1 - \tau_{m+1}) [1 - \tau(\psi)_m] (1 - \alpha_m) [1 - r(\psi)_m] S_m \\ SW_{sky} \end{bmatrix} \tag{5.43}$$

where, alb_0 represents the albedo of the soil surface.

The system of equations at the soil surface can be expressed as a function of soil optical properties and the radiation reaching the ground surface as

$$\tau_0 = 0 \quad (5.44)$$

$$SWd0_0 = alb_0 S_0 \quad (5.45)$$

$$\alpha_0 = 1 - alb_0 \quad (5.46)$$

$$r_0 = 1 \quad (5.47)$$

where alb_0 is the albedo of the soil surface and S_0 is the direct shortwave radiation reaching the soil surface. The system of equation at the top layer, which is an atmospheric layer transparent to both directional and hemispheric radiation, can be described in terms shortwave radiation received from the sky (SW_{sky}) and atmospheric optical properties as

$$\tau_{m+1} = 0 \quad (5.48)$$

$$r_{m+1} = 0 \quad (5.49)$$

$$SWd_{m+1} = SWd0_{m+1} = SW_{sky} \quad (5.50)$$

The solution for this system of equations can be determined using a Gauss-Jordan method which was implemented in MATLAB. Once the SWu_0 and SWd_0 terms are solved for the different canopy layers they can be put back into equations (5.31) and (5.37) to get the total hemispherical and directional radiation reaching each canopy layer after taking multiple scattering.

5.2.4. Long wave radiative transfer model: LRTM

Long wave radiative transfer processes govern the leaf temperature in a plant canopy and thus determine the rate of various biochemical reactions involved in photosynthesis. The long wave radiative transfer in plant canopies have been described in terms of the longwave radiative transfer equations (Ross, 1981). Since the long wave emissions from the leaves depend upon the leaf temperature, which can be an unknown variable in canopy biophysical models, iterative methods have to be employed to solve the long wave radiative transfer. Gu (1998b) proposed an alternative method, where the solution of all the radiative transfer equation are computed once as a long wave radiative transfer matrix (LRTM). This avoids computational burden as the net long

wave absorbed by each layer from the soil surface can be estimated from the LRTM and the profile of leaf temperature and long wave radiation at the top of the canopy as

$$\begin{pmatrix} \Delta \mathcal{N}_1 \\ \Delta \mathcal{N}_2 \\ \vdots \\ \Delta \mathcal{N}_{m+1} \\ \Delta \mathcal{N}_{m+2} \end{pmatrix} = LRTM \begin{pmatrix} \sigma T_s^4 \\ \sigma T_{l2}^4 \\ \vdots \\ \sigma T_{l(m+1)}^4 \\ \mathfrak{R}_a \end{pmatrix} \quad (5.51)$$

where $\Delta \mathcal{N}_1$, $\Delta \mathcal{N}_{m+1}$, and $\Delta \mathcal{N}_{m+2}$ describe the net long wave radiation absorbed by the soil, top canopy layer and the atmosphere respectively. σ is the Stephan-Boltzman constant ($5.67 \times 10^{-8} \text{ W m}^{-2} \text{ K}^{-4}$), and $T_s \dots T_{l(m+1)}$, represent the leaf temperature (K) from the soil surface to the top canopy layer, \mathfrak{R}_a represents downwelling longwave irradiance (W m^{-2}). The LRTM represents the soil as the first layer (m), with m+1 canopy layers and a top atmospheric layer (m+2). Thus, the elements of the LRTM form a $m+2 \times m+2$ matrix which can be represented as

$$LRTM = \begin{pmatrix} \alpha_{11} & \alpha_{12} & \cdots & \alpha_{1(m+1)} & \alpha_{1(m+2)} \\ \alpha_{21} & \alpha_{22} & \cdots & \alpha_{2(m+1)} & \alpha_{2(m+2)} \\ \vdots & \vdots & \cdots & \vdots & \vdots \\ \alpha_{(m+1)1} & \alpha_{(m+1)2} & \cdots & \alpha_{(m+1)(m+1)} & \alpha_{(m+1)(m+2)} \\ \alpha_{(m+2)1} & \alpha_{(m+2)2} & \cdots & \alpha_{(m+2)(m+1)} & \alpha_{(m+2)(m+2)} \end{pmatrix} \quad (5.52)$$

The elements of the LRTM are described following Gu (1998b) as

$$\left\{ \begin{array}{l} -1 \\ \mathfrak{F}(\ell_t - \ell_{j-1}) - \mathfrak{F}(\ell_t - \ell_j) \\ \mathfrak{F}(\ell_t) \\ \mathfrak{F}(\ell_j - \ell_{i-1}) - \mathfrak{F}(\ell_{j-1} - \ell_{i-1}) - \mathfrak{F}(\ell_j - \ell_i) + \mathfrak{F}(\ell_{j-1} - \ell_i) \\ 2\mathfrak{F}(\Delta \ell_i) - 2 \\ \mathfrak{F}(\ell_i - \ell_{j-1}) - \mathfrak{F}(\ell_i - \ell_j) - \mathfrak{F}(\ell_{i-1} - \ell_{j-1}) + \mathfrak{F}(\ell_{i-1} - \ell_j) \\ \mathfrak{F}(\ell_t) \\ \mathfrak{F}(\ell_j) - \mathfrak{F}(\ell_{j-1}) \\ -1 \end{array} \right. \left. \begin{array}{l} i = j = 1 \\ i = 1, j = 2, 3, \dots, m+1 \\ i = 1, j = m+2 \\ i = 2, 3, \dots, m+1, j = 2, 3, \dots, i-1 \\ i = 2, 3, \dots, m+1, j = i \\ i = 2, 3, \dots, m+1, j = i+1, \dots, m+1 \\ i = m+2, j = 1 \\ i = m+2, j = 2, 3, \dots, m+1 \\ i = m+2, j = m+2 \end{array} \right. \quad (5.53)$$

where $\mathfrak{I}(\ell)$ is the 'canopy longwave integral function' and ℓ_i represents the cumulative leaf area from the top of the canopy to the layer i . Detailed description of the implementation of the LRTM methodology along with the derivation of model parameters can be found in Gu (1998b) and (Barr, 2005).

5.2.5. Scalar dispersion in plant canopies- Localized Near Field theory

In the implementation of the canopy biophysical model, the scalar concentration values at a reference level are used to develop initial gas (i.e. water vapor or carbon dioxide) concentration profiles to determine the source/sink strength distribution within the plant canopy. The concentration profile of a scalar inside the plant canopy develops as a result of the turbulent exchange processes which controls the exchange of mass and energy from the leaf surface. In a Lagrangian frame work, the concentration of a scalar at a vertical level (z) at a time (t) under steady state conditions with no advection can be represented as (Baldochhi, 1992)

$$C(z, t) = \int S(z_0, t_0) P(z, t | z_0, t_0) dt_0 dz_0 \quad (5.54)$$

where $S(z_0, t_0)$ is the source/sink strength of a scalar from a unit volume of phyto-elements and $P(z, t | z_0, t_0)$ is the transition probability density function that defines the probability that an air parcel released at a time t_0 from a location z_0 , being observed at a position z at a time t . Several methodologies have been proposed to estimate the transition probability density function. Baldochchi (1992) utilized a Lagrangian random walk model, where a large number of marked particles are released from different layers of a canopy, to determine what proportion of fluid particles reside at a particular height after traveling for a specific time span. This methodology requires extensive computational time as the random nature of fluid particles in air have to be simulated a large number of times and hence may not be suitable for simulations on longer time scales. Other scientists (Raupach, 1989a; Raupach, 1989b) developed an analytical expression for the transition probability density function by decomposing it into a near-field and far-field components. The resulting near-field concentration is produced by persistence, whereas the far-field concentration is associated with atmospheric diffusion. The near-field concentration profile ($C_n(z)$) can be described in terms of the profiles of standard deviation of vertical velocity $\sigma_w(z)$ and Lagrangian time scale ($T_L(z)$) as a function of the source strength (S_{zs}) at source height z_s as

$$C_n(z) = \int_0^\infty \frac{S(z_s)}{\sigma_w(z_s)} \left[k_n \left\{ \frac{z - z_s}{\sigma_w(z_s) T_L(z_s)} \right\} + k_n \left\{ \frac{z + z_s}{\sigma_w(z_s) T_L(z_s)} \right\} \right] dz_s \quad (5.55)$$

where k_n is the near-field kernel function which can be approximated analytically (Raupach, 1989a). The far-field concentration profile $C_f(z)$ can be derived based on the gradient diffusion approach as

$$C_f(z) = C(z_R) - C_n(z_R) + \int_z^{z_R} \frac{F(z)}{K_f(z)} dz \quad (5.56)$$

$$F(z) = -K_f(z) \frac{dC_f(z)}{dz} \quad (5.57)$$

where $K_f(z)$ is the far-field atmospheric diffusivity defined as $K_f(z) = \sigma_w^2(z) T_L(z)$, $C(z_R)$ is the concentration of a scalar at a reference level, $C_n(z_R)$ is the near field concentration at a reference level and $F(z)$ is the flux of the scalar at the measurement point. The source/sink strength can be related to the concentration difference between a point within the canopy ($C_{a,i}$) to the concentration at a reference layer ($C_{a,ref}$) following Raupach (1989a) as

$$C_{a,i} - C_{a,ref} = \sum_{j=1}^n S_j \Delta z D_{ij} \quad (5.58)$$

S_j denotes the source/sink strength, Δz denotes the thickness of the source layer and D_{ij} is the dispersion matrix expressed in units of s^{-1} . The dispersion matrix represents the transitional probability density function which relates the source strength to the concentration profile and is expressed as

$$D_{ij} = \frac{C_{a,i} - C_{a,ref}}{S_j \Delta z_j} \quad (5.59)$$

Warland and Thurtell (2000) defined a mixing matrix (s^{-2}) which describes the dispersion from the near to far field continuously, which was found to have comparable performance with the LNF theory (Qiu and Warland, 2006; Wohlfahrt, 2004). In this chapter, the localized near field theory (Raupach, 1989a) is utilized to infer concentration profiles of scalars (e.g., CO_2 , temperature, and vapor pressure) within and above the plant canopy. Additional details about the methodology adopted for estimating the concentration profile from known source strength can be found in Gu (1998b).

5.2.6. Wind and turbulent statistics within and above plant canopies

It is essential to specify the profiles of wind velocity and turbulent statistics such as standard deviation of vertical velocity (σ_w) and Lagrangian time scale (T_L) for estimating several model variables such as boundary layer conductances for heat, water vapor and CO₂ and for describing the dispersion matrix to relate the source strength to concentration profile. The wind velocity profile above the canopy is modeled as a logarithmic function

$$u(z) = \frac{u_*}{k} \left[\ln \left(\frac{z-d}{z_0} \right) - \psi_m \left(\frac{z-d}{L}, \frac{z_0}{L} \right) \right] \quad (5.60)$$

where $u(z)$ is the wind velocity at height z , z_0 is roughness length for momentum ($0.1h$, h is the height of the canopy) and d is the zero plane displacement (assumed to be $0.63h$), The value ψ_m denotes the diabatic functions, which depends on L , the Monin-Obukhov length. Since sensible and latent heat flux values are essential to calculate the value of L , they are assumed to be 30 and 50 percent of the net radiation. The description of the diabatic functions can be found in Businger *et al.* (1971). The profiles of σ_w and T_L were obtained following the work of Leuning *et al.* (2000) based on observations over a rice canopy. Since *Spartina alterniflora* has a similar morphology as rice, these relationships were adopted in the present model. The stability corrections for the profiles of σ_w and T_L proposed by Leuning *et al.* (2000) were also incorporated in the turbulence module. The profile of standard deviation of vertical velocity under neutral stability conditions can be described as

$$\frac{\sigma_w}{u_*} = \begin{cases} c_1 \exp(c_2 \times z/h) & z < 0.8h \\ \frac{(az/h + b) - \sqrt{(az/h + b)^2 - 4\theta abz/h}}{2\theta} & z \geq 0.8h \end{cases} \quad (5.61)$$

where the constants are $a=0.85$, $b=1.25$, $c_1=0.2$, $c_2=1.5$ and θ is 0.98, z is the height and h is the height of the canopy. The profile of normalized T_L can be defined as

$$\frac{T_L u_*}{h} = \begin{cases} \frac{(4az/h + b_1) - \sqrt{(4az/h + b_1)^2 - 16\theta ab_1 z/h}}{2\theta} & z < 0.25h \\ \frac{(a_2(z/h - 0.8) + b_2) + \sqrt{(a_2(z/h - 0.8) + b_2)^2 - 4\theta a_2 b_2 (z/h - 0.8)}}{2\theta} & z \geq 0.25h \end{cases} \quad (5.62)$$

where the constants are $a=0.85$, $a_2=0.256$, $b_1=0.41$, $b_2=0.40$ and $\theta=0.98$; The Monin-Obukhov similarity functions appropriate for the inertial sub layer were used to correct for atmospheric stability in the profiles of σ_w and T_L following

$$\frac{\sigma_w(\zeta)}{\sigma_w(0)} = \frac{\phi_w(\zeta)}{1.25} \quad (5.63)$$

$$\frac{\tau_L(\zeta)}{\tau_L(0)} = \frac{1}{\phi_h(\zeta)} \frac{1.25^2}{\phi_w^2(\zeta)} \quad (5.64)$$

where ζ is the stability parameter defined as a function of L (Monin-Obukhov length) and $z_{ref}=2.3h$, is the height of transition from the roughness sub layer to the inertial layer.

$$\zeta = \begin{cases} h/L & z < z_{ref} \\ (z-d)/L & z \geq z_{ref} \end{cases}$$

The values $\Phi_w(\zeta)$ and $\Phi_h(\zeta)$ denote the stability functions for water vapor and heat, respectively which are given by (Kaimal and Finnigan, 1994).

5.2.7. Model Implementation

The model is solved as a system of nonlinear-equations within the different layers of the canopy. The canopy is divided into 6 layers and the set of four equations (5.1 to 5.4) are solved in each canopy layer, thus producing a system of 24 non-linear equations. The model is initialized with guesses for the unknowns namely leaf temperature (T_l), stomatal conductance to water vapor (g_{sv}), intercellular CO_2 mixing ration (C_i), and mesophyll CO_2 mixing ratio (C_m). The initial air temperature, humidity and CO_2 profiles within the canopy are assumed from measured values at fixed levels and the system of equations are solved for the unknowns. Once the unknown values are solved, they are used to derive the source strength of heat, moisture and CO_2 , which can then be used to predict the profiles of air temperature, water vapor and CO_2 utilizing the LNF theory. This procedure is repeated until the profiles of scalars converge. A schematic representation of the model implementation is provided below (Figure 5.1).

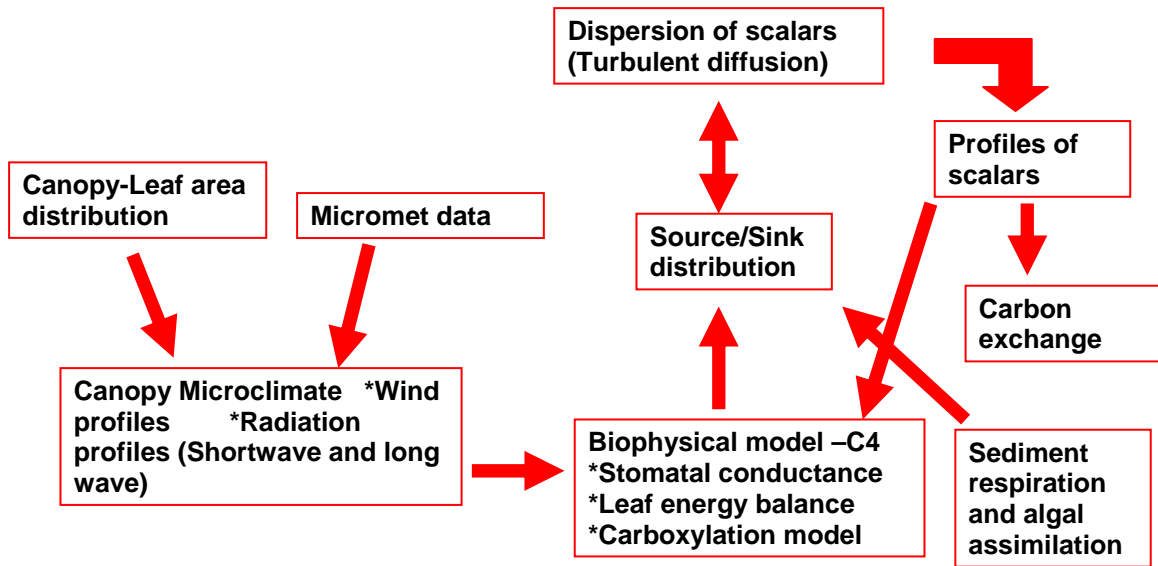


Figure 5.1 Schematic representation of the canopy biophysical model.

Once the profiles of scalars are resolved for a particular half hour, the fluxes of CO₂ and energy can be obtained by summing up the source/sink strength from the different canopy layers

following

$$H = H_0 + \sum_{i=1}^m S_{hi} \Delta \ell_i \quad (5.65)$$

$$LE = LE_0 + \sum_{i=1}^m \lambda S_{wi} \Delta \ell_i \quad (5.66)$$

$$F_{CO_2} = \sum_{i=1}^m A_{ni} \Delta \ell_i - R_{soil} \quad (5.67)$$

5.3. Results and Discussion

5.3.1. Model representation of canopy processes

In order to test the accuracy in the representation of ecosystem-atmosphere exchange processes represented in the canopy biophysical model, model subroutine outputs were compared for two days which represents clear (day of year 187) and cloudy sky conditions (day of year 202) during the peak of the growing season. The photosynthetic active radiation (PAR) and the near infrared radiation absorbed by the different layer of the canopy as simulated by the multiple scattering radiative transfer model are presented in Figure 5.2 and 5.3. The leaves, which have a higher absorptivity for PAR, absorb much of the incoming PAR in the top layers of the canopy where

there is more leaf area. The NIR being more transmissive penetrates deeper into the canopy. In the case of the sunny day (DOY 187) a uniform absorption pattern is observed within the canopy for PAR throughout the day, whereas during the cloudy day the radiation absorption pattern is not uniform. The absorbed radiation in the different layers is higher for the cloudy sky conditions, but most of it is absorbed by the top layers of the canopy. The radiative transfer model does not produce reliable outputs under very high solar elevation angles and hence, light interception during early morning and late evening hours are not properly accounted in the model. The low solar zenith angles produce unreliable estimates of canopy extinction coefficients which can produce erroneous values of radiation disposition within the plant canopies. This can lead to underestimation of fluxes during these periods and results should be interpreted with caution.

The temperature profiles are generated inside the biophysical model from the source/sink strength of heat using the LNF theory. The temperature profiles for DOY 187 and 202 are provided in Figure 5.4. The canopy becomes a source of heat as indicated by the increased temperatures observed in the canopy layers of the model shortly after 10:00 hours for both clear and cloudy sky conditions. The cloudy sky conditions produced lower air temperatures which can be observed in the modeled temperature profiles compared to clear sky conditions (Figure 5.4). The higher leaf temperatures are simulated by the model to occur inside the plant canopy at a level corresponding with the largest leaf area index.

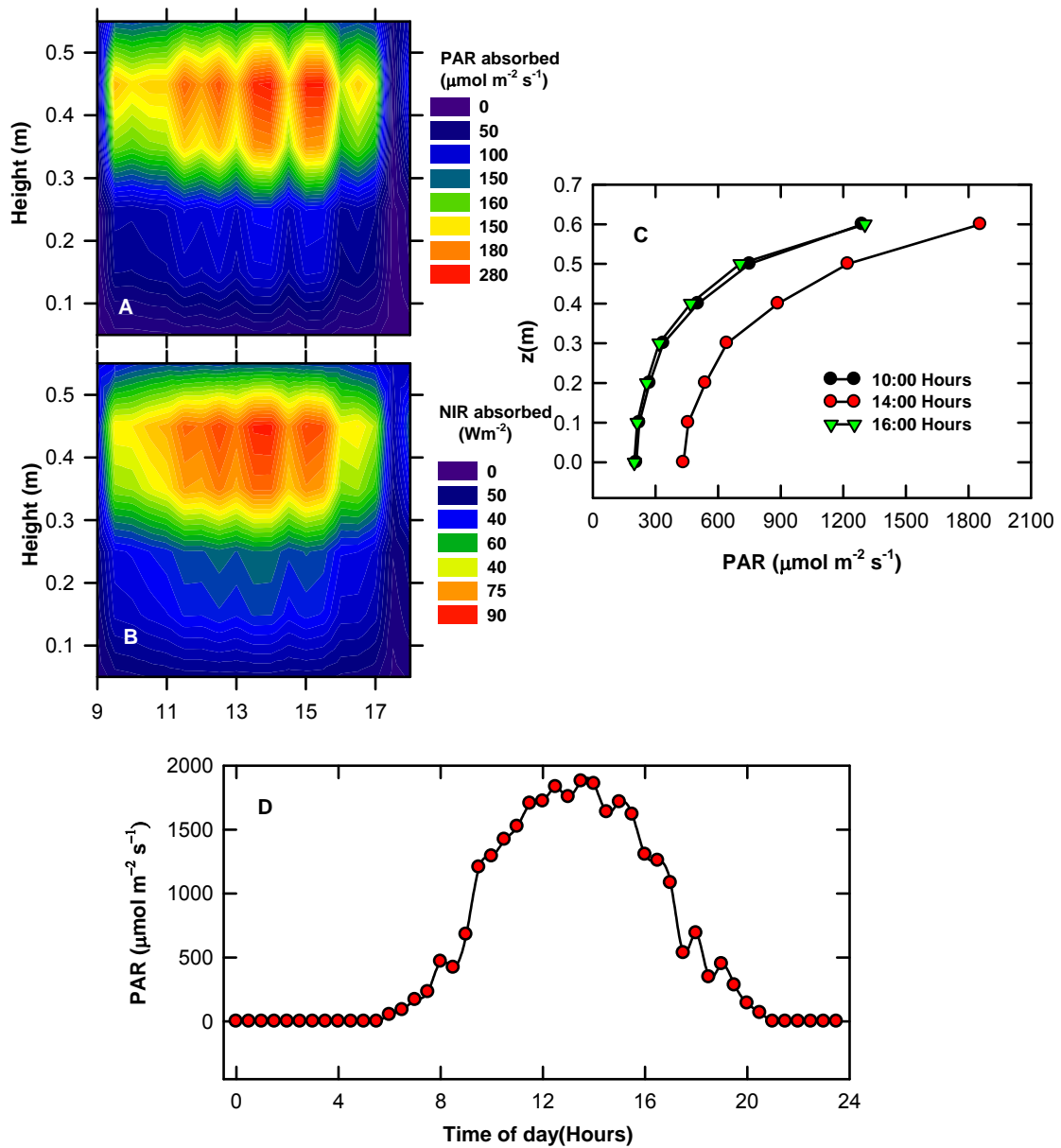


Figure 5.2. (A) PAR and (B) NIR absorption within the different layers of the canopy simulated by the multiple scattering model for clear sky conditions (DOY 187). The disposition of PAR within the canopy (C) is also provided along with the observed diurnal PAR values measured above the canopy (D).

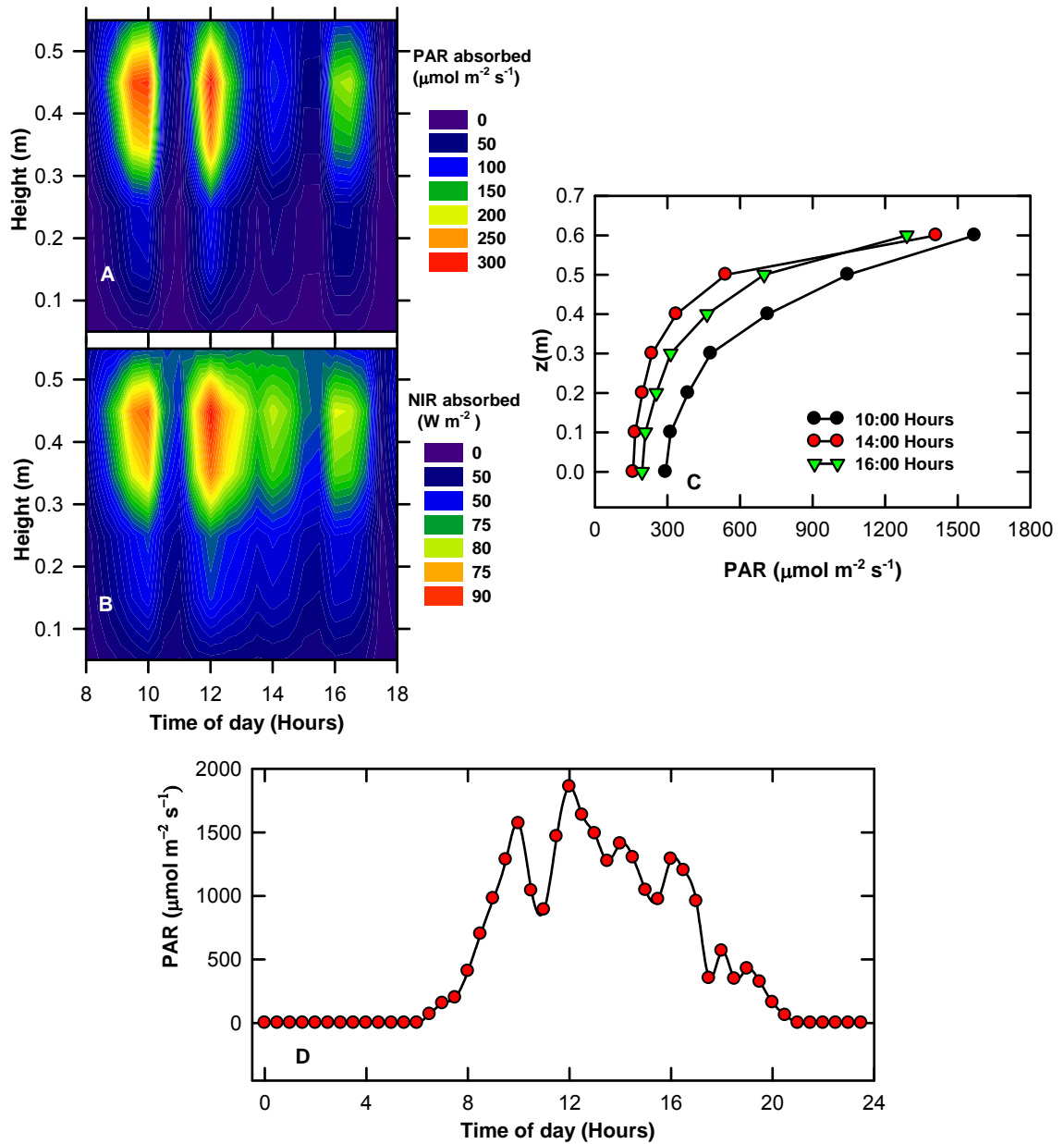


Figure 5.3. (A) PAR and (B) NIR absorption within the different layers of the canopy simulated by the multiple scattering model for cloudy sky conditions (DOY 202). The disposition of PAR within the canopy (C) is also provided along with the observed diurnal PAR values above the canopy (D).

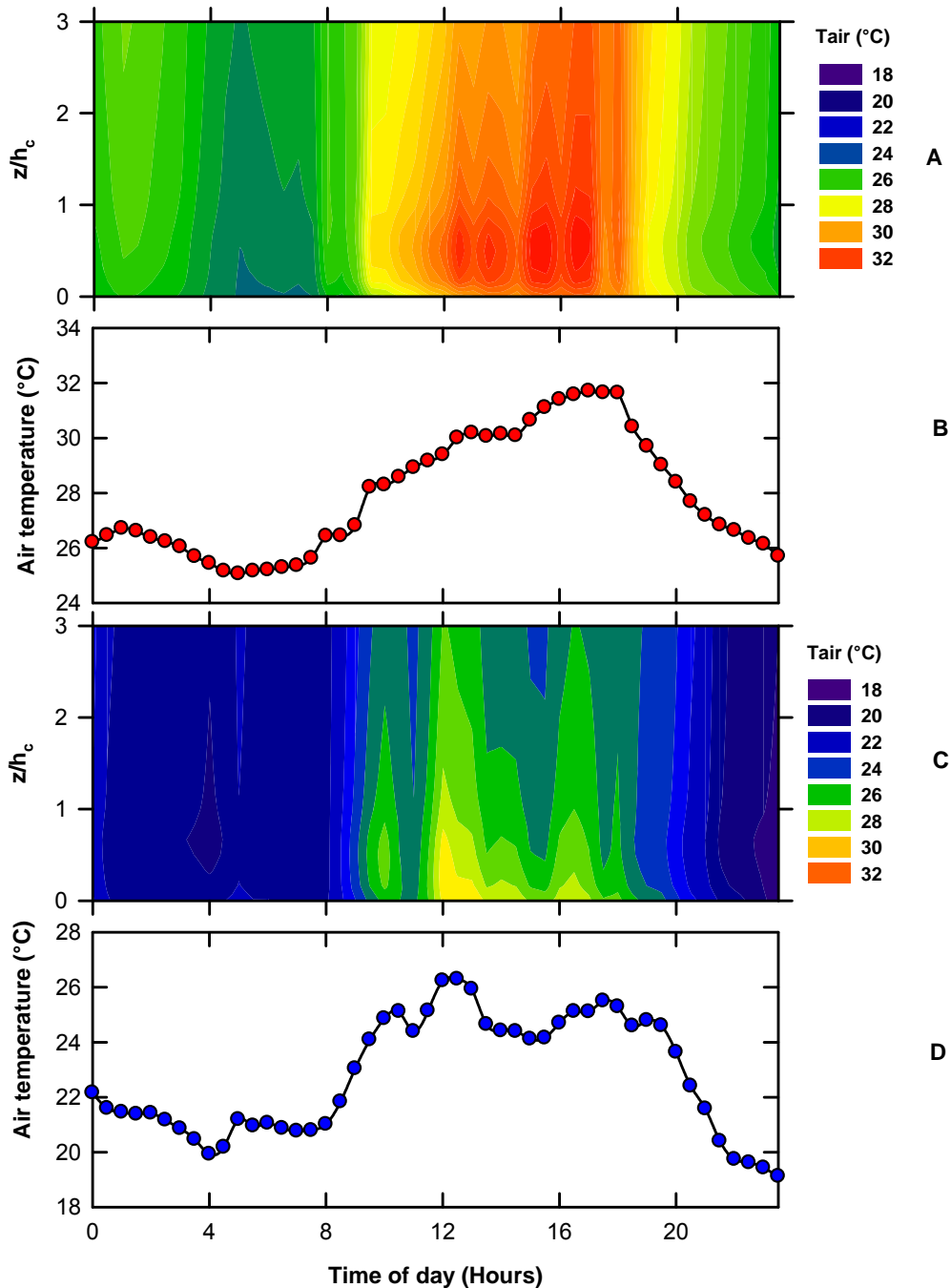


Figure 5.4. Modeled air temperature profiles between clear (DOY 187) and cloudy days (DOY 202). Modeled air temperature profiles for clear day (A), observed diurnal temperature variation above the canopy for clear day (B), modeled air temperature profiles for cloudy day (C) and observed diurnal temperature variation above canopy for clear day (D).

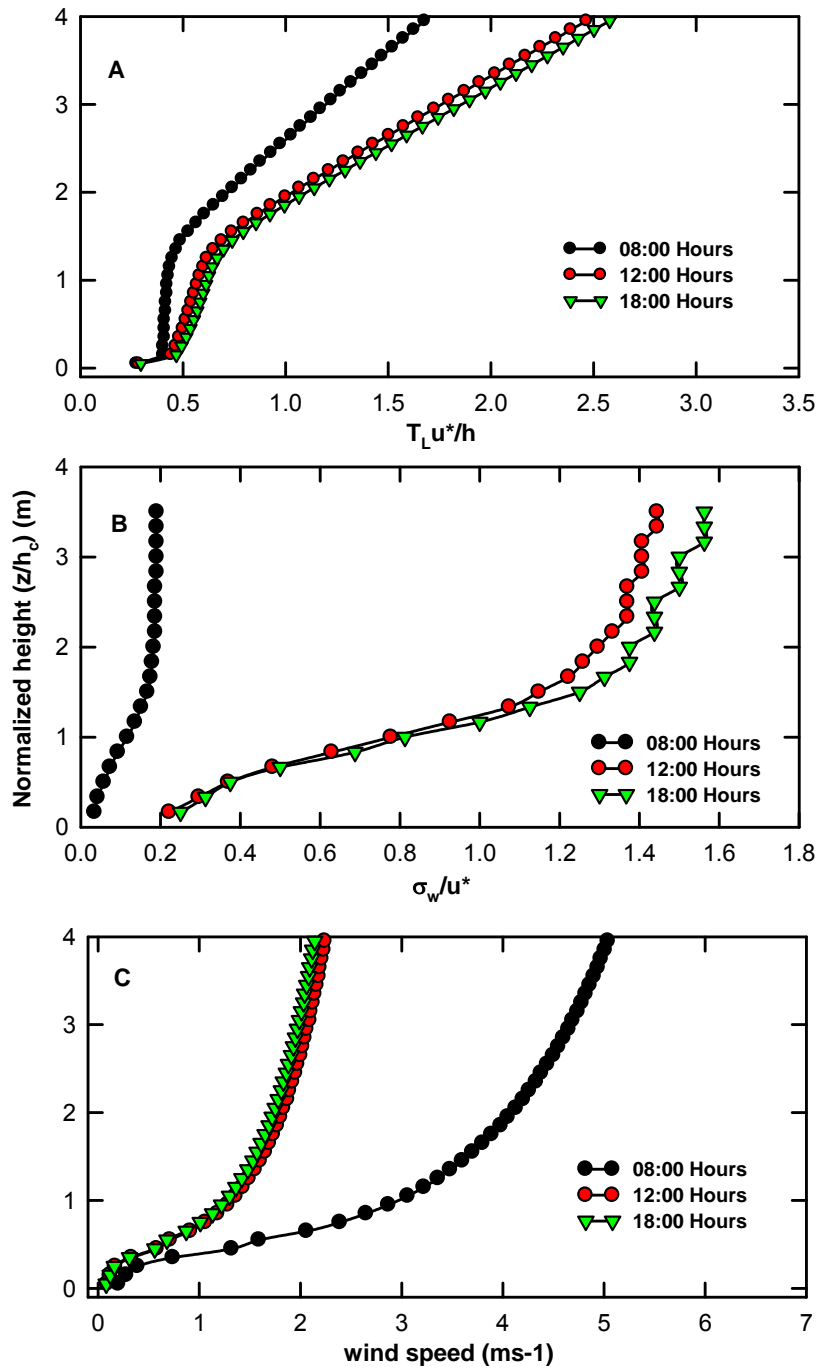


Figure 5.5. Normalized profiles of (A) the Lagrangian time scale ($T_L u^*/h$) as a function of normalized height, and (B) the standard deviation of vertical velocity (σ_w/u^*) calculated following Leuning *et al* (2000). The wind velocity profiles are also provided for the same time periods (C)

The variation in the normalized profiles of standard deviation of vertical velocity and Lagrangian time scale for DOY 187 is presented in Figure 5.5. The profiles of the turbulent statistics show a smooth transition from within to above the canopy for all time periods. High sustained wind velocities were observed during the early morning period leading to decreased Lagrangian time scales (time scales in which the eddies are correlated with each other) and decreased σ_w values. To further verify whether the model can estimate scalar profiles to determine CO_2 fluxes, the profiles of CO_2 within and above the plant canopy for DOY 187 for three time periods are presented in Figure 5.6.

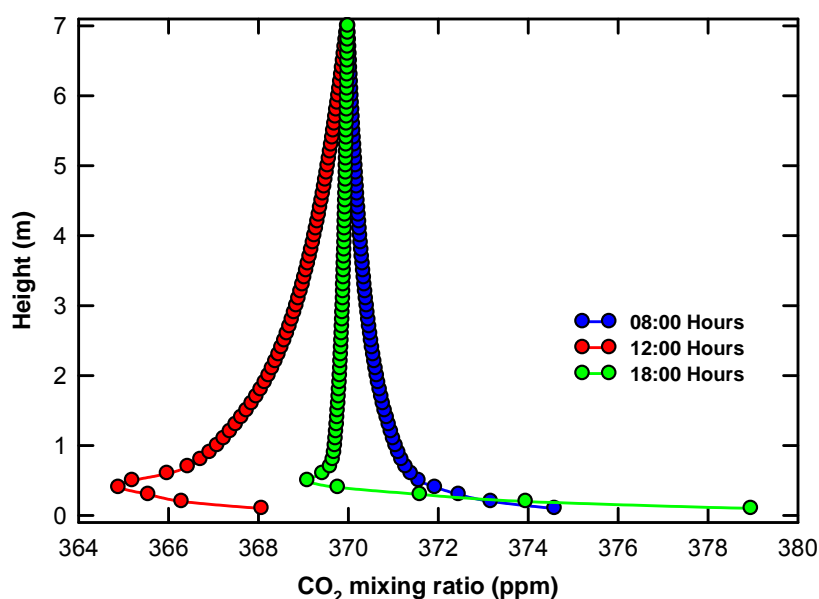


Figure 5.6. Profiles of CO_2 mixing ratios modeled above and below the plant canopy as generated from the output obtained from the LNF module of the biophysical model for DOY 187. The profiles provided are for 08:00, 12:00 and 18:00 hours.

The noon time (12:00 hours) CO_2 mixing ratio profiles indicate a lower mixing ratios of CO_2 within the canopy indicating a net flow from the top to the canopy. This trend is reversed during early morning and late evening hours, when respiration activity produces higher CO_2 mixing ratios at the base of the canopy. The biophysical model thus could capture the CO_2 drawdown happening as a result of canopy photosynthesis, during peak assimilation period producing lower CO_2 mixing ratios inside the canopy.

5.3.2. Model outputs –clear and cloudy sky comparisons

A comparison between the estimated and modeled fluxes of CO₂, latent heat and sensible heat flux for a clear (DOY 187) and cloudy (DOY 202) are provided in Figure 5.7 and 5.8, respectively. In the case of the clear sky conditions the model realistically describes the trends in fluxes of scalars. The night time modeled sensible heat fluxes are lower than the observed values, which can be attributed to errors in determining the net long wave radiation emitted from the surface. The modeled latent heat fluxes are slightly lower than the estimated values, with a large underestimation during the late afternoon hours. A corresponding overestimation of sensible heat fluxes is also observed during this period. The advection of moisture from the ocean during the late afternoon hours leads to enhancement and a greater conversion of available energy for latent heating, thus increasing latent heat fluxes and decreasing sensible heat. Since the model assumes complete closure of energy balance, the advective effects are not considered in the model, leading to underestimation of latent heating and over estimation of sensible heat during periods of advection. The sensible and latent heat fluxes during the early morning and late evening hours are underestimated as the short wave radiative transfer modules are initialized only at positive solar elevation angles.

A decrease in assimilation rate was observed in the estimated flux values compared to the modeled values during the late afternoon hours as the decreased stomatal conductance occurring in the late afternoon period is not accurately represented in the model subroutines. In the case of a cloudy sky conditions (DOY 202), the model underestimated the energy and carbon fluxes compared to the estimated values. The latent heat fluxes were the most underestimated with the modeled and estimated fluxes differing by about 180 W m⁻² during late afternoon hours (Figure 5.8). The underestimation of NEE can be attributed to the inadequacy of the plant physiology subroutines to account for the increased light use efficiency during diffuse sky radiation conditions (Gu *et al.*, 2002) which is prevalent under cloudy skies. Since assimilation and transpiration are related through stomatal conductance, a corresponding decrease in latent heat fluxes is also observed.

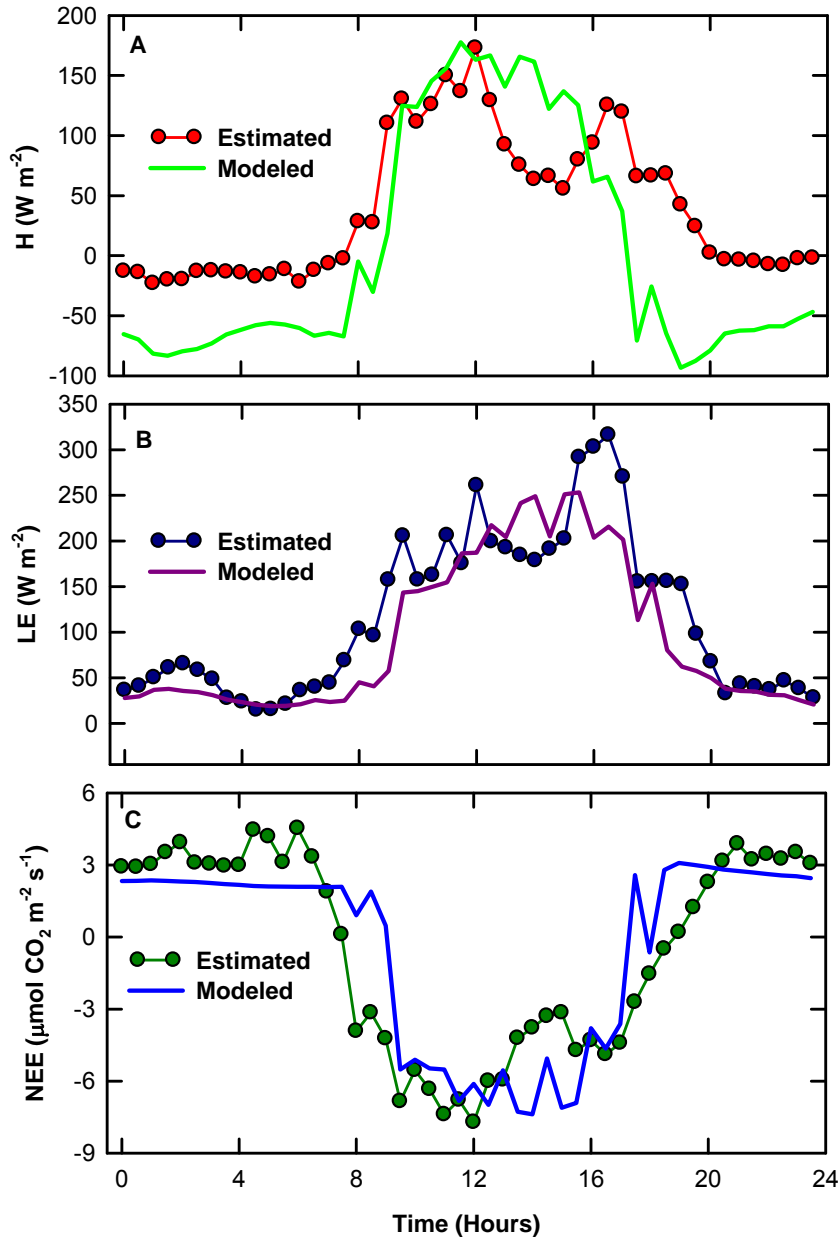


Figure 5.7. Comparison between estimated and modeled sensible (A) latent heat (B) and CO_2 (C) fluxes for clear sky conditions (DOY 187).

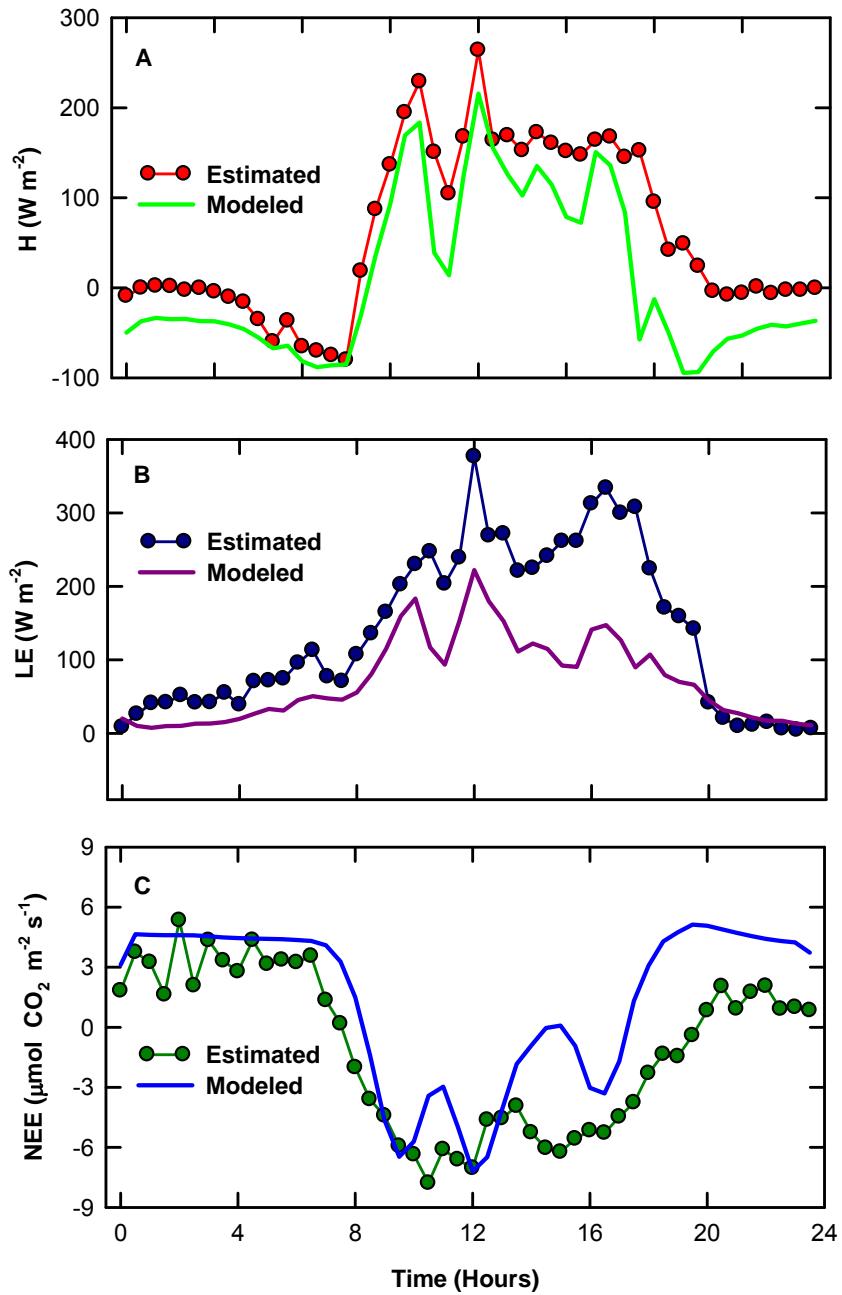


Figure 5.8. Comparison between measured and modeled sensible (A) and latent heat (B) and CO_2 (C) fluxes for cloudy sky conditions (DOY 204).

The lack of proper representation of net radiation within the different layers of the canopy under cloudy sky conditions by the radiative transfer schemes can also account for the underestimations. Further, the effects of advection can increase latent heat and decrease sensible heat fluxes which the model fails to describe. The rapid changes in soil respiration observed was not predicted by the biophysical model as respiration is expressed as a function of soil temperature, but actual rates may be controlled by other factors such as size of the available carbon pool and presence of water on the marsh surface.

5.3.3. Model performance: tidal influences

Tidal activity has an important role in modulating the exchange of energy and carbon in intertidal ecosystems. Submergence of the canopy can cause decrease in plant physiological activity and reduce the active leaf area available for exchange processes. The presence of standing water on the marsh surface increases the partitioning of energy for latent heating thus decreasing the sensible heat fluxes. A more detailed explanation of the energy and carbon transformations occurring under flooded conditions can be found in Chapters 2 and 3. In this section a comparison is made between two days: 1) with high tide occurring during peak assimilation period (DOY 244), and 2) with exposed or low tide conditions occurring during peak assimilation periods. The comparison between estimated and modeled carbon and energy fluxes during flooded conditions is presented in Figure 5.9. The model fails to represent the trends in carbon assimilation and energy fluxes during the high tide periods. The tidal modulation which causes the drop in carbon assimilation and increased latent heat fluxes with a corresponding decrease in sensible heat flux is not properly estimated by the model. In its present form the model has a static canopy leaf area distribution and hence it cannot account for the changes in source/sink distribution of scalars consequential of the high tide event. Moreover, the reduction in plant physiological activity brought about by submergence is not accounted in the plant physiology modules, thereby leading to over prediction of assimilation. Submergence also affects other ecosystem exchange processes such radiative transfer, ecosystem respiration, and soil temperatures which are not currently represented in the model implementation.

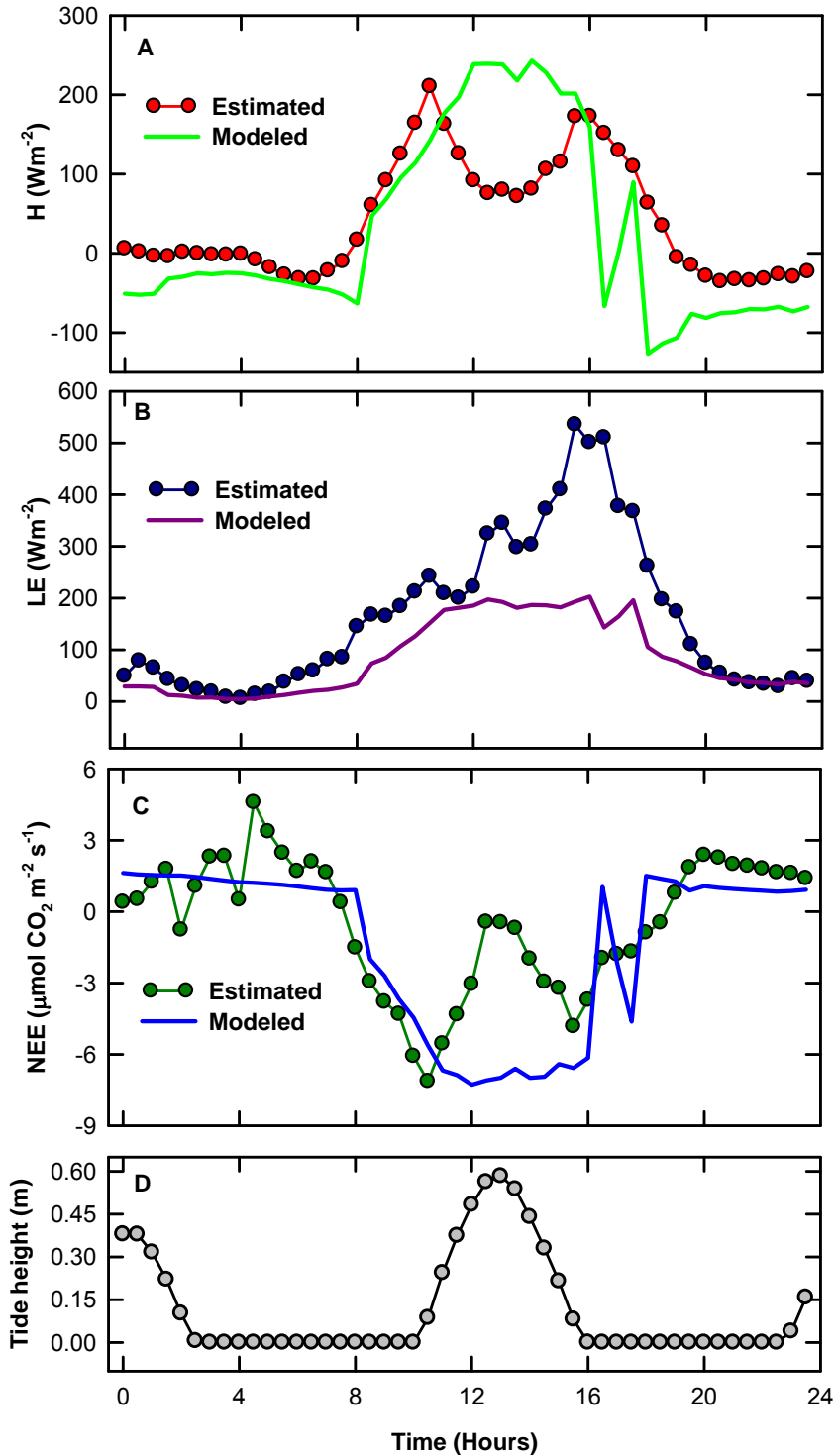


Figure 5.9. Comparison between estimated and modeled fluxes of sensible heat (A) latent heat (B) CO_2 (C), for high tide conditions during midday. The water level on the marsh surface is also provided (D).

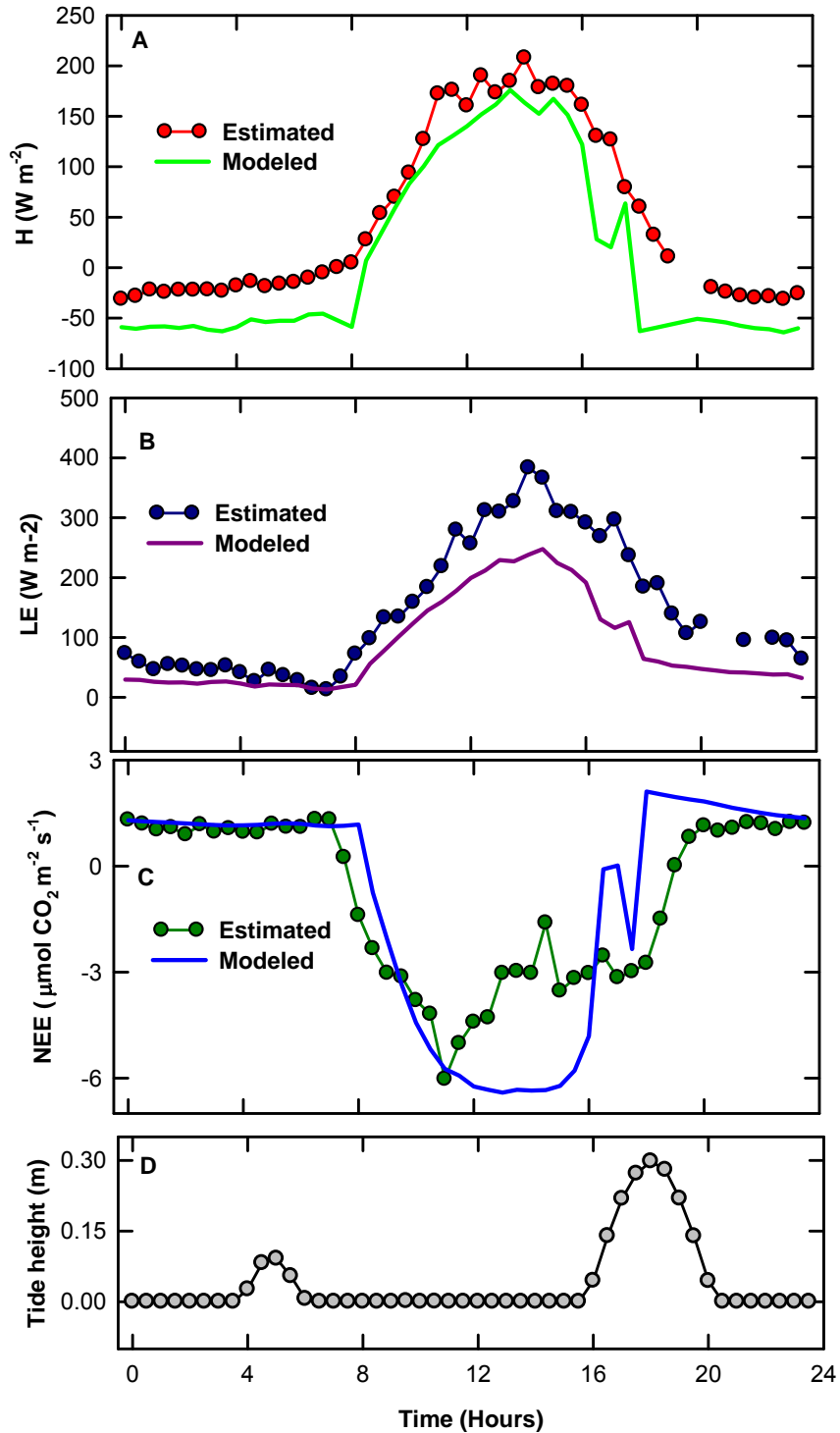


Figure 5.10. Comparison between estimated and modeled fluxes of sensible heat (A), latent heat (B) and CO_2 fluxes (A), for low tide conditions during midday. The water level on the marsh surface is also provided (D).

In contrast, for day with low tide occurring during peak assimilation hours the model is able to capture the trends in carbon and energy exchange processes (Figure 5.10). The NEE is overestimated during the afternoon hours possibly due to reduction in stomatal conductance

under high temperatures which is not accounted for in the stomatal conductance modules. The latent heat fluxes are underestimated during the afternoon hours as advection of moisture from the ocean surface is not accounted for in the model.

5.3.4. Factors affecting model performance

The canopy biophysical model performance is affected by several environmental factors which are not accounted for in the model description. One important drawback of the current model is its underestimation of latent heat fluxes, especially in the afternoon hours. Latent heat fluxes are predicted as a function of leaf temperature and stomatal conductance. Although the NEE values tend to decrease during the afternoon periods, the latent heat fluxes tend to increase, indicating other possible sources of moisture contributing to latent heat fluxes. Hussey and Odum (1974) indicated that in intertidal salt marshes evapotranspiration is not related to leaf area index of the vegetation as observed in freshwater marshes, indicating greater control of surface characteristics rather than vegetation on evaporation. The tidal activity can leave pools of water on the marsh surface which can evaporate at potential rates even if stomatal conductance is restricted, leading to evaporation rates greater than predicted by plant transpiration and soil evaporation. Advection of moisture by tidal activity is another important process which is not accounted in the model as it assumes complete energy balance closure. Moreover, the temperature relations utilized for predicting soil respiration may not hold well in intertidal ecosystems with large available carbon pool which are constantly perturbed by tidal activity (Falge *et al.*, 2002). Further *Spartina alterniflora* being a seasonal plant exhibits rapid changes in leaf area and plant physiological properties with the progress of the seasons, which at present is not represented in the biophysical model description. *Spartina alterniflora* being a C₄ plant can continue to photosynthesize even under conditions of stomatal closure as it can concentrate CO₂ in its bundle sheath cell, thus the stomatal conductance to assimilation relationships may not hold well under periods of water stress. The environmental forcings on an intertidal salt marsh system are complex and varied and the inaccuracies that exist in the representation of these physical processes can limit the model performance. The biophysical models developed for terrestrial ecosystems especially for tall canopies perform better in predicting the fluxes of scalars (e.g. Gu, 1999, Baldocchi and Wilson, 2001, Wilson *et al.*, 2003; Wohlfahrt, 2004) compared to the model

developed in this study. Although other salt marsh biophysical models are unavailable for comparison, results from a mangrove biophysical model (Barr, 2005) produce better results, although the sensible heat fluxes are over estimated. The *Spartina* biophysical model performs well under ideal conditions, where there is not tidal activity on the marsh surface or in the absence of land-sea breeze systems. The closeness to the ocean and the dynamic nature of the site makes it physically complex to be represented accurately in canopy models.

5.4. Summary

Although many multilayer canopy models have been developed and used extensively to predict fluxes of carbon and energy from terrestrial ecosystems, the biophysical model described herein incorporates several new features. The *Spartina alterniflora* biophysical model incorporates a detailed representation of the C₄ photosynthesis mechanism. The radiative transfer in plant canopies is represented using a multi-scattering approach and the PAR and NIR wave bands are considered separately for predicting the net shortwave radiation absorbed. The model also solves for the mesophyll concentration of CO₂ which is a key factor driving the C₄ photosynthesis. The biophysical model performs well under conditions where there is no tidal activity and advection of energy, but with the presence of standing water on the marsh surface and sea-land breeze systems the partitioning of available energy is affected, leading to under determination of moisture fluxes. Suitable modifications in the model description to account for processes such as air-water CO₂ gas transfer, a dynamic canopy layer which can be adjusted with the water level to account for changes in source/sink distribution due to tidal activity and changes in energy balance partitioning brought about by advection can improve the performance of the biophysical model. Air-water CO₂ transport process may play an important role under high tide conditions in transporting CO₂ from the marsh surface as CO₂ dissociated in water at a much slower rate. The decreased assimilation rates observed under submerged conditions may still make a salt marsh a net sink for CO₂ under submerged conditions, which can be recreated in the model with suitable modifications to plant physiology variables, but not detected by eddy covariance measurements.

References

- Baldocchi, D.D. and Wilson, K.B. 2001. Modeling CO₂ and water vapor exchange of a temperate broadleaved forest across hourly to decadal time scales. *Ecological Modeling*, 142: 155-184
- Baldocchi, D. and Meyers, T. 1998. On using eco-physiological, micrometeorological and biogeochemical theory to evaluate carbon dioxide, water vapor and trace gas fluxes over vegetation: a perspective. *Agricultural and Forest Meteorology*, 90: 1-25.
- Baldocchi, D. 1992. A Lagrangian random-walk model for simulating water-vapor, CO₂ and sensible heat-flux densities and scalar profiles over and within a soybean canopy. *Boundary-Layer Meteorology*, 61: 113-144.
- Ball, J.T., Woodrow, I.E. and Berry, J.A. 1987. A model predicting stomatal conductance and its contribution to the control of photosynthesis under different environmental conditions. *Progress in Photosynthesis Research, IV*. Martinus-Nijhoff Publishers, Dordrecht, The Netherlands., 221–224 pp.
- Barr, J.G. 2005. Carbon assimilation by riverine mangroves in the Florida Everglades. Dissertation thesis, University of Virginia, Charlottesville, VA, USA.
- Bernacchi, C.J., Portis, A.R., Nakano, H., von Caemmerer, S. and Long, S.P. 2002. Temperature response of mesophyll conductance. Implications for the determination of Rubisco enzyme kinetics and for limitations to photosynthesis in vivo. *Plant Physiology*, 130: 1992-1998.
- Berry, J.A. and Farquhar, G.D., 1978. The CO₂ concentration function of C₄ photosynthesis: a biochemical model. In: D. Hall, J. Coombs and T. Goodwind (Editors), *Proceedings of the 4th international congress on photosynthesis*. Biochemical Society, London, pp. 119-131.
- Bonan, G.B. 1996. A land surface model (LSM version 1.0) for ecological, hydrological, and atmospheric studies: Technical description and user's guide. NCAR/TN-4171STR.
- Businger, J.A., Wyngaard, J.C., Izumi, Y. and Bradley, E.F., 1971. Flux-profile relationships in the atmospheric surface layer. *Journal of the Atmospheric Sciences*, 28: 181-189.
- Campbell, G.S. 1986. Extinction coefficients for radiation in plant canopies calculated using an ellipsoidal inclination angle distribution. *Agricultural and Forest Meteorology*, 36: 317-321.

- Campbell, G.S. and Norman, J.M. 1998. An Introduction to Environmental Biophysics. Springer, New York.
- Campbell, G.S. and van Evert, F.K. 1994. Light interception by plant canopies: Efficiency and architecture. In: J.L. Monteith, R.K. Scott and M.H. Unsworth (Editors), Resource Capture by Crops. Nottingham University press, U. K, Nottingham, pp. 35-52.
- Chen, D.X., Coughenour, M.B., Knapp, A.K. and Owensby, C.E., 1994. Mathematical simulation of C₄ grass photosynthesis in ambient and elevated CO₂. Ecological Modeling, 73: 63-80.
- Collatz, G.J., Ball, J.T., Grivet, C. and Berry, J.A. 1991. Physiological and environmental-regulation of stomatal conductance, photosynthesis and transpiration - a model that includes a laminar boundary-Layer. Agricultural and Forest Meteorology, 54: 107-136.
- Dai, Y.J., Dickinson, R.E. and Wang, Y.P. 2004. A two-big-leaf model for canopy temperature, photosynthesis, and stomatal conductance. Journal of Climate, 17: 2281-2299.
- Dai, T. and Weigert, R. G. 1996. Estimation of primary productivity of *Spartina alterniflora* using a canopy model. Ecography, 19: 410-423
- Davis, R.E. and Dolan, R. 1993. Noreasters. American Scientist 81: 428-439.
- Evans, J.R. 1987. The dependence of quantum yield on wavelength and growth irradiance. Australian Journal of Plant Physiology, 14: 69-79.
- Evans, J.R. 1989. Photosynthesis and nitrogen relationships in leaves Of C₃ Plants. Oecologia, 78: 9-19.
- Falge, E., Baldocchi D., Tenhunen, J., Aubinet, M., Bakwin P., Berbigier, P., Bernhofer, C., Burba, G., Clement, R., Davis, K.J., Elbers, J.A., Goldstein, A.H., Grelle, A., Granier, A., Guðmundsson, J., Hollinger, D., Kowalski, A.S., Katul, G., Law, B.E., Malhi, Y., Meyers, T., Monson, R.K., Munger, J.W.; Oechel, W.; Paw, U.K.T., Pilegaard, K., Rannik, U., Rebmann, C., Suyker, A., Valentini, R., Wilson, K. and Wofsy, S. 2002. Seasonality of ecosystem respiration and gross primary production as derived from FLUXNET measurements. Agricultural and Forest Meteorology, 113: 53-74.
- Farquhar, G.D., Caemmerer, S.V. and Berry, J.A. 1980. A biochemical-model of photosynthetic CO₂ assimilation in leaves of C₃ Species. Planta, 149: 78-90.

- Foley, J.A., Prentice, I.C., Ramankutty, N., Levis, S., Pollard, D., Sitch, S. and Haxeltine, A. 1996. An integrated biosphere model of land surface processes, terrestrial carbon balance, and vegetation dynamics. *Global Biogeochemical Cycles*, 10: 603-628.
- Goudriaan, J. 1977. *Crop micrometeorology: a simulation study*. Simulation monographs, Pudoc, Wageningen.
- Gu, L.H. 1998a. Comments on "A practical method for relating scalar concentrations to source distributions in vegetation canopies" by M. R. Raupach. *Boundary-Layer Meteorology*, 87: 515-524.
- Gu, L.H. 1998b. Modeling biophysical exchanges and micro-meteorology in soil-vegetation-atmosphere continuums-results from a two-storey boreal aspen forest. Dissertation Thesis, University of Virginia, Charlottesville, Virginia, USA.
- Gu, L.H., Baldocchi, D., Verma, S. B., Black, T. A., Vesala, T., Falge, E. M. and Dowty, P.R. 2002. Advantages of diffuse radiation for terrestrial ecosystem productivity. *Journal of Geophysical Research-Atmospheres*, 107(D5-6).
- Gu, L.H., Shugart, H.H., Fuentes, J.D., Black, T.A. and Shewchuk, S.R. 1999. Micrometeorology, biophysical exchanges and NEE decomposition in a two-story boreal forest - development and test of an integrated model. *Agricultural and Forest Meteorology*, 94: 123-148.
- Hussey, B. and Odum, W. 1974. Evapotranspiration in tidal marshes. *Estuaries and Coasts*, 15: 59.
- Kaimal, J.C and Finnigan, J.J. 1994. *Atmospheric Boundary Layer Flows*. Oxford university press, New York. pp 16.
- Kelly, C.T. 1995. Iterative methods for linear and nonlinear equations. *Frontiers in Applied Mathematics*, 16. SIAM, Philadelphia, PA, USA.
- Knohl, A., and Baldocchi, D. D. 2008. Effects of diffuse radiation on canopy gas exchange processes in a forest ecosystem. *Journal of Geophysical Research*. 113, G02023
- Leonard, S., Turner, J and Milton, S. 1997. An assessment of UK meteorological office numerical weather prediction analyses and forecasts for the Antarctic. *Antarctic Science*, 9:100-109.
- Leuning, R. 1990. Modeling stomatal behavior and photosynthesis in *Eucalyptus grandis*. *Australian Journal of Plant Physiology*, 17: 159-175.

- Leuning, R., Denmead, O.T., Miyata, A. and Kim, J. 2000. Source/sink distributions of heat, water vapor, carbon dioxide and methane in a rice canopy estimated using Lagrangian dispersion analysis. *Agricultural and Forest Meteorology*, 104: 233-249.
- Peisker, M. 1987. Modeling of C₄ photosynthesis at low quantum flux densities. In: S. Vacklinova (Editor), *International Symposium on Plant Mineral Nutrition and Photosynthesis. Vol. II Photosynthesis*. Bulgarian Academy of Sciences, Sofia, pp. 226-234.
- Qiu, G.W. and Warland, J.S. 2006. Inferring profiles of energy fluxes within a soybean canopy using Lagrangian analysis. *Agricultural and Forest Meteorology*, 139: 119-137.
- Raupach, M.R. 1989a. Applying Lagrangian fluid-mechanics to infer scalar source distributions from concentration profiles in plant canopies. *Agricultural and Forest Meteorology*, 47: 85-108.
- Raupach, M.R. 1989b. A practical Lagrangian method for relating scalar concentrations to source distributions in vegetation canopies. *Quarterly Journal of the Royal Meteorological Society*, 115: 609-632.
- Raupach, M.R. 1998. Response to Gu (1998), "Comments on 'a Practical Lagrangian Method for Relating Scalar Concentrations and Source Distributions in Plant Canopies' by M. R. Raupach (1989: Quarterly Journal of the Royal Meteorology Society. 115, 609–632)". *Boundary-Layer Meteorology*, 87: 525.
- Ross, J. 1975. Radiative transfer in plant communities. In: J.L. Monteith (Editor), *Vegetation and the Atmosphere*. Academic press, New York, USA, pp. 22.
- Ross, J. 1981. *The radiation regime and architecture of plant stands*. Dr W. Junk Publishers, London, UK, 391 pp.
- Sellers, P.J., Randall, D.A., Collatz, G.J., Berry, J.A. Field, C.B. Dazlich, D.A. Zhang, C., Collelo, G.D. and Bounoua, L. 1996. A revised land surface parameterization (SiB2) for atmospheric GCMs .1. Model formulation. *Journal of Climate* 9: 676
- von Caemmerer, S. 1999. *Biochemical models of leaf photosynthesis*. CSIRO Publishing, Victoria.
- von Caemmerer, S. and Furbank, R.T. 1999. The modeling of C₄ photosynthesis. In: R. Sage and R. Monson (Editors), *The biology of C₄ photosynthesis*. Academic press, New York, USA, pp. 169-207.

- Wang, Y.P. and Jarvis, P.G. 1990. Description and Validation of an array model - Maestro. *Agricultural and Forest Meteorology*, 51: 257-280.
- Warland, J.S. and Thurtell, G.W. 2000. A Lagrangian solution to the relationship between a distributed source and concentration profile. *Boundary-Layer Meteorology*, 96: 453-471.
- Wohlfahrt, G. 2004. Modeling fluxes and concentrations of CO₂, H₂O and sensible heat within and above a mountain meadow canopy: A comparison of three Lagrangian models and three parameterization options for the Lagrangian time scale. *Boundary-Layer Meteorology*, 113: 43-80.
- Xue, Y.K., Fennessy, M.J. and Sellers, P.J. 1996. Impact of vegetation properties on US summer weather prediction. *Journal of Geophysical Research-Atmospheres*, 101: 7419-7430.
- Zang, Y., Li, C., Trettin, C.C., Li, H and Sun, G. 2002. An integrated model of soil hydrology and vegetation for carbon dynamics in wetland ecosystems. *Global Biogeochemical Cycles*, 16 : x1-x18.
- Zhao, W.G. and Qualls, R.J. 2005. A multiple-layer canopy scattering model to simulate shortwave radiation distribution within a homogeneous plant canopy. *Water Resources Research*, 41: W08409.

Synthesis

Spartina alterniflora salt marshes are highly dynamic and unique ecosystems in terms of carbon and energy cycling. Intertidal salt marshes are the most susceptible systems to rapid sea level rise associated with global warming as they form the interface between terrestrial and marine ecosystems. It is critical to quantify and understand the energy transformations and transport processes in coastal ecosystems to better predict the response of these systems to sea level rise and other disturbances such as hurricanes.

The major objective of this dissertation work was to quantify the carbon assimilation by intertidal salt marshes using tower based eddy covariance methodology. The key questions asked here include 1) what are the primary forcings on carbon assimilation on diurnal and seasonal scales 2) what is the role of tidal activity in modulating the ecosystem-atmosphere exchange processes and 3) to predict ecosystem response to local and global climatic changes through development of a canopy biophysical model. The study was initiated with the setting up of a 20 feet tall flux tower at the eastern shore of Virginia, at the VCR-LTER site in a lagoonal salt marsh. The dominant vegetation in these marshes, *Spartina alterniflora* plays a major role in the survival of these marshes and in carbon sequestration by aiding the processes of sediment accretion and burial. Leaf level physiology measurements were conducted to identify environmental limitations on canopy photosynthesis and to scale leaf level processes to ecosystem scale. Although classified as a C₄ plant, *Spartina alterniflora* exhibits distinct physiological characteristics which include a low light saturation level, low PEP carboxylase activity and higher temperature optimum for carboxylation reactions. The possibility of existence of alternate biochemical pathways comparable to C₃-C₄ intermediate plants in *Spartina alterniflora* was one of the key conclusions of this study. The biochemical parameters which are essential for modeling canopy photosynthesis and associated temperature relationships were also developed in this study. Ecosystem level flux measurements indicated that the salt marsh ecosystems are moderate sink of carbon fixing about 8-10 $\mu\text{mol m}^{-2} \text{s}^{-1}$ of CO₂. Tidal activity can play a major role in reducing carbon assimilation as the vegetation can be completely or partially submerged by high tides, which induces physiological stress on the plants, reducing assimilation. High tides over the marsh surface can also affect energy partitioning in this system with increased latent heating and decreased sensible heating observed during periods of high tide. An important consequence of

this result is a probable response of salt marshes to rapid sea level rise, which can increase the hydro-period over the marsh surface and thus reduce the carbon assimilation capacity. On a seasonal basis, changes in air temperature and specific humidity exert strong control on NEE patterns by modulating ecosystem respiration and stomatal conductance. Advection of energy brought about by land-sea breeze is important in intertidal coastal systems and should be accounted for when interpreting energy balance estimates. Advective enhancement is typically observed during late afternoon periods when the sea-breeze activity is high. Thus intertidal salt marshes are dynamic and complex systems modulated by several forcings including diurnal tidal activity, land-sea breeze systems and a rapidly changing carbon pools owing to horizontal transport processes. A multilayer biophysical model was developed to predict fluxes of scalars from intertidal marsh systems incorporating the theories of turbulent transport. Since the model assumes complete energy balance closure its performance is undermined under periods of high tide and energy advection induced by land-sea breeze systems. Future modifications suggested include a dynamic canopy layer which change with the water level over the marsh surface and inclusion of air-sea CO₂ transport processes to simulate gas exchange under submerged conditions. The model performance is comparable to other multilayer models developed for tall canopies in terrestrial ecosystems in the absence of tidal activity and energy advection. Although several key conclusions were derived from this study, detailed studies are further required to answer key questions including quantification of soil respiration processes, biochemical investigations to understand physiological response to flooding in *Spartina alterniflora* and estimating the contribution of advective flows to estimated flux values.

Appendix A

Data logger program used for data acquisition form micromet sensors

'This is the data logger program used to collect data from the meteorological sensors. The data 'logger used is CR 3000. the programming language is CR Basic

'CR3000

'Created by Short Cut (2.5) and modified for serial output

'Declare Variables and Units

Public Batt_Volt

Public CM3Up

Public CM3Dn

Public CG3Up

Public CG3Dn

Public CNR1TC

Public CNR1TK

Public NetRs

Public NetRI

Public Albedo

Public UpTot

Public DnTot

Public NetTot

Public CG3UpCo

Public CG3DnCo

Public PAR_Den

Public PAR_Tot

Public PAR_Den_2

Public PAR_Tot_2

Public WS_ms

Public WindDir

Public BP_kPa

Public Temp_C

Public So

"Declaring Strings

Public OutString1 as string

Public OutString2 as string

Public OutString3 as string

Public OutString4 as string

Public OutString5 as string

Public OutString6 as string

Public OutString7 as string

Public OutString8 as string

Public OutString9 as string

Public OutString10 as string

Units Batt_Volt=Volts

Units CM3Up=W/meter²

Units CM3Dn=W/meter²

Units CG3Up=W/meter²

Units CG3Dn=W/meter²

Units CNR1TC=Deg C

Units CNR1TK=K

Units NetRs=W/meter²

Units NetRI=W/meter²

Units Albedo=W/meter²

Units UpTot=W/meter²

Units DnTot=W/meter²

Units NetTot=W/meter²

Units CG3UpCo=W/meter²

Units CG3DnCo=W/meter²

Units PAR_Den=μmol/s/m²

Units PAR_Tot=mmol/m²

Units PAR_Den_2=μmol/s/m²

Units PAR_Tot_2=mmol/m²

Units WS_ms=meters/second

Units WindDir=Degrees

Units BP_kPa=kPa

```

Units Temp_C=Deg C
Units So=W/meter2
'Define Data Tables
DataTable(Table1,True,-1)
    DataInterval(0,1,Min,10)
    Average(1,CM3Up,FP2,False)
    Average(1,CM3Dn,FP2,False)
    Average(1,CG3Up,FP2,False)
    Average(1,CG3Dn,FP2,False)
    Average(1,CNR1TC,FP2,False)
    Average(1,CNR1TK,FP2,False)
    Average(1,NetRs,FP2,False)
    Average(1,NetRI,FP2,False)
    Average(1,Albedo,FP2,False)
    Average(1,UpTot,FP2,False)
    Average(1,DnTot,FP2,False)
    Average(1,NetTot,FP2,False)
    Average(1,CG3UpCo,FP2,False)
    Average(1,CG3DnCo,FP2,False)
    Average(1,PAR_Den,FP2,False)
    Totalize(1,PAR_Tot,IEEE4,False)
    Average(1,PAR_Den_2,FP2,False)
    Totalize(1,PAR_Tot_2,IEEE4,False)
    Average(1,WS_ms,FP2,False)
    Sample(1,WindDir,FP2)
    Average(1,BP_kPa,FP2,False)
    Average(1,Temp_C,FP2,False)
    Average(1,So,FP2,False)
EndTable
DataTable(Table2,True,-1)
    DataInterval(0,1440,Min,10)
    Minimum(1,Batt_Volt,FP2,False,False)
EndTable
'Main Program
BeginProg
    Scan(1,Sec,1,0)
'opening serial port for data communication
    SerialOpen (ComRS232,115200,0,0,10000)
'Default Datalogger Battery Voltage measurement Batt_Volt:
Battery(Batt_Volt)
'CNr1 Net Radiometer measurements CM3Up, CM3Dn, CG3Up, CG3Dn, CNr1TC, CNr1TK,
    NetRs, NetRI, Albedo, UpTot, DnTot, NetTot, CG3UpCo, and CG3DnCo:
    VoltDiff(CM3Up,1,mV20,1,True,0,_60Hz,94.0733,0)
    VoltDiff(CM3Dn,1,mV20,2,True,0,_60Hz,94.0733,0)
    VoltDiff(CG3Up,1,mV20,3,True,0,_60Hz,94.0733,0)
    VoltDiff(CG3Dn,1,mV20,4,True,0,_60Hz,94.0733,0)
    BrHalf4W(CNR1TC,1,mV50,mV50,5,1,1,4200,True,True,0,_60Hz,1,0)
    PRT(CNR1TC,1,CNR1TC,1,0)
    CNR1TK=CNR1TC+273.18
    NetRs=CM3Up-CM3Dn
    NetRI=CG3Up-CG3Dn
    Albedo=CM3Dn/CM3Up
    UpTot=CM3Up+CG3Up
    DnTot=CM3Dn+CG3Dn
    NetTot=UpTot-DnTot
    CG3UpCo=CG3Up+5.67*10-8*CNR1TK4
    CG3DnCo=CG3Dn+5.67*10-8*CNR1TK4
'2 PAR sensors one facing up and the other down
'LI190SB Quantum Sensor measurements PAR_Tot and PAR_Den:
    VoltDiff(PAR_Den,1,mV20,7,True,0,_60Hz,1,0)
    If PAR_Den<0 Then PAR_Den=0
    PAR_Tot=PAR_Den*0.24527
    PAR_Den=PAR_Den*245.278
'LI190SB Quantum Sensor measurements PAR_Tot_2 and PAR_Den_2:
    VoltDiff(PAR_Den_2,1,mV20,8,True,0,_60Hz,1,0)
    If PAR_Den_2<0 Then PAR_Den_2=0

```

```

    PAR_Tot_2=PAR_Den_2*0.23384
    PAR_Den_2=PAR_Den_2*233.845
'Wind direction and velocity using a propellor anemometer
'05103 Wind Speed & Direction Sensor measurements WS_ms and WindDir:
PulseCount(WS_ms,1,1,1,1,0.098,0)
BrHalf(WindDir,1,mV5000,17,1,1,5000,True,0,_60Hz,355,0)
If WindDir>=360 Then WindDir=0

'Pressure sensor
'CS105 Barometric Pressure Sensor measurement BP_kPa:
PortSet(1,1)
VoltSE(BP_kPa,1,mV5000,18,1,0,_60Hz,0.184,600.0)
BP_kPa=BP_kPa*0.1
'Type T (copper-constantan) Thermocouple measurements Temp_C:
TCDiff(Temp_C,1,mV20C,11,TypeT,Temp_C,True,0,_60Hz,1,0)
'Generic Differential Voltage measurements So:
VoltDiff(So,1,mV20,10,True,0,_60Hz,0.0336,0.0)
'Call Data Tables and Store Data
CallTable(Table1)
CallTable(Table2)
'Convert values in Table 1 to strings

OutString1 = Table1.NetTot_Avg(1,1)+ CHR (09) +Table1.CM3Up_Avg(1,1) + CHR
(09)+Table1.CM3Dn_Avg(1,1)+CHR(09)
OutString2 = CHR (09)+ Table1.CG3Up_Avg(1,1)+ CHR (09)+ Table1.CG3Dn_Avg(1,1)+CHR(09)
OutString3 = CHR (09)+ Table1.CNR1TC_Avg(1,1)+ CHR (09)+ Table1.CNR1TK_Avg(1,1)+CHR(09)
OutString4 = CHR(09)+ Table1.NetRs_Avg(1,1)+ CHR(09)+ Table1.NetRL_Avg(1,1)+CHR(09)
OutString5 = CHR(09)+ Table1.Albedo_Avg(1,1)+ CHR(09)+ Table1.UpTot_Avg(1,1)+ CHR(09)+
Table1.DnTot_Avg(1,1)+CHR(09)
OutString6 = CHR(09)+ Table1.CG3UpCo_Avg(1,1)+ CHR(09)+ Table1.CG3DnCo_Avg(1,1)+CHR(09)
OutString7 = CHR(09)+ Table1.PAR_Den_Avg(1,1)+ CHR(09)
OutString8 = CHR(09)+ Table1.PAR_Den_2_Avg(1,1)+CHR(09)
OutString9 = CHR(09)+ Table1.WS_ms_Avg(1,1)+CHR(09)
OutString10 = CHR(09)+ Table1.BP_kPa_Avg(1,1)+ CHR(09)+ Table1.Temp_C_Avg(1,1)+ CHR(09)+
Table1.So_Avg(1,1)+ CHR(09)+ CHR(13)+ CHR(10)
'Output minute averages
    If IfTime (0,1,Min) Then
        SerialOut (ComRS232,OutString1,"",0,100)
        SerialOut (ComRS232,OutString2,"",0,100)
        SerialOut (ComRS232,OutString3,"",0,100)
        SerialOut (ComRS232,OutString4,"",0,100)
        SerialOut (ComRS232,OutString5,"",0,100)
        SerialOut (ComRS232,OutString6,"",0,100)
        SerialOut (ComRS232,OutString7,"",0,100)
        SerialOut (ComRS232,OutString8,"",0,100)
        SerialOut (ComRS232,OutString9,"",0,100)
        SerialOut (ComRS232,OutString10,"",0,100)
        SerialOut (ComRS232,CHR(10)+CHR(13),"",0,100)
    EndIf

NextScan
EndProg

```

Appendix-B

Matlab code utilized in processing eddy covariance high frequency data

%Matlab script used for flux calculations-adapted from Jordan Barr and Steven Chan, %Department of environmental sciences, University of Virginia

```

clear all
tic;
clc; % clearing the screen
yr = '07'; % year of file creation
mon = '07'; % month of file creation
dy2 = [1:7 16:31]; % days in the month having data
jck=1;
warning off
for pp = 1:length(dy2)
if dy2(pp)>9
dy = num2str(dy2(pp));
else
dy = strcat('0',num2str(dy2(pp)));
end
dire = dir;
for i=3:size(dire,1) %ignores first 2 entries: '.' and '..'
filename1{i-2}=dire(i).name; %pulls all the filenames out from the directory
end
comps = [yr mon dy];
filename = char(filename1);
flies = filename((strmatch(comps,filename)),:);
%warning messages if files are non-existent
if isempty(flies)
disp('No files exists for that day')
disp('try another day')
break
end
for j =1:(size(flies,1))
a=['.....Processing file number ' num2str(j) ' of day ' num2str(dy2(pp))...
' of total ' num2str(dy2(end)) ' days....>>'];
disp(a)
flies1 = (flies(j,:));
data = load(flies1);
fd=size(data);
if fd(2)>10
data=[data(:,1:5) data(:,8:11)];
end
fdat=[];
warning off
% removing erroneous data
inde1 = (find(data(:,2)>10 & data(:,2)<70 & data(:,3)>400 & data(:,3)<5500 & data(:,5)>80 & data(:,5)<110 &
data(:,4)>0 & data(:,4)<45 ...
& data(:,9)>-10 & data(:,9)<45));
data6=data(inde1,:);
meant=mean(data6(:,4));
indt=find(data6(:,9)< meant+8 & data6(:,9)>meant-8);
data6=data6(indt,:);
%spike detection and removal
lt3sigma = find(abs(data6(:,8)-mean(data6(:,8)))<std(data6(:,8))*4);%
data7=data6(lt3sigma,:);
lt3sigma2 = find(abs(data7(:,2)-mean(data7(:,2)))<std(data7(:,2))*4);%
data7=data7(lt3sigma2,:);
lt3sigma3 = find(abs(data7(:,3)-mean(data7(:,3)))<std(data7(:,3))*4);%
data7=data7(lt3sigma3,:);
lt3sigma4 = find(abs(data7(:,6)-mean(data7(:,6)))<std(data7(:,6))*4);%
data7=data7(lt3sigma4,:);
lt3sigma5 = find(abs(data7(:,7)-mean(data7(:,7)))<std(data7(:,7))*4);%
data7=data7(lt3sigma5,:);
lt3sigma6 = find(abs(data7(:,8)-mean(data7(:,8)))<std(data7(:,8))*4);%
data7=data7(lt3sigma6,:);
fg=length(data7);

```

```

if length(data7)>2000% data analysis undertaken only if data has a specific length
u = data7(:,6); % u in m/s
v = data7(:,7); % v in m/s
w = data7(:,8); % w in m/s
%Co-ordinate rotation-see (Kaimal and Finnigan(1994) pp-236)
thet1=atan((mean(v)/mean(u)));
u2=u*cos(thet1)+v*sin(thet1);
v2=-u*sin(thet1)+v*cos(thet1);
w2=w;
phi=atan((mean(w2)/mean(u2)));
u3=u2*cos(phi)+w2*sin(phi);
v3=v2;
w3=-u2*sin(phi)+w2*cos(phi);
psi=0.5*atan((mean(2*v3.*w3)/(mean(v3.^2)-mean(w3.^2))));
u4=u3;
v4=v3*cos(psi)+w3*sin(psi);
w4=-v3*sin(psi)+w3*cos(psi);
u=u4;
v=v4;
w=w4;
Tair = data7(:,9); % Tv in C
CO2 = data7(:,2); & in
H2O = data7(:,3);
Temp = data7(:,4);
Press = data7(:,5);%in Kpa
Wave = mean(w);
Uave = mean(sqrt(u.^2+v.^2)); %mean horizontal Wspeed
Uinst = (sqrt(u.^2+v.^2)); %instantaneous horizontal Wspeed
CO2ave = mean(CO2);
H2Oave = mean(H2O);
Tave = mean(Tair+273.15);
Pave = mean(Press); %in kPa
%perturbations from mean quantities
Tairp = Tair - Tave;
Wp = w - Wave;
Up = Uinst - Uave;
CO2p = CO2 - CO2ave;
H2Op = H2O - H2Oave;
%Quantities defined for Webb-Pearman-Leuning (1980) algorithm
rhoa = 120.28*Pave*(Tave)^(-1); %air density in mol m-3
ma = 28.964; %molecular wt of dry air (g mol-1)
mv = 18.015; %molecular wt of water vapor (g mol-1)
%covariance terms
wc=mean(CO2p.*Wp);
wh=mean(H2Op.*Wp);
wtv=mean(Tairp.*Wp);
%webb correction for CO2-terms
term1 = wc*1000;
term2 = ma*CO2ave*wh/(mv*rhoa);
term3 = (1 + 10^(-3)*ma*H2Oave/(mv*rhoa))*1000*(CO2ave/(Tave))*wtv;
Fco2 = term1 + term2 + term3; %CO2 flux micromol m-2 s-1
lambda = 43.74; %units: J mmol-1-latent heat of vaporization
LE = lambda*mean(H2Op.*Wp); %LE without Webb correction (W m-2)
Cp = 1; %air heat capacity (J g-1 K-1)
H = rhoa*ma*Cp*wtv; %W m-2
UWave = mean(Up.*Wp);
Tau = 1.2*UWave; %momentum flux
ustar = sqrt(abs(UWave)); %friction velocity (m s-1)
mew=ma/mv;
sigma=(H2Oave*10^(-3))/rhoa;% rowv/rowa;%convert millimoles/m3 to mol/m3
LE1 =(43.74*10^3)*((1 + (mew*sigma))*((wh*10^-3)+((H2Oave*10^-3)/Tave)*wtv));% with webb correction
time = flies1;
times = str2num(time(7:10))/100;
outpu3=[times Uave Wave CO2ave H2Oave H LE LE1 ustar Fco2 ];% output matrix
else
time = flies1;

```

```

times = str2num(time(7:10))/100;% creating time stamp
output3=[times NaN NaN NaN NaN NaN NaN NaN NaN NaN];
end
output3(j,:)=output3;
end
dlimwrite(['lag' comps '.txt'],output3,'t');% outputing files
clear output3
if jck==2
close
figure(1)
subplot(2,2,1)
plot(output3(:,1),output3(:,6),'r-*');
xlabel('Time')
ylabel('H (W m^-^2)')
subplot(2,2,2)
plot(output3(:,1),output3(:,8),'b-*');
xlabel('Time')
ylabel('LE (W m^-^2)')
subplot(2,2,3)
plot(output3(:,1),output3(:,10),'g-*');
xlabel('Time')
ylabel('FCO_2 \mu mol m^-^2 sec^-^1')
subplot(2,2,4)
plot(output3(:,1),output3(:,9),'k-*');
xlabel('Time')
ylabel('ustar,m/sec')
saveas(gcf, strcat('lag',comps),'fig')
saveas(gcf, strcat('lag',comps),'jpg')
end
end
toc % for displaying elapsed time

```

Appendix C

Canopy Bio-physical Model-Mainmodel.m

```

%Canopy Biophysical model -adapted from Jordan G Barr- from his dissertation work Carbon %assimilation
by riverine mangroves
clear all
close all
clc
warning off
%building matrices for filling outputs
bigmat=[];
kmat2=[];
%starting and ending days
%loading the met data file
data1 = load('alldata.txt');
mn=input('Enter the month to do analysis: '); %
indem=find(data1(:,2)==mn);
data2=data1(indem,:);% doing only for that month
dly2=1:10; % This is the days for which the model is run (here 1 to 10)
%starting the loop to go through each day
for pfg=1:length(dly2)
dly=dly2(pfg);
nlrs=6; % number of layers in the model
cnt=1; % initiating a counter
%some initial global parameters
global vcmx25 vpmax25 jmax25
global swav
%plant physiological constants for spartina
vcmx25=44.25;
vpmax25=13.03;
jmax25=109.03;
%% indexing out data for a particular day
daynow = dlyindel=find(data2(:,3)==daynow);
data=data2(indel,:);% doing only for that day
yr=data(1,1); %extracting the year
mons=data(1,2);%extracting the month
kdown=data(:,14);% this is the kdown(solar)
ind2=find(kdown<=0);% finding all the negative values and making them zero
global h % declaring canopy height as global
h = 0.60; %canopy in meters
global LAIall % declaring Leaf area index as global
LAIall = 2.086144; % total leaf area index of Spartina alterniflora
%using Kdown instead of PAR to derive PAR as PAR sensor measurements are
%not reliable
p1=1.927;% constant from linear curve fit
p2=50.58; % constant from linear curve fit
modpar= p1*kdown + p2; % get a beautiful estimate of par
modpar(ind2)=0; % getting the negative values out corresponding to kdown
data(:,31)=modpar; % making data column 31 as the PAR value now
PART = data(:,31); %average PAR (micromol m-2 s-1)

%PART = data(:,31); %average PAR (micromol m-2 s-1)
%Get the time
global DecDOY
DecDOY = dayofyear(yr,mons,daynow); % calling the function dayofyear which will give the %decimal day of
year
time = data(:,4)+data(:,5); %decimal time
day = DecDOY + time/24; %decimal day of year
global dLAI % declaring the
xc = 0.96; %the leaf orientation distribution for grass;
[Pabs1,dLAI] = multishort(data,xc); % calling the multiple scattering function –outputs are dLAI, %which is
the LAI in each layer and Pabs1, which is the absorbed PAR
[Nabs1,dLAI] = multinir(data,xc); % calling the multiple scattering function –outputs are dLAI, %which is the
LAI in each layer and Nabs1, which is the absorbed NIR
%Transposing the absorbed PAR and NIR values- this is for an entire day
Pabs=Pabs1';

```

```

Nabs=Nabs1';
%getting dLAI from top to bottom.
dLAI=flipr(dLAI);
% alphaLRTM is the longwave radiative transfer matrix - only computed once
[alphaLRTM] = LRTM(LAIall); %Takes total LAI as input from user
global alphaLRTM % declaring global
% Declare global variables - used by PhotosynC.m-which is the C4 photosynthesis model function used to
solve in the system of equations
global datanow
global Pabsnow
global Nabsnow
global Uinow %Ui profile at current time step
global ustrnow %ustar at current time step
global Ta
global RH
global l
h = 0.60; %canopy height (m)
The initial guesses for solving the system of equations
%now running the model for each half hour of the day.
for i = 1:length(day);
x1 =nlrs*[0.12 0.12 0.12 0.12 0.12 0.12]; %This is Gsv at all 6 levels in mol m-2 s-2
x2 = 220*ones(1,nlrs); %This is Ci at all 6 levels now dealing with Ci
x3 = 220*ones(1,nlrs); %This is Cm at all 6 levels now dealing with Ci
Ta0 = data(i,35)*ones(1,nlrs); %base leaf temp is air temp
x3b = 2*ones(1,nlrs); %add to air temp.
x4 = Ta0 + x3b; %This is Tleaf at all 6 levels
x0 = [x4,x2,x3,x1]'; % The initial values for unknowns
%The unknowns are Ci (intercellular CO2 concentration, Cm mesophyll CO2 concentration TI, leaf
%temperature and gsv –stomatal conductance to water vapor
% for night time periods the initial values are the one declared above but for other periods, the %initial
values are the previous solutions for the unknowns
if PART(i) > 20 %
break %use the current initialized variables
end
end
xstart = x0;
%Loop in time.
Time = []; %Initialize final output (starts as empty)
%This is: (gsv,ci,TI) at all 20 levels, each column is for one time interval
FinalSol = [];
Energy = []; %This is: (H,LE,Rnet,Fco2) at each time step
Energy2 = []; %accounting for storage (H, LE, Fco2)
%Output scalar profiles
TaAll = []; %in deg. C
RHAll = []; %dimensionless %
CaAll = []; %in micromol mol-1
counter = 0; % initializing a counter
for i = 1:length(day); %Go through all time steps.
dynow = day(i); %current decimal DOY
datanow = data(i,:); %data row at the current time step
apres=datanow(27)*1000; % pressure in pascal
global apres;
Pabsnow =flipr((Pabs(i,:))); %PAR absorbed by each layer from top to bottom
Nabsnow =flipr((Nabs(i,:))); %PAR absorbed by each layer from top to bottom
if max(Pabsnow) < 5
Pabsnow = zeros(1,length(Pabsnow));
end
if max(Nabsnow) < 5
Nabsnow = zeros(1,length(Nabsnow));
end
%Wind speed profiles at each time step
global Uinow
[Ui,ustar] = WindProf3(datanow); % calling function for wind profiles
Uinow = Ui(65:70); %wind speed in all layers at current time step top to bottom layer
ustrnow = ustar; %ustar computed from WindProf3.m at current time step
%Initialize scalar profiles at first time step.

```

```

%Otherwise, previous scalar solution is used.d
%if counter == 1; %For the first half-hour during the day
Ta = datanow(35)*ones(1,6); %current air temperature [layer 1 = TOP]
RH = datanow(36)*ones(1,6); %relative humidity [layer 1 = TOP]
global CaRef
CaRef = 370*ones(1,6); reference CO2 mixing ratio in air in ppm
%Fixed quantities at the reference height (zR), and soil temp. (Ts)
global TaFix; global Ts; global RHFix; global CaFix;
global CaRef; global datanow;
TaFix = datanow(35);%at reference level
Ts = datanow(40);
if Ts == 0
Ts = TaFix;
end
RHFix = datanow(36);
CaFix = 370;
%parameters needed for non-linear solver-solver used is nsol.by C.T Kelly
parms = [100,100,0.9,2,20];
tol = [1.d-6,1.d-6]; % tolerance limits for non-linear solver
[sol,errs,ierr] = nsol(x0,'photosynC4',tol, parms); % solving the system using non-linear solver
% -PhotosynC4 is the function which provides the system of equations to solve
%-It contains the system of non-linear equations which contain the leaf energy balance equations
% and stomatal conductance-assimilation models.
%Use PhotoOut1.m takes (gsv,Ci,Tl) and provides computed quantities to LNF.m
[RHref,TairRef,Tsoil,gsv,Tl,Sheat,Sh2o,SCO2,ci] = PhotoOut4(sol);
%PhotoOut4 is the function which takes in the solution and provides fluxes of energy and carbon.
% To relate the sources to concentration profiles the LNF theory is utilized in the function LNFJ.m
Uallnow = Uinow'; %Windspeed in 10 foliage layers (0.90 m to 0.1 m) at current time step

%LNFJ inputs
%INPUTS Tsoil, Tleaf (K) (length =6, Tl starts at TOP)
% TairRef in (K)
% Sheat (J m-3 s-1), Sh2o (mmol m-3 s-1), SCO2 (micromol m-3 s-1)
% All Source's start at TOP
% Uallnow (m s-1) [length = 20], Ui starts at top of canopy- wind velocity
% ustar (m s-1), dLAI (m2 m-3) (length = 20, starts at TOP)
% gsv (mmol m-2 s-1) and ci (micromol m-2 s-1) [both length = 20, start at TOP]
% (micromol mol-1)
% OUTPUT 1) Tair -air temperature (K), 2) Ea and eastar (Actual and saturated vapor %
pressure) (Pa), 3) Ca-CO2 concentration in the air (micromol m-3)-, 4) Fg-soil respiration % (micromole
m-2 s-1), Le
% calling the LNF function
[TairOut,EaOut,eastarOut,CaOut,Hsoil,LEsoil,Fg] = ...
LNFJ(Sheat,Sh2o,SCO2,Tsoil,Uallnow,Tl,TairRef,dLAI,gsv,CaRef,RHref,ci);
%This loop iterates the scalar profiles and intrinsic profiles (gsv,ci,Tl) 15 iterations are done
for j = 1:15;
% These quantities will be used as the initial guess after the 1st time step is complete.
Ta = flipud(TairOut(1:6))-273.15;
RHOut = 100*(EaOut./eastarOut);
RH = flipud(RHOut(1:6));
CaRef = flipud(CaOut(1:6))*0.0244;
x0 = sol; %Use "old" solution as guess for "new" solution
if ierr == 1 %If the solution fails, then....
x0 = xstart; %the original guess
end
% solving again for the unknowns using nsol
[sol, errs, ierr] = nsol(x0,'photosynC4',tol, parms);
%using the solution to find the fluxes of energy and carbon
[RHref,TairRef,Tsoil,gsv,Tl,Sheat,Sh2o,SCO2,cm] = PhotoOut4(sol);
%Update atmospheric profiles using source strength and LNF theory
[TairOut,EaOut,eastarOut,CaOut,Hsoil,LEsoil,Fg] = ...
LNFJ(Sheat,Sh2o,SCO2,Tsoil,Uallnow,Tl,TairRef,dLAI,gsv,CaRef,RHref,ci);
% if there is no error after 5 iterations, the iteration is broken
if(ierr==0&& j>5)
disp(i)

```

```

break
end
end
% All the output in time matrix
Time = [Time,daynow];
FinalSol = [FinalSol,sol]; % all the solutions stored in finalSol
% now finding the fluxes of scalars
%integrating the source layers and adding soil contribution
LE = trapz(xc,(Sh2o*43.70)) + LEsoil; % Latent heat in Wm-2
H = trapz(xc,Sheat) + Hsoil;
%compute the net radiation absorbed by the canopy
[delL] = longfunc2(Tl-273,Tsoil-273,TaFix,RHFix);
Lnet = sum(delL); % net long wave absorbed
Snet=(Pabsnow*0.235)+(Nabsnow); % net shortwave in Wm-2
Fco2 = sum(-Sco2)+ Fg;
if ierr==1
Fco2=NaN;
H=NaN;
LE=NaN;
End
% net radiation
Rnet = Lnet + Snet;
Eall = [H LE Rnet Fco2]; %column of energy terms and CO2 flux
Energy = [Energy;Eall]; %Keep a record of energy balance terms
%Output scalar profiles
TaAll = [TaAll,TairOut-273]; %in deg. C
RHAll = [RHAll,100*EaOut./eastarOut]; %dimensionless %
CaAll = [CaAll,CaOut*0.0244]; %in micromol mol-1
Eall2 = [H LE Rnet Fco2]; % making a matrix of energy terms
Energy2 = [Energy2;Eall2]; % filling up the matrix for the time period for which the model is run
%*****
end %End the loop to iterate in time
% plotting the figures -Output
figure(1)
subplot(3,1,1)
plot(Energy2(:,4),'b-')
title('FCO2 Flux modeled (Blue) and measured (Red)');
hold on
plot(data(:,10),'r-')
hold off
subplot(3,1,2)
plot(Energy2(:,1))
title('Sensible heat Flux modeled (Blue) and measured (Green)');
hold on
plot(data(:,12),'g-')
hold off
subplot(3,1,3)
plot(Energy2(:,2))
title('Latent heat Flux modeled(Blue) and measured (Cyan)');
hold on
plot(data(:,11),'c-')
hold off
disp('its done')
end

```

The sub functions are given below

1) Function-LNFJ-m- implementation of LNF theory-(Raupach, 1989)-adapted from Barr, J. G. 2005

```

function [Tair,Ea,eastar,Ca,Hsoil,LEsoil,Fg] = ...
LNFJ(Sheat,Sh2o,Sco2,Tsoil,Ui,Tleaf,TairRef,dLAI,GSV,CaRef,RHref,ci)
%INPUTS Tsoil, Tleaf (length = 20), TairRef in (K)
% Sheat (J m-3 s-1), Sh2o (mmol m-3 s-1), Sco2 (micromol m-3 s-1)
% Ui (m s-1) [length = 20], starts at TOP
% ustrnow (m s-1), dLAI (m2 m-3) [length = 20]
% GSV (mmol m-2 s-1) and ci (micromol m-2 s-1) [both length = 20]
% CaRef (micromol mol-1), RHref (%) humidity at ref. height

```

```

% OUTPUT Tair (K), Ea and eastar (Pa), Ca (micromol m-3)
% Hsoil and LSoil (H and LE from soil layer in W m-2)
% Fg is soil Fco2 (micromol m-2 s-1)

%input constants
global ustrnow; %friction velocity in m/s
zref = 7; %ref. height in m
global h; %canopy height in m (set here as 10 m)
delz = h/6; %divide canopy into 6 layers (in m)
layers = zref/delz;
sourcelay = h/delz; %
ustar=ustrnow;
%source strength for heat, 1st 6 layers, units: J m-3 s-1
S = fliplr(Sheat);
%source strength for H2O, 1st 6 layers, units: mmol m-3 s-1
S2 = fliplr(Sh2o);
%source strength for CO2, 1st 6 layers, units: micromol m-3 s-1
S3 = fliplr(Sco2);

%Soil respiration flux: Fg in units (micromol m-2 s-1)
Ftref=0.82;
Fg=(Ftref*exp((45212.85/(283.16*8.314))*(1-(283.16/Tsoil))));
%The soil respiration model is derived from night time flux data
%turbulence properties
kv = 0.41; %von-karman constant
d = 0.63*h; %zero-plane displacement depth
for i=1:layers
    z(i)=delz*(i-0.5); % z position is located in the middle of a layer
end
%Global Inputs
global Uinow
global h;
global LAlall;

%Call the Leuning function to get standard deviation of vertical velocity and Lagrangian time %scale
%based on Leuning, 2000
[sigw,Tl] = leuning1(h,z);

%*****
%Dispersion matrix for heat
for i=1:layers
    for j=1:sourcelay
        %See p.156 L.Gu Dissertation for term I.D.s
        %Go to delz/4 to either side of center of layer.
        %This is done to prevent evaluation of kernel(0) when i==j
        term1a(i,j) = (S(j)*delz/sigw(j))*...
        (kernel((z(i)-z(j)-0.25*delz)/(sigw(j)*Tl(j)))+kernel((z(i)+z(j))/(sigw(j)*Tl(j))));
        term1b(i,j) = (S(j)*delz/sigw(j))*...
        (kernel((z(i)-z(j)+0.25*delz)/(sigw(j)*Tl(j)))+kernel((z(i)+z(j))/(sigw(j)*Tl(j))));
        %average term1a and term1b
        term1(i,j) = (term1a(i,j)+term1b(i,j))/2;
        sum = 0; %keep a running sum to find term2, initialize as 0
        for k=i:layers %for summing from i to top layer
            if k >= j
                sum = sum + S(j)*delz*delz/((sigw(k))^2*Tl(k));
            end
        end
        term2(i,j) = sum;
        term3(i,j) = -(S(j)*delz/(sigw(j)))*kernel((z(layers)-z(j)+delz/10)/(sigw(j)*Tl(j)));
        delC(i,j) = term1(i,j)+term2(i,j)+term3(i,j);
        %Dispersion matrix
        Dij(i,j) = delC(i,j)/(S(j)*delz);
    end %end the inner j-loop
end %end the outer i-loop
%end Dispersion matrix calculations

```

```

%*****
%Compute the Fi term. It is the same for all scalars
for i=1:layers
sum = 0; %keep a running sum to find Fi, initialize as 0
for k=i:layers %for summing from i to top layer
sum = sum + delz/((sigw(k))^2*Tl(k));
end
Fi(i) = sum; %see p.159 L.Gu Dissertation to determine what this term means
end
%Begin Tleaf to Tair inversion code
%flip wind speed so u(1) is Ui at the forest floor
Ui = fliplr(Ui);
u = Ui;
ugr = u(1); %wind velocity next to the ground
z0s = 0.03; %temp. Roughness length for momentum for soil surface
%campbell and norman pg 69 and 96
z0s=0.4*10^-2*0.2; %temp. Roughness length for heat transfer from soil surface
gbh0 = kv^2*ugr/(log(0.5*0.05/z0s))^2; %conductance for soil heat transfer in 1st layer (m s-1)
DI = 0.72*1*0.01; %leaf dimension in m (0.72 x width of leaf(1cm) campbell and norman pg 107)
gbh = 6.62*10^(-3)*(u/DI).^0.5; %boundary layer conductance for heat (in m s-1)
Ts0 = Tsoil; %soil temperature in Kelvin
global TaFix;
TzR = TaFix+273; %air temperature at ref. height (converted from C to K)
delL = fliplr(dLAI); %LAI in 20 source layers. Make layer 1 = layer next to ground.
Tleaf = fliplr(Tleaf); %Need to flip Tleaf vector. Layer 1 = layer next to ground.
for i = 1:sourcelay;
for j = 1:sourcelay;
delta(i,j) = 2*delL(j)*Dij(i,j)*gbh(j); %see p. 162 L. Gu dissertation
if j==1
AT(i,j) = Fi(i)*gbh0 + delta(i,j);
elseif j > 1
AT(i,j) = delta(i,j);
end %end "if" statement
end %end "j" loop
%see p.163 L.Gu dissertation
sum = 0; %used to sum, initialize as zero
for k=1:sourcelay;
sum = sum + delta(i,k)*Tleaf(k);
end;
BT(i) = sum + Fi(i)*Ts0*gbh0 + TzR;
end %end "i" loop
BT = BT'; %make BT into a column vector
Ident = eye(sourcelay); %identity matrix w/ size (20 by 20)
TairA = inv(Ident + AT)*BT; %Tair for source layers
TairAadd = [TairA;zeros(1,layers-sourcelay)]; %tack on 0's to make vector 27 rows
%air temperature for non-source layers (i = 21 to 27)
for i = sourcelay+1:layers
sum = 0; %used to sum, initialize as zero
for j=1:sourcelay;
sum = sum + 2*delL(j)*Dij(i,j)*(Tleaf(j) - TairA(j))*gbh(j);
end;
TairB(i) = sum + Fi(i)*(Ts0 - TairA(1))*gbh0 + TzR;
end
TairB = TairB'; %make TairB into a column vector
Tair = TairAadd + TairB; %combine source and non-source layers
%end the Tleaf to Tair inversion code
%This is H from soil (W m-2)
Hsoil=1177*(Tsoil-TairA(1))*gbh0;
%*****
%Begin code for water vapor profile
%bulk conductance for soil water evaporation
gw0 = gbh0/0.924; % (based upon heat transfer from soil)
gbw = 7.294*10^(-3)*(u/DI).^0.5; %b.l. conductance for h2o per layer
gbw=gbh0/0.924;
%gbw=gbh;
GSV = (fliplr(GSV)*10^3); %flip so 1st layer is next to soil

```

```

gsw = GSV*22.4e-6; %stomatal conductance for h2o per layer (converted to m s-1)
gbsw = (gbw.*gsw)/(gbw + gsw); %combined conductance for h2o
%vector of sat. pressures based on Tleaf profile
estar = 611*exp(17.502*(Tleaf-273.15)/((Tleaf-273.15)+240.97)); %sat press at Tleaf (Pa)
hu = 1; %humidity (unitless) at soil surface
estarS = 611*exp(17.502*(Ts0-273.15)/((Ts0-273)+240.97)); %sat press at soil surface (Pa)
global RHFix;
ezR = 611*exp(17.502*(TzR-273)/((TzR-273.15)+240.97))*(RHFix/100); %press at z=R (Pa)
%Redo dispersion matrix, this time for water vapor
Dij = [];
for i=1:layers
for j=1:sourcelay
%See p.156 L.Gu Dissertation for term I.D.s
%Go to delz/4 to either side of center of layer.
%This is done to prevent evaluation of kernel(0) when i==j
term1a(i,j) = (S2(j)*delz/sig(j))*...
(kernel((z(i)-z(j)-0.25*delz)/(sig(j)*TI(j)))+kernel((z(i)+z(j))/(sig(j)*TI(j))));
term1b(i,j) = (S2(j)*delz/sig(j))*...
(kernel((z(i)-z(j)+0.25*delz)/(sig(j)*TI(j)))+kernel((z(i)+z(j))/(sig(j)*TI(j))));
%average term1a and term1b
term1(i,j) = (term1a(i,j)+term1b(i,j))/2;
sum = 0; %keep a running sum to find term2, initialize as 0
for k=i:layers %for summing from i to top layer
if k >= j
sum = sum + S2(j)*delz*delz/((sig(k))^2*TI(k));
end
end
term2(i,j) = sum;
term3(i,j) = -(S2(j)*delz/(sig(j)))*kernel((z(layers)-z(j)+delz/10)/(sig(j)*TI(j)));
%This (Ci-CR)i,j
delC(i,j) = term1(i,j)+term2(i,j)+term3(i,j);
%Dispersion matrix
Dij(i,j) = delC(i,j)/(S2(j)*delz);
end %end the inner j-loop
end %end the outer i-loop
%end Dispersion matrix calculations
%*****
%dDij=Dij*10;
for i = 1:sourcelay;
for j = 1:sourcelay;
beta(i,j) = delL(j)*Dij(i,j)*gbsw(j); %see p. 167 L. Gu dissertation
if j==1
AW(i,j) = Fi(i)*gw0 + beta(i,j);
elseif j > 1
AW(i,j) = beta(i,j);
end %end "if" statement
end %end "j" loop
%see p.168 L.Gu dissertation
sum = 0; %used to sum, initialize as zero
for k=1:sourcelay;
sum = sum + beta(i,k)*(estar(k)/Tleaf(k));
end;
BW(i) = sum + Fi(i)*hu*(estarS/Ts0)*gw0 + ezR/TzR;
end %end "i" loop
BW = BW'; %make BT into a column vector
EaA = TairA.*(inv(Ident + AW)*BW); %Ea in (Pa) for source layers
EaAadd = [EaA;zeros(1,layers-sourcelay)']; %tack on 0's to make vector 27 rows
%water vapor pressure for non-source layers (i = 21 to 27)
for i = sourcelay+1:layers
sum = 0; %used to sum, initialize as zero
for j=1:sourcelay;
sum = sum + delL(j)*Dij(i,j)*(estar(j)/Tleaf(j) - EaA(j)/TairA(j))*gbsw(j);
end;
EaB(i) = Tair(i)*(sum + Fi(i)*(estarS*hu/Ts0 - EaA(1)/TairA(1))*gw0 + ezR/TzR);
end
EaB = EaB'; %make TairB into a column vector

```

```

Ea = EaAadd + EaB; %combine source and non-source layers
eastar = 611*exp(17.502*(Tair-273)./((Tair-273)+240.97)); %sat press at Tair (Pa)
%This ends the water vapor profile part
LEsoil =(estarS*hu*(TairA(1)/Ts0) - EaA(1))*gw0; %LE from soil (W m-2)
%*****
%Begin the CO2 partial pressure code
%conductances in (m/s)
gbc = (7.294*10^(-3)*(u/DI).^0.5)/1.4; %b.l. conductance for h2o per layer
gsc = gsw/1.6; %stomatal conductance for CO2 per layer (m s-1)
gbsc = gbc.*gsc./(gbc + gsc); %combined conductance for CO2
ci = fliplr(ci); %flipped ci so 1st layer next to ground
Ci = (1000/24.4)*ci; %converted ci from (micromol mol-1) to (micromol m-3)..This is cm
global CaFix;
CzR = (1000/24.4)*CaFix;
%Redo dispersion matrix, this time for CO2
%Dij = [];
for i=1:layers
for j=1:sourcelay
%See p.156 L.Gu Dissertation for term I.D.s
%Go to delz/4 to either side of center of layer.
%This is done to prevent evaluation of kernel(0) when i==j
term1a(i,j) = (S3(j)*delz/sigw(j))*...
(kernel((z(i)-z(j)-0.25*delz)/(sigw(j)*TI(j)))+kernel((z(i)+z(j))/(sigw(j)*TI(j))));
term1b(i,j) = (S3(j)*delz/sigw(j))*...
(kernel((z(i)-z(j)+0.25*delz)/(sigw(j)*TI(j)))+kernel((z(i)+z(j))/(sigw(j)*TI(j))));
%average term1a and term1b
term1(i,j) = (term1a(i,j)+term1b(i,j))/2;
sum = 0; %keep a running sum to find term2, initialize as 0
for k=i:layers %for summing from i to top layer
if k >= j
sum = sum + S3(j)*delz*delz/((sigw(k))^2*TI(k));
end
end
term2(i,j) = sum;
term3(i,j) = -(S3(j)*delz/(sigw(j)))*kernel((z(layers)-z(j)+delz/10)/(sigw(j)*TI(j)));
%This (Ci-CR)i,j
delC(i,j) = term1(i,j)+term2(i,j)+term3(i,j);
%Dispersion matrix
Dij(i,j) = delC(i,j)/(S3(j)*delz);
end %end the inner j-loop
end %end the outer i-loop
%end Dispersion matrix calculations
%Dij=Dij/10;
for i = 1:sourcelay;
for j = 1:sourcelay;
gamma(i,j) = delL(j)*Dij(i,j)*gbsc(j); %see p. 167 L. Gu dissertation
AC(i,j) = gamma(i,j);
end %end "j" loop
%see p.168 L.Gu dissertation
sum = 0; %used to sum, initialize as zero
for k=1:sourcelay;
sum = sum + gamma(i,k)*(Ci(k)/Tleaf(k));
end;
BC(i) = sum + Fi(i)*Fg/Tair(1) + CzR/TzR;
end %end "i" loop
BC = BC'; %make BT into a column vector
CaA = TairA.*(inv(Ident + AC)*BC); %Ca in (micromol m-3) for source layers
CaAadd = [CaA;zeros(1,layers-sourcelay)']; %tack on 0's to make vector 27 rows
%CO2 concentration for non-source layers (i = 21 to 27)
for i = sourcelay+1:layers
sum = 0; %used to sum, initialize as zero
for j=1:sourcelay;
sum = sum + delL(j)*Dij(i,j)*(Ci(j)/Tleaf(j) - CaA(j)/TairA(j))*gbsc(j);
end;
CaB(i) = Tair(i)*(sum + Fi(i)*Fg/TairA(1) + CzR/TzR);
end

```

```
CaB = CaB'; %make CaB into a column vector
Ca = CaAadd + CaB; %combine source and non-source layers
% end function LNFJ
```

2) Sub-function PhotosynC4.m-adapted from Barr, J. G. (2005)

```
function equ = photosynC4(xx)
% This function forms the 24 equations which involve the energy balance equation and photosynthesis-
stomatal conductance equations
% declaring the global variables
global dLAI
global datanow
global Pabsnow
global Nabsnow
global Uinow
global Ta %Vector (1 by 9)
global RH %Vector (1 by 9)
global I
global Uinow
global CaRef %Vector (1 by 9)
global TaFix; %fixed reference height temperature (deg C)
global Ts; %fixed soil temp. at 2 cm depth (deg C)
global RHFix
global apres;
global swav
Tsoil=Ts+273.15;
%associate variables with "xx" these are the initial values.....
for i = 1:6
    TI(i) = xx(i);
    ci(i) = xx(i+6);
    cm(i)= xx(i+12);
    gsv(i)=xx(i+18);
end
equ = zeros(24,1); %all 24 functions set to 0
%***** inputs *****
u = Uinow; %VECTOR wind speed in m s-1
DI = 0.72*1.0*0.01; %leaf dimension in m (0.72 x width of leaf(1cm) campbell and norman pg %107)
%DI=0.035;
Ca = CaRef; %atmospheric CO2 mixing ratio at ALL heights (micromol mol-1)
gs0 = 0.038; %Ball and Berry intercept
gs1 =3.24; %Ball and Berry slope
%*****
%computed quantities
gbh = 6.62*10^(-3)*(u/DI).^0.5; %Vector boundary layer conductance for heat (in m s-1)
if size(Ta,1)==1
    Ta=Ta';
end
gbc = 232.6*(u/DI).^0.5; %VECTOR b.l. conductance for CO2 (mmol m-2 s-1)
gbw = 1.4*gbc; %VECTOR b.l. conductance for H2O (mmol m-2 s-1)
Ras=Pabsnow*0.25;% This converts back to Wm-2 for energy exchange
Nas=Nabsnow;
sigma = 5.67*10^(-8); %Stephan Boltzman constant (in W m-2 K-4)
frn=(Ras+Nas); % net shortwave
%Developing the functions
global datanow;
% Calling theLongwave radiative transfer matrix
[delINb] = longfunc2b(TI,Ts,TaFix); %takes Tleaf from 20 layers, Tsoil, and Tair
%The energy balance equations
for i = 1:6 %equations 1:20 are leaf energy balance equations
    estar(i) = 611*exp(17.502*TI(i)/(TI(i)+240.97)); %sat press at Tleaf (Pa)
    ea(i) = (RH(i)/100)*611*exp(17.502*Ta(i)/(Ta(i)+240.97)); %vapor press at Ta (Pa)
    Sh(i) = (1177*gbh(i)*(TI(i)-Ta(i))*dLAI(i)); %sensible heat transfer (in W m-2)
    lamdaSw(i) = 44.04*((estar(i)-ea(i))/apres)*(1/((1/gbw(i)) + (1/(gsv(i)*10^3))))*dLAI(i);
    %latent heat transfer
    equ(i) = Sh(i) + lamdaSw(i) - frn(i)-delINb(i);
end
%Photosynthesis equations are developed here
```

```

%calculations for mesophyll conductance Plant Physiology, December 2002,
%Vol. 130, pp. 1992–1998
delha=49.6;
dels=1.4;
cmes=20.0;
delhd=437.4;
R7=0.008314;
global vcmx25 vpmx25 jmx25
%photosynthesis constants
kc25=650;
ko25=450*10^3;
kp25=80;
Rgas=8.314 ;%(J k-1 mol)
gamma=0.000193; % rubisco specificity
oa=210*10^3;% assuming oxygen concentration in air
q = 0.40; %quantum light use efficiency (micromol e- (micromol photons)-1)
thetaJ=0.7; % theta for Jmax
x=0.4;% Partitioning factor
gs=3*10^-3;% in units of micromol m^-2 s^-2%conductance to bundle sheath
alfa=0.50;% constant for converting mesophyll concentration to bundle sheath.
% constants for vpmx and Vcmx temperature relationships
Evp=152271.166;
Hvp=727809.94;
Svp=2349.49;

Evj=70000.00;
Hvj=174243.92;
Svj=571.15;

Evc=43113.99;
Hvc=1116346.17;
Svc=3533.227;
% constants for kc, ko, kp
qkc=2.1;
qko=1.2;
qkp=2.1;

%%the initial outside Caref is used
for i = 1:6
g1(i)=10^3*0.1025*exp(cmes-(delha/(R7*(TI(i)+273.15))))/(1+exp((dels*(TI(i)+273.15)-
delhd)/(R7*(TI(i)+273.15))));
%g1 is mesophyll conductance units are mmol m-2 s-1
%cm(i)=0.7*Ca(i)*(((1.674-(6.1296*10^-2*TI(i)))+(1.1688*10^-3*(TI(i))^2)-(8.8741*10^-
6*(TI(i))^3))/0.73547);% Chen et al 1994-eq(12);
om(i)=oa*(((4.7*10^-2)-(1.3087*10^-3*TI(i)))+(2.5603*10^-5*TI(i)^2)-(2.1441*10^-7*TI(i)^3))/(2.6934*10^-
2));% chen et 1994 eqs(13)
%% temperature dependence for Kp Kc and Ko from Chen et al
kc(i)=kc25*qkc^(TI(i)-25)/10;
ko(i)=ko25*qko^(TI(i)-25)/10;
kp(i)=kp25*qkp^(TI(i)-25)/10;
%%relationships from Chen et al (Ecological modeling 73(1994) 63-80
vcmx(i)=vcmx25*(exp(-(Evc/Rgas)*((1/(TI(i)+273.15))-(1/298.15))))*(1+exp(((Svc*298.15)-
Hvc)/(Rgas*298.15)))/...
(1+exp(((Svc*(TI(i)+273.15))-Hvc)/(Rgas*(TI(i)+273.15))));
vpmx(i)=vpmx25*(exp(-(Evp/Rgas)*((1/(TI(i)+273.15))-(1/298.15))))*(1+exp(((Svp*298.15)-
Hvp)/(Rgas*298.15)))/...
((1+exp(((Svp*(TI(i)+273.15))-Hvp)/(Rgas*TI(i)+273.15))));
jmx(i)=jmx25*(exp(-(Evj/Rgas)*((1/(TI(i)+273.15))-(1/298.15))))*(1+exp(((Svj*298.15)-
Hvj)/(Rgas*298.15)))/...
((1+exp(((Svj*(TI(i)+273.15))-Hvj)/(Rgas*TI(i)+273.15))));
rd(i)=0.02*vcmx(i);
rm(i)=0.5*rd(i);
dPdL(i) = Pabsnow(i); %absorbed PAR per m2
vp(i)=(cm(i)*vpmx(i))/(cm(i)+kp(i));
vpr(i)=0.55*vpmx(i);
vp(i)=min(vp(i),vpr(i));

```

```

a1(i) = 1 - ((alfa/0.047) * (kc(i)/ko(i)));
b1(i) = -((vp(i)-rm(i)+(gs*cm(i)))+(vcmax(i)-rd(i))+gs*(kc(i)*(1+(om(i)/ko(i))))+(alfa/0.047)...
*(gamma*vcmax(i)+(rd(i)*kc(i)/ko(i))));
c1(i) = (vcmax(i)-rd(i))*(vp(i)-rm(i)+(gs*cm(i)))-((vcmax(i)*gs*gamma*om(i))+rd(i)*gs*kc(i)*(1+(om(i)/ko(i))));
Ac(i) = (-b1(i)-sqrt(b1(i)^2-(4*a1(i)*c1(i))))/2*a1(i);
os(i) = ((alfa*Ac(i))/(0.0473*10^3))+om(i);
cs(i) = ((gamma*os(i)+(kc(i)*(1+(os(i)/ko(i))))*(Ac(i)+rd(i))/vcmax(i)))/...
(1-(Ac(i)+rd(i))/vcmax(i));
jt(i) = ((q*dPdL(i)+jmax(i)) - ((q*dPdL(i)+jmax(i))^2 - 4*thetaJ*q*jmax(i)*dPdL(i))^0.5)/...
(2*thetaJ);
a2(i) = 1 - ((7*gamma*alfa)/(3*0.047));
b2(i) = - ( ((x*jt(i))/2)-rm(i)+(gs*cm(i)) + (((1-x)*jt(i))/3)-rd(i)) + (gs*((7*gamma*om(i))/3))...
+(((alfa*gamma)/0.047)*(((1-x)*jt(i))/3)+((7*rd(i))/3)) );
c2(i) = ( (((x*jt(i))/2)-rm(i)+(gs*cm(i)))*(((1-x)*jt(i))/3)-rd(i))...
-((gs*gamma*om(i))*(((1-x)*jt(i))/3)+((7*rd(i))/3)) );
Aj(i) = (-b2(i)-sqrt(b2(i)^2-(4*a2(i)*c2(i))))/(2*a2(i));
thetaW = 0.98;
An1(i) = (Aj(i)+Ac(i)-((Aj(i)+Ac(i))^2-4*thetaW*Aj(i)*Ac(i))^0.5)/(2*thetaW);
gmms(i) = (gamma*om(i)+(kc(i)*(1+(om(i)/ko(i))))*(rd(i)/vcmax(i)))/(1+rd(i)/vcmax(i));
gsc(i) = (gsv(i)*10^3)/1.6; %stomatal conductance for CO2 % to convert to mmol m-2 s-1;
gmma(i) = ((3*10^-3*kp(i)*gmms(i))/vpmax(i))+((rm(i)+kp(i))/vpmax(i));
An2(i) = An1(i)*(1-gmma(i)/ci(i))-rd(i); %net photosynthesis rate
An(i) = An2(i)*dLAI(i); %this is what happens in a layer
Cscorr(i) = ((Ca(i)*gbc(i)+(ci(i)*gsc(i)))/(gsc(i)+gbc(i)) - gmma(i);
BB(i) = (0.01*RH(i)*(An(i)/dLAI(i)))/Cscorr(i); %
equ(i+6) = -10^(-3)*(ci(i)-Ca(i))*((1/gbc(i)) + (1/gsc(i)))^(-1) - (An(i)/dLAI(i));
equ(i+12) = -10^(-3)*((cm(i)-ci(i))*g1(i)) - (An(i)/dLAI(i));
equ(i+18) = -gsv(i) + gs0 + gs1*BB(i);%
end %end "for" statement to loop though layers for stomatal conductance and carboxylation

```

3) PhotoOut4-function which outputs the source strength-adapted from Barr, J. G. (2005)

```

function [RHref,TairRef,Tsoil,gsv,Tl,Sheat,Sh2o,SCO2,cj] = PhotoOut4(sol)
%using the solution from PhotoSolve.m to output source strength of scalars
xx = sol;
%associate variables with "xx"
for i = 1:6
Tl(i) = xx(i);
ci(i) = xx(i+6);
cm(i) = xx(i+12);
gsv(i) = xx(i+18); % this is in molm-2 s-2
end
global Uinow
u = Uinow;
DI = 0.72*1.0*0.01; %leaf dimension in m (0.72 x width of leaf(1cm) campbell and norman pg %107)
global CaRef; %atmospheric CO2 mixing ratio (micromol mol-1) [Average inside the canopy]
global Ta
global RH %used in "BB" computation
global dLAI
global TaFix
global Ts
global apres
Ca = CaRef;
gs0 = 0.038;
gs1 = 3.24; %Ball and Berry slope from James
gbh = 6.62*10^(-3)*(u/DI).^0.5; %VECTOR boundary layer conductance for heat (in m s-1)
if size(Ta,1) == 1
Ta = Ta';
end
gbc = 232.6*(u/DI).^0.5; %VECTOR b.l. conductance for CO2 (mmol m-2 s-1)
gbw = 1.4*gbc; %VECTOR b.l. conductance for H2O (mmol m-2 s-1)
%declaring global variables
global Pabsnow
global Nabsnow
Ras = Pabsnow*0.235; % This converts back to watts/m2 for energy exchange (or divide by 4.6
Nas = Nabsnow;
sigma = 5.67*10^(-8); %Stephan Boltzman constant (in W m-2 K-4)

```

```

global vcmx25 vpmx25 jmx25 apres;
%photosynthesis constants
%the three below are in microbar
kc25=650;
ko25=450*10^3;
kp25=80;
Rgas=8.314 ;%(J k-1 mol-)
gamma=0.000193; % rubusci specificity
oa=210*10^3;% oxygen concentration in air
q = 0.40; %quantum light use efficiency (micromol e- (micromol photons)-1)
thetaJ=0.7; % theta for Jmax
x=0.4;% Partitioning factor
gs=2.5*10^-3;% in units of mol m^-2 s^-2%conductance to bundle sheath
alfa=0.50;% constant for converting mesophyll concetration to bundle sheath.

% constants for vpmx and vcmx
% for vpmx and Jmax
Evp=152271.166;
Hvp=727809.94;
Svp=2349.49;
Evj=70000.00;
Hvj=174243.92;
Svj=571.15;
%for vcmx
Evc=43113.99;
Hvc=1116346.17;
Svc=3533.227;
% constants for kc, ko, kp
qkc=2.1;
qko=1.2;
qkp=2.1;
%%for mesophyll conductance
delha=49.6;
dels=1.4;
cmes=20.0;
delhd=437.4;
R7=0.008314;

%from top to ground layer.
%*****
for i = 1:6 %equations 1:20 are leaf energy balance equations
estar(i) = 611*exp(17.502*TI(i)/(TI(i)+240.97)); %sat press at Tleaf (Pa)
ea(i) = (RH(i)/100)*611*exp(17.502*Ta(i)/(Ta(i)+240.97)); %vapor press at Ta (Pa)
Sh(i) = 1174*gbh(i)*(TI(i)-Ta(i))*dLAI(i); %sensible heat transfer (in W m-2)
lamdaSw(i) = 44.04*((estar(i)-ea(i))/apres)*(1/((1/gbw(i)) + (1/(gsv(i)*10^3))))*dLAI(i);

%%*****this is photosynthesis part*****
%cm(i)=0.7*Ca(i)*(((1.674-(6.1296*10^-2*TI(i)))+(1.1688*10^-3*(TI(i))^2)-(8.8741*10^-6*(TI(i))^3))/0.73547);% Chen et al 1994-eq(12);
om(i)=oa*(((4.7*10^-2)-(1.3087*10^-3*TI(i)))+(2.5603*10^-5*TI(i)^2)-(2.1441*10^-7*TI(i)^3))/(2.6934*10^-2);% chen et 1994 eqs(13)
%% temperature dependence for Kp Kc and Ko from Chen et al
kc(i)=kc25*qkc^((TI(i)-25)/10);
ko(i)=ko25*qko^((TI(i)-25)/10);
kp(i)=kp25*qkp^((TI(i)-25)/10);
%%relationships from Chen et al (Ecological modeling 73(1994) 63-80
g1(i)=10^3*0.1025*exp((cmes-(delha/(R7*(TI(i)+273.15))))/(1+exp((dels*(TI(i)+273.15)-delhd)/(R7*(TI(i)+273.15)))));
%g1 is mesophyll conductance units are mmol m-2 s-1
vcmx(i)=vcmx25*(exp(-(Evc/Rgas)*((1/(TI(i)+273.15))-(1/298.15)))) *(1+exp(((Svc*298.15)-Hvc)/(Rgas*298.15)))/...
(1+exp(((Svc*(TI(i)+273.15)-Hvc)/(Rgas*(TI(i)+273.15)))));
vpmx(i)=vpmx25*(exp(-(Evp/Rgas)*((1/(TI(i)+273.15))-(1/298.15)))) *(1+exp(((Svp*298.15)-Hvp)/(Rgas*298.15)))/...
((1+exp(((Svp*(TI(i)+273.15)-Hvp)/(Rgas*TI(i)+273.15)))));

```

```

jmax(i)=jmax25*(exp(-(Evj/Rgas)*((1/(TI(i)+273.15))-(1/298.15)))) *(1+exp(((Svj*298.15)-
Hvj)/(Rgas*298.15)))/...
((1+exp(((Svj*(TI(i)+273.15)-Hvj)/(Rgas*TI(i)+273.15)))));
rd(i)=0.02*vcmax(i);
rm(i)=0.5*rd(i);
dPdL(i) = Pabsnow(i);
vp(i)=(cm(i)*vpmax(i))/(cm(i)+kp(i));
vpr(i)=0.55*vpmax(i);
vp(i)=min(vp(i),vpr(i));
%Photosynthesis C4 model, von Caemmerer (1999)
a1(i) = 1-((alfa/0.047)*(kc(i)/ko(i)));
b1(i)=-((vp(i)-rm(i)+(gs*cm(i)))+(vcmax(i)-rd(i))+gs*(kc(i)*(1+(om(i)/ko(i))))+(alfa/0.047)...
*(gamma*vcmax(i)+(rd(i)*kc(i)/ko(i))));
c1(i)=(vcmax(i)-rd(i))*(vp(i)-rm(i)+(gs*cm(i)))-((vcmax(i)*gs*gamma*om(i))+rd(i)*gs*kc(i)*(1+(om(i)/ko(i))));
Ac(i)=-b1(i)-sqrt(b1(i)^2-(4*a1(i)*c1(i)))/2*a1(i);
os(i)=((alfa*Ac(i))/0.047)+om(i);
cs(i)=((gamma*os(i))+(kc(i)*(1+(os(i)/ko(i))))*(Ac(i)+rd(i))/vcmax(i))/...
(1-((Ac(i)+rd(i))/vcmax(i)));
jt(i) = ((q*dPdL(i)+jmax(i)) - ((q*dPdL(i)+jmax(i))^2 - 4*thetaJ*q*jmax(i)*dPdL(i))^0.5)/...
(2*thetaJ);
a2(i)=1-((7*gamma*alfa)/(3*0.047));
b2(i)=-(((x*jt(i))/2)-rm(i)+(gs*cm(i))) + (((1-x)*jt(i))/3)-rd(i) + (gs*((7*gamma*om(i))/3))...
+((alfa*gamma)/0.047)*(((1-x)*jt(i))/3)+((7*rd(i))/3)) );
c2(i)=( (((x*jt(i))/2)-rm(i)+(gs*cm(i)))*(((1-x)*jt(i))/3)-rd(i))...
-((gs*gamma*om(i))*(((1-x)*jt(i))/3)+((7*rd(i))/3)) );
Aj(i)=-b2(i)-sqrt(b2(i)^2-(4*a2(i)*c2(i)))/(2*a2(i));
thetaW=0.98;
%smooth function for transition between light limited and CO2 limited stages
An1(i) = (Aj(i)+Ac(i)-((Aj(i)+Ac(i))^2-4*thetaW*Aj(i)*Ac(i))^0.5)/(2*thetaW);
gsc(i) = (10^3*gsv(i))/1.6; %stomatal conductance for CO2 in mmol m-2 s-1;
gmms(i)=(gamma*om(i)+(kc(i)*(1+(om(i)/ko(i))))*(rd(i)/vcmax(i)))/(1+rd(i)/vcmax(i));
gmma(i)=((3*10^-3*kp(i)*gmms(i))/vpmax(i))+((rm(i)+kp(i))/vpmax(i));
%CO2 compensation point
An2(i) = An1(i)*(1-gmma(i)/ci(i))-rd(i); %net photosynthesis rate
An(i)=An2(i)*dLAI(i);
end

%%%%%%%%%% Finished the output from equation solving.
%*****

RHref = RH;
%CaRef is global (defined above)
TairRef = Ta+273; %Convert to Kelvin
%ustrnow defined at current time step above
Tsoil = Ts+273; %Convert soil temp. to Kelvin
TI = TI+273.15; %Convert leaf temp. to Kelvin
Sheat =Sh;
Sh2o = lamdaSw/44.04;% units are mmol m^-2 s^-1
Sco2 = An; %in units of micromol m^-2 s^-1
%end of function

```

3) Multiple scattering model-for PAR and NIR-based on Zhao and Qualls, 2007-function-multishort.m

```

%Same model implemented for NIR wave length also
function [Pabs,dLAI] = multishort(data,xc)
%the input is in micromoles m-2 s-1
%Define all variables needed from "data" and otherwise.
global DecDOY
time = data(:,4)+data(:,5); %decimal time
PART = data(:,31); %average PAR (micromol m-2 s-1)
yr=data(1,1); %extracting the year
mons=data(1,2);%extracting the month

for pt=1:length(PART)
location.longitude = -75.82482; % longitude of fowling point
location.latitude =37.41510 ; % latitude for fowling point
location.altitude = 0.0;% at sea level
times.year = 2007;% year is fixed

```

```

times.month = mons;
times.day = unique(data(:,3));
times.hour = data(pt,4);
minut=data(pt,5);
if minut==0
times.min = 0;
else
times.min = (minut-0.20)*100;
end
times.sec = 0;
if DecDOY >= 95
times.UTC = -4; %add 1 to the time day light saving-accounting
else
times.UTC = -5;
end
Ssc = 1370; %solar constant (W m-2)
%extra-terrestrial irradiance
sun = sun_position(times, location); %sun.zenith and sun.
%This function compute the sun position (zenith and azimuth angle at the observer
% location) as a function of the observer local time and position.
%Reda, I., Andreas, A. (2003) Solar position algorithm for solar
%radiation application. National Renewable Energy Laboratory (NREL)
%Technical report NREL/TP-560-34302.
suzen(pt)=0.0174532925*(sun.zenith);
sinele(pt) = cosd(sun.zenith);% as zenith and elevation angles are complementary
% sin of solar elevation angle is in radians
bet1=asin(sinele(pt));% solar elevation angle in radians
bet(pt)=(180/pi)*(bet1);% solar elevation angle in degrees
Se(pt) = Ssc*(1+0.033*cos(2*pi*DecDOY/365))*sinele(pt);
end
%Compute the diffuse PAR component -Spitters et al 1986 *****
S = data(:,14); %solar irradiance (W m-2)
Ssc = 1370; %solar constant (W m-2)
inse=find(Se<0);
Se(inse)=0;
%clearness index (kt)
kt = S./Se';
kt(isinf(kt))=0;
kt(find(kt<0))=0;
for i = 1:length(kt);
if kt(i)>= 0 & kt(i)<=0.3
fract(i) = kt(i)*(1.020-(0.254*kt(i))+(0.0123*sinele(i)));
end
if kt(i) > 0.3 & kt(i) < 0.78
fract(i)= kt(i)*(1.400-(1.749*kt(i))+(0.177*sinele(i)));
end
if kt(i) >= 0.78
fract(i) = kt(i)*((0.486*kt(i))-(0.182*sinele(i)));
end
q(i)=fract(i)/kt(i);
rati(i)=((1+(0.3*(1-q(i)^2)))^q(i))/(1+(1-q(i)^2)*(cosd(90-bet(i)))^2*(cosd(bet(i)))^3);% ratio of diffused to direct
end
rati=rati';
PARf = rati.*PART; %diffuse PAR vector
PARd = PART - PARf; %direct PAR vector
lefare = load('grass.txt');
xx = lefare(:,1);
yy = lefare(:,2);
%yy represents the cumulative leaf area from bottom to top
% leaf area in each layer is added up-the first is the bottom layer
%now getting leaf area in each layer-the first is the bottom layer
for j=1:6;
dLAI(j) = yy(j+1)-yy(j);
end;
dLAI2=fliplr(dLAI); % flipping this so that the first is the top layer;
yy2=cumsum(dLAI2); %now we have a cumulative from the top to bottom;

```

```

%now to flip this so that the first value represents the cumulative at the
%ground, we dont need that in the calculations so we start from the 2nd value
% to the last value
yy3=flipr(yy2);
LAlall = 2.086144; %total LAI of the canopy
%% extinction coefficient from Campbell and Norman, (Campbell, 1986)
%%now doing for each time step in the day and then build a matrix for a day
ak=sqrt(xc^2+tan(suzen.^2));
bk=xc+(1.774*(xc+1.182)^-0.7333);
kpsi=ak/bk;
ind=find(PARt<5);
kpsi(ind)=0;
ind2=find(cos(suzen)<0.001);
kpsi(ind2)=0;
for f=1:length(PARf)
if kpsi(f)>0
sg(f) =PARd(f)-PARd(f)*(1-exp((-kpsi(f)*LAlall)); % direct light on ground
%now finding light on other layers , the top layer receives the full
%light and so we start from the layer just above ground as the ground
%layer receives the sg(1)
for p = 2:length(yy3)
S4(p-1) = PARd(f) - PARd(f)*(1-(exp((-kpsi(f)*yy3(p)))));
end
S1 = [S4';PARd(f)]; % this is profile of direct light, the first value is the light
%on the layer just above the ground and the last value is what reaches
%the top of the canopy..There are five values for six layers
m = 6;%(number of layers of the canopy)
a = zeros(2*m+2,2*m+2); %defining A;
C = zeros(2*m+2,1);
ref_leaf=0.11;%leaf reflection coefficient (http://www.cgd.ucar.edu/tss/clm/pfts/pft-physiology.htm)
%%loop to find transmissivity of different layers
% here we need the leaf area of different layers as we are trying to find
% transmissivity of that section.
diffused = PARf(f); % diffuse radiation reaching top of canopy
alf=0.80;% leaf absorptivity coefficient -Campbell and Norman;
beta = 0.12;%leaf reflection coefficient (http://www.cgd.ucar.edu/tss/clm/pfts/pft-physiology.htm)
delt = 0.08; %leaf transmission coefficient(http://www.cgd.ucar.edu/tss/clm/pfts/pft-physiology.htm).
r = ((2/3)*(beta/(beta+delt)))+(1/3)*(delt/(delt+beta));% this is the forward scattering for any layer
%backward scattering is 1-r for diffuse radiation
%since scattering involves both reflection and transmission, the absorption
%of diffuse radiation for a layer is 1-((1-r)+r);
%alfa=0.80; %absorbitivity of diffuse radiation for a layer-constant
%as alfa bet and delt are assumed to be same through out canopy
for kl=1:6% number of layers % going from bottom to top;
tpsi(kl)=exp(-sqrt(alf)*kpsi(f)*dLAI(kl));
%campbell and Norman, pg no 254)from gourdiaan, 1977
%the 0.80 is the leaf absorptivity for PAR and dLAI is alinged from
%bottom to top, dLAI(1) is the thickness of the layer above ground
zenang=suzen(f);
lai=dLAI(kl);
td1(kl)=quad(@tdiff,0,pi/2);
td(kl)=2*td1(kl);
kdi(kl)=-log(td(kl))/dLAI(kl);
rp(kl)=((2*kdi(kl))/(kdi(kl)+1))*0.056;
rp2(kl)=rp(kl)-(rp(kl)-0.1100)*exp(-2*sqrt(0.8)*kdi(kl)*dLAI(kl));
rp2(kl)=0.09;
td(kl)=0.06;
%assuming reflectivity for diffuse radiation as 0.09
alfa(kl)=1-(td(kl)+rp2(kl)); % absorbtivity for diffused radiation
%campbell and Norman, pg no 255)
end
ref_soil = 0.1100; % soil reflectivity for PAR (based on data from dark soils)
alfa0 = 1-ref_soil;
%% part-a from bottom to top
numlayers=6;

```

```

a(1,1)=1;
for i = 1:numlayers;
a(2*i,2*i-1) = -(td(i) + ((1-td(i))* (1-alfa(i))*(1-r)));
if i == 1
a(2*i,2*i) = -1*(td(i) + ((1-td(i))*(1-alfa(i))*(1-r)))*(1-alfa0)*(1-0);
else
a(2*i,2*i) = -r*(td(i) + ((1-td(i))*(1-alfa(i))*(1-r)))*(1-alfa(i-1))*(1-td(i-1));
end
if i ==1
a(2*i,2*i+1) = (1-(1*r*(1-alfa0)*(1-0)*(1-alfa(i))*(1-td(i))));
else
a(2*i,2*i+1) = (1-(r*r*(1-alfa(i-1))*(1-td(i-1))*(1-alfa(i))*(1-td(i))));
end
if j == numlayers
a(2*i+1,2*i) = (1-(r*0*(1-alfa(i))*(1-td(i))*(1-0)*(1-1)));
else
a(2*i+1,2*i) = (1-(r*r*(1-alfa(i))*(1-td(i))*(1-alfa(i+1))*(1-td(i+1))));
end
if i == numlayers
a(2*i+1,2*i+1) = -0*(td(i)+((1-td(i))*(1-alfa(i))*(1-r)))*(1-0)*(1-1);
else
a(2*i+1,2*i+1) = -r*(td(i)+((1-td(i))*(1-alfa(i))*(1-r)))*(1-alfa(i+1))*(1-td(i+1));
end
a(2*i+1,2*i+2) = -(td(i)+((1-td(i))*(1-alfa(i))*(1-r)));
end
a(2*numlayers+2,2*numlayers+2) = 1;
rpsi = 0.5+(0.334*(beta-delt)/(beta+delt))*cosd(suzen(f));
Sg = sg(f);
C(1) = ref_soil*Sg;
j = 2 ;
for i = 1:numlayers
if i == 1
C(j) = (1-(1*r*(1-alfa0)*(1-0)*(1-alfa(i))*(1-td(i))))*rpsi*(1-tpsi(i))*(1-alfa(i))*S1(i);
else
C(j) = (1-(r*r*(1-alfa(i-1))*(1-td(i-1))*(1-alfa(i))*(1-td(i))))*rpsi*(1-tpsi(i))*(1-alfa(i))*S1(i);
end
if i+1 > numlayers
C(j+1) = (1- (r*0 *(1-alfa(i))*(1-td(i))*(1-0)*(1-1)))*(1-tpsi(i))*(1-alfa(i))*(1-rpsi)*S1(i);
else
C(j+1) = (1- (r*r *(1-alfa(i))*(1-td(i))*(1-alfa(i+1))*(1-td(i+1))))*(1-tpsi(i))*(1-alfa(i))*(1-rpsi)*S1(i);
end
j = j+2;
end
C(end) = diffused;
x = thomas(a,C); % solving the system of linear equations using function Thomas.m
swu = x(1:2:length(x));% Upward fraction
swd = x(2:2:length(x));% downward fraction
%The downward hemispheric PAR flux from layer i to i+1, no soil layer
%so technically speaking you are dealing with SWd(i+1), which refers to the
%first layer above the ground to the one layer- below the transparent
%atmospheric layer, which is the top plant layer
for i = 1:length(swd)-1
if i ==1 % for soil
SWd(i) = (swd(i)/((1-(1*r*(1-alfa0)*(1-0)*(1-alfa(i))*(1-td(i)))))...
+ ((r*(1-alfa(i))*(1-td(i))*swu(i))/(1-(1*r*(1-alfa0)*(1-0)*(1-alfa(i))*(1-td(i))));
else
SWd(i) = (swd(i)/((1-(r*r*(1-alfa(i-1))*(1-td(i-1))*(1-alfa(i))*(1-td(i)))))...
+ ((r*(1-alfa(i-1))*(1-td(i-1))*swu(i))/(1-(r*r*(1-alfa(i-1))*(1-td(i-1))*(1-alfa(i))*(1-td(i))));
end
end
%This is the total upward hemispheric radiation from each layer. The soil
%layer is not considered here as we are not interested in the net radiation
%from the soil layer
for i = 2:length(swu)
if i == length(swu)
SWu(i) = (swu(i)/((1-(r*0*(1-alfa(i-1))*(1-td(i-1))*(1-0)*(1-1)))))...

```

```

+ ((r*(1-alfa(i-1))*(1-td(i-1))*swd(i))/(1-(r*0*(1-alfa(i-1))*(1-td(i-1))*(1-0)*(1-1)))));
else
SWu(i) = (swu(i)/((1-(r*r*(1-alfa(i-1))*(1-td(i-1))*(1-alfa(i))*(1-td(i)))))...
+ ((r*(1-alfa(i-1))*(1-td(i-1))*swd(i))/(1-(r*r*(1-alfa(i-1))*(1-td(i-1))*(1-alfa(i))*(1-td(i))))));
end
end
SWg = SWd(1);
%redeclaring the total hemispheric upward and downward components
swu1 = SWu(2:end);
swd1 = SWd;
Spar = [Sg;S1];
%direct PAR absorbed in the different canopy layers
parabs = diff(Spar);
f3 = size(parabs);
if f3(2) > 1
parabs = parabs';
end
Pabs(1:length(parabs),f) = parabs+(swd1-swu1)';
else
Pabs(1:6,f) = zeros(6,1);
end
end
function tpsi=tdiff(x5)
%the input of zenith angle should be in radians
%tidrr is the direct transmissivity for a layer
alf=0.80;
global zenang lai
tpsi= exp(-sqrt(alf).*(sqrt(0.96^2+tan(zenang^2)))/0.96+(1.774*(0.96+1.182).^
0.7333)).*lai).*sin(x5).*cos(x5);
% function tdi=tdiffu(td2,x5)
% %the input of zenith angle should be in radians
% %tidrr is the diffuse transmissivity for a layer
% tdi=td2.*sin(x5).*cos(x5);

```

4) Wind profile sub-function-adapted from Barr, J. G. 2005-function-WindProf3.m

```

%This function outputs wind speed through the canopy (Ui) at each level (xx)
%Ustar is computed based on neutral conditions
function [Uall,ustar] = WindProf3(data); %data input is "datanow"
global h %Total height of the canopy = 20 m
lefare = load('grass.txt'); % loading leaf area
%[xx,yy] = betadist2(h);
xx = lefare(:,1)';
yy = lefare(:,3)'; % use cumulative LAI from height h to 0
%Identify required variables
Ta = data(38) + 273.15; %air temperature (in K)
Rnet = data(24); %in (W m-2)
%I assume that H = LE and H+LE = 0.7*Rnet
LE = 0.51*Rnet; %latent heat flux (W m-2)
H = 0.31*Rnet; %sensible heat flux (W m-2)
Uref = data(28); %Ws (m/s)
%Determine the horizontal wind speed profile in the canopy
hc = 0.60; %Top of the canopy (m)
global LAIall;
Cd = 0.2; %drag coeff. of foliage elements (see p. 89)
Pm = 1; %Momentum shelter factor
zeta_h = (Cd/Pm)*LAIall; %zeta at height, h.
%d is the displacement height in the canopy
d = 0.635*hc;
z0 = 0.10*hc; %zero-plane displacement height (m)
zR = 7; %wind speed measurement reference height (m)
g=9.8;
rho=1.2;
Cp=1010;
k = 0.4; %The von karman constant
%Compute diabatic psi functions
z1 = hc; %Do this at z1 = hc

```

```

%Need an artificial ustar (not from sonic)
ustar = 0.32*Uref; %friction velocity (m/s), parameterized by Massman
ustar=(Uref*0.41)/(log((7-d)/z0));
L = -(ustar^3/0.4)/((9.8/Ta)*H/(rho*Cp)); %L is in meters.
zadd = [0.7 :0.1: 7]'; %levels above the canopy to the reference height
jd=length(zadd);
%assume neutral conditions if L is not available
if L == 0
psim = zeros(jd,1);
end
%Determine diabatic correction
if L > 0;
psim = -5*zadd/L;
elseif L < 0;
x = (1-16*zadd/L).^0.25;
psim = log(((1+x.^2)/2).*((1+x)/2).^2)-2*atan(x)+pi/2;
end;
Uhc = (ustar/0.4)*(log((z1-d)/z0));%psim(1); %Ws at height, hc (m/s)
U2 = (ustar/0.4)*(log((zadd-d)/z0));%psim); %wind speed from 0.60 to 7 m
%*****
%Determine wind speed profile inside the canopy
u_h = Uhc; %Ws at the top of the canopy
%Get the cumulative LAI from height 0 to z. lefare = load('grass.txt');
%the second line of this file is LAI from 0 to h
xx = lefare(:,1)';
yy = lefare(:,3)';
yy = LAIall - yy;
xx = flipud(xx)'; %heights from 0 to h
z = xx(2:end); %height from 1 to h
yy=flipud(yy)';
dL = yy(2:end); %cumulative LAI from 0 to z (for z = 1 to h)
%Zeta is the cumulative leaf area drag area per unit planform area
zeta = (Cd/Pm)*dL;
%Define the total energy variance:
%(sigma_e)^2 = (sigma_u)^2 + (sigma_v)^2 + (sigma_w)^2
%Define constants first:
nu1 = 0.3024; nu2 = 3.441; nu3 = 36.15; %see p.86
n = zeta_h*u_h^2/(2*ustar^2);
U1 = Uhc*exp(-n*(1-zeta/zeta_h)); %wind speed from 0.7 to 7 m
Uall = [U1;U2]; %wind speed from 1 to 7 m
Uall = flipud(Uall); %wind speed from 7 to 1 m
% end of function for wind profile

```

5) Lagrangian time scale and standard deviation of vertical velocity following Leuning, 2000- function-leuning1.m

```

function [sigwn,tln] = leuning1(h,z)
global ustrnow
ustar = ustrnow;
if ustar == 0
ustar = 0.4;
end
global Uinow
%close to the surface theta can be assumed to be temperature
u_h = Uinow(1); %Ws at the top of the canopy
global datanow;
global Pabsnow;
rnets=sum(Pabsnow)*0.55;
thet=273.15+datanow(35);
g=9.8; %acceleration due to gravity
nlys=6; % number of layers
c1=0.2;
c2=1.5;
%the z/hc values
%diabatic correction terms
hflex=datanow(12);
if isnan(hflex)

```

```

    hflex=rnets*0.35;
else
    hflex=hflex;
end
khf=hflex/1126.72;
L=-(ustar^3*thet)/(0.41*9.8*khf);
zref=2.3*0.6;% transition layer.
zall=z;
zhc=zall/h;
%for sigw
a=0.850;
b=1.25;
d=-1;
thet=0.98;
%for TL
a2=0.256;
a3=0.850;
b2=0.40;
b3=0.41;
d2=1;
d3=-1;
for p=1:length(zhc)
if zall(p)<0.8*h
sigw(p)=ustar*c1*exp(c2*zhc(p));
else
sigw(p)=ustar*(((a*zhc(p))+b)+(d*sqrt(((a*zhc(p))+b)^2-(4*thet*a*b*(zhc(p))))))/(2*thet);
end
if zhc(p)>=0.25
zhc(p)=zhc(p)-0.8;
tl(p)=((((a2*zhc(p))+b2)+(d2*sqrt(((a2*zhc(p))+b2)^2-(4*thet*a2*b2*(zhc(p))))))/(2*thet))*h)/ustar;
elseif zhc(p)<0.25
zhc(p)=4*zhc(p);
tl(p)=((((a3*zhc(p))+b3)+(d3*sqrt(((a3*zhc(p))+b3)^2-(4*thet*a3*b3*(zhc(p))))))/(2*thet))*h)/ustar;
end
end
sig_wall=sigw';
TLall=tl';
%its from bottom to top
for i=1:length(z)
if z(i)<zref
wrig=0.60/L;
else
wrig=(z(i)-(0.65*z(i)))/L;
end
zbyl=z(i)/L;
if zbyl<-2
zbyl=-2;
elseif zbyl>1
zbyl=1;
end
if(zbyl>=-2 & zbyl <=0)
phiw(i)=1.25*(1+(3*abs(zbyl)))^(1/3);
phih(i)=(1+(16*abs(zbyl)))^(-1/2);
else (zbyl>=0 & zbyl <=1);
phiw(i)=(1.25*(1+(0.2*abs(zbyl))));
phih(i)=(1+(5*(zbyl)));
end
sigwn(i)=(sigw(i)*phiw(i))/1.25;
tln(i)=tl(i)*(1/phih(i)*(1.25^2/phiw(i)^2));
end

```

6) LRTM –Long wave radiative transfer Matrix, following Gu, 1998.code adapted from Barr, J. G. (2005)-function LRTM.m

%This function solves the long wave radiative transfer matrix
function [alpha] = LRTM(lat) %takes total LAI as input

```

h = 0.60; %Total height of the canopy (in m)
lefare = load('grass.txt');
xx = lefare(:,1);
yy = lefare(:,3); % this case use the cumulative from top to bottom
yyp=yy(2:end);
m = length(yyp); %# of foliage layers
%soil = layer 1; sky = layer m+2
for i = 2:m+1;
    la(i) = yyp(m+2-i);
end;
temp = la; %store current "la" in temp
clear la; %remove "la"
la = [temp(2:end),0]; %"la" is now cum LAI at top of layer i
alpha = [];
for i=1:m+2;
for j=1:m+2;
    if (i==1 & j==1) | (i==m+2 & j==m+2); %1 and 9 ok
alpha(i,j) = -1;
elseif i==1 & j>1 & j<m+2; %2
alpha(i,j) = CLIF(lat-la(j-1))-CLIF(lat-la(j));
elseif (i==1 & j==m+2) | (i==m+2 & j==1); %3 and 7 ok
alpha(i,j) = CLIF(lat);
elseif i>2 & i<m+2 & j<=i-1 & j>1; %4 ok
alpha(i,j) = CLIF(la(j)-la(i-1))-CLIF(la(j-1)-la(i-1))-...
CLIF(la(j)-la(i))+CLIF(la(j-1)-la(i));
elseif i>1 & i<m+2 & j==i; %5
alpha(i,j) = 2*CLIF(la(i-1)-la(i))-2;
elseif i>1 & i<m+2 & j>=i+1 & j<m+2; %6 ok
alpha(i,j) = CLIF(la(i)-la(j-1))-CLIF(la(i)-la(j))-...
CLIF(la(i-1)-la(j-1))+CLIF(la(i-1)-la(j));
elseif i==m+2 & j>1 & j<m+2; %8 ok
alpha(i,j) = CLIF(la(j))-CLIF(la(j-1));
elseif i>1 & i<m+2 & j==m+2; %10 ok
alpha(i,j) = CLIF(la(i))-CLIF(la(i-1));
elseif i>1 & i<m+2 & j==1; %11 ok
alpha(i,j) = CLIF(lat-la(i-1))-CLIF(lat-la(i));
end; %end if,else if
end; %end the inner j loop
end; %end the outer i loop
%This is a sub-function called by LRTM
%canopy longwave integral function
%For a spherical shaped canopy
function [CLISum] = CLIF(l);
for i = 1:51;
    mu(i) = (i-0.9999)/50; %goes from 0 to 1
    fun(i) = 2*exp(-l*0.5/mu(i))*mu(i);
end;
sum = 0;
for i = 1:50;
integ(i) = 0.5*(fun(i+1)+fun(i))*(mu(i+1)-mu(i)); %integral of each piece
sum = sum+integ(i); %sum up all the pieces for total integral
end;
CLISum = sum; %output the total integrated area

```

7) Longwave absorbed calculations –function longfunc2b.m-adapted from Barr, J. G (2005).

```

%longfunc takes leaf temperature profile (layers 1:20, top=1) as input
%as well as soil temp (Tsoil) and air temp (Tair)
%Output = delNb. This is net longwave absorbed (W m-2) per foliage layer (layer 1 is top layer)
function [delNb] = longfunc2b(Tlprof,Tsoil,Tair)
global alphaLRTM;
global datanow
rhsky=datanow(36); % rh in air
tsky=datanow(35)+273.15; % tair
essky= 10*0.6112*exp((17.67*(tsky-273.15))/((tsky-273.15)+243.5)); %in hpa % saturation pressure in air
in hpa
easky=(rhsky/100)*essky;% in hpa

```

```
esky=1.24*(easky/tsky)^(1/7); % emissivity of sky
%%estimate sky emissivity.....
%Prata, 1996 A.J. Prata, A new long-wave formula for estimating downward clear-sky radiation at the
surface, Q. J. R. Meteorol. Soc. 122 (1996),
%pp. 1127–1151. Full Text via CrossRef | View Record in Scopus | Cited %By in Scopus (52)
Ti = flipud(Tlprof); %flip leaf temperature profile
Ti = [Tsoil;Ti;Tair]; %Tsoil, Ti (20 layers), Tair
sigma = 5.67*10^(-8);
emit = sigma*(Ti+273.15).^4;
emit(end)=emit(end)*esky;
delN = alphaLRTM*emit; %net longwave absorbed soil=1, sky=22
delNflip = flipud(delN); %flip delN sky=1, soil=22
delNb = delNflip(2:7); %output only delN for foliage layers (layer 1 %= top layer)
```